



FRIEDRICH-SCHILLER- UNIVERSITÄT JENA

Functional Carbon Nanomembrane: Microfabrication and Functionalization

Dissertation
(kumulativ)

zur Erlangung des akademischen Grades
doctor rerum naturalium (Dr. rer. nat)

vorgelegt dem Rat der Chemisch-Geowissenschaftlichen Fakultät der
Friedrich-Schiller-Universität Jena

von Zian Tang, M. Sc.

geboren am 31.08.1988 in Hebei China

Dissertation, Friedrich-Schiller-Universität Jena, [2020]

Gutachter:

1. Prof. Dr. Andrey Turchanin.

Institut für Physikalische Chemie, Friedrich-Schiller-Universität Jena.

2. Prof. Dr. Benjamin Dietzek.

Institut für Physikalische Chemie, Friedrich-Schiller-Universität Jena.

Tag der Verteidigung: 17.06.2020

Table of Contents

Table of Contents	4
List of Abbreviations	6
1. Introduction.....	8
2. Experimental	14
2.1 Sample Preparation.....	14
2.1.1 Preparation of CNMs	14
2.1.2 Synthesis of Graphene.....	15
2.1.3 Chemical Functionalization of CNMs	15
2.1.4 Transfer of Graphene and CNMs	16
2.1.5 Loading (or Unloading) Metal Ions on (or from) the CNMs	17
2.2 Experimental Methods.....	18
2.2.1 X-Ray Photoelectron Spectroscopy.....	18
2.2.2 Raman Spectroscopy.....	19
2.2.3 Electrical Transport Measurements	19
2.2.4 Helium Ion Microscopy.....	19
2.2.5 Atomic Force Microscopy	20
2.2.6 Other Microscopic Techniques	20
3. Results and Discussion.....	21
3.1 Electrochemical Delamination Assisted Transfer of CNMs	21
3.2 Nanoporous CNMs for Selective Ion Sieving.....	29
3.3 CNM Based Optical Metamembranes.....	34
3.4 Smart Molecular Nanosheets for Electron Cryo-microscopy.....	37
3.5 Photoswitchable CNMs for Implementation in Graphene Field-Effect Transistors	43
4. Summary.....	50
5. Zusammenfassung	54
6. Reference.....	58
7. Curriulum Vitae.....	77
8. Publication List	78
Publications for This Thesis: P1 to P5.....	80

P1. Electrochemical delamination assisted transfer of molecular nanosheets	80
P2. Selective ion sieving through arrays of sub-nanometer nanopores in chemically tunable 2D carbon membranes	89
P3. Plasmonic metasurfaces situated on ultrathin carbon nanomembranes	97
P4. Smart molecular nanosheets for advanced preparation of biological samples in electron cryo-microscopy.....	105
P5. Optically triggered control of the charge carrier density in chemically functionalized graphene field effect transistors	143
Documentation of Authorship.....	151
Declaration on Consent Given by the Co-Authors.....	156
Declaration of Consent by the Supervisor.....	157
Declaration of Originality/Selbständigkeitserklärung.....	158
Acknowledgement.....	159

List of Abbreviations

2D/3D	two/three dimensional
AFM	atomic force microscopy
BPT	1,1'-biphenyl-4-thiol
BSA	bovine serum albumin
CE	chemical etching
CNM	carbon nanomembrane
CPD	critical point dryer
CV	current–voltage
CVD	chemical vapor deposition
cryoEM	cryogenic electron microscopy
DMF	dimethylformamide
ECD	electrochemical delamination
EDTA	ethylenediaminetetraacetic acid
GFET	graphene field effect transistors
HR-TEM	high-resolution transmission electron microscopy
h-BN	hexagonal boron nitride
HIM	helium ion microscopy
His or HIS	histidine
IRRAS	infrared reflection absorption spectroscopy
LED	light-emitting diode
NBPT	4'-nitro-1,1'-biphenyl-4-thiol
NPs	nanoparticles
NTA	nitrilotriacetic acid
PG	polyglycerol
PMMA	poly(methyl methacrylate)
PTFE	Polytetrafluoroethylene
RSF or R.S.F	relative sensitivity factor
SAM	self-assembled monolayer
SE	secondary electrons

SEM	scanning electron microscopy
SPR	surface plasmon resonance
SRR	split-ring-resonator
TEM	transmission electron microscopy
TMD	transition metal dichalcogenides
TPT	1,1',4',1''-terphenyl-4-thiol
UV	ultraviolet
VD	vapor deposition
vdW	van der Waals
XPS	X-ray photoelectron spectroscopy

1. Introduction

2D materials always stay under the spotlight on the stage of material science in recent years.¹⁻⁵ Initiated by the isolation of single-layer graphene sheet in 2004,⁶ research efforts on the 2D materials including hexagonal boron nitride (hBN),⁷⁻⁹ transition metal dichalcogenides (TMDs),^{10, 11} MXenes^{12, 13} and carbon nanomembranes (CNMs)^{14, 15} have been explosively increased. In the beginning, these materials were typically obtained by the “top-down” methods (**Figure 1.1**), such as i.e. ultrasound assisted exfoliation,¹⁶ micromechanical exfoliation,¹⁷ liquid-phase exfoliation¹⁸ or electrochemical exfoliation^{19, 20}. These methods enable the low-cost mass production of 2D materials, however, they also possess certain limitation. For instance, the random flake shapes and wide flake size distributions,²¹ undesired phase transformations^{22, 23} and poorly controlled orientations after the transfer onto target substrates²⁴. After the first successful synthesis of high-quality graphene on copper foils via the chemical vapour deposition (CVD),^{25, 26} the “bottom-up” synthesis of 2D materials has been intensively studied and became the most popular strategy to fabricate large-area 2D materials.²⁷ The 2D materials that are grown via the “bottom-up” method usually need to be transferred onto new substrates to enable further applications.²⁸⁻³⁰ To this end, a variety of techniques for transferring the 2D materials were developed. The simplest way to achieve the transfer is the removal of the growth substrate via the chemical etching (CE) and then replace it with the target substrates.^{14, 31-33} A polymeric protection layer that supports the 2D sheet is indispensable in this process. The critical disadvantage of the CE method is the precipitation of metal contaminants on the nanosheets, which limits their implementation in research areas such as nanoelectronics or nanobiotechnology.³⁴⁻³⁷ Moreover, the toxic pollutions caused by the etching solution and the etching waste³⁸ pose a serious potential hazard to human health and the environment. An alternative method, etching free transfer, by techniques such as mechanical delamination,³⁹ electrochemical delamination⁴⁰ or gas intercalation⁴¹ has been proved to cleave the 2D materials from their growth substrates effectively. In such techniques, harmful chemicals are absent during the whole process and the isolated nanosheets are free of metal residues. Moreover, the etching free process also enables the reusability of the noble metal substrate,⁴⁰ which reduces the production cost for the future commercialization. Notably, the application of etching free transfer, especially the electrochemical delamination (ECD) assisted transfer is not restricted only to the 2D materials that are attached to the growth substrate via the van der Waals interaction. It is also

promising for a large variety of materials that are covalently bound to the growth substrates. Nevertheless, challenges of this method remain, such as maintaining the structural integrity of the transferred materials, removing the residues of the supporting polymers and upgrading the production scale.^{37, 42}

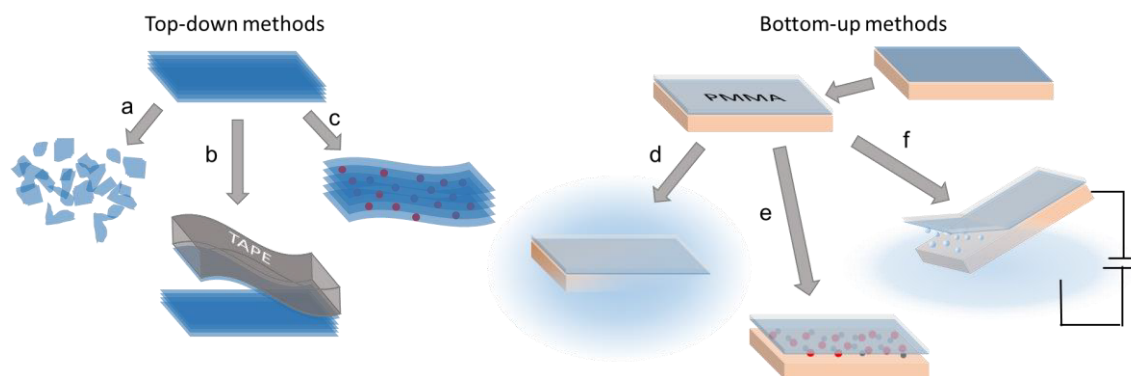


Figure 1-1. Common methods to delaminate single-layer 2D materials: (a) ultrasonic exfoliation, (b) mechanical delamination with tapes, (c) ionic intercalation, (d) chemical etching of growth substrate, (e) gas intercalation, (f) electrochemical delamination. In the procedure of the delamination of CVD grown 2D materials, a polymer supporting layer is indispensable.

Owing to their sub-nanometer thickness, 2D materials own attractive physical and chemical properties, which can be applied in the domain of electronic devices,^{43, 44} materials protection,⁴⁵ energy storage,^{3, 46} catalysis⁴⁷ and so forth^{5, 48-51}. To obtain additional novel functions and to construct a new road for the application of 2D materials, the post functionalization of already existed 2D materials is a promising approach. However, many 2D materials like graphene or h-BN are chemically inert.⁵²⁻⁵⁵ Moreover, the covalent functionalization will modify their original physical and chemical properties,⁵⁶⁻⁵⁹ whereas the noncovalent functionalization is not stable enough for many applications under environmental conditions^{60, 61}. Therewith, the non-destructive functionalization of 2D materials is still a difficult task. Up to now, there is not any universal solution to it. Fortunately, the short range ordered molecular 2D materials like CNMs do not suffer from such problems. CNMs are fabricated via cross-linking the aromatic self-assembled monolayers (SAMs) with low-energy electron irradiation.^{5, 14, 15, 62, 63} Since the functional groups of SAMs are present in CNMs after the cross-linking, CNMs can be functionalized, e.g. with activated cross-linkers such as NHS esters or isothiocyanates.⁶⁴ Note that through the formation of vertical van der Waals (vdW) heterostructures,

CNMs can firmly immobilize functional groups onto other 2D materials.⁶⁵ This flexibility makes the CNMs an excellent molecular interposer for the non-destructive functionalization of these materials, paving a way for developing unique applications. For instance, by transferring aptamers functionalized NH₂-CNMs onto graphene, biomimetic recognition sites that can trigger the specific coupling of the biomarkers on top of the graphene field-effect transistors enabling the applications in bio-sensing.⁶⁶

In addition to the modification of the CNMs functions via post-treatment, choosing different precursors before cross-linking can also tailor the functional properties of CNMs.¹⁵ Although the cross-linking changes the chemical structure of the precursor, some specific functional groups can be controllably introduced into CNMs. Thus, it has been proven that upon the cross-linking of 4'-nitro-1,1'-biphenyl-4-thiol (NBPT) SAMs, the nitro groups are reduced to amino groups resulting in the formation of amino-terminated CNMs.^{64, 67, 68} Some aromatic groups can also sustain under the low-energy electron beam.⁶⁹ Therefore, CNMs can inherit these groups from the precursors and obtain the desired chemical functionality. Moreover, some functional groups in the precursors can be deliberately eliminated by cross-linking. For example, by the fabrication of chemically inert CNMs, Neumann et al. used the cleavage of the carboxylic binding groups during the cross-linking process to effectively remove the carboxylic anchor on the bottom of CNMs.⁷⁰ This de-functionalization procedure is very pure, as it is conducted in vacuum and upon the process only the electron beam is used. In addition to e-beam induced cross-linking, CNMs can also be synthesized via EUV irradiation induced cross-linking⁷¹ and chemical cross-linking,⁷² which widens the possibility of the pre-adjustment of CNMs' functions.

As the first reported organic 2D material, CNMs have been intensively studied due to their numerous unique properties and potential applications (**Figure 1.2**). Firstly, unlike graphene, which only allows the hot protons to penetrate, CNMs have sub-nanometer to nanometer sized pores that enable the permeation of molecules or ions. Yang et al. reported that TPT-CNMs permit rapid permeation of water molecules,⁷³ while the translocation of ions, including protons, is efficiently hindered.⁷⁴ Demytyev et al. studied the behavior of the molecular permeation in free-standing bilayer CNMs and confirmed the suitability of CNM for dehydration of azeotropic mixtures.⁷⁵ These results showed the huge potential of CNMs in the application of seawater desalination and small molecules filtration. Secondly, CNMs possess Young's moduli of ca. 10 GPa.^{76, 77} This property

makes them much more sensitive to the vibrations generated by mechanical forces,⁷⁸ which opens a new avenue to sensing air pressure and adsorbed specimens.

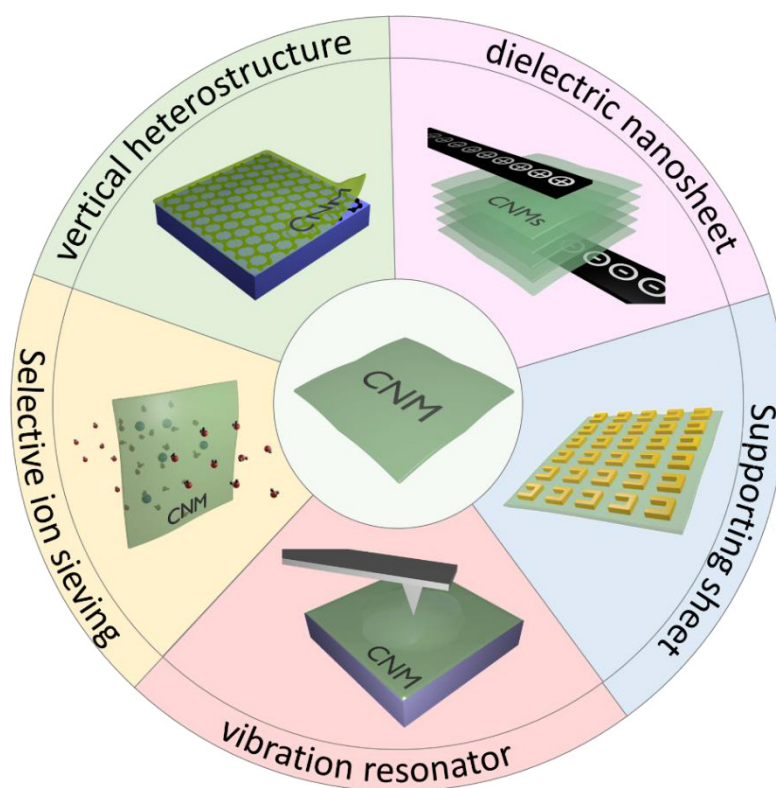


Figure 1-2. Various applications of carbon nanomembranes based on their ultimate thinness, high mechanical stability, high tunneling resistance, homogeneous porosity, adjustable chemical functionality and high transmittance to light (wavelength range: 400 nm to 1500 nm).

Thirdly, CNMs are mechanically stable even as free-standing sheets supported on the grids (free-standing lateral dimensions over 500 micrometres).⁵ Considering their only ~1 nm thickness⁶⁹ and high transparency (with a transmittance exceeding 99% over the wavelength range from 400 nm to 1900 nm),⁷⁹ they are suitable materials that can be used as supporting sheets for optical application. As studied by Rhinow et al., using CNM as a supporting sheet considerably enhanced the signal-to-noise ratio of TEM images.⁸⁰ Their outstanding structural homogeneity also benefits the imaging quality by avoiding the intrinsic granularity carbon support films prepared by conventional deposition processes. Fourthly, CNMs are insulating in all lateral dimensions.⁸¹ Their high vertical tunneling resistance enables their applications in the fabrication of carbon based nano-capacitors. Using multilayer CNM stack as a dielectric, Zhang et al. successfully fabricated 2D all-carbon nano-

capacitors with a capacitor area up to $1200 \mu\text{m}^2$ and an average capacitance density of $0.3 \mu\text{F}/\text{cm}^2$.³⁸ Last but not least, CNMs are of high thermal stability under inert condition up to 700 K.⁸² Afterward, with increasing temperature, the CNMs undergo pyrolysis and finally result in the formation of single layer graphene with adjustable crystallinity and porosity.^{14, 82-85}

This thesis demonstrates the ECD transfer and the chemical functionalization of CNMs, and their applications including selective ion sieving, building photo-switchable graphene field-effect transistor (GFET), immobilizing biospecimens for TEM imaging and fabricating optical metasurfaces. All these results are presented in the following chapters:

Chapter 3.1 describes the CNM transfer technique based on the findings in **P1**, in which the ECD assisted transfer method was established to transfer CNMs that are covalently attached to the growth substrates to arbitrary solid or holey substrates. By using XPS, it was possible to characterize the elemental composition of the CNMs precisely. In combination with atomic force microscopy (AFM) measurements, a correlation between the topographical features of the synthesis substrates and the structure of the formed and transferred CNMs was found, which offers an avenue towards forming 3D structured CNMs using 3D templates.

In Chapter 3.2, CNMs were used as filtration membranes for selective ion sieving in aqueous solutions, which is presented in **P2**. When exposed to a range of concentration gradients of KCl, CsCl and MgCl_2 , CNM demonstrated a selectivity towards the ion transport. The membrane potential and the selectivity of the membrane towards K^+ over Cl^- ions were measured at a 10 to 1 concentration ratio. Moreover, the pore size was studied by high-resolution transmission electron microscopy (HR-TEM) and correlated with the average membrane conductance, enabling the determination of the size and density of the nanopores.

Chapter 3.3 demonstrates an application of CNMs in nanophotonics, which was reported in **P3**. By regularly arranging the nanoresonators onto free-standing TPT-CNM, an ultrathin metamembrane was fabricated. It has a thickness of only about 1 nm and shows a negligible interaction with the incident light field. The metamembrane was characterized by linear-optical transmittance spectroscopy. The obtained data were compared with the simulated results.

In Chapter 3.4, CNMs were used as smart molecular nanosheets with biorecognition functions to immobilize specific biotargets and therewith to facilitate the biological specimen preparation and

the analysis for the electron cryo-microscopy (cryoEM) imaging. To this end, CNMs were functionalized with biorepellent polyglycerol (PG) layer to avoid undesired biological fouling and with Ni-NTA moieties to achieve selective adhesion of His-tagged proteins. X-ray photoelectron spectroscopy (XPS) and infrared reflection absorption spectroscopy (IRRAS) analysis were used to confirm the successful functionalization. The obtained smart molecular nanosheets are only about 10 nm thick and showed outstanding selectivity to His-tagged protein samples. Additionally, after the treatment with the EDTA solution, the Ni ions that coordinated with NTA could be released, which showed the possibility of reusing the nanosheets. The details of the study are presented in **P4**.

Chapter 3.5 shows the results of **P5**. In this paper, a NH₂-CNM was functionalized with azobenzene and then transferred on to graphene to fabricate photo-switchable azo-CNM-Graphene FET (azo-CNM-GFET). Triggered by the illumination with UV light (355 nm), the nonpolar *trans*-azobenzene molecules on the CNM underwent photoisomerization and switched to polar *cis* conformation. Acting as a molecular top gate, the polar *cis*-azobenzene molecules generated a vertical electric field on the dielectric CNM layer, resulting in a negative doping in the graphene FET and a respective shift of the Dirac point. This electric field could be simply removed by illuminating the azo-CNM-GFET with blue light (455 nm), which can switch the *cis* conformation azobenzene gate back to the *trans* conformation. A simple model was applied and could explain very well the observed modification of the charge carrier concentration in the graphene channel.

2. Experimental

This chapter briefly describes the fabrication methods and characterization techniques used for preparing, processing and characterizing the samples in **P1** to **P5**. Detailed procedures were listed in the corresponding paper. **P1**: Z. Tang, C. Neumann, A. Winter, A. Turchanin. Electrochemical delamination assisted transfer of molecular nanosheets. *Nanoscale* **2020**, *12*, 8656 - 8663. **P2**: P. van Deursen, Z. Tang, A. Winter, M. Mohn, U. Kaiser, A. Turchanin, G. Schneider. Selective ion sieving through arrays of sub-nanometer nanopores in chemically tunable. *Nanoscale* **2019**, *11*, 20785-20791. **P3**: Y. Denizhan Sırmacı, Zian Tang, Stefan Fasold, Christof Neumann, Thomas Pertsch, Andrey Turchanin, and Isabelle Staude. Plasmonic Metasurfaces Situated on Ultrathin Carbon Nanomembranes. *ACS Photonics* **2020**, *7*, 1060-1066. **P4**: Julian Scherr, Zian Tang, Maria Küllmer, Theresa Weber, Andreas Winter, Kristian Parey, Alexander Rittner, Martin Grininger, Volker Zickermann, Werner Kühlbrandt, Daniel Rhinow, Andreas Terfort, Andrey Turchanin (under review in *ACS Nano* **2020**). **P5**: Z. Tang, A. George, A. Winter, D. Kaiser, C. Neumann, T. Weimann, A. Turchanin. Optically triggered control of the charge carrier density in chemically functionalized graphene field effect transistors. *Chem. Eur. J.* **2020**, DOI: 26.10.1002/chem.202000431.

2.1 Sample Preparation

2.1.1 Preparation of CNMs

Formation of self-assembled monolayers (SAMs)

1,1'-Biphenyl-4-thiol (BPT, Sigma Aldrich 97%, **Figure 2.1a**) and 4'-nitro-1,1'-biphenyl-4-thiol (NBPT, Taros 98%, sublimated before use, **Figure 2.1b**) SAMs were prepared by immersing oxygen plasma cleaned Au substrates to a ~0.1 mM solution of BPT (or NBPT) dissolved in degassed *N,N*-dimethylformamide (DMF, Alfa Aesar 99.9 %) for 72 h under inert conditions.⁷¹ After the substrates were taken out, they were immediately washed with DMF followed by ethanol (Sigma Aldrich > 98 %) for three times to remove physically adsorbed molecules on the surface. The samples were afterward dried by a stream of nitrogen.

1,1',4',1''-Terphenyl-4-thiol (TPT, Sigma Aldrich 97%, **Figure 2.1c**) SAMs were prepared by immersing Au substrates to a ~0.1 mM solution of TPT dissolved in degassed DMF. The solution was then heated at 70 °C for 24 h under inert condition. After the samples were taken out, the same treatment as for cleaning of BPT SAMs was applied.

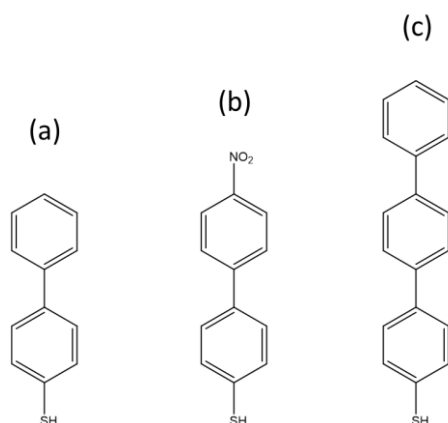


Figure 2-1. Structures of molecular compounds used for the synthesis of CNMs: (a) 1,1'-biphenyl-4-thiol (BPT), (b) 4'-nitro-1,1'-biphenyl-4-thiol (NBPT), (c) 1,1',4',1''-terphenyl-4-thiol (TPT).

Electron irradiation of BPT, NBPT and TPT SAMs

The SAMs were cross-linked into carbon nanomembranes (CNMs) by a low-energy electron gun (Specs FG 15/40) using electron energy of 100 eV with a dose of 50 mC/cm² in a high vacuum chamber (< 10⁻⁸ mbar).⁶⁹

2.1.2 Synthesis of Graphene

Single-layer graphene is grown by chemical vapor deposition (CVD) on Cu foils following the protocol of Li et al.²⁵ adapted to the experimental conditions of this thesis^{65, 86}.

2.1.3 Chemical Functionalization of CNMs

Grafting polyglycerol from NH₂-CNMs (cross-linked NBPT SAMs)

The CNM/Au substrate was placed in a PTFE vial with 5 mL of freshly distilled Glycidol. The vial was sealed and heated to 140 °C for 2.5 h under argon condition. Afterwards, the reaction vial was cooled to room temperature and the substrate was taken out. To remove the physically adsorbed monomer, the CNM/Au substrate was rinsed with water and ethanol and dried in a stream of nitrogen.⁸⁷ Further functionalization with NTA moieties see **P5** experimental part.

Immobilizing azobenzene groups onto NH₂-CNMs

4-[4-(Dimethylamino)phenylazo]-benzoic acid N-succinimidyl ester (azobenzene-NHS, Sigma Aldrich 98%) was used as an azobenzene derivative to functionalize the NH₂-CNMs.⁸⁸ The NH₂-CNM on an Au substrate was placed in a clean test tube along with 2 mL DMF, 10 mL TEA and ~0.1 mg azobenzene-NHS in the dark condition for 72 h at room temperature. Afterward, the sample was rinsed with isopropanol and then dried under a stream of nitrogen.

2.1.4 Transfer of Graphene and CNMs

Transfer of the CNMs and graphene using the electrochemical delamination (ECD)

CNMs (or graphene) on the growth substrate were first coated by a PMMA layer (70 nm, Mw.495K, Microchem, 2% in Anisole). By adding negative potential, the CNMs (or graphene) layers were delaminated from growth substrate by the hydrogen evolution at the CNMs-substrate (or graphene-substrate) interface. After sufficient washing with pure water, the CNMs (or graphene) with PMMA supporting layer were fished out by the target substrate and dried at room temperature followed by baking at 90 °C for 30 minutes (for graphene 120 °C, 2.5 hours). In the end, the PMMA supporting layer was removed by acetone.

Transfer of the CNMs and graphene with the chemical etching method

In this method, the CNMs were protected by two PMMA layers: the first layer, 100 nm, 50 kDa (All-Resist); the second layer, 200 nm, 950 kDa (All-Resist).¹⁴ To cleave the CNMs from the Au/SiO₂/Si substrates, the samples were floating on the 45 °C, 0.5 M KOH solution for 60-90 minutes. The KOH solution will then intercalate in the CNM-substrate interface and break the Au sulfur bond, thus eliminate the covalent interaction between the CNMs and the growth substrates. The buoyant force of the CNM-PMMA will then peel the CNMs layer from the substrates. To remove the KOH residues, the CNMs were washed by floating on three pure water baths successively. Afterward, the CNMs were transferred to the target substrates and the PMMA supporting layer was removed by acetone. To transfer the CNMs from Au/mica substrates onto target substrates, the Au-CNM-PMMA layers were cleaved from the mica substrates by gradually dipping the samples into the water using the surface tension of the water and buoyant force of the CNM-PMMA layer. Then the Au-CNM-PMMA sandwich sheets were transferred to the gold etching solution (I₂/KI/H₂O; 1:4:10) to remove the gold layers.⁶⁵ The post-cleaning process was carried out in the same way as for the transfer from Au/SiO₂/Si substrate.

Preparing free-standing CNMs

To obtain free-standing CNMs, the same transfer protocol was applied to transfer the structures onto the TEM grids (Quantifoil TEM grid R2/2, Plano) with the exception that the PMMA layer was removed using a CO₂ critical point dryer (CPD, Autosamdri 815, Tousimis). This procedure avoids ruptures in the CNMs caused by the surface tension of the evaporating acetone as well as undesired contaminations during the cleaning process.^{89, 90}

2.1.5 Loading (or Unloading) Metal Ions on (or from) the CNMs

To load Ni²⁺ on the NTA-PG-CNM nanosheets, the samples were immersed in a NiSO₄ (Merck, 99%) solution (1.0 %) for 30 minutes, followed by rinsing in high-purity water bath three times (each time 15 minutes) to remove the physical adsorbed Ni ions. To unload coupled Ni²⁺ from the NTA-PG-CNM nanosheets, the samples were first immersed in EDTA-Na₂ solution (0.5 mmol/L) for 30 minutes, then rinsed with pure water for 30 minutes.

2.2 Experimental Methods

2.2.1 X-Ray Photoelectron Spectroscopy

XPS is a surface sensitive characterization technique. By measuring the kinetic energy and amount of electrons generated by the X-ray irradiation, elemental composition as well as chemical or electronic states of the element in the surface region (down to 10 nm depth) can be accurately determined. In this work, XPS measurements were performed in a UHV (pressure $< 5 \times 10^{-10}$ mbar) Multiprobe system (Scienta Omicron) using a monochromatic X-ray source (Al K α) and an electron analyzer (Argus CU) with a spectral resolution of 0.6 eV.

Surface elemental composition analysis

Before data processing, all signals were calibrated with the most intensive substrate signal Au 4f_{7/2} peak at 84.0 eV or the Si 2p peak at 103.6 eV. All peaks were fitted using Voigt functions with a ratio of Gaussian-Lorentzian functions 70:30 after a linear (S 2p, N 1s, O 1s, Ni 2p,) or Shirley (C 1s, Au 4f and Si 2p) background subtraction was performed. The peak fitting of the sulfur doublet was performed using the fixed intensity ratios due to the spin-orbit coupling of the p-photoelectrons. For the elemental ratios mentioned in the thesis, the relative sensitivity factors (RSF) in **Table 2.1** were used.⁹¹

Table 2.1 The relative sensitivity factors (RSF) of the elements.

	C 1s	O 1s	N 1s	S 2p _{3/2}	Ni 2p _{3/2}	Au 4f _{7/2}	Zn 2p _{3/2}
R.S.F.	1.0	2.9	1.8	1.1	14.6	9.6	18.9

Thickness analysis

The effective thickness analysis and calculation of functionalization efficiency are based on the Beer-Lambert law for XPS⁹²

$$I_s = I_0 \exp(-d/\lambda \cos \theta), \quad (2.1)$$

where I_s is the intensity of the substrate signal, I_0 is the intensity of a bare substrate reference sample; θ is the angle between the normal of the sample and the analyzer and λ is the inelastic attenuation length of the photoelectrons. The values of λ in carbon materials for different photoelectrons were taken from the literature and listed in **Table 2.2**.⁹³

Table 2.2 Values of the inelastic attenuation length λ of different photoelectrons in carbon materials.⁹³

	Au 4f	C 1s	Si 2p	N 1s	S 2p
λ	3.5 nm	3.1 nm	3.5 nm	2.9 nm	3.3 nm

2.2.2 Raman Spectroscopy

Raman spectroscopy is a robust spectroscopic technique for characterizing crystalline 2D materials.⁹⁴ It has the capability of characterizing the structural properties of 2D materials, as well as detecting the layer thickness, strain effects, type of doping, concentration of defects, electron-phonon coupling, and interlayer coupling.⁹⁵ The excitation source of a Raman spectrometer is usually a laser. In this thesis, all Raman spectroscopy data were obtained using a commercial Raman spectrometer (Bruker Tensor 37 with Hyperion microscope and HT-X High throughput module). Measurements were carried out with 2 mW, 532 nm frequency-doubled Nd:YAG Laser, a 50x objective and a thermoelectrically cooled CCD detector with a resolution of 2 - 3 cm^{-1} . All peaks were calibrated with the Si-peak at 520.7 cm^{-1} .

2.2.3 Electrical Transport Measurements

Sheet resistivity (or conductivity) is a significant parameter to judge the performance of 2D materials. With the adjustment of the gate voltage, the charge carrier density in the 2D materials can be tuned, resulting in changing the sheet resistivity and the shift of the Dirac point.^{96, 97} In this thesis, the electrical characterization of the graphene field-effect transistor was carried out with a Lakeshore TTPX needle probe station in a high vacuum ($< 10^{-5}$ mbar) at room temperature.

2.2.4 Helium Ion Microscopy

Helium Ion Microscopy (HIM) is an advanced technology that allows imaging and the nanofabrication of conductive as well as insulating materials with sub-nanometer resolution. It works similarly to the scanning electron microscopy, but instead of using a focused beam of electrons, it uses helium ions.⁹⁸ Owing to the short De Broglie wavelength of the helium ions, a more focused beam can be formed, resulting in a better image resolution. Moreover, HIM can achieve higher contrasts between different materials compare with SEM,^{99, 100} since the helium ion beam produces more secondary electrons than the electron beam. HIM measurements in **P1** was carried out with a Carl Zeiss Orion Plus Microscope. The helium ion beam was operated at 35 kV

acceleration voltage at currents of 0.2 - 0.5 pA. A 10 μm aperture was used and the working distance was 14 - 37 mm. Secondary electrons were collected by an Everhart-Thornley detector at 500 V grid voltage.

2.2.5 Atomic Force Microscopy

Among the techniques used to obtain the topographic feature of the material surface, AFM is the most widely applied technique due to its simple operation and high accuracy.¹⁰¹ The AFM measurements in this thesis were performed using an N-tegra (NT-MDT) atomic force microscope. Measurements are carried out in semi-contact mode under N_2 conditions using n-doped silicon cantilevers (NSG01, NT-MDT) with resonant frequencies of 87- 230 kHz and a tip radius of < 6 nm.

2.2.6 Other Microscopic Techniques

Scanning electron microscopy

The SEM images were taken with a Zeiss Sigma VP at a beam energy of 10 kV and the inlens detector of the system was used.

Optical microscopy

The optical microscopy images were obtained by a Zeiss Axio Imager Z1.m microscope equipped with a 5 megapixel CCD camera (AxioCam ICc5) in the bright field mode.

Transmission electron microscopy

Dodecyl maltoside-solubilized complex I (with His-tag) was obtained as described in the previous work,¹⁰² the GroEL (without His-tag) from *E. coli* was purchased from Sigma Aldrich. Functionalized nanosheets mounted on holey carbon TEM grids (Quantifoil) were incubated with a 3 μL 0.1% NiSO_4 solution and subsequently rinsed three times with dist. H_2O . Nanosheets were incubated with a 1.16:1 mixture of complex I and GroEL (1 mg/mL each) in a TSK buffer containing 0.025% DDM and subsequently rinsed three times with a TSK buffer. Samples were blotted for 10-15 s in an FEI Vitrobot and plunged into liquid ethane. CryoEM images were recorded and processed as described previously.¹⁰³ For the control experiment, samples were negatively stained using uranyl acetate.

3. Results and Discussion

3.1 Electrochemical Delamination Assisted Transfer of CNMs

In this chapter, the general synthesis strategy and the electrochemical delamination assisted transfer of CNMs are described. The latter part was published in **P1**: Electrochemical delamination assisted transfer of molecular nanosheets. Zian Tang, Christof Neumann, Andreas Winter, Andrey Turchanin. *Nanoscale*. **2020**, 12, 8656 - 8663.

The synthesis of CNMs has been intensively studied during the last years.^{5, 62, 63} Generally, CNMs were fabricated via cross-linking of aromatic self-assembled monolayers (SAMs). Well-ordered SAMs can be obtained directly via vapour deposition (VD) on substrates or by immersing solid substrates into a solution of molecules with specific anchor groups.^{70, 71, 85} The VD method is normally carried out in a high vacuum ($< 10^{-5}$ bar). The SAMs formed at high vacuum conditions have less possible trace contaminations and thus the respective CNMs formed by their conversion too.^{65, 83} However, it is difficult to produce large area SAMs due to the restriction of the high vacuum equipment. Moreover, the fabrication of SAMs requires the use of expensive equipment. In contrast, the SAMs prepared in solution may suffer from the trace impurities, but their preparation is low-cost and easy to handle. In the thesis, all the CNMs were synthesized from the SAMs prepared in solution. To obtain highly ordered SAMs, the substrates were immersed in the solution of precursor molecules for 72 hours at room temperature. With increasing self-assembly temperature, the time can be reduced to 24 hours, however, at elevated temperatures the decomposition and deactivation of the precursor molecules can take place.^{104, 105}

Next, to convert a SAM into a CNM, strong covalent interaction needs to be introduced between the adjacent molecules in a SAM. To achieve this cross-linking, low energy electrons,⁶³ helium ions¹⁰⁶ or UV⁷¹ irradiation can be employed. Upon the irradiation, the C-H bonds in the aromatic SAMs become broken, partial molecular dissociation takes place and the remaining molecular fragments cross-link with each other forming a 2D molecular network.⁶⁹ The mechanistic details of this process have been recently studied,¹⁰⁷ clearly demonstrating that besides the primary electrons also the secondary electrons (generated in the substrate) and photoelectrons contribute to the cross-linking.^{69, 71}

In addition to the irradiation induced cross-linking, chemical cross-linking may also be useful for the synthesis of 2D carbon materials.⁷² By fabrication of CNMs on 3D templates, the efficiency of the electron irradiation may be reduced due to the shadowing effects. For instance, forming shell-like CNMs from SAMs grown on silicon nanoparticles (NPs) via electron irradiation has been found to be difficult in this work. However, through the Friedel–Crafts reaction,^{108, 109} the aromatic molecules on the NP surface can be effectively cross-linked.

So far CNMs have been typically prepared on the metal substrate,⁵ therefore, their transfer onto target substrates is indispensable for applications in electronics or photonics. However, most of the methods for delamination of 2D materials from their growth substrates were developed for the materials, which are weakly attached to the substrates.¹¹⁰⁻¹¹³ CNMs synthesized from the thiol based SAMs are covalently bound to the substrates.^{69, 114} For the delamination, mechanical forces would be insufficient to cleave CNMs from the substrates without damage. Therefore, techniques such as gas intercalation and mechanical peeling are not suitable for the delamination of CNMs. Chemical etching, as an alternative method, is effective but also suffers from several drawbacks. One of the most influential drawbacks is that the corrosive etching solutions used in the process contain normally heavy metals and oxidants, which can contaminate or even damage the functional groups on the CNMs.^{105, 115, 116} This significantly restricts the applications of CNMs in nanotechnology and in particular in areas such as nanoelectronics or nanobiotechnology.^{34-36, 117} Electrochemical delamination is a powerful technique to realize the transfer of 2D material without etchant. It has already been adopted to transfer graphene and WS₂ monolayer grown on metal substrates.^{118, 119} Note that, this method involves not only physical but also electrochemical processes, which can efficiently break the covalent bonds between the 2D sheets and the substrates due to the activation of the respective redox reactions.¹²⁰⁻¹²² Based on this background, the implementation of ECD assisted transfer to Carbon Nanomembranes (CNMs) is demonstrated in this thesis. To verify the universality of this method with respect to CNMs, CNMs with three representative molecular precursor 1,1'-biphenyl-4-thiol (BPT), 4'-nitro-1,1'-biphenyl-4-thiol (NBPT) and 1,1',4',1''-terphenyl-4-thiol (TPT) grown on various gold substrates were tested.^[P1]

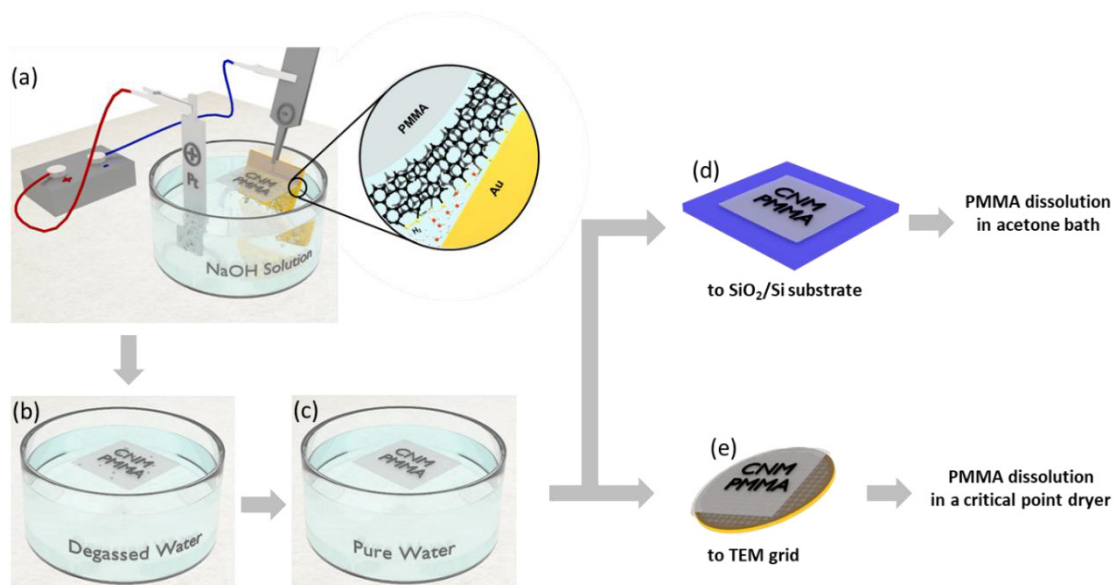


Figure 3.1.1. Schematic representation of the ECD assisted transfer: (a) ECD set-up and CNM/substrate interface during ECD; (b) Dissolution of hydrogen bubbles in degassed water; (c) Washing with pure water; (d) Transfer onto SiO₂/Si substrate; (e) Transfer onto a TEM grid. (Reprinted from **P1** with permission from the Royal Society of Chemistry)

The procedures of the CNMs transfer are schematically shown in **Figure 3.1.1**. After stabilization with the PMMA layer, the sample was introduced into an electrolysis cell as a cathode. By applying a negative voltage of 2.5 – 3.6 V, hydrogen bubbles were generated on the gold substrate, detaching the PMMA-CNM layer from the gold substrates. With further dipping the sample into the electrolyte, the PMMA-CNM was completely peeled off and floats in finally on the solution surface. Generally, a NaOH solution (0.1 M – 1 M) is used as the standard electrolyte in the ECD process. However, the high pH value alkaline electrolyte dissolves the silicon substrate, making the reusability of the growth Au/SiO₂/Si substrates impossible. Besides that, the dissolved Si-contained substances may also contaminate the CNMs. To avoid these unwanted effects, the ammonia-based electrolyte (aqueous ammonia, 30 wt. %) was applied to delaminate the CNM samples on the Au/SiO₂/Si substrates. In addition, gas bubbles can provide an obstacle for fabricating clean and rupture free CNMs. They are sticking to the bottom part of the CNM, preventing it from the contact to pure water. If transferred on a solid substrate, gas bubbles will also suspend the CNMs and finally result in large area ruptures. To solve this problem, an extra procedure was introduced after the delamination, in which the gas bubbles below the CNMs were dissolved by the degassed water. Next, the CNMs were washed in pure water for several times then transferred to target substrates.

The PMMA layer was removed by acetone at the ambient condition or in a critical point drier as described in the previous reports.^{14, 86}

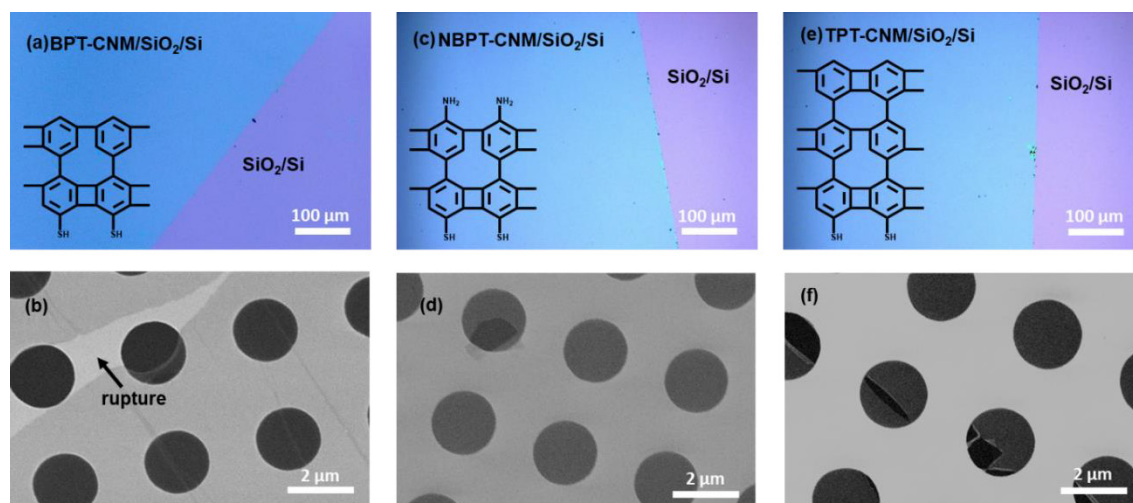


Figure 3.1.2. Optical microscopy and scanning electron microscopy images of CNMs synthesized on 30 nm Au/Si substrates and transferred onto SiO₂/Si and Quantifoil transmission electron microscope (TEM) grids: (a) and (b) BPT-CNM; (c) and (d) NBPT-CNM; (e) and (f) TPT-CNM. (Reprinted from **P1** with permission from the Royal Society of Chemistry)

All studied CNMs were transferred both onto SiO₂/Si substrates and TEM grids and then characterized by optical microscopy and scanning electron microscopy, respectively. To achieve better contrast between CNMs and bare substrate, the SiO₂/Si substrates with a 300 nm oxide layer were chosen as the supporting substrates for the optical microscope imaging. These substrates result in an enhanced CNM contrast.¹²³ The results are shown in **Figure 3.1.2**. All studied CNMs were homogeneously transferred to these substrates without macroscopic ruptures.

For analyzing free-standing CNMs with SEM, the delaminated CNMs were transferred to Quantifoil holey carbon film (with 2 μm holes) on a copper grid. It can be seen from **Figure 3.1.2** that all studied CNMs can be homogeneously transferred to these substrates without macroscopic ruptures. Note that in case of the suspended CNMs on TEM grids with ~2 μm openings, ruptured places were imaged in order to visualize the CNMs, as otherwise their presence on the grids is difficult to confirm due to a very homogenous contrast of the free-standing areas.

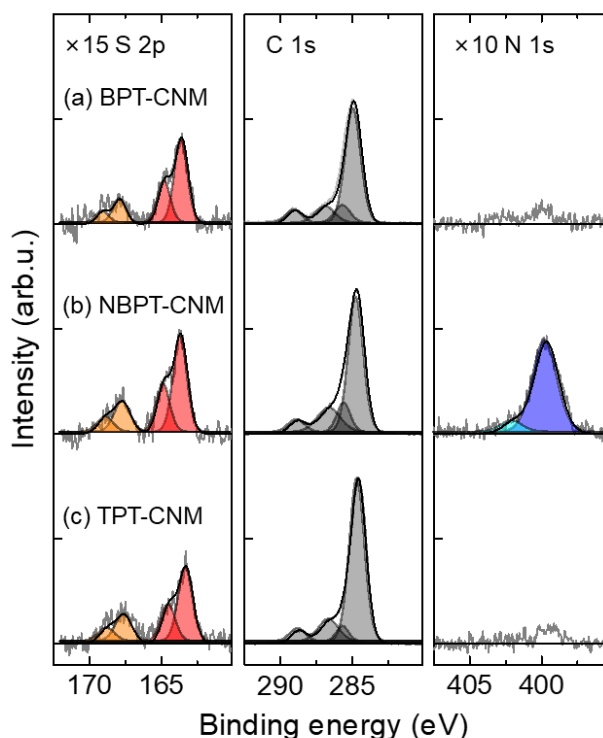
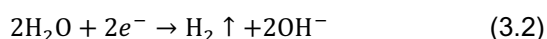
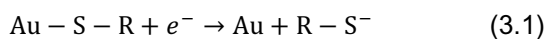


Figure 3.1.3. XP spectra of CNMs synthesized on Au/mica substrates and transferred using ECD assisted transfer onto oxidized Si wafers with 300 nm of SiO₂: (a) BPT-CNM, (b) NBPT-CNM, (c) TPT-CNM. (Reprinted from **P1** with permission from the Royal Society of Chemistry)

In contrast to inorganic monolayers, which are only weakly bonded to the growth substrates, CNMs interact with the substrate via covalent thiolate bonds. The Au-S bonds that are anchoring the SAMs to the gold substrate were shown to be already broken by applying a negative voltage of 1.0 – 1.3 V.¹²⁴ Considering the overpotential on the electrodes,¹²⁵ a relatively higher potential (2.5 – 3.5 V) was applied to induce the delamination of CNMs. At this voltage, the electrochemical half-reactions at the gold electrode¹²⁶ are:



The lower oxidation state of sulfur on the bottom side of CNM is conserved by the alkaline environment and the negative potential. After the Au-S bonds are cleaved, the hydrogen bubbles generated from the gold surface also push the CNMs away from the substrate, making the detachment irreversible.

The above-discussed behaviour is confirmed by the XPS measurements. **Figure 3.1.3** shows the XP spectra of the CNMs transferred on a SiO₂/Si substrate. As can be seen, for all three types of the CNMs, the S 2p spectrum consists of two doublets with the S 2p_{3/2} binding energies (BEs) of 163.3 eV and 167.6 eV. The doublet with the lower BEs assigned to the R-S-H as well as the R-S-S-R species.^{127, 128} They cannot be distinguished by the XPS. The doublet with the higher BEs is attributed to oxidized sulfur species.^{129, 130} Its intensity is significantly lower in comparison to the R-S-H/R-S-S-R species. These oxidized sulfur species were probably introduced either upon the washing process (**Figures 3.1.1c**) or during the transfer of the samples at ambient conditions, or due to the interaction with the SiO₂ substrate. Additionally, besides the cleavage of the Au-S bonds, a partial cleavage of the C-S bonds was also observed during the delamination. This was reflected in both the reduced S:N and S:C elemental ratios in comparison with the CNMs on their original gold substrates as well as in some remaining sulfur on these substrates after the applied ECD.

The C 1s XP spectrum of the CNMs after the ECD transfer onto SiO₂/Si substrates can be divided into four different peaks. The peak located at 284.6 eV is assigned to the aromatic moieties in the CNMs; the peak at 285.3 eV indicates the presence of the C-S bonds as well as the C-N bonds in the NBPT-CNMs; the peaks located at 286.5 eV and 288.6 eV are attributed to the C-O and the O=C-O carbons respectively, which are most likely due to residues of the PMMA supporting layer after the transfer.^{89, 131, 132} Considering these detected trace contaminations, a respective increase of the BPT-CNM, NBPT-CNM as well as TPT-CNM effective thicknesses was detected. Thus, the thickness values on the original gold substrates were about 0.9 nm, 1.0 nm and 1.3 nm whereas on the SiO₂ substrates to about 1.2 nm, 1.7 nm and 1.8 nm for BPT-CNM, NBPT-CNM and TPT-CNM, respectively. As expected, for the transferred NBPT-CNMs onto SiO₂ substrate,¹³³ the amino group on the top of CNMs was well protected. As shown in the spectrum, the N 1s spectrum consists of a peak at 399.5 eV due to amino groups⁷⁶ as well as a low intensity shoulder at 402.0 eV, which is assigned to the protonated nitrogen.¹³⁴ Interestingly, after the transfer of the CNMs onto the gold substrates, part of the sulfur on CNMs can rebind to the substrate via the formation of thiolate, which can be confirmed by XPS. These results further demonstrate the preserving of the functional CNMs properties after their ECD assisted transfer.

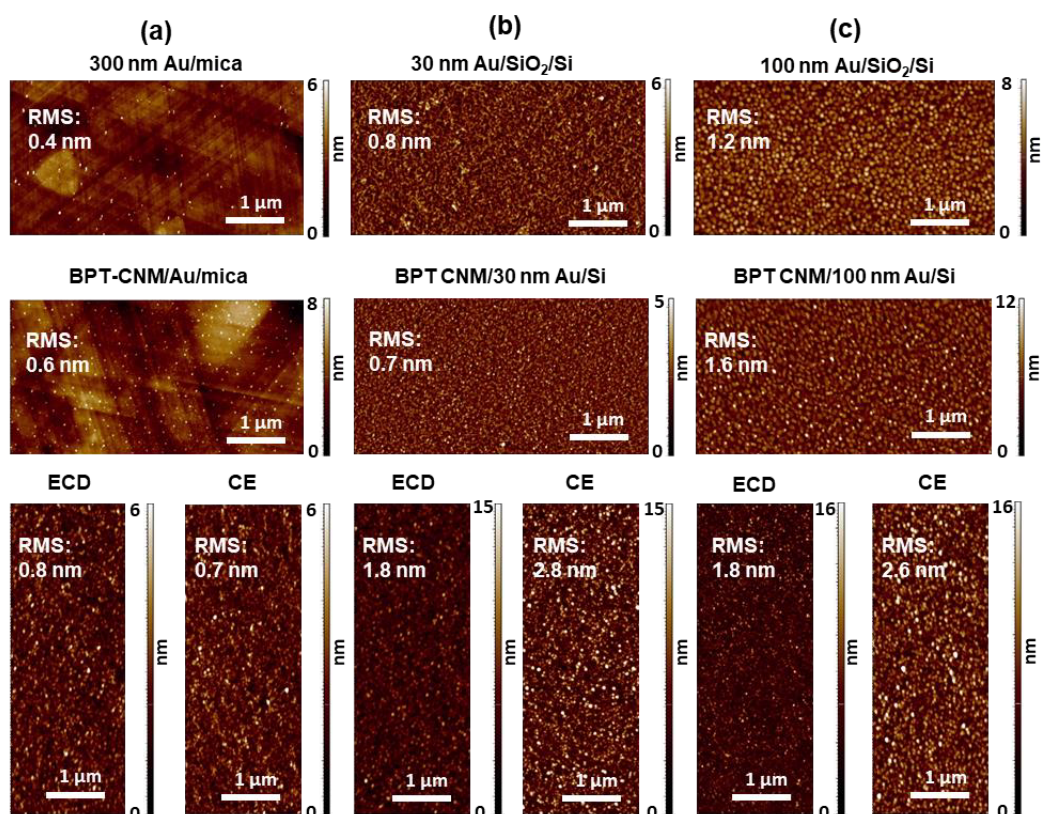


Figure 3.1.4. AFM images of BPT-CNMs grown on Au substrates with different roughness before and after transfer onto target SiO₂/Si substrates (RMS: 0.2 nm) by both ECD and CE assisted transfer procedures. (a-c) CNMs grown on 300 nm Au/mica (a), 30 nm Au/Si (b), and on a 100 nm Au/Si (c) substrates. (Reprinted from **P1** with permission from the Royal Society of Chemistry)

The influence of the growth substrate on the topography of CNMs was studied by AFM. Using the ECD or CE⁶⁵ methods, CNM samples grown on gold substrates with different roughness were transferred on to SiO₂/Si substrates, which has RMS roughness of only 0.2 nm. The results of this study are summarized in **Figure 3.1.4**. As shown, the CNMs grown on the flattest Au/mica substrate (RMS: 0.4 nm) appear the lowest surface roughness (0.8 nm) after the transfer, which indicates a clear correlation between the RMS values of the growth substrate and the respectively transferred CNM roughness on the SiO₂/Si substrates. However, the transferred CNMs do not completely reflect the topographical features of the growth substrates, since the surface tension upon washing and removal of the PMMA layer may influence their final configuration. Besides that, the roughness of CNMs transferred by the ECD method is generally lower than the roughness of CNMs transferred by the CE method. This effect can be attributed to the harsh conditions involved in the etching process such as relative high temperature (45 °C) and concentrated basic solution (0.5 mol/L KOH).

Since CE assisted transfer of CNMs grown on the Au/mica substrates uses less harsh KI/I₂ solution at room temperature, the transferred CNMs appear lower roughness than the CNMs transferred by ECD method. Additionally, using the same Au/SiO₂/Si substrate, three successive growth/delamination procedures were performed, and the respective BPT-CNMs were transferred onto SiO₂/Si wafers. In comparison with the first growth, no diminishing of quality was detected.

To sum up, chemical etching and electrochemical delamination are both very well applicable methods to detach CNMs from the growth substrates. Chemical etching process does not need any special equipment; however, it is time-consuming and involves harsh chemicals. On the other hand, for electrochemical delamination, a specific electrochemical cell has to be constructed, and it works only for samples on conductive substrates, however, it is conducted at mild conditions and is environment friendly.

3.2 Nanoporous CNMs for Selective Ion Sieving

Parts of this chapter were published in **P2**: Selective ion sieving through arrays of sub-nanometer nanopores in chemically tunable 2D carbon membranes. Pauline van Deursen, Zian Tang, Andreas Winter, Michael J. Mohn, Ute Kaiser, Andrey A. Turchanin, Grégory F. Schneider. *Nanoscale*. **2019** 11, 20785-20791.

As already mentioned in the introduction, one of the potential applications of CNMs is ultrafiltration, such as seawater desalination, dialysis and separation of heavy metal ions. These applications are based on the porosity of CNMs, which is usually determined by the precursors.¹⁵ Unlike the commercially used osmosis polymer membranes, some CNMs can only have pores with diameters below 1 nm that can block specific ionic passage being simultaneously permeable for water.⁷⁴ It has already been shown that the TPT-CNMs possess a high density of sub-nanometer (sub-nm) pores, which allow the water molecules to penetrate.⁷³ The high areal density of the pores in CNMs enables a high water flow. Note that, due to their ultra-small size of the pores, TPT-CNMs possess high ion rejection.⁷⁴ They act as barriers against the ionic movement, therefore, are not suitable for selective ion sieving. A promising candidate for ion sieving is the thinner BPT-CNM. As discussed before, CNMs are also mechanically stable against most of the organic and inorganic solvents. However, the porosity of the BPT-CNM has not been characterized to date. In this chapter, the pore density in the BPT-CNM was determined using various techniques, including high-resolution transmission electron microscopy (HR-TEM) and ionic conductance measurements. To perform the characterization, BPT-CNMs were transferred to Si₃N₄ chips with round apertures using the CE method. (**Figure 3.2.1a**) The diameter of the nanoapertures was ranging between 20 and 80 nm.¹³⁵

Figure 3.2.1b presents the aperture imaged by TEM before BPT-CNM was transferred. The aperture was then imaged again after the BPT-CNM transfer. As demonstrated in **Figure 3.2.1c**, the free-standing membrane does not reveal any visible pores. Therewith, one can assume that the general pore size in BPT-CNM does not exceed 1 nm.^[P2] This estimation was made on the following basis. The instrumental resolution that can be reached by employed TEM is 0.18 nm. To avoid the deterioration of the BPT-CNM under the electron beam, the applicable electron dose for imaging was limited below $10^5 \text{ e}^- \text{ nm}^{-2} \cdot \text{s}^{-1}$, which reduces the final resolution. Moreover, to obtain sufficient contrast from the amorphous BPT-CNM membrane, a high defocus was required during imaging.

Considering these two factors, the upper limit of the pore size was conservatively estimated to 1 nm. [P2]

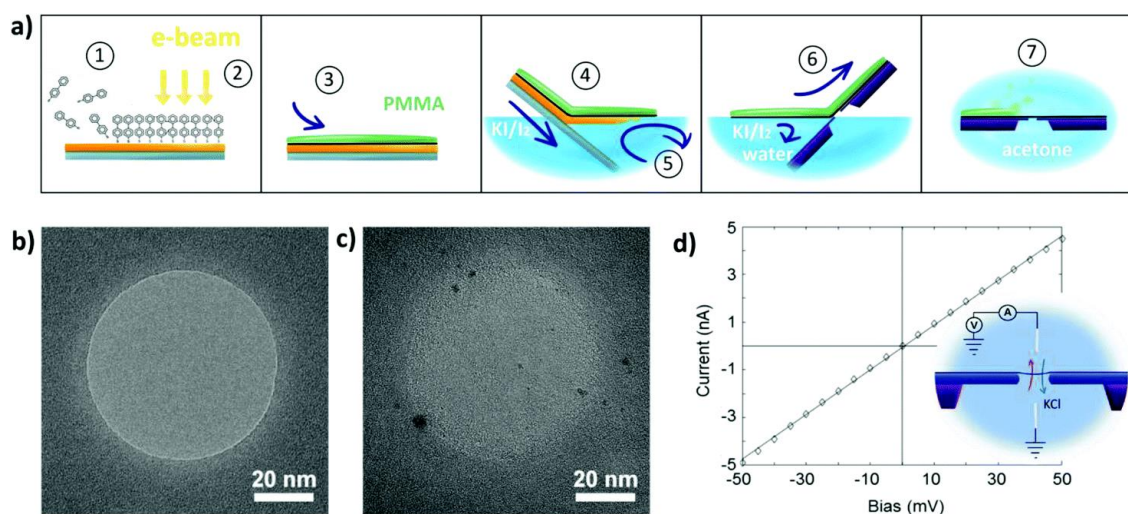


Figure 3.2.1. (a) The schematic procedure used to fabricate suspended biphenyl thiol carbon nanomembrane (BPT-CNM) chips. (b) A 60 nm diameter aperture in Si_3N_4 after drilling by the focused beam of a TEM. (c) The aperture after deposition of the BPT-CNM imaged by HR-TEM. (d) Typical I-V curve measured on a CNM suspended over a Si_3N_4 aperture in 1 M KCl solution. Inset: The suspended BPT-CNM integrated into the ionic conductivity measurement circuit, in between two electrolyte compartments both connected through Ag/AgCl electrodes. (Reprinted from P2 with permission from the Royal Society of Chemistry)

To collect information about the pores in the BPT-CNM, trans-membrane ionic conductance measurements were performed.^[P2] The ionic conductance through the CNM exposed by the Si_3N_4 aperture was determined from current-voltage curves recorded in the flow cell, as shown in the inset of **Figure 3.2.1**. By evaluating the conductance measurements, the pores on the CNMs can be considered as 2D nanochannels. Therefore, if the classic model for the description of conductance through nanopores in Si_3N_4 membranes is applied to CNMs, the measured ionic conductance can be expressed in terms of the length and the diameter of one single 2D channel. Given the area that exposed to the solution was defined by the aperture, **Equation 3.3**¹³⁶ can be obtained:

$$G = \sigma_e \left(\frac{4l}{\pi d^2} + \frac{1}{d} \right)^{-1} \quad (3.3)$$

where d and l describe the average diameter and length of a single pore through which the conductance G is measured. The bulk electrolyte conductivity σ_e , with the units Siemens/meter ($S \cdot m^{-1}$), is determined by the ionic strength of the solution. Note that, the CNM has more than one pore. Therefore, **Equation 3.3** can be adjusted to **Equation 3.4**:

$$n_A = \frac{G_{\text{meas}}}{\sigma_e} \cdot \left(\frac{4l}{\pi \langle d \rangle^2} + \frac{1}{\langle d \rangle} \right) \quad (3.4)$$

Here, G_{meas} is the measured conductance, n_A is the number of pores in the suspended membrane area A and $\langle d \rangle$ is the average pore diameter. The ionic conductance through the CNM suspended over the Si_3N_4 aperture was determined from current-voltage (I-V) curves recorded in the flow cell, both before and after the CNM deposition. To avoid the measurements being affected by the dehydration phenomena in the confinement of 2D nanochannels,¹³⁷⁻¹³⁹ the conductance was determined by applying Ohm's law in the region close to zero bias. There, the conductance of hydrated ions is most closely approximated. The results are presented in **Figure 3.2.2a**. Due to the CNM barrier, the measured conductance dropped 30% compared to the bare Si_3N_4 aperture. The conductance of the CNM samples shows a linear relation to the free-standing area, confirming that the ionic current through the membrane makes the main contribution to the conductance.

The porosity of the BPT-CNM was analyzed based on the average measured membrane conductance per area in 1 M KCl solution. It can be calculated from the linear regression of the conductance value in **Figure 3.2.2a**. After subtraction of the bare aperture conductance, the conductance per area of the membrane was found to be $G_{\text{CNM}} = 4.8 \frac{nS}{100nm^2}$. By substituting this value into **Equation 3.4**, the porosity of the BPT-CNM can be estimated. Note that **Equation 3.4** includes two variables, which are n_A , the number of pores contributing to ion transport and $\langle d \rangle$, the average diameter of the pores. Thus, **Equation 3.4** can be converted into a simple function:

$$f(\langle d \rangle) = n_A \quad (3.5)$$

The function graph was plotted in **Figure 3.2.2b**. As discussed above, the domain of the factor $\langle d \rangle$ is not infinite. It is limited by the observed result from the HR-TEM and the size of the hydrated ions. Taken the hydrated diameter of K^+ as 0.56 nm,¹⁴⁰ it can be obtained that $\langle d \rangle \in [0.56, 1)$. Therefore, the range of n_A lies between 2.7 and 1 (unit: pores per 100 nm², the yellow region in **Figure 3.5.2b**),

which means in the free-standing area over the 60 nm aperture (as shown in **Figure 3.2.1c**), about 60 pores partook as conductive channels.

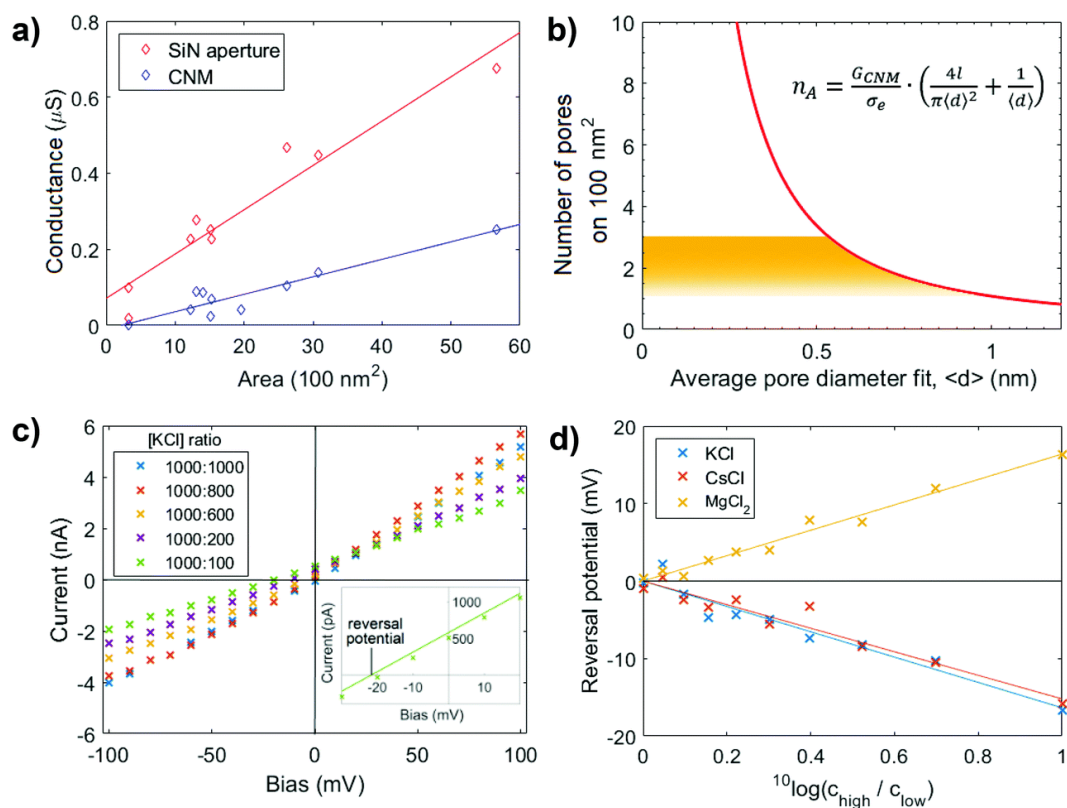


Figure 3.2.2. Ion transport measurements. (a) Ionic conductance through BPT-CNM with varying free-standing membrane area exposed on both sides to 1 M KCl solution. (b) Geometric model relating the average pore diameter to the number of pores in a 100 nm² area. (c) Ionic current-voltage (CV) curves measured in the presence of an electrolyte concentration gradient over a 50 nm diameter CNM membrane. (d) The reversal potential over the membrane in (c) at concentration ratios ranging between 1 and 10, with the higher concentration kept constant at 1000 mM. (Reprinted from **P2** with permission from the Royal Society of Chemistry)

Next, the membrane potential across the BPT-CNM was determined following Nernst-Planck membrane theory.¹⁴¹ In the presence of concentration gradient, the chemical potential drives ions from the higher to the lower concentration side of the membrane. If one type of ion is preferentially diffusing down its concentration gradient over its counter-ion, a diffusion potential and an associated net ionic current are generated across the membrane. CV characterization was performed in the presence of varying concentration ratios. As shown in the inset in **Figure 3.2.2c**, after linear fitting of the data point, the x-intercept is the value of the reversal potential with which the selective ionic

current was exactly compensated. For instance, at a concentration ratio of 1:10 in KCl, the reversal potential was found to be -16.6 mV (**Figure 3.2.2d**). Therefore, the corresponding membrane potential is $+16.6$ mV. This result is not surprising since BPT-CNM has a negative surface charge due to the functional groups such as sulfinic acid or sulfonyl hydroxide. Note, the theoretical Nernst membrane potential can be calculated through the Nernst equation:

$$V_{\text{Nernst}} = 0.05916 \frac{RT}{FZ} \lg \left(\frac{\gamma_{\text{C high}} c_{\text{high}}}{\gamma_{\text{C low}} c_{\text{low}}} \right) \quad (3.6)$$

The obtained value is 52 mV. The BPT-CNM membrane potential is thus 32% of the theoretical Nernst potential. This lower barrier effect might be caused by the ultimate thinness of the BPT-CNM. In the commercial porous membranes, ion selectivity arises due to a bulk membrane phase that is distinct from the adjacent electrolyte phases. In BPT-CNM, on the other hand, the about 1 nm long pore channels cannot effectively impede the ion transport. Moreover, the counter-ion Cl^- has a similar hydrated ion diameter as K^+ but much higher mobility. It makes the selection of ions through the pore size less effective. The latter is also reflected in the repeated measurement of the membrane potential in MgCl_2 solution. Since the divalent MgCl_2 solution has three times higher ionic strength than a monovalent KCl solution of the same concentration, the negative electrostatic charges on the pore edge could be more efficiently screened.^{142, 143} Therefore, ion mobility becomes the factor that determines selective transport. The Cl^- ions, with a higher diffusion coefficient than the Mg^{2+} ions, tend to dominate the charge transfer, resulting in the change of the membrane potential sign.

To conclude, the selective ion permeation through free-standing BPT-CNM was studied. The results revealed that the pore density of the BPT-CNM located in a range of $1 - 2.7$ per 100 nm^2 . The selectivity of the membrane is mainly caused by the negative electrostatic charges on the membrane surface. Therefore, by changing the chemical composition of the membrane, specific interactions between membrane and electrolyte could be obtained to further tune the selectivity.

3.3 CNM Based Optical Metamembranes

Parts of this chapter were published in **P3**: Plasmonic Metasurfaces Situated on Ultrathin Carbon Nanomembranes. Y. Denizhan Sirmaci, Zian Tang, Stefan Fasold, Christof Neumann, Thomas Pertsch, Andrey Turchanin, and Isabelle Staude. *ACS Photonics*. **2020**, 7, 1060-1066.

Transferred CNMs possess a high mechanical and thermal stability.^{5, 62} Some of the CNMs can be prepared free-standing over $500 \times 500 \mu\text{m}^2$ openings^{5, 100} and sustain temperatures up to 700 K without significant structural changes.¹⁴ The mechanical properties of CNMs can be analyzed with bulge tests using an AFM to measure the membrane's deflection.¹⁴ By applying pressure to one side of the freestanding CNMs, they undergo deformations, changing the deflection of the cantilever at the center of the free-standing area. The Young's modulus, tensile strength, and residual stress can be calculated from the obtained pressure–deflection curves. As presented by the work of Zhang et al.,⁷⁷ TPT-CNMs have Young's moduli about 10 GPa while possessing residual stress of only 3 MPa, therefore become promising candidates for the fabrication of the supporting nanosheet. As the ~1 nm thick BPT- and TPT-CNMs have almost no interaction with light in the specific wavelength range (**Figure 3.3.1e**), this property enables the broadband operation of the CNMs in photonics.

In the advanced photonic research, the optical metasurfaces have been widely adopted to manipulate phase, polarization and modality of electromagnetic waves over subwavelength thickness, only a few years after the concept was born.¹⁴⁴⁻¹⁴⁷ They are constructed by 2D well-arranged artificial nanoresonators typically on macroscopically thick supporting substrates, which are transparent materials such as glass¹⁴⁸ or polymer.¹⁴⁹ However, due to the nature of these materials and the restriction of their processing techniques, the thickness of these supporting substrates cannot be reduced to the nanoscale.^{150, 151} The light absorption in these substrate materials limits the broadband operation of the photonic metasurfaces.¹²⁷ In this thesis, an optical metasurface fabricated using TPT-CNMs as supporting substrate is introduced. To this end, a square array of U-shaped split-ring-resonator (SRR, **Figure 3.3.1a**, $l = 260 \text{ nm}$, $t = 45 \text{ nm}$, $a = 350 \text{ nm}$, and $k = 75 \text{ nm}$) was nanofabricated on the TPT-CNM/Au surface using electron-beam lithography (EBL) based process.¹⁵²⁻¹⁵⁴ Then, ECD assisted transfer was used to transfer the CNM-supported metasurface from the gold substrate to a TEM grid. To prove the successful preparation of quasi free-standing metamembrane, the sample was characterized by SEM. Using high

magnification, the free-standing areas can be distinguished from the grid supported areas due to different contrast: dark and bright, respectively. (Figure 3.3.1b, c). With further zooming in, the morphological features of the nanometer-scale gold resonators can also be clearly identified (Figure 3.3.1d).

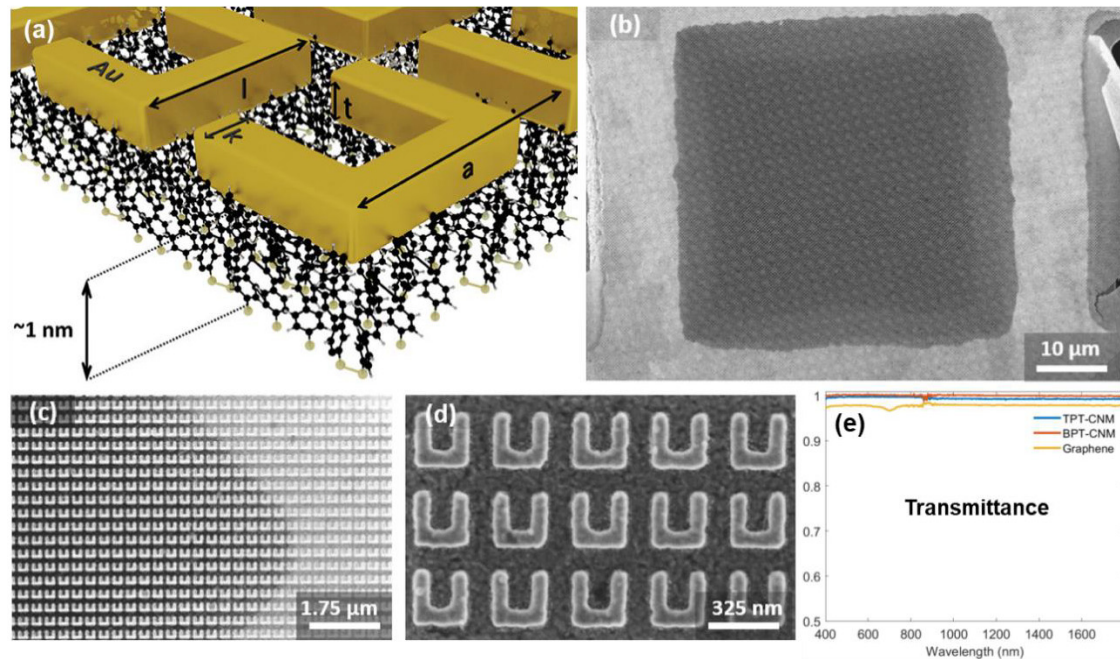


Figure 3.3.1. (a) Schematic representation of the CNM supported SRRs. (b-d) TEM images of the metasurface in different magnifications. (e) Measured linear-optical transmittance spectra of the TPT-CNM (blue), BPT-CNM (red) and graphene (yellow). (Reprinted with permission from P3. Copyright (2020) American Chemical Society.)

Next, the linear-optical transmittance spectra were obtained to characterize the optical quality of the SRR metamembrane. Measurements taken with a Si and an InGaAs detector were combined to achieve the full coverage of the entire relevant spectral range from visible to near-infrared wavelengths. Using a knife-edge aperture, the measurement area was confined only to the openings of the TEM grid ($30 \times 30 \mu\text{m}^2$), where the SRR metamembrane is free-standing. A linear polarizer is introduced in the illumination beam path to selectively measure the metamembrane's optical response along with the two different lattice directions of the SRR metamembrane.

Assuming that the SRR arrays are suspended in a vacuum and using the numerical finite-integral frequency-domain calculation (software: CST Microwave Studio),^[P3] the simulated transmittance spectra were obtained, which is displayed in Figure 3.3.2a.^[P3] These data is in a good agreement

with the experimental result (**Figure 3.3.2b**), which also shows two transmittance minimum for x-polarized light (1619 nm and 780 nm) and one minimum for y-polarized light (820 nm). As expected, the fundamental mode of the SRR metasurface occurring at 1685 nm for the x-polarized excitation is characterized by a circulating current along the entire SRR loop, giving rise to a magnetic dipole moment out of the SRR plane. The second-order mode, which appears for the y-polarized incident light at 805 nm, is an electric-dipole dominated mode characterized by in-phase currents along the two legs of the SRR. Finally, the third-order resonance observed at 775 nm for x-polarized excitation, is an electric quadrupolar dominated mode with out-of-phase currents in the SRR legs.^{152, 154} The small differences observed between calculated and measured transmittance spectra can be attributed to the non-normal incidence conditions present in the experiment, sample imperfections as well as possible deviations of the CNM morphology from a planar membrane caused by the gravity.

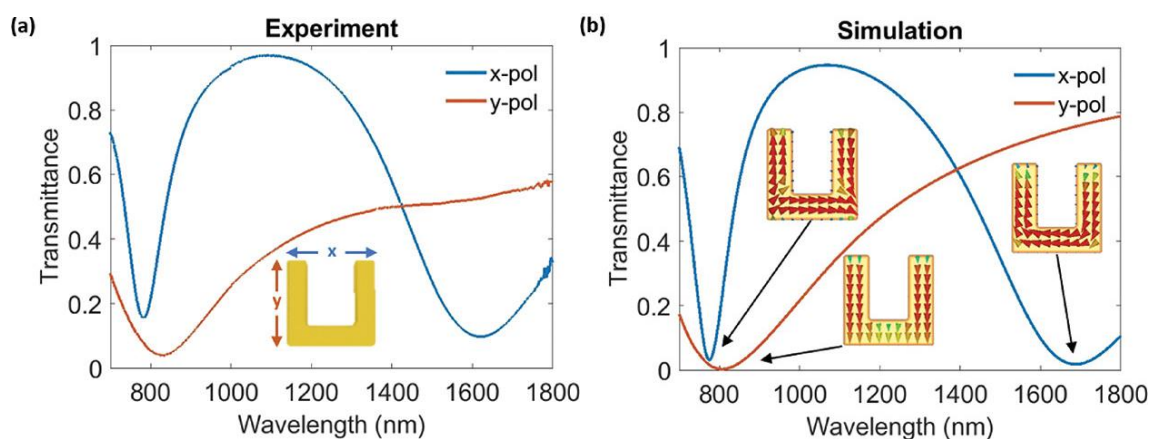


Figure 3.3.2. (a) Measured and (b) numerically calculated normal incidence linear-optical transmittance spectra for x-polarized (blue) and y-polarized (red) light. In (b), calculated surface current distributions at the three different resonances are presented by the insets. (Reprinted with permission from **P3**. Copyright (2020) American Chemical Society.)

In conclusion, using TPT-CNMs as an about 1 nm supporting substrate for metasurface, a photonic metamembrane operating at near-infrared frequencies has been successfully realized. In this metamembrane, the gold split-ring resonators (SRRs) are quasi free-standing due to the ultimate thinness of the TPT-CNMs. Transmittance spectra of the fabricated free-standing photonic metamembranes have revealed the expected resonant properties.

3.4 Smart Molecular Nanosheets for Electron Cryo-microscopy

Results of this chapter were reported in **P4**: Smart molecular nanosheets for electron cryo-microscopy (cryoEM) of biological samples. Julian Scherr, [Zian Tang](#), Maria Küllmer, Sebastian Balsler, Alexander Stefan Scholz, Andreas Winter, Kristian Parey, Alexander Rittner, Martin Grininger, Volker Zickermann, Daniel Rhinow, Andreas Terfort, Andrey Turchanin. *Submitted to ACS Nano (under review)*.

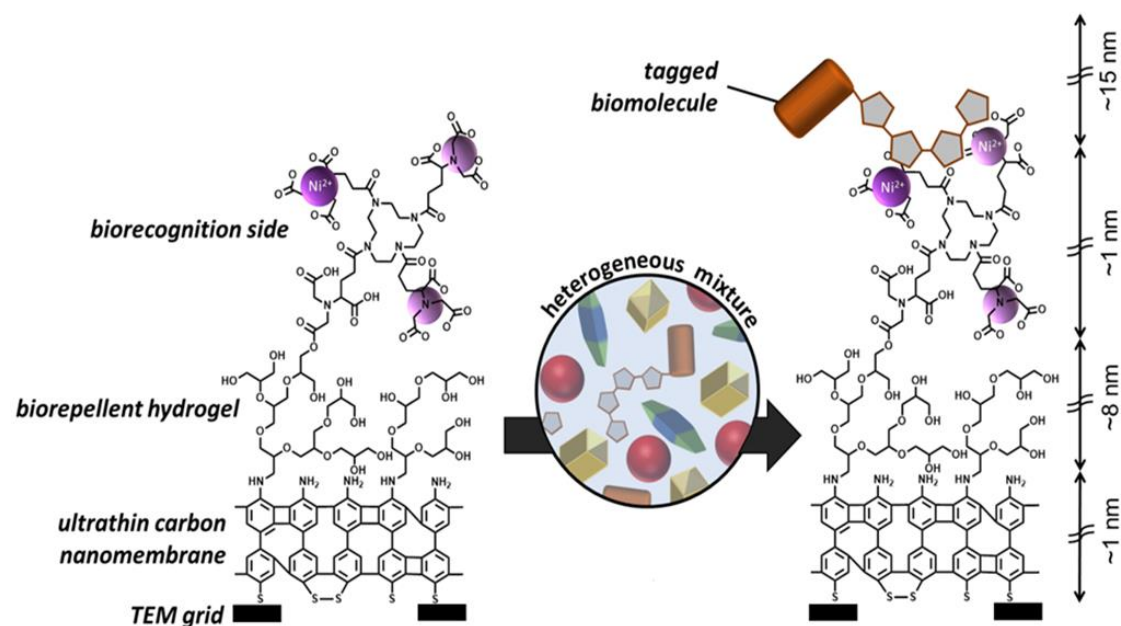


Figure 3.4.1. Schematic representation of the structure and the functional principle of the developed smart nanosheets for biological TEM. The functionalized nanosheets contain an NTA₄cyclen moiety as well as a biorepellent hydrogel, which enables selective immobilization of His-tagged biomolecules for their subsequent analysis by cryoEM while preventing the unspecific binding of other proteins.

As CNMs can be chemically functionalized,^{64, 68} they are suitable not only for the top down fabrication of metallic nanostructures (see Chapter 3.3) but also for the bottom-up assembly of complex organic/bio-organic hierarchical nanostructures. An example is using CNM to make smart nanosheet for biological TEM.^[P4] Current preparation of vitrified biological samples for cryoEM starts with sample isolation and purification, followed by the fixation in a free-standing layer of amorphous ice. Samples are typically embedded in a thin layer of vitreous ice on holey carbon films to avoid electron-beam induced structure disturbances. In an effort to improve the TEM sample preparation, it would be advantageous to deposit the specimen particles onto nanosheets that are

thin enough to allow the undisturbed transmission of electrons. To this end, carbon nanomembranes (CNMs) have been established as alternative support films for TEM. Unlike other support films that are typically employed in cryoEM such as metallic glasses,^{155, 156} graphene¹⁵⁷⁻¹⁶⁰ or gold¹⁶¹, CNMs possess active functional groups, which are suitable for the functionalization with biorecognition sites and anti-fouling polymers. This functionalization enables the *in situ* isolation and purification of the specimens before the TEM imaging. Compared with graphene oxide nanosheets,¹⁶² the functionalization of CNMs is more controllable and straight forward. Note that, CNMs are stable against detergents,⁵ making them compatible with structural analysis of, e.g., detergent-solubilized membrane proteins. Therewith, the supporting nanosheets for cryoEM analysis based on CNMs have the following advantages: they (i) minimize inelastic scattering of electrons, (ii) have high mechanical stability, (iii) allow introduction of specific biorecognition sites as well as biorepellent background. In this chapter, the preparation of CNM-based smart molecular nanosheets is presented. 4'-nitro-4-Biphenylthiol (NBPT) was selected as the precursor to fabricate the CNM platform for the smart nanosheets. Upon cross-linking into CNMs, the terminal nitro groups in NBPT molecules are reduced to amino groups, which are used later as active sites to initiate surface polymerization of biorepellent polymer. Note that the biorepellent layer should also possess sufficient reactive groups to bind biorecognition moieties. For this reason, the hyperbranched polyglycerol (PG) was chosen as the anti-fouling polymer,¹⁶³ which was directly grafted on the amino-terminated surface of CNMs. The obtained PG functionalized nanosheets (PG-CNMs) have a total thickness of about 9 nm. With further functionalization with NTA-Ni units, smart nanosheets for biorecognition of His-tagged protein specimens were assembled (**Figure 3.4.1**).

The fabrication steps were monitored by the infrared reflection absorption spectroscopy (IRRAS) and the X-ray photoelectron spectroscopy (XPS). The IRRAS data of PG-CNM (black) and NTA-PG-CNM (red) were shown in **Figure 3.4.2**. The band at 3200-3600 cm^{-1} (OH-stretching mode), 2875 cm^{-1} and 2940 cm^{-1} (sym/asym C-H stretching mode), as well as the band at 1140 cm^{-1} (C-O-C stretching mode), proved the existence of the PG-layer.¹⁶⁴ The band at 1740 cm^{-1} is assigned to carbonyl groups. It appears in the PG-CNM due to the rearrangement of the epoxy groups during the polymerization at high temperature ($\sim 140^\circ\text{C}$) and intensified in the NTA-PG-CNM due to the introduction of additional carboxylic acid and carboxylic ester moieties. The band at 1645 cm^{-1} ,

which is only shown in the NTA-PG-CNM spectrum, is caused by C=O stretching vibrations of the amide groups, confirming the successful functionalization of the NTA derivative.¹⁶⁵

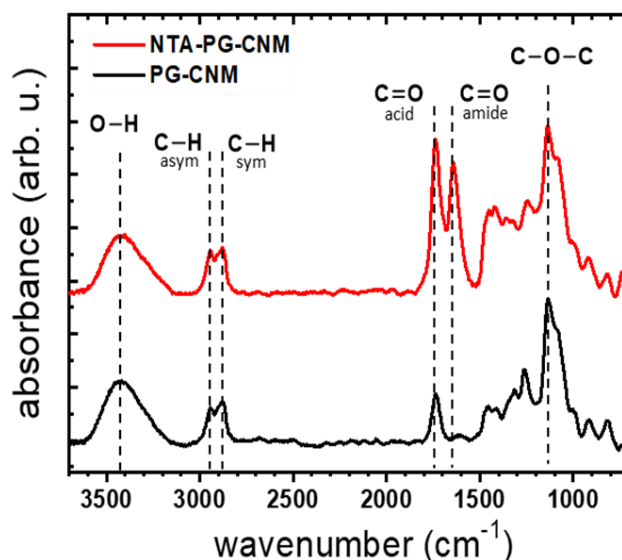


Figure 3.4.2. Analysis of the engineered nanosheets by IRRAS: PG polymerization on the NH₂-CNM (black) and subsequent NTA functionalization of the PG (red).

Further evidence for the successful functionalization was provided by XPS. In **Figure 3.4.3**, the C 1s, N 1s, S 2p and O 1s spectra of different fabrication steps are shown. The spectra of the pristine NH₂-CNM shown in **Figure 3.4.3a** are consistent with previous reports.⁶² Note that only one single peak at 399.5 eV is present in the N1 spectrum of the pristine NH₂-CNM,^{68, 133} which indicates a complete conversion of the nitro groups into the amino groups upon e-beam irradiation. The functionalization with PG drastically changed the surface compositions, as shown in **Figure 3.4.3c**. Because of the signal attenuation through the 8 nm thick PG layer, the N 1s and S 2p peaks vanish. On the other hand, the O 1s signal significantly increases and shifts to 533.4 eV due to the formation of the ether groups in the PG layer.¹⁶⁶ As expected, the ether C 1s signal at 286.3 eV dominates the total carbon signal. The remaining constituents of the C 1s signal at 285.3 eV, 287.8 eV and 289.5 eV are assigned to the aliphatic,¹⁶⁷ carbonylic¹⁶⁸ and carboxylic carbon,¹⁶⁸ respectively. After the grafting of the NTA₄cyclen units, an attenuation of the C 1s signal at 286.3 eV is observed, which enables to calculate a thickness increment by 1 nm. Moreover, because of the introduction of the amide groups, a new C 1s peak at 288.7 eV appears in the spectrum. The N 1s peak of the NTA groups with a protonated nitrogen shoulder also appears in the spectrum at 400.4 eV and

402.1 eV.^{169, 170} Note that also traces of Zn^{2+} signals were found in the NTA-PG-CNM after the synthesis, most probably due to impurities in the used solvents. Since the collected Zn^{2+} can be completely replaced by Ni^{2+} , these results additionally demonstrated the functionality of the attached NTA chelators. After the loading with Ni^{2+} , the quantitative ratio of $Ni:N = 1:2.4$ was observed, which matches very well with the expected ratio of 1:2.7. Overall, the XPS results show good agreement with the IRRAS data and further confirm the grafting on an NH_2 -CNM of the biofunctional layer as schematically presented in **Figure 3.4.1**.

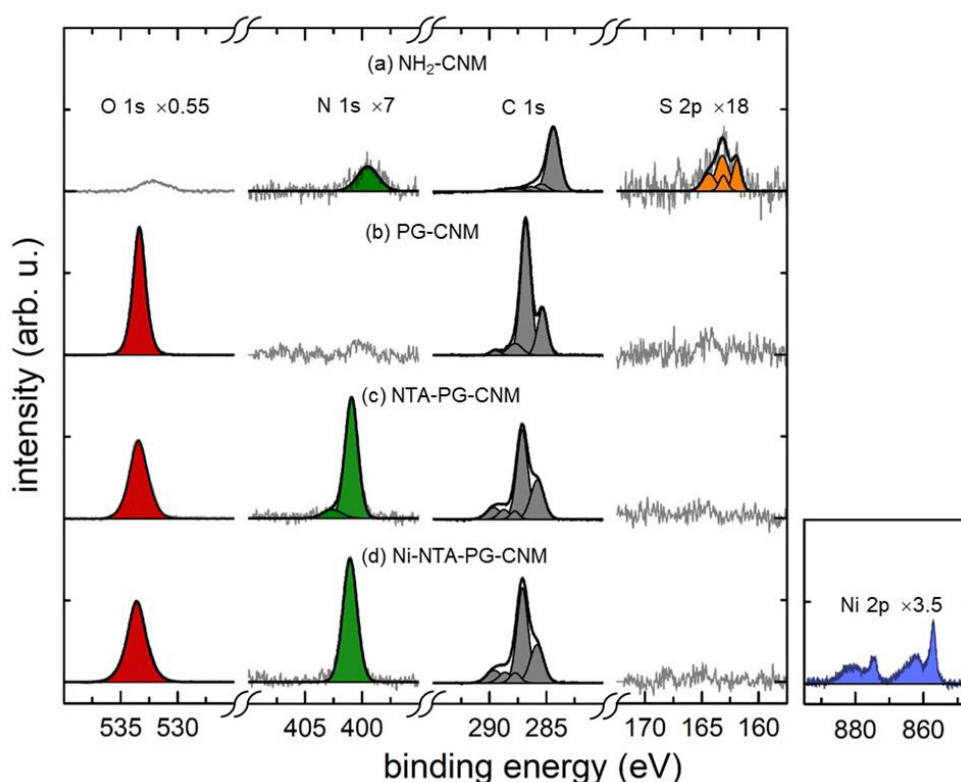


Figure 3.4.3. XPS analysis of the subsequent functionalization steps. High-resolution XP spectra of the O 1s, N 1s, C 1s, S 2p and Ni 2p. The spectra are scaled for better visibility as indicated. (a) Pristine NH_2 -CNM on Au/mica. (b) Grafting of the PG layer, PG-CNM. (c) Grafting of the NTA₄cyclen layer, NTA-PG-CNM. (d) Chelating of Ni^{2+} to NTA-PG-CNM.

To test the selectivity to the specific biological specimen, the nanosheet was incubated with bovine serum albumin (BSA, without His-tag to test for unspecific bioadhesion, 67 kDa) and His8-tagged green fluorescent protein (His8-GFP, as a specific analyte, 39 kDa)¹⁷¹ successively and studied by surface plasmon resonance (SPR) measurements. From the SPR results, untagged BSA was found

to be washed away from the nanosheet by the buffer solution, demonstrating the protein repellent properties of the fabricated substrate, whereas the His-tagged GFP was selectively attached to it.

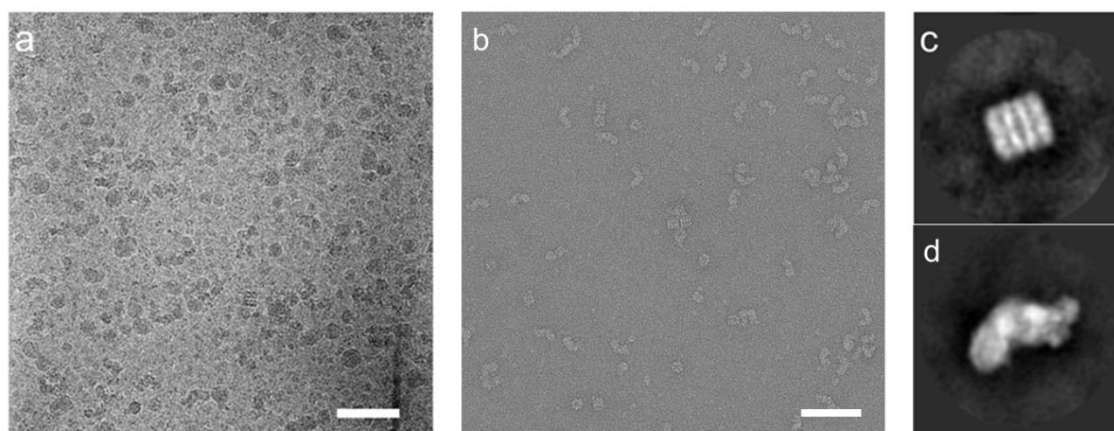


Figure 3.4.4. CryoEM analysis of His-tagged complex I selectively bound to NTA-PG-CNM with ~10 nm thickness. CryoEM images of a vitrified sample: (a) the Ni²⁺-activated NTA-PG-CNM and (b) conventional films of amorphous carbon were exposed to a 1.16:1 mixture of complex I and GroEL. The scale bar is 100 nm. (c) Representative class average of complex I. (d) Representative class average of GroEL.

Finally, the feasibility of *in situ* isolation of His-tagged proteins from a heterogeneous mixture by the smart nanosheets platform is presented. The results were analyzed by cryoEM (**Figure 3.4.4a**). His-tagged complex I from *Yarrowia lipolytica* and GroEL (without His-tag) from *E. coli* were selected as the test specimens.^{172, 173} A continuous amorphous carbon film was tested as a reference sample. After treating with a 1.16:1 mixture of tenside-stabilized complex I and GroEL, the reference sample did not show any selective binding for complex I or GroEL (**Figure 3.4.4b**). By incubating the smart nanosheets with the same mixture, the preferable immobilization of the His-tagged complex I (**Figure 3.4.4a**) was clearly observed. In the obtained 73 images, 1176 His-tagged complex I particles and 41 GroEL particles were identified, corresponding to a recognition efficiency of about 97%. Their orientation was found to be random, which is advantageous for structural analysis. Note that, due to the fixation onto the smart nanosheet, the specimens were embedded in a thin vitrified water film thus prevent proteins from denaturing at the air-water interface.¹⁷⁴

To summarize, a novel supporting nanosheet for cryoEM imaging of biospecimens based on NH₂-CNM was successfully established. The smart nanosheet contains three functional components,

i.e., CNM carrier layer, PG biorepellent layer and Ni-NTA biorecognition units. Strengthened by the mechanically stable CNMs, the total thickness of the smart nanosheets was achieved to be about 10 nm allowing almost undisturbed penetration of the electron beam. The homogeneous distribution of the biorecognition sites and the softness of the nanosheets lead to an optimized orientation of the particles, which is advantageous for further structural analysis. Furthermore, the nanosheets are stable in detergents, enabling the advanced preparation of biosamples.

3.5 Photoswitchable CNMs for Implementation in Graphene Field-Effect Transistors

Parts of this chapter were published in **P5**: Optically triggered control of the charge carrier density in chemically functionalized graphene field effect transistors. Z. Tang, A. George, A. Winter, D. Kaiser, C. Neumann, T. Weimann, A. Turchanin. *Chem. Eur. J.* **2020**, DOI: 10.1002/chem.202000431.

As demonstrated above, CNMs are an excellent platform to attach novel chemical or biochemical functions. In contrast, the functionalization of 2D materials as, e.g., graphene is not trivial.^{175, 176} Its chemical inertness restricts the covalent attachment of specific groups.⁵² Moreover, the covalent functionalization of graphene will introduce in its structure therewith diminishing its original physical properties (**Figure 3.5.1a**).^{177, 178} The noncovalent functionalization of graphene is typically based on the molecular adsorption and is not very stable (**Figure 3.5.1b**).^{162, 179-182} Therefore, both routes provide significant challenges for implementation in functional graphene-based devices.

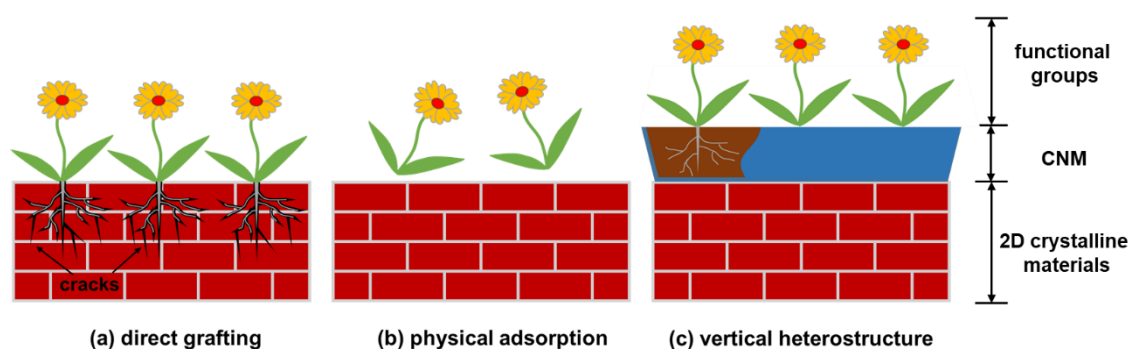


Figure 3.5.1. Illustration of different strategies to achieve functionalization of 2D crystalline materials. (a) Covalent functionalization, which leads to the damage of the structure. (b) Non-covalent functionalization based on molecular adsorption. (c) Immobilization of the functional groups via the formation of a vertical van der Waals heterostructure.

The CNMs can be easily functionalized with desired functional molecules. Such functionalized CNMs can be transferred onto graphene or other 2D materials, and in this way, van der Waals heterostructures can be formed.⁶⁵ (**Figure 3.5.1c**). Therewith a non-destructive functionalization of graphene or other inorganic 2D materials can be achieved. Based on this idea, in this thesis, an optically switchable graphene field-effect transistor (GFET) was realized. An azobenzene derivative

molecule was chosen to this end, to induce the photoswitchability. The azobenzene molecules undergo reversible transformations between *cis* (dipole ~ 3 D) and *trans* (dipole ~ 0 D) molecular conformations under exposure to 365 nm and 455 nm light, respectively.^{180, 183-186} This photo switching effect between *cis*- and *trans*-conformation will modulate the effective molecular field acting on the GFET channel, thus changing doping level of the device.^{184, 187} In a first step they were chemically bound to the NH₂-CNM using the NHS-ester coupling reaction⁸⁸ and then the hybrid azo-CNM was transferred on the GFET channel to assemble the vertical vdW heterostructure (**Figure 3.5.3**).^[P5]

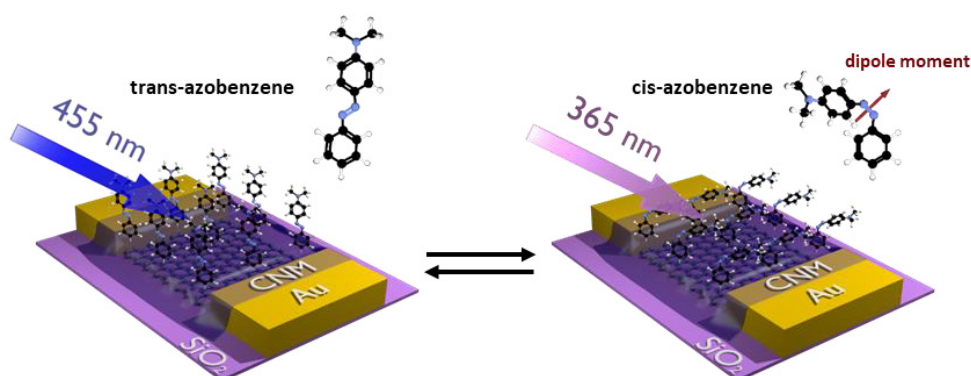


Figure 3.5.2. Schematic illustration of the working principle of an optically switchable GFET device. The azobenzene molecules immobilized on the amino-CNM undergo *cis*- and *trans*-transformations by exposure to 365 nm and 455 nm light, respectively. The red arrow in the magnified azobenzene molecule points towards the direction of the molecular dipole moment. (Reprinted from **P5** with permission from the European Chemical Societies Publishing)

XPS was performed to control the azobenzene functionalization on the NH₂-CNM. Based on the attenuation of the substrate Au 4f signal, an increase of the NH₂-CNM effective thickness from 1.2 nm to 1.4 nm was detected after the functionalization. The high-resolution N 1s and C 1s XP spectra are shown in **Figure 3.5.3**. The N 1s signal in pristine NH₂-CNM is presented as a single symmetric peak at 399.4 eV (blue), which is assigned to uncharged amino (-NH₂) groups on the CNM. After grafting of azobenzene, the N 1s peak acquires an asymmetric shape, indicating more than one nitrogen species present on the surface, which can be represented by two peaks at 399.1 eV (blue) and 400.3 eV (red). The peak at lower binding energy is assigned to amino and tertiary amine groups,¹⁸⁸ while the peak at high binding energy corresponds to the nitrogen in azo groups¹⁸⁹ and

amide groups¹⁷⁰. The quantitative analysis of the N 1s intensity before and after functionalization demonstrates that $20 \pm 3 \%$ of the amino groups are functionalized with azobenzene. This estimation was made based on the assumption that all immobilized azobenzene molecules have *trans*-conformation. Furthermore, the change of the C 1s signal also confirmed the effective attachment of azobenzene. After the functionalization, an enhancement of the intensity at 285.5 eV (blue) was observed, which is due to the carbon connected to azo and tertiary amine groups in the azobenzene. The amide group that links azobenzene to the CNM results in an increase ($\sim 17\%$) of the C 1s intensity at 288.1 eV (green), corresponding to a highly oxidized carbon species.¹⁹⁰ Moreover, due to an attenuation caused by the grafted azobenzene layer, the C 1s peaks representing the aromatic (284.3 eV, red) and ketone (286.9 eV, orange) carbon species became less intensive.

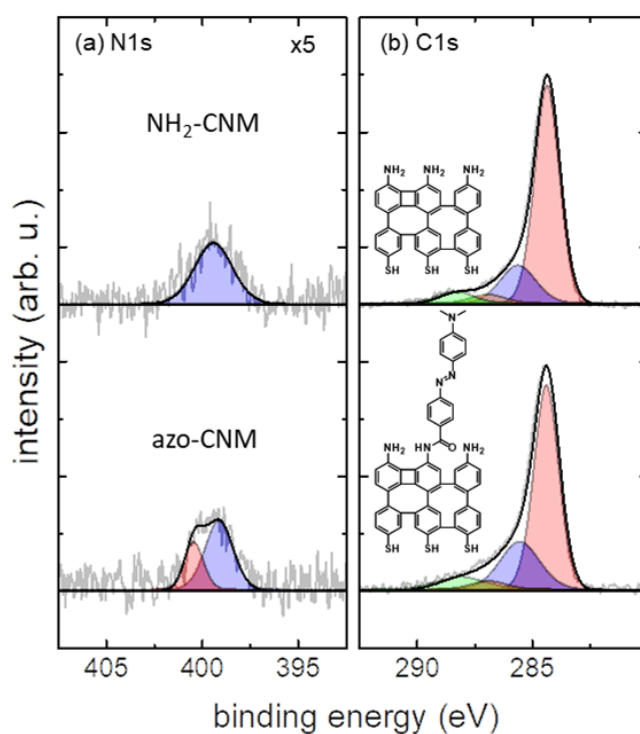


Figure 3.5.3. High-resolution (a) N 1s and (b) C 1s XP spectra of NH₂-CNM and azo-CNM. (Reprinted from **P5** with permission from the European Chemical Societies Publishing)

The azobenzene functionalized NH₂-CNM (azo-CNM) was transferred onto an array of GFET devices (**Figure 3.5.4a inset**). In this way, the vertical vdW heterostructure was formed at the channel region of the GFETs (azo-CNM/GFETs). Next, field-effect transport measurements were performed to investigate the electrical characteristics and to test the optical switchability of the azo-

CNM/GFETs. Two light-emitting diodes (LED) with emission wavelengths of 365 nm and 455 nm were used to control the light induced isomerization of azobenzene. As demonstrated in **Figure 3.5.4a**, illumination with 365 nm light shifts the Dirac point of the device to a lower gate voltage (V_G), whereas illumination with 455 nm light leads its position to a higher V_G . These changes correspond to the introduction and removal of the negative doping effect in the graphene FET. To study the time-dependent switching behavior of the device, transfer curves were recorded every minute during the exposures. As can be seen in **Figure 3.5.4b**, before illumination the Dirac point of the device was at 131 V. After exposure to 365 nm wavelength light for about one hour, a shift of Dirac point to 94 V was observed, which indicates a doping with negative charge carriers. The following exposure with 455 nm light removes the negative doping. The Dirac point shifted therewith back to 125 V.

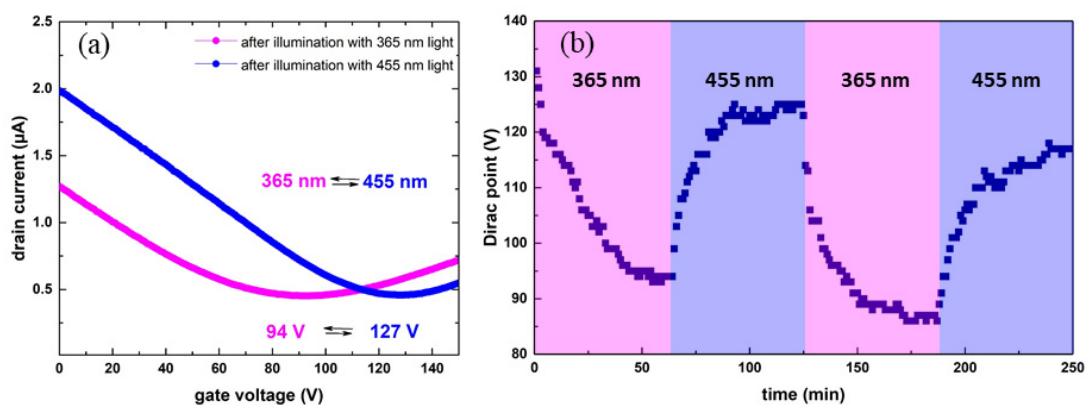


Figure 3.5.4. Photoresponsive behaviour of azo-CNM/GFET devices. (a) The transfer curves of an azo-CNM/GFET after illumination for 60 min with 365 nm and 455 nm light. (b) Time-dependent change of the position of Dirac point upon sequential illumination with 365 nm and 455 nm light. (Reprinted from **P5** with permission from the European Chemical Societies Publishing)

As studied before, the photoisomerization of azobenzene follows first-order reaction kinetics,^{191, 192} therewith the dynamic behavior of the device follows an exponential relation with illumination time. Therewith obtained time constants of both *trans* to *cis* and *cis* to *trans* photoisomerization have a value of 10 (± 0.5) min. Note that, the intensity of the 455 nm light source was a factor of 1.5 times higher than the 365 nm light in the experiment. It indicates that the switching rate of *trans* to *cis* is higher than its reverse switching, which is similar as reported for azobenzene SAMs.¹⁹³ Employing

this finding, we used subsequent 15 min irradiations with 365 nm and 455 nm to modulate a reversible shift of the Dirac point by ~ 20 V in the azo-CNM/GFETs. The results showed good reproducibility. Additionally, the transport curves of a device before and after single irradiation with 365 nm wavelength were shown in **Figure 3.5.5a**. The black curve represents the transfer characteristics of the pristine device. The Dirac point of the device is at 69 V. The purple curve represents the transfer characteristics after irradiation with 365 nm wavelength, which results in a shift of the Dirac point to 35 V. The grey curve represents the transfer curve of the device after thermal relaxation at room temperature (RT) for 48 hours, which demonstrates that the device restored the original position of the Dirac point, i.e. its doping level. We estimate from the time dependent measurements the time constant of the thermally induced *cis* to *trans* relaxation to ~ 15 h, which is in good qualitative agreement with an earlier study for azobenzene SAMs.¹⁹⁴

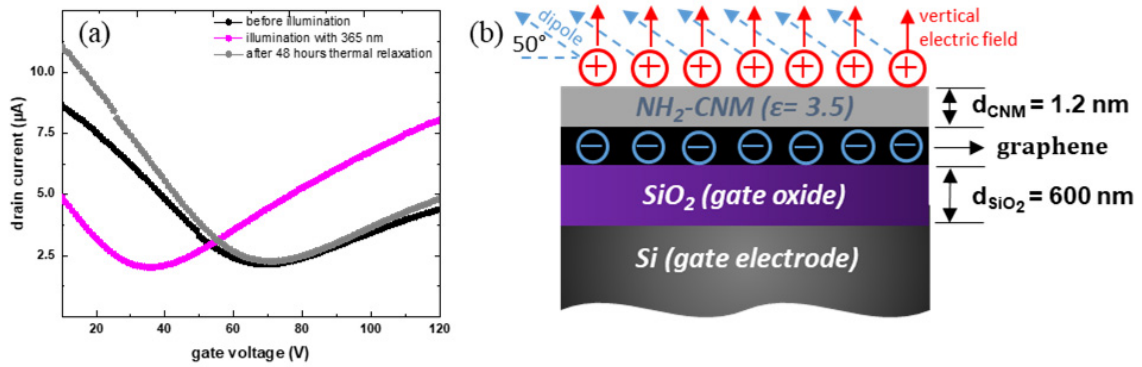


Figure 3.5.5. (a) Transfer curves of an azo-CNM/GFET device recorded before exposure, after exposure with 365 nm light and after thermal relaxation at RT for two days. (b) Schematic illustration of the induced electric field effect due to the conformational change of azobenzene from *trans* to *cis*. (Reprinted from **P5** with permission from the European Chemical Societies Publishing)

Next, the mechanism of the photoswitching effect was analyzed using a simple model. From our transport measurements, the variation in charge carrier concentration can be estimated with the **Equation 3.7**¹⁹⁵

$$\Delta n = \frac{C_{\text{SiO}_2}(\Delta V_{\text{Dirac}})}{e} \quad (3.7)$$

where C_{SiO_2} is the capacitance of the silicon oxide layer of thickness 600 nm (see **Figure 3.5.5b**), which is calculated to be 5.75×10^{-5} F/m². ΔV_{Dirac} is the shift in Dirac point. Its value is on average

35 V. therefore, the estimated change in charge carrier concentration from the transport measurement is $1.26 \times 10^{12}/\text{cm}^2$. To compare the experimental results with a model, estimation of the charge carriers variation was made based on the physical properties of azobenzene and CNMs. Azobenzene moieties grafted on the CNMs have a dipole moment $\mu_{trans} \approx 0$ D when appearing in *trans*-state, whereas the *trans-cis* isomerization will introduce a ~ 3 D dipole moment to the molecule.¹⁹⁶ Assuming that all azobenzene groups are initially standing perpendicular on the surface in *trans*-state, the effective electric field induced by the azobenzene molecules can be calculated then using the relation:

$$\Delta V_{cis \rightarrow trans} = N \left(\frac{\sin \theta \Delta \mu_{mol}}{\epsilon_r \epsilon_0} \right) \quad (3.8)$$

where N is the surface density, $\Delta \mu_{mol}$ is the dipole moment difference between the *cis* and *trans* form of the molecule, θ is the angle between the dipole moment and the surface, which is approximately 50° and ϵ_r is the relative dielectric constant within the azobenzene layer. The density of amino groups in an NH_2 -CNM is ~ 3.3 molecules/ nm^2 (*i.e.*, $3.3 \times 10^{14}/\text{cm}^2$). Considering that about 20% of these groups are functionalized with azobenzene, their surface density is then $6.6 \times 10^{13}/\text{cm}^2$. Taken the typical value of the relative dielectric constant of organic molecules as 3,^{195, 197} the effective gate voltage applied to the NH_2 -CNM can be calculated as 0.19 V. Furthermore, using **Equation 3.9**, the capacitance of the NH_2 -CNM can be calculated,

$$C_{\text{CNM}} = \epsilon_0 \epsilon_{\text{CNM}} / d_{\text{CNM}} \quad (3.9)$$

where the dielectric constant $\epsilon_{\text{CNM}} = 3.5$ and $d_{\text{CNM}} = 1.2$ nm.¹⁹⁸ The calculated capacitance possesses a value of 2.6×10^{-2} F/ m^2 . Therewith, the variation of the charge carrier concentration induced by the presence of the molecular dipoles can be calculated using **Equation 3.10**:

$$\Delta n_{cis \rightarrow trans} = \frac{C_{\text{CNM}} \Delta V_{cis \rightarrow trans}}{e} \quad (3.10)$$

where C_{CNM} is the capacitance of NH_2 -CNM, $\Delta V_{cis \rightarrow trans}$ is the variation in the top gate voltage caused by the molecular dipoles and e is the charge of an electron. Thus the charge carrier concentration induced by the molecular field can be estimated to be $3.11 \times 10^{12}/\text{cm}^2$. This estimated value is in overall good agreement with the corresponding experimental result.

In summary, optically triggered control of the charge carrier density in GFET devices has been realized by their indirect functionalization with azo-CNMs via the van der Waals heterostructure assembly. By illuminating the azo-CNM/GFET devices with 365 nm light, the azobenzene molecules change their conformation inducing the top gate voltage, which results in the negative doping of the graphene sheet. The reverse switching can be triggered using 455 nm light. The experimental data are in good agreement with the model calculation. The obtained results demonstrate the non-destructive chemical functionalization of graphene FETs for device applications.

4. Summary

In this thesis, the preparation, processing and several applications of carbon nanomembranes (CNMs) were investigated. As a short-range ordered two-dimensional (2D) material, CNMs are synthesized via electron irradiation induced cross-linking of aromatic self-assembled monolayers (SAMs).⁵ The post-processing of CNMs including delamination from growth template substrate and transfer to target substrate is indispensable for most of the applications of CNMs. Routinely, the transfer method can be divided into two categories: (i) the etching transfer and (ii) the etching-free transfer.³⁷ The etching transfer is only suitable for small area samples whose growth substrate can be easily etched away. In this respect, etching-free transfer, such as electrochemical delamination (ECD) assisted transfer, can be adapted to most of the samples, which are physically or chemically attached to the conducting growth substrate. In this thesis, both of the two transfer methods were adopted to realize the transfer of the 2D materials. The performance of the ECD assisted transfer in CNMs processing was specifically studied. Generally speaking, the ECD assisted transfer can effectively detach the CNMs from their substrates. The process is quick, simple and reproducible. Interestingly, the roughness of the transferred CNMs is correlating with the roughness of their growth substrate. This topographical correlation should be considered during the synthesis and could also be utilized for potential applications.^[P1]

The delaminated and transferred free-standing CNMs can be used as molecule sieves or ion sieves.⁷⁴ A BPT-CNM, as the thinnest mechanical stable CNM, possesses subnanometer pores and thus can be used as a dialysis membrane to impede specific ion penetration. Its porosity was characterized using ionic conductance measurement with the assistance of high-resolution TEM (HR-TEM). By limiting the upper limit of the pore diameter to 1 nm based on the HR-TEM results, the density of pores contributing to ion transport in the BPT-CNM was 1 – 2.7 pores per 100 nm². This performance is comparable with the high-end top-down approaches where pores are induced in post-modification steps involving ion or electron bombardment. The selectivity of the BPT-CNM can be attributed to its surface groups. Generally, due to ionization in the aqueous solution, these groups are negatively charged, therefore hinder the negatively charged ions from approaching. However, the membrane charge can be effectively screened or even change its sign if the ionic strength of the positive ion in the electrolyte is high enough. Under this situation, the ion selectivity

could be reversed. This effect was observed when MgCl_2 was used as the electrolyte upon measurement since the divalent magnesium ion solution has three times higher ionic strength than a monovalent ion solution of the same concentration.^[P2] Additionally, it is also straightforward to come to the idea that the selectivity can be manipulated by adjusting the surface functional groups. Note that the transferred CNMs is still mechanically stable,⁵ thus suitable for supporting nano-objects. Two specific applications as supporting nanosheets were demonstrated in the thesis employing the transferred free-standing CNMs. Firstly, the TPT-CNMs were used as supporting substrates for optical nanoresonators. It provides a new approach to realize the ultrathin plasmonic metamembranes. Due to the ultimate transmittance of TPT-CNMs to visible and near-infrared light, the quasi free-standing nanoresonators can manipulate light in a broad range. In the discussed example, the gold split-ring resonators on TPT-CNMs was illuminated with polarized light in a spectral range spanning from visible to near-infrared wavelengths and the transmittance spectra were measured. For x-polarization, two pronounced transmission minima at 1619 nm and 780 nm were observed. For y-polarization, a single transmission minimum was observed at 820 nm. These data are in consonance with theoretical modelling. Only small differences were found, which can be attributed to several reasons including sample imperfection and gravity induced deformation. However, they are negligible compared to the entire measured spectral width.^[P3] Secondly, NH_2 -CNM based smart nanosheets were fabricated for supporting biospecimens during cryoEM imaging. In this case, an NH_2 -CNM was first functionalized with a biorepellent polyglycerol (PG) layer via surface-initiated polymerization. The next, bio-recognition units (Ni-NTA) were covalently effectively attached on to the top of the PG-CNM layer for selectively immobilizing the His-tagged specimens. The obtained smart nanosheets possess only ~10 nm thickness, which extensively reduced the interference to the penetrated electrons during cryoEM imaging. They are also stable enough to hold the samples against the forces applied during immobilization, blotting, and vitrification. At the same time, the softness they possess optimized the orientational distribution of the specimens, thus paving the way for further meticulous structural analysis. Furthermore, since the specimens are fixed to the membrane, they are far under the water-air interface during vitrification, therefore prevent proteins from denaturation. In the practical test, the smart nanosheets were treated with a mixture of His-tagged complex I and normal GroEL followed by sufficient washing with buffer

solution. During the TEM imaging, up to 97% of selectivity to the His-tagged complex I was observed, which shows the promising perspective of application in cryoEM imaging.^[P4]

NH₂-CNMs have on both sides active functional groups, which can be easily functionalized without harsh reaction condition.⁵ Therefore, using CNMs as an interposer to immobilize functional groups onto a chemical inert surface in the form of vertical heterostructure becomes an alternative strategy to achieve non-destructive functionalization of 2D crystalline materials. Based on this idea, a photoswitchable graphene field-effect transistor (GFET) was fabricated, and in this thesis, its performance was studied. In this GFET, the graphene channel was completely covered under azobenzene functionalized NH₂-CNM. The azobenzene moieties on top of the CNM will undergo photoisomerization when expose to UV (365 nm) or blue (455 nm) light. The therewith produced polarity difference will apply different electric fields on top of the dielectric CNM, therefore, triggers the injection or removal of the charge carriers in the graphene sheets. According to the characterization results, the photoswitching process follows an exponential behavior. The time constants of both *trans* to *cis* and *cis* to *trans* photoswitching reaction were found to be of a similar value of 10 ± 0.5 min under our experimental condition. Furthermore, using the shift of Dirac point, the variation of the charge carrier density in the graphene channel was obtained. The result showed good agreement with the estimated value, which was calculated based on the physical properties of azobenzene molecule and CNM.^[P5]

To summarize, CNMs possess numerous promising properties, which make them a group of outstanding molecular nanomaterials among the 2D materials family. The combination of CNMs with other crystalline 2D materials in the form of van der Waals heterostructures offers an excellent solution to non-destructive functionalization of the otherwise chemically inert inorganic 2D materials, e.g., graphene. Therewith this new road to an effective and controllable fabrication of the 2D material based electronic and optoelectronic devices (e.g., using transition metal dichalcogenides) can be established. Moreover, within the research of advanced optical elements, the demand for further integration of nanostructures is getting higher and higher. CNMs, with their negligible light absorbance and weight, ultimate thinness and mechanical robustness, are promising optical nanomaterials to address this challenge. Due to the presence of subnanometer nanopores in CNMs, this material offers also many perspectives in ultrafiltration, as was exemplarily demonstrated in this work for the nanosieving of ionic species in aqueous solutions. In addition, CNMs are electrically

insulating molecular nanosheets with a high Young's modulus, acid and alkali resistance, as well as high thermal stability, etc. The study of all these scientifically attractive aspects and practically important properties of CNMs opens broad avenues for future research, which goes far beyond the borders of this thesis.

5. Zusammenfassung

In dieser Dissertation wurden die Herstellung, die Bearbeitung und verschiedene Anwendungen von Kohlenstoffnanomembranen (CNMs) untersucht. Als kurzreichweitig geordnetes zweidimensionales (2D)-Material werden CNMs durch Elektronenstrahl-induzierte Vernetzung aromatischer selbstassemblierter Monoschichten (SAMs) hergestellt.⁵ Für die meisten CNM-Anwendungen ist aber deren Nachbehandlung einschließlich Ablösung und Transfer vom Wachstums- auf das Zielsubstrat unverzichtbar. Grundsätzlich können die Transferverfahren in zwei Kategorien unterteilt werden: (i) Ein Transfer beruhend auf nasschemischen Ätzverfahren und (ii) ein Ätzlösungs-freier Transfer.³⁷ Der auf nasschemischen Ätzprozessen basierende Übertrag ist nur für kleinflächige Proben geeignet, deren Wachstumssubstrate leicht weggeätzt werden können. Ein Ätzlösungs-freier Transfer ist in dieser Hinsicht weniger restriktiv. Der Transfer mit Hilfe von elektrochemischer Delaminierung (ECD) eignet sich prinzipiell für Proben, bei denen das zu transferierende Material physikalisch oder chemisch an ein leitendes Wachstumssubstrat gebunden ist. In dieser Arbeit wurden beide Transferklassen für die Übertragung der 2D-Materialien angewendet, wobei im speziellen der Einfluss des ECD-unterstützten Transfers auf CNMs untersucht wurde. Dabei wurde festgestellt, dass CNMs unterstützt durch ECD effektiv von den Wachstumssubstraten gelöst werden konnten. Der Prozess ist schnell, einfach und reproduzierbar. Interessanterweise korrelieren die topografischen Merkmale wie die Rauigkeit der übertragenen CNMs mit der Rauigkeit ihres Wachstumssubstrats. Diese Korrelation sollte während der Synthese berücksichtigt werden, könnte aber auch gezielt für weitere Anwendungen eingesetzt werden.^[P1]

Delaminierte und freistehend präparierte CNMs können als Molekularsieb oder Ionensieb verwendet werden.⁷⁴ BPT-CNM ist die dünnste mechanisch stabile CNM. Sie besitzt Poren im Subnanometerbereich und kann daher als Dialysemembran Anwendung finden, um die spezifische Ionenpenetration zu behindern. In dieser Dissertation wurde die Porosität mittels Ionenleitfähigkeitsmessung, sowie mit Hilfe von hochauflösendem TEM (HR-TEM) charakterisiert. Durch die obere Begrenzung des Porendurchmessers auf 1 nm (basierend auf den HR-TEM Ergebnissen) beträgt die Dichte der Poren, die zum Ionentransport in BPT-CNMs beitragen, 1–2,7 Poren pro 100 nm². Dieses Ergebnis/diese Dichte ist vergleichbar mit vielversprechendsten Top-Down-Ansätzen, bei denen Poren nachträglich durch Ionen- oder Elektronenbeschuss erzeugt

werden. Die Selektivität des Ionentransports durch BPT-CNM kann ihren Oberflächengruppen zugeschrieben werden. Im Allgemeinen sind diese Gruppen aufgrund der Ionisierung in wässriger Lösung negativ wodurch die Membran abweisend gegenüber Transport von negativ geladenen Ionen ist. Die Membranladung kann jedoch effektiv abgeschirmt werden oder sogar ihre positive Werte erreichen, wenn die Ionenstärke des positiven Ions im Elektrolyten hoch genug ist. In dieser Situation kann so die Ionenselektivität umgekehrt werden. Dieser Effekt wurde beispielsweise bei der Verwendung von MgCl_2 als Elektrolyt beobachtet. Das zweiwertige Magnesiumion besitzt eine wesentlich höhere Ionenstärke als eine einwertige Ionenlösung derselben Konzentration.

Es ist erwähnenswert, dass die übertragenen CNMs mechanisch sehr stabil sind und sich daher als Trägerstrukturen für Nanoobjekte eignen.⁵ In dieser Dissertation wurden transferierte, freistehende CNMs auf zwei verschiedene Arten als stützende Nanoblätter eingesetzt. Zunächst wurden TPT-CNMs als Trägersubstrat für optische Nanoresonatoren verwendet. Auf diese Weise konnten ultradünne plasmonische Metamembranen realisiert werden. Aufgrund der nahezu vollständigen Lichtdurchlässigkeit von TPT-CNMs im sichtbaren und nahem Infrarot-Bereich kann mit den quasi freistehenden Nanoresonatoren Licht über einen weiten Wellenlängenbereich manipuliert werden. Hier wurden beispielhaft Gold-Split-Ring-Resonatoren auf TPT-CNMs mit polarisiertem Licht vom sichtbaren bis in den NIR-Spektralbereich beleuchtet und die Transmissionsspektren gemessen. Für die x-Polarisation wurden zwei ausgeprägte Transmissionsminima bei 1619 nm und 780 nm gefunden. Für die y-Polarisation wird andererseits ein einzelnes Transmissionsminimum bei 820 nm beobachtet. Diese Daten stimmen mit den theoretischen Modellen überein. Es wurden nur kleine Abweichungen gefunden, die verschiedene Ursachen haben können, einschließlich Probeninhomogenitäten und schwerkraftbedingter Verformung. Sie sind jedoch bezogen auf den gesamten gemessenen spektralen Breite vernachlässigbar.^[P3] Zweitens wurden so genannte Smart Nanosheets auf Grundlage von NH_2 -CNMs hergestellt, um Biospezies während der CryoEM-Bildgebung zu immobilisieren und zu stabilisieren. In diesem Fall wurde NH_2 -CNM zunächst mit einer bioabweisenden Polyglycerin (PG) Schicht durch oberflächeninitiierte Polymerisation funktionalisiert. Als nächstes wurden Biorekognitionseinheiten (Ni-NTA) kovalent an die Oberseite der PG-CNM-Schicht gebunden, um die mit Polyhistidin funktionalisierten Proteine zu immobilisieren. XPS, AFM und IRRAS wurden verwendet, um den gesamten Herstellungsprozess detailliert zu charakterisieren. Die erhaltenen

intelligenten Nanoblätter besitzen eine Dicke von ~10 nm, wodurch Interferenzen der Elektronen während der cryoEM-Bildgebung stark reduziert wurden. Des Weiteren sind diese auch stabil genug, um die Proben gegen die auftretenden Kräfte zu schützen, welche während der Immobilisierung, des Blottings und der Vitrifizierung entstehen. Außerdem optimiert ihre Flexibilität die Orientierungsverteilung der Proteine und ermöglicht die weitere sorgfältige Strukturanalyse. Da die biologischen Spezies direkt an der Membran gebunden sind, befinden sie sich während der Vitrifizierung weit unter der Wasser-Luft-Grenzfläche und verhindern daher die Denaturierung von Proteinen. Diese Smart Nanosheets wurden in der Praxis auf eine Mischung aus Polyhistidin getaggt Komplex I und GroEL angewendet. Während der TEM-Bildgebung wurden bis zu 97% Selektivität für den mit His-Tag versehenen Komplex I beobachtet, was eine sehr gute Perspektive für die Anwendung in der CryoEM-Bildgebung aufzeigt.^[P4]

NH₂-CNMs haben auf beiden Seiten aktive funktionelle Gruppen, die ohne harsche Reaktionsbedingungen funktionalisiert werden können.⁵ Die Verwendung von CNMs als Interposer zur Immobilisierung funktioneller Gruppen auf einer chemisch inerten Oberfläche in Form einer vertikalen Heterostruktur wird deshalb zu einer alternativen Strategie, um eine zerstörungsfreie Funktionalisierung von kristallinen 2D-Materialien zu erreichen. Basierend auf dieser Idee wurde in dieser Arbeit ein photoschaltbarer Graphen-Feldeffekttransistor (GFET) hergestellt und untersucht. In diesem GFET war der Kanalmaterial (Graphen) vollständig mit Azobenzol-funktionalisierter NH₂-CNM bedeckt. Die Azobenzoleinheiten auf der CNM werden einer Photoisomerisierung unterzogen, wenn sie UV- (365 nm) oder blauem (455 nm) Licht ausgesetzt werden. Die damit erzeugte Polaritätsdifferenz induziert unterschiedliche elektrische Felder in die dielektrische CNM und löst daher die Injektion oder Entfernung der Ladungsträger in der Graphenschicht aus. Entsprechend den Charakterisierungsergebnissen folgt der Photoschalt-Prozess einem exponentiellen Verhalten. Die Zeitkonstante sowohl der trans-zu-cis- als auch der cis-zu-trans-Reaktion hatte unter unseren Versuchsbedingungen einen Wert von 10±0,5 min. Weiterhin wurde unter Verschiebung des Dirac-Punktes eine Variation der Ladungsträgerdichte im Kanalmaterial (Graphen) beobachtet. Das Ergebnis zeigt eine gute Übereinstimmung mit dem theoretischen Wert basierend auf den physikalischen Eigenschaften des Azobenzolmoleküls und der CNM.^[P5]

Zusammenfassend lässt sich sagen, dass CNMs zahlreiche vielversprechende Eigenschaften besitzen, die sie zu einem herausragenden molekularen Nanomaterial in der Familie der 2D-

Materialien machen. Die Kombination von CNMs mit anderen kristallinen 2D-Materialien in Form von Van-der-Waals-Heterostrukturen bietet eine ausgezeichnete Methode für die zerstörungsfreie Funktionalisierung der ansonsten chemisch inerten anorganischen 2D-Materialien wie z. B. Graphen. Damit kann einer effektiven und kontrollierbaren Herstellung der auf 2D-Material basierenden elektronischen und optoelektronischen Bauteile (z. B. unter Verwendung von Übergangsmetalldichalkogeniden (TMDs)) realisiert werden. Darüber hinaus steigt im Bereich der fortschrittlichen optischen Elemente die Nachfrage nach weiterer Integration von Nanostrukturen. CNMs mit ihrer vernachlässigbaren Lichtabsorption und ihrem minimalen Gewicht und Dicke sowie ihrer mechanischen Robustheit sind aussichtsreiche optische Nanomaterialien, um dieser Herausforderung zu begegnen. Aufgrund ihrer Subnanometer-Poren in CNMs bietet dieses Material auch viele Perspektiven für die Ultrafiltration, wie in dieser Arbeit diskutiert *Nanosieving* ionischer Spezies in wässrigen Lösungen. Außerdem sind CNMs elektrisch isolierende molekulare Nanoblätter mit einem hohen Elastizitätsmodulus, einer hohen Säure- und Alkalibeständigkeit sowie thermischen Stabilität, etc.⁵ Die Untersuchung all dieser wissenschaftlich attraktiven Aspekte und praktisch wichtigen Eigenschaften von CNMs zeigt Perspektiven für die zukünftige Forschung auf, die weit über die Grenzen dieser Dissertation hinausgehen.

6. Reference

1. Backes, C.; Abdelkader, A. M.; Alonso, C.; Andrieux-Ledier, A.; Arenal, R.; Azpeitia, J.; Balakrishnan, N.; Banszerus, L.; Barjon, J.; Bartali, R.; Bellani, S.; Berger, C.; Berger, R.; Ortega, M. M. B.; Bernard, C.; Beton, P. H.; Beyer, A.; Bianco, A.; Bøggild, P.; Bonaccorso, F., *et al.*, Production and processing of graphene and related materials. *2D Materials* **2020**, *7* (2), 022001.
2. Briggs, N.; Subramanian, S.; Lin, Z.; Li, X.; Zhang, X.; Zhang, K.; Xiao, K.; Geohegan, D.; Wallace, R.; Chen, L.-Q.; Terrones, M.; Ebrahimi, A.; Das, S.; Redwing, J.; Hinkle, C.; Momeni, K.; van Duin, A.; Crespi, V.; Kar, S.; Robinson, J. A., A roadmap for electronic grade 2D materials. *2D Materials* **2019**, *6* (2), 022001.
3. Jun, B.-M.; Kim, S.; Heo, J.; Park, C. M.; Her, N.; Jang, M.; Huang, Y.; Han, J.; Yoon, Y., Review of MXenes as new nanomaterials for energy storage/delivery and selected environmental applications. *Nano Research* **2019**, *12* (3), 471-487.
4. Khan, K.; Tareen, A. K.; Aslam, M.; Wang, R.; Zhang, Y.; Mahmood, A.; Ouyang, Z.; Zhang, H.; Guo, Z., Recent developments in emerging two-dimensional materials and their applications. *Journal of Materials Chemistry C* **2020**, *8* (2), 387-440.
5. Turchanin, A.; Götzhäuser, A., Carbon Nanomembranes. *Advanced Materials* **2016**, *28* (29), 6075-6103.
6. Novoselov, K. S.; Geim, A. K.; Morozov, S. V.; Jiang, D.; Zhang, Y.; Dubonos, S. V.; Grigorieva, I. V.; Firsov, A. A., Electric Field Effect in Atomically Thin Carbon Films. *Science* **2004**, *306* (5696), 666.
7. Mishra, N. S.; Saravanan, P., A Review on the Synergistic Features of Hexagonal Boron Nitride (White Graphene) as Adsorbent-Photo Active Nanomaterial. *ChemistrySelect* **2018**, *3* (28), 8023-8034.
8. Sajid, A.; Ford, M. J.; Reimers, J. R., Single-photon emitters in hexagonal boron nitride: a review of progress. *Reports on Progress in Physics* **2020**, *83* (4), 044501.
9. Song, L.; Ci, L.; Lu, H.; Sorokin, P. B.; Jin, C.; Ni, J.; Kvashnin, A. G.; Kvashnin, D. G.; Lou, J.; Yakobson, B. I.; Ajayan, P. M., Large Scale Growth and Characterization of Atomic Hexagonal Boron Nitride Layers. *Nano Letters* **2010**, *10* (8), 3209-3215.
10. Mak, K. F.; Lee, C.; Hone, J.; Shan, J.; Heinz, T. F., Atomically Thin MoS₂: A New Direct-Gap Semiconductor. *Physical Review Letters* **2010**, *105* (13), 136805.

11. Chen, D.; Chen, W.; Ma, L.; Ji, G.; Chang, K.; Lee, J. Y., Graphene-like layered metal dichalcogenide/graphene composites: synthesis and applications in energy storage and conversion. *Materials Today* **2014**, *17* (4), 184-193.
12. Lukatskaya, M. R.; Mashtalir, O.; Ren, C. E.; Dall'Agnese, Y.; Rozier, P.; Taberna, P. L.; Naguib, M.; Simon, P.; Barsoum, M. W.; Gogotsi, Y., Cation Intercalation and High Volumetric Capacitance of Two-Dimensional Titanium Carbide. *Science* **2013**, *341* (6153), 1502.
13. Ghidui, M.; Lukatskaya, M. R.; Zhao, M.-Q.; Gogotsi, Y.; Barsoum, M. W., Conductive two-dimensional titanium carbide 'clay' with high volumetric capacitance. *Nature* **2014**, *516* (7529), 78-81.
14. Turchanin, A.; Beyer, A.; Nottbohm, C. T.; Zhang, X.; Stosch, R.; Sologubenko, A.; Mayer, J.; Hinze, P.; Weimann, T.; Götzhäuser, A., One Nanometer Thin Carbon Nanosheets with Tunable Conductivity and Stiffness. *Advanced Materials* **2009**, *21* (12), 1233-1237.
15. Angelova, P.; Vieker, H.; Weber, N.-E.; Matei, D.; Reimer, O.; Meier, I.; Kurasch, S.; Biskupek, J.; Lorbach, D.; Wunderlich, K.; Chen, L.; Terfort, A.; Klapper, M.; Müllen, K.; Kaiser, U.; Götzhäuser, A.; Turchanin, A., A Universal Scheme to Convert Aromatic Molecular Monolayers into Functional Carbon Nanomembranes. *ACS Nano* **2013**, *7* (8), 6489-6497.
16. Gao, H.; Zhu, K.; Hu, G.; Xue, C., Large-scale graphene production by ultrasound-assisted exfoliation of natural graphite in supercritical CO₂/H₂O medium. *Chemical Engineering Journal* **2017**, *308*, 872-879.
17. Sinclair, R. C.; Suter, J. L.; Coveney, P. V., Micromechanical exfoliation of graphene on the atomistic scale. *Physical Chemistry Chemical Physics* **2019**, *21* (10), 5716-5722.
18. Huo, C.; Yan, Z.; Song, X.; Zeng, H., 2D materials via liquid exfoliation: a review on fabrication and applications. *Science Bulletin* **2015**, *60* (23), 1994-2008.
19. Achee, T. C.; Sun, W.; Hope, J. T.; Quitzau, S. G.; Sweeney, C. B.; Shah, S. A.; Habib, T.; Green, M. J., High-yield scalable graphene nanosheet production from compressed graphite using electrochemical exfoliation. *Scientific Reports* **2018**, *8* (1), 14525.
20. Yang, Y.; Hou, H.; Zou, G.; Shi, W.; Shuai, H.; Li, J.; Ji, X., Electrochemical exfoliation of graphene-like two-dimensional nanomaterials. *Nanoscale* **2019**, *11* (1), 16-33.
21. Turner, P.; Hodnett, M.; Dorey, R.; Carey, J. D., Controlled Sonication as a Route to in-situ Graphene Flake Size Control. *Scientific Reports* **2019**, *9* (1), 8710.

22. Eda, G.; Yamaguchi, H.; Voiry, D.; Fujita, T.; Chen, M.; Chhowalla, M., Photoluminescence from Chemically Exfoliated MoS₂. *Nano Letters* **2011**, *11* (12), 5111-5116.
23. Fan, X.; Xu, P.; Zhou, D.; Sun, Y.; Li, Y. C.; Nguyen, M. A. T.; Terrones, M.; Mallouk, T. E., Fast and Efficient Preparation of Exfoliated 2H MoS₂ Nanosheets by Sonication-Assisted Lithium Intercalation and Infrared Laser-Induced 1T to 2H Phase Reversion. *Nano Letters* **2015**, *15* (9), 5956-5960.
24. Jiang, S.; Zeng, Y.; Zhou, W.; Miao, X.; Yu, Y., One-Minute Room-Temperature Transfer-Free Production of Mono- and Few-Layer Polycrystalline Graphene on Various Substrates. *Scientific Reports* **2016**, *6* (1), 19313.
25. Li, X.; Cai, W.; An, J.; Kim, S.; Nah, J.; Yang, D.; Piner, R.; Velamakanni, A.; Jung, I.; Tutuc, E.; Banerjee, S. K.; Colombo, L.; Ruoff, R. S., Large-Area Synthesis of High-Quality and Uniform Graphene Films on Copper Foils. *Science* **2009**, *324* (5932), 1312.
26. Li, X.; Colombo, L.; Ruoff, R. S., Synthesis of Graphene Films on Copper Foils by Chemical Vapor Deposition. *Advanced Materials* **2016**, *28* (29), 6247-6252.
27. Geng, D.; Yang, H. Y., Recent Advances in Growth of Novel 2D Materials: Beyond Graphene and Transition Metal Dichalcogenides. *Advanced Materials* **2018**, *30* (45), 1800865.
28. Liang, X.; Sperling, B. A.; Calizo, I.; Cheng, G.; Hacker, C. A.; Zhang, Q.; Obeng, Y.; Yan, K.; Peng, H.; Li, Q.; Zhu, X.; Yuan, H.; Hight Walker, A. R.; Liu, Z.; Peng, L.-m.; Richter, C. A., Toward Clean and Crackless Transfer of Graphene. *ACS Nano* **2011**, *5* (11), 9144-9153.
29. Lin, Y.-C.; Jin, C.; Lee, J.-C.; Jen, S.-F.; Suenaga, K.; Chiu, P.-W., Clean Transfer of Graphene for Isolation and Suspension. *ACS Nano* **2011**, *5* (3), 2362-2368.
30. Kim, S. J.; Choi, K.; Lee, B.; Kim, Y.; Hong, B. H., Materials for Flexible, Stretchable Electronics: Graphene and 2D Materials. *Annual Review of Materials Research* **2015**, *45* (1), 63-84.
31. Reina, A.; Son, H.; Jiao, L.; Fan, B.; Dresselhaus, M. S.; Liu, Z.; Kong, J., Transferring and Identification of Single- and Few-Layer Graphene on Arbitrary Substrates. *The Journal of Physical Chemistry C* **2008**, *112* (46), 17741-17744.
32. Li, X.; Zhu, Y.; Cai, W.; Borysiak, M.; Han, B.; Chen, D.; Piner, R. D.; Colombo, L.; Ruoff, R. S., Transfer of Large-Area Graphene Films for High-Performance Transparent Conductive Electrodes. *Nano Letters* **2009**, *9* (12), 4359-4363.

33. Gölzhäuser, A.; Nottbohm, C.; Beyer, A. Method for transferring a monolayer. European Patent 2144711 US Patent 8377243 B2, 11, 2007.
34. Sudibya, H. G.; He, Q.; Zhang, H.; Chen, P., Electrical Detection of Metal Ions Using Field-Effect Transistors Based on Micropatterned Reduced Graphene Oxide Films. *ACS Nano* **2011**, *5* (3), 1990-1994.
35. Ambrosi, A.; Pumera, M., The CVD graphene transfer procedure introduces metallic impurities which alter the graphene electrochemical properties. *Nanoscale* **2014**, *6* (1), 472-476.
36. Wang, C.; Cui, X.; Li, Y.; Li, H.; Huang, L.; Bi, J.; Luo, J.; Ma, L. Q.; Zhou, W.; Cao, Y.; Wang, B.; Miao, F., A label-free and portable graphene FET aptasensor for children blood lead detection. *Scientific Reports* **2016**, *6* (1), 21711.
37. Ma, L.-P.; Ren, W.; Cheng, H.-M., Transfer Methods of Graphene from Metal Substrates: A Review. *Small Methods* **2019**, *3* (7), 1900049.
38. Chang, Y.; Deng, L.; Meng, X.; Zhang, W.; Wang, C.; Wang, Y.; Zhao, S.; Lin, L.; Crittenden, J. C., Closed-Loop Electrochemical Recycling of Spent Copper(II) from Etchant Wastewater Using a Carbon Nanotube Modified Graphite Felt Anode. *Environmental Science & Technology* **2018**, *52* (10), 5940-5948.
39. Lock, E. H.; Baraket, M.; Laskoski, M.; Mulvaney, S. P.; Lee, W. K.; Sheehan, P. E.; Hines, D. R.; Robinson, J. T.; Tosado, J.; Fuhrer, M. S.; Hernández, S. C.; Walton, S. G., High-Quality Uniform Dry Transfer of Graphene to Polymers. *Nano Letters* **2012**, *12* (1), 102-107.
40. Wang, Y.; Zheng, Y.; Xu, X.; Dubuisson, E.; Bao, Q.; Lu, J.; Loh, K. P., Electrochemical Delamination of CVD-Grown Graphene Film: Toward the Recyclable Use of Copper Catalyst. *ACS Nano* **2011**, *5* (12), 9927-9933.
41. Ma, D.; Zhang, Y.; Liu, M.; Ji, Q.; Gao, T.; Zhang, Y.; Liu, Z., Clean transfer of graphene on Pt foils mediated by a carbon monoxide intercalation process. *Nano Research* **2013**, *6* (9), 671-678.
42. Liu, L.; Liu, X.; Zhan, Z.; Guo, W.; Xu, C.; Deng, J.; Chakarov, D.; Hyldgaard, P.; Schröder, E.; Yurgens, A.; Sun, J., A Mechanism for Highly Efficient Electrochemical Bubbling Delamination of CVD-Grown Graphene from Metal Substrates. *Advanced Materials Interfaces* **2016**, *3* (8), 1500492.

43. Fiori, G.; Bonaccorso, F.; Iannaccone, G.; Palacios, T.; Neumaier, D.; Seabaugh, A.; Banerjee, S. K.; Colombo, L., Electronics based on two-dimensional materials. *Nature Nanotechnology* **2014**, 9 (10), 768-779.
44. Wang, Q. H.; Kalantar-Zadeh, K.; Kis, A.; Coleman, J. N.; Strano, M. S., Electronics and optoelectronics of two-dimensional transition metal dichalcogenides. *Nature Nanotechnology* **2012**, 7 (11), 699-712.
45. Böhm, S., Graphene against corrosion. *Nature Nanotechnology* **2014**, 9 (10), 741-742.
46. Liu, J., Charging graphene for energy. *Nature Nanotechnology* **2014**, 9 (10), 739-741.
47. Deng, D.; Novoselov, K. S.; Fu, Q.; Zheng, N.; Tian, Z.; Bao, X., Catalysis with two-dimensional materials and their heterostructures. *Nature Nanotechnology* **2016**, 11 (3), 218-230.
48. Choi, W.; Choudhary, N.; Han, G. H.; Park, J.; Akinwande, D.; Lee, Y. H., Recent development of two-dimensional transition metal dichalcogenides and their applications. *Materials Today* **2017**, 20 (3), 116-130.
49. Wang, J.; Ma, F.; Sun, M., Graphene, hexagonal boron nitride, and their heterostructures: properties and applications. *RSC Advances* **2017**, 7 (27), 16801-16822.
50. Coroş, M.; Pogăcean, F.; Măgeruşan, L.; Socaci, C.; Pruneanu, S., A brief overview on synthesis and applications of graphene and graphene-based nanomaterials. *Frontiers of Materials Science* **2019**, 13 (1), 23-32.
51. Khazaei, M.; Mishra, A.; Venkataramanan, N. S.; Singh, A. K.; Yunoki, S., Recent advances in MXenes: From fundamentals to applications. *Current Opinion in Solid State and Materials Science* **2019**, 23 (3), 164-178.
52. Rodríguez-Pérez, L.; Herranz, M. a. Á.; Martín, N., The chemistry of pristine graphene. *Chemical Communications* **2013**, 49 (36), 3721-3735.
53. Smerieri, M.; Celasco, E.; Carraro, G.; Lusuan, A.; Pal, J.; Bracco, G.; Rocca, M.; Savio, L.; Vattuone, L., Enhanced Chemical Reactivity of Pristine Graphene Interacting Strongly with a Substrate: Chemisorbed Carbon Monoxide on Graphene/Nickel(1 1 1). *ChemCatChem* **2015**, 7 (15), 2328-2331.
54. Li, X.; Yin, J.; Zhou, J.; Guo, W., Large area hexagonal boron nitride monolayer as efficient atomically thick insulating coating against friction and oxidation. *Nanotechnology* **2014**, 25 (10), 105701.

55. Späth, F.; Soni, H. R.; Steinhauer, J.; Düll, F.; Bauer, U.; Bachmann, P.; Hieringer, W.; Görling, A.; Steinrück, H.-P.; Papp, C., Oxygen Functionalization of Hexagonal Boron Nitride on Ni(111). *Chemistry – A European Journal* **2019**, *25* (37), 8884-8893.
56. Zhu, Y.; Murali, S.; Cai, W.; Li, X.; Suk, J. W.; Potts, J. R.; Ruoff, R. S., Graphene and Graphene Oxide: Synthesis, Properties, and Applications. *Advanced Materials* **2010**, *22* (35), 3906-3924.
57. Lonkar, S. P.; Deshmukh, Y. S.; Abdala, A. A., Recent advances in chemical modifications of graphene. *Nano Research* **2015**, *8* (4), 1039-1074.
58. Luo, P.; Zhuge, F.; Zhang, Q.; Chen, Y.; Lv, L.; Huang, Y.; Li, H.; Zhai, T., Doping engineering and functionalization of two-dimensional metal chalcogenides. *Nanoscale Horizons* **2019**, *4* (1), 26-51.
59. Zheng, Z.; Cox, M.; Li, B., Surface modification of hexagonal boron nitride nanomaterials: a review. *Journal of Materials Science* **2018**, *53* (1), 66-99.
60. Kong, L.; Enders, A.; Rahman, T. S.; Dowben, P. A., Molecular adsorption on graphene. *Journal of Physics: Condensed Matter* **2014**, *26* (44), 443001.
61. Marcia, M.; Hirsch, A.; Hauke, F., Perylene-based non-covalent functionalization of 2D materials. *FlatChem* **2017**, *1*, 89-103.
62. Turchanin, A.; Götzhäuser, A., Carbon nanomembranes from self-assembled monolayers: Functional surfaces without bulk. *Progress in Surface Science* **2012**, *87* (5), 108-162.
63. Turchanin, A., Synthesis of Molecular 2D Materials via Low-energy Electron Induced Chemical Reactions. *CHIMIA International Journal for Chemistry* **2019**, *73* (6), 473-479.
64. Zheng, Z.; Nottbohm, C. T.; Turchanin, A.; Muzik, H.; Beyer, A.; Heilemann, M.; Sauer, M.; Götzhäuser, A., Janus Nanomembranes: A Generic Platform for Chemistry in Two Dimensions. *Angewandte Chemie International Edition* **2010**, *49* (45), 8493-8497.
65. Woszczyzna, M.; Winter, A.; Grothe, M.; Willunat, A.; Wundrack, S.; Stosch, R.; Weimann, T.; Ahlers, F.; Turchanin, A., All-Carbon Vertical van der Waals Heterostructures: Non-destructive Functionalization of Graphene for Electronic Applications. *Advanced Materials* **2014**, *26* (28), 4831-4837.
66. Reinecke, P.; Putze, M.-T.; Georgi, L.; Kahle, R.; Kaiser, D.; Hüger, D.; Livshits, P.; Weidenmüller, J.; Weimann, T.; Turchanin, A.; Braun, T.; Becker, K.-F.; Schneider-Ramelow,

M.; Lang, K.-D., Scalable hybrid microelectronic-microfluidic integration of highly sensitive biosensors. *International Symposium on Microelectronics* **2018**, 2018 (1), 000672-000679.

67. Eck, W.; Stadler, V.; Geyer, W.; Zharnikov, M.; Götzhäuser, A.; Grunze, M., Generation of Surface Amino Groups on Aromatic Self-Assembled Monolayers by Low Energy Electron Beams—A First Step Towards Chemical Lithography. *Advanced Materials* **2000**, 12 (11), 805-808.

68. Turchanin, A.; Tinazli, A.; El-Desawy, M.; Großmann, H.; Schnietz, M.; Solak, H. H.; Tampé, R.; Götzhäuser, A., Molecular Self-Assembly, Chemical Lithography, and Biochemical Tweezers: A Path for the Fabrication of Functional Nanometer-Scale Protein Arrays. *Advanced Materials* **2008**, 20 (3), 471-477.

69. Turchanin, A.; Käfer, D.; El-Desawy, M.; Wöll, C.; Witte, G.; Götzhäuser, A., Molecular Mechanisms of Electron-Induced Cross-Linking in Aromatic SAMs. *Langmuir* **2009**, 25 (13), 7342-7352.

70. Neumann, C.; Szwed, M.; Frey, M.; Tang, Z.; Koziel, K.; Cyganik, P.; Turchanin, A., Preparation of Carbon Nanomembranes without Chemically Active Groups. *ACS Applied Materials & Interfaces* **2019**, 11 (34), 31176-31181.

71. Turchanin, A.; Schnietz, M.; El-Desawy, M.; Solak, H. H.; David, C.; Götzhäuser, A., Fabrication of Molecular Nanotemplates in Self-Assembled Monolayers by Extreme-Ultraviolet-Induced Chemical Lithography. *Small* **2007**, 3 (12), 2114-2119.

72. Wang, Y.; Xiong, R.; Dong, L.; Hu, A., Synthesis of carbon nanomembranes through cross-linking of phenyl self-assembled monolayers for electrode materials in supercapacitors. *Journal of Materials Chemistry A* **2014**, 2 (15), 5212-5217.

73. Yang, Y.; Dementyev, P.; Biere, N.; Emmrich, D.; Stohmann, P.; Korzetz, R.; Zhang, X.; Beyer, A.; Koch, S.; Anselmetti, D.; Götzhäuser, A., Rapid Water Permeation Through Carbon Nanomembranes with Sub-Nanometer Channels. *ACS Nano* **2018**, 12 (5), 4695-4701.

74. Yang, Y.; Hillmann, R.; Qi, Y.; Korzetz, R.; Biere, N.; Emmrich, D.; Westphal, M.; Büker, B.; Hütten, A.; Beyer, A.; Anselmetti, D.; Götzhäuser, A., Ultrahigh Ionic Exclusion through Carbon Nanomembranes. *Advanced Materials* **2020**, 32 (8), 1907850.

75. Dementyev, P.; Yang, Y.; Rezvova, M.; Götzhäuser, A., Molecular Jamming in Tortuous Nanochannels. *The Journal of Physical Chemistry Letters* **2020**, 11 (1), 238-242.

76. Kankate, L.; Turchanin, A.; Götzhäuser, A., On the Release of Hydrogen from the S–H groups in the Formation of Self-Assembled Monolayers of Thiols. *Langmuir* **2009**, *25* (18), 10435-10438.
77. Zhang, X.; Neumann, C.; Angelova, P.; Beyer, A.; Götzhäuser, A., Tailoring the Mechanics of Ultrathin Carbon Nanomembranes by Molecular Design. *Langmuir* **2014**, *30* (27), 8221-8227.
78. Zhang, X.; Waitz, R.; Yang, F.; Lutz, C.; Angelova, P.; Götzhäuser, A.; Scheer, E., Vibrational modes of ultrathin carbon nanomembrane mechanical resonators. *Applied Physics Letters* **2015**, *106* (6), 063107.
79. Sirmaci, Y. D.; Tang, Z.; Fasold, S.; Neumann, C.; Pertsch, T.; Turchanin, A.; Staude, I., Plasmonic Metasurfaces Situated on Ultrathin Carbon Nanomembranes. *ACS Photonics* **2020**.
80. Rhinow, D.; Büenefeld, M.; Weber, N.-E.; Beyer, A.; Götzhäuser, A.; Kühlbrandt, W.; Hampp, N.; Turchanin, A., Energy-filtered transmission electron microscopy of biological samples on highly transparent carbon nanomembranes. *Ultramicroscopy* **2011**, *111* (5), 342-349.
81. Penner, P.; Zhang, X.; Marschewski, E.; Behler, F.; Angelova, P.; Beyer, A.; Christoffers, J.; Götzhäuser, A., Charge Transport through Carbon Nanomembranes. *The Journal of Physical Chemistry C* **2014**, *118* (37), 21687-21694.
82. Turchanin, A., Graphene Growth by Conversion of Aromatic Self-Assembled Monolayers. *Annalen der Physik* **2017**, *529* (11), 1700168.
83. Neumann, C.; Kaiser, D.; Mohn, M. J.; Fuser, M.; Weber, N.-E.; Reimer, O.; Götzhäuser, A.; Weimann, T.; Terfort, A.; Kaiser, U.; Turchanin, A., Bottom-Up Synthesis of Graphene Monolayers with Tunable Crystallinity and Porosity. *ACS Nano* **2019**, *13* (6), 7310-7322.
84. Turchanin, A.; Weber, D.; Büenefeld, M.; Kisielowski, C.; Fistul, M. V.; Efetov, K. B.; Weimann, T.; Stosch, R.; Mayer, J.; Götzhäuser, A., Conversion of Self-Assembled Monolayers into Nanocrystalline Graphene: Structure and Electric Transport. *ACS Nano* **2011**, *5* (5), 3896-3904.
85. Matei, D. G.; Weber, N.-E.; Kurasch, S.; Wundrack, S.; Woszczyzna, M.; Grothe, M.; Weimann, T.; Ahlers, F.; Stosch, R.; Kaiser, U.; Turchanin, A., Functional Single-Layer Graphene Sheets from Aromatic Monolayers. *Advanced Materials* **2013**, *25* (30), 4146-4151.

86. Winter, A.; George, A.; Neumann, C.; Tang, Z.; Mohn, M. J.; Biskupek, J.; Masurkar, N.; Reddy, A. L. M.; Weimann, T.; Hübner, U.; Kaiser, U.; Turchanin, A., Lateral heterostructures of two-dimensional materials by electron-beam induced stitching. *Carbon* **2018**, *128*, 106-116.
87. Weber, T.; Gies, Y.; Terfort, A., Bacteria-Repulsive Polyglycerol Surfaces by Grafting Polymerization onto Aminopropylated Surfaces. *Langmuir* **2012**, *28* (45), 15916-15921.
88. Cline, G. W.; Hanna, S. B., Kinetics and mechanisms of the aminolysis of N-hydroxysuccinimide esters in aqueous buffers. *The Journal of Organic Chemistry* **1988**, *53* (15), 3583-3586.
89. Nottbohm, C. T.; Turchanin, A.; Beyer, A.; Götzhäuser, A., Direct e-beam writing of 1nm thin carbon nanoribbons. *Journal of Vacuum Science & Technology B: Microelectronics and Nanometer Structures Processing, Measurement, and Phenomena* **2009**, *27* (6), 3059-3062.
90. Winter, A.; Ekinici, Y.; Götzhäuser, A.; Turchanin, A., Freestanding carbon nanomembranes and graphene monolayers nanopatterned via EUV interference lithography. *2D Materials* **2019**, *6* (2), 021002.
91. Wagner, C. D., Sensitivity factors for XPS analysis of surface atoms. *Journal of Electron Spectroscopy and Related Phenomena* **1983**, *32* (2), 99-102.
92. Watts, J. F.; Wolstenholme, J., In *An Introduction to Surface Analysis by XPS and AES*, John Wiley & Sons, Ltd.: 2003; pp 79-111.
93. Lindberg, B. J.; Hamrin, K.; Johansson, G.; Gelius, U.; Fahlman, A.; Nordling, C.; Siegbahn, K., Molecular Spectroscopy by Means of ESCA II. Sulfur compounds. Correlation of electron binding energy with structure. *Physica Scripta* **1970**, *1* (5-6), 286-298.
94. Jorio, A.; Saito, R.; Dresselhaus, G.; Dresselhaus, M. S., *Raman spectroscopy in graphene related systems*. Wiley - VCH Verlag GmbH & Co. KGaA: Germany, 2011.
95. Liang, F.; Xu, H.; Wu, X.; Wang, C.; Luo, C.; Zhang, J., Raman spectroscopy characterization of two-dimensional materials. *Chinese Physics B* **2018**, *27* (3), 037802.
96. Hong, Y. K.; Liu, N.; Yin, D.; Hong, S.; Kim, D. H.; Kim, S.; Choi, W.; Yoon, Y., Recent progress in high-mobility thin-film transistors based on multilayer 2D materials. *Journal of Physics D: Applied Physics* **2017**, *50* (16), 164001.
97. Sangwan, V. K.; Hersam, M. C., Electronic Transport in Two-Dimensional Materials. *Annual Review of Physical Chemistry* **2018**, *69* (1), 299-325.

98. Zhou, Y.; Fox, D. S.; Zhang, H., Helium Ion Microscopy for Two-Dimensional Materials. In *Helium Ion Microscopy*, Hlawacek, G.; Götzhäuser, A., Eds. Springer International Publishing: Cham, 2016; pp 245-262.
99. Guo, H.; Gao, J.; Ishida, N.; Xu, M.; Fujita, D., Characterization of two-dimensional hexagonal boron nitride using scanning electron and scanning helium ion microscopy. *Applied Physics Letters* **2014**, *104* (3), 031607.
100. Beyer, A.; Vieker, H.; Klett, R.; Meyer zu Theenhausen, H.; Angelova, P.; Götzhäuser, A., Imaging of carbon nanomembranes with helium ion microscopy. *Beilstein Journal of Nanotechnology* **2015**, *6*, 1712-1720.
101. Giessibl, F. J., Advances in atomic force microscopy. *Reviews of Modern Physics* **2003**, *75* (3), 949-983.
102. Heeres, J. T.; Kim, S.-H.; Leslie, B. J.; Lidstone, E. A.; Cunningham, B. T.; Hergenrother, P. J., Identifying Modulators of Protein-Protein Interactions Using Photonic Crystal Biosensors. *Journal of the American Chemical Society* **2009**, *131* (51), 18202-18203.
103. Scherr, J.; Parey, K.; Klusch, N.; Murphy, B. J.; Balsler, S.; Neuhaus, A.; Zickermann, V.; Kühlbrandt, W.; Terfort, A.; Rhinow, D., Self-Perforated Hydrogel Nanomembranes Facilitate Structural Analysis of Proteins by Electron Cryo-Microscopy. *ACS Nano* **2017**, *11* (6), 6467-6473.
104. Tarbell, D. S.; Harnish, D. P., Cleavage of the Carbon-Sulfur Bond in Divalent Sulfur Compounds. *Chemical Reviews* **1951**, *49* (1), 1-90.
105. Schilter, D., Thiol oxidation: A slippery slope. *Nature Reviews Chemistry* **2017**, *1* (2), 0013.
106. Zhang, X.; Vieker, H.; Beyer, A.; Götzhäuser, A., Fabrication of carbon nanomembranes by helium ion beam lithography. *Beilstein Journal of Nanotechnology* **2014**, *5*, 188-194.
107. Neumann, C.; Wilhelm, R.; Küllmer, M.; Turchanin, A., Low-energy electron irradiation induced synthesis of molecular nanosheets: An influence of the electron beam energy. *Faraday Discussions* **2020**.
108. Li, B.; Gong, R.; Wang, W.; Huang, X.; Zhang, W.; Li, H.; Hu, C.; Tan, B., A New Strategy to Microporous Polymers: Knitting Rigid Aromatic Building Blocks by External Cross-Linker. *Macromolecules* **2011**, *44* (8), 2410-2414.

109. Dawson, R.; Stevens, L. A.; Drage, T. C.; Snape, C. E.; Smith, M. W.; Adams, D. J.; Cooper, A. I., Impact of Water Coadsorption for Carbon Dioxide Capture in Microporous Polymer Sorbents. *Journal of the American Chemical Society* **2012**, *134* (26), 10741-10744.
110. Batzill, M., The surface science of graphene: Metal interfaces, CVD synthesis, nanoribbons, chemical modifications, and defects. *Surface Science Reports* **2012**, *67* (3), 83-115.
111. Zhan, Y.; Liu, Z.; Najmaei, S.; Ajayan, P. M.; Lou, J., Large-Area Vapor-Phase Growth and Characterization of MoS₂ Atomic Layers on a SiO₂ Substrate. *Small* **2012**, *8* (7), 966-971.
112. Zhang, Y.; Yao, Y.; Sendeku, M. G.; Yin, L.; Zhan, X.; Wang, F.; Wang, Z.; He, J., Recent Progress in CVD Growth of 2D Transition Metal Dichalcogenides and Related Heterostructures. *Advanced Materials* **2019**, *31* (41), 1901694.
113. Zhang, Z.; Yang, P.; Hong, M.; Jiang, S.; Zhao, G.; Shi, J.; Xie, Q.; Zhang, Y., Recent progress in the controlled synthesis of 2D metallic transition metal dichalcogenides. *Nanotechnology* **2019**, *30* (18), 182002.
114. Love, J. C.; Estroff, L. A.; Kriebel, J. K.; Nuzzo, R. G.; Whitesides, G. M., Self-Assembled Monolayers of Thiolates on Metals as a Form of Nanotechnology. *Chemical Reviews* **2005**, *105* (4), 1103-1170.
115. Bagiyan, G. A.; Koroleva, I. K.; Soroka, N. V.; Ufimtsev, A. V., Oxidation of thiol compounds by molecular oxygen in aqueous solutions. *Russian Chemical Bulletin* **2003**, *52* (5), 1135-1141.
116. Lupina, G.; Kitzmann, J.; Costina, I.; Lukosius, M.; Wenger, C.; Wolff, A.; Vaziri, S.; Östling, M.; Pasternak, I.; Krajewska, A.; Strupinski, W.; Kataria, S.; Gahoi, A.; Lemme, M. C.; Ruhl, G.; Zoth, G.; Luxenhofer, O.; Mehr, W., Residual Metallic Contamination of Transferred Chemical Vapor Deposited Graphene. *ACS Nano* **2015**, *9* (5), 4776-4785.
117. Nag, A.; Mitra, A.; Mukhopadhyay, S. C., Graphene and its sensor-based applications: A review. *Sensors and Actuators A: Physical* **2018**, *270*, 177-194.
118. Gao, L.; Ren, W.; Xu, H.; Jin, L.; Wang, Z.; Ma, T.; Ma, L.-P.; Zhang, Z.; Fu, Q.; Peng, L.-M.; Bao, X.; Cheng, H.-M., Repeated growth and bubbling transfer of graphene with millimetre-size single-crystal grains using platinum. *Nature Communications* **2012**, *3* (1), 699.

119. Gao, Y.; Liu, Z.; Sun, D.-M.; Huang, L.; Ma, L.-P.; Yin, L.-C.; Ma, T.; Zhang, Z.; Ma, X.-L.; Peng, L.-M.; Cheng, H.-M.; Ren, W., Large-area synthesis of high-quality and uniform monolayer WS₂ on reusable Au foils. *Nature Communications* **2015**, *6* (1), 8569.
120. Lee, L. Y. S.; Lennox, R. B., Electrochemical Desorption of n-Alkylthiol SAMs on Polycrystalline Gold: Studies Using A Ferrocenylalkylthiol Probe. *Langmuir* **2007**, *23* (1), 292-296.
121. Tencer, M.; Berini, P., Toposelective Electrochemical Desorption of Thiol SAMs from Neighboring Polycrystalline Gold Surfaces. *Langmuir* **2008**, *24* (21), 12097-12101.
122. Kemnade, N.; Chen, Y.; Muglali, M. I.; Erbe, A., Electrochemical reductive desorption of alkyl self-assembled monolayers studied in situ by spectroscopic ellipsometry: evidence for formation of a low refractive index region after desorption. *Physical Chemistry Chemical Physics* **2014**, *16* (32), 17081-17090.
123. Nottbohm, C. T.; Turchanin, A.; Beyer, A.; Stosch, R.; Götzhäuser, A., Mechanically Stacked 1-nm-Thick Carbon Nanosheets: Ultrathin Layered Materials with Tunable Optical, Chemical, and Electrical Properties. *Small* **2011**, *7* (7), 874-883.
124. Beulen, M. W. J.; Kastenbergh, M. I.; van Veggel, F. C. J. M.; Reinhoudt, D. N., Electrochemical Stability of Self-Assembled Monolayers on Gold. *Langmuir* **1998**, *14* (26), 7463-7467.
125. Lefrou, C.; Fabry, P.; Poignet, J.-C., Electrochemistry: The Basics, With Examples. In *Electrochemistry: The Basics, With Examples*, Springer Berlin Heidelberg: Berlin, Heidelberg, 2012; pp 1-50.
126. Schneider, T. W.; Buttry, D. A., Electrochemical quartz crystal microbalance studies of adsorption and desorption of self-assembled monolayers of alkyl thiols on gold. *Journal of the American Chemical Society* **1993**, *115* (26), 12391-12397.
127. Laibinis, P. E.; Whitesides, G. M.; Allara, D. L.; Tao, Y. T.; Parikh, A. N.; Nuzzo, R. G., Comparison of the structures and wetting properties of self-assembled monolayers of n-alkanethiols on the coinage metal surfaces, copper, silver, and gold. *Journal of the American Chemical Society* **1991**, *113* (19), 7152-7167.
128. Castner, D. G.; Hinds, K.; Grainger, D. W., X-ray Photoelectron Spectroscopy Sulfur 2p Study of Organic Thiol and Disulfide Binding Interactions with Gold Surfaces. *Langmuir* **1996**, *12* (21), 5083-5086.

129. Setiawan, L. D.; Baumann, H.; Gribbin, D., Surface studies of keratin fibers and related model compounds using ESCA. I—intermediate oxidation products of the model compound 1-cystine and their hydrolytical behaviour. *Surface and Interface Analysis* **1985**, *7* (4), 188-195.
130. Liu, F.-J.; Wei, X.-Y.; Wang, Y.-G.; Li, P.; Li, Z.-K.; Zong, Z.-M., Sulfur-containing species in the extraction residue from Xianfeng lignite characterized by X-ray photoelectron spectrometry and electrospray ionization Fourier transform ion cyclotron resonance mass spectrometry. *RSC Advances* **2015**, *5* (10), 7125-7130.
131. Lee, J.; Kim, Y.; Shin, H.-J.; Lee, C.; Lee, D.; Moon, C.-Y.; Lim, J.; Chan Jun, S., Clean transfer of graphene and its effect on contact resistance. *Applied Physics Letters* **2013**, *103* (10), 103104.
132. Holroyd, C.; Horn, A. B.; Casiraghi, C.; Koehler, S. P. K., Vibrational fingerprints of residual polymer on transferred CVD-graphene. *Carbon* **2017**, *117*, 473-475.
133. Schnietz, M.; Turchanin, A.; Nottbohm, C. T.; Beyer, A.; Solak, H. H.; Hinze, P.; Weimann, T.; Götzhäuser, A., Chemically Functionalized Carbon Nanosieves with 1-nm Thickness. *Small* **2009**, *5* (23), 2651-2655.
134. Ederer, J.; Janoš, P.; Ecorchard, P.; Tolasz, J.; Štengl, V.; Beneš, H.; Perchacz, M.; Pop-Georgievski, O., Determination of amino groups on functionalized graphene oxide for polyurethane nanomaterials: XPS quantitation vs. functional speciation. *RSC Advances* **2017**, *7* (21), 12464-12473.
135. van Deursen, P. M. G.; Tang, Z.; Winter, A.; Mohn, M. J.; Kaiser, U.; Turchanin, A. A.; Schneider, G. F., Selective ion sieving through arrays of sub-nanometer nanopores in chemically tunable 2D carbon membranes. *Nanoscale* **2019**, *11* (43), 20785-20791.
136. Kowalczyk, S. W.; Grosberg, A. Y.; Rabin, Y.; Dekker, C., Modeling the conductance and DNA blockade of solid-state nanopores. *Nanotechnology* **2011**, *22* (31), 315101.
137. Cruz-Chu, E. R.; Aksimentiev, A.; Schulten, K., Ionic Current Rectification through Silica Nanopores. *The Journal of Physical Chemistry C* **2009**, *113* (5), 1850-1862.
138. Jain, T.; Rasera, B. C.; Guerrero, R. J. S.; Boutilier, M. S. H.; O'Hern, S. C.; Idrobo, J.-C.; Karnik, R., Heterogeneous sub-continuum ionic transport in statistically isolated graphene nanopores. *Nature Nanotechnology* **2015**, *10* (12), 1053-1057.

139. Feng, J.; Liu, K.; Graf, M.; Dumcenco, D.; Kis, A.; Di Ventra, M.; Radenovic, A., Observation of ionic Coulomb blockade in nanopores. *Nature Materials* **2016**, *15* (8), 850-855.
140. Marcus, Y., Ionic radii in aqueous solutions. *Chemical Reviews* **1988**, *88* (8), 1475-1498.
141. Sata, T., In *Ion Exchange Membranes: Preparation, Characterization, Modification and Application*, The Royal Society of Chemistry: 2004; pp 13-16.
142. Yuan-Hui, L.; Gregory, S., Diffusion of ions in sea water and in deep-sea sediments. *Geochimica et Cosmochimica Acta* **1974**, *38* (5), 703-714.
143. He, Y.; Gillespie, D.; Boda, D.; Vlassiouk, I.; Eisenberg, R. S.; Siwy, Z. S., Tuning Transport Properties of Nanofluidic Devices with Local Charge Inversion. *Journal of the American Chemical Society* **2009**, *131* (14), 5194-5202.
144. Yu, N.; Capasso, F., Flat optics with designer metasurfaces. *Nature Materials* **2014**, *13* (2), 139-150.
145. Chang, S.; Guo, X.; Ni, X., Optical Metasurfaces: Progress and Applications. *Annual Review of Materials Research* **2018**, *48* (1), 279-302.
146. Neshev, D.; Aharonovich, I., Optical metasurfaces: new generation building blocks for multi-functional optics. *Light: Science & Applications* **2018**, *7* (1), 58.
147. Hail, C. U.; Michel, A.-K. U.; Poulikakos, D.; Eghlidi, H., Optical Metasurfaces: Evolving from Passive to Adaptive. *Advanced Optical Materials* **2019**, *7* (14), 1801786.
148. Meinzer, N.; Barnes, W. L.; Hooper, I. R., Plasmonic meta-atoms and metasurfaces. *Nature Photonics* **2014**, *8* (12), 889-898.
149. Kasyanova, I. V.; Gorkunov, M. V.; Artemov, V. V.; Geivandov, A. R.; Mamonova, A. V.; Palto, S. P., Liquid crystal metasurfaces on micropatterned polymer substrates. *Opt. Express* **2018**, *26* (16), 20258-20269.
150. Amin, I.; Steenackers, M.; Zhang, N.; Beyer, A.; Zhang, X.; Pirzer, T.; Hugel, T.; Jordan, R.; Götzhäuser, A., Polymer Carpets. *Small* **2010**, *6* (15), 1623-1630.
151. Garner, S.; Chowdhury, D.; Lewis, S., Ultrathin Glass Substrates for Thin, Lightweight, Flexible OLED Lighting. *Information Display* **2019**, *35* (4), 9-13.
152. Linden, S.; Enkrich, C.; Wegener, M.; Zhou, J.; Koschny, T.; Soukoulis, C. M., Magnetic Response of Metamaterials at 100 Terahertz. *Science* **2004**, *306* (5700), 1351.

153. Enkrich, C.; Wegener, M.; Linden, S.; Burger, S.; Zschiedrich, L.; Schmidt, F.; Zhou, J. F.; Koschny, T.; Soukoulis, C. M., Magnetic Metamaterials at Telecommunication and Visible Frequencies. *Physical Review Letters* **2005**, *95* (20), 203901.
154. Rockstuhl, C.; Lederer, F.; Etrich, C.; Zentgraf, T.; Kuhl, J.; Giessen, H., On the reinterpretation of resonances in split-ring-resonators at normal incidence. *Opt. Express* **2006**, *14* (19), 8827-8836.
155. Rhinow, D.; Kühlbrandt, W., Electron cryo-microscopy of biological specimens on conductive titanium–silicon metal glass films. *Ultramicroscopy* **2008**, *108* (7), 698-705.
156. Yoshioka, C.; Carragher, B.; Potter, C. S., Cryomesh™: A New Substrate for Cryo-Electron Microscopy. *Microscopy and Microanalysis* **2010**, *16* (1), 43-53.
157. Nair, R. R.; Blake, P.; Blake, J. R.; Zan, R.; Anissimova, S.; Bangert, U.; Golovanov, A. P.; Morozov, S. V.; Geim, A. K.; Novoselov, K. S.; Latychevskaia, T., Graphene as a transparent conductive support for studying biological molecules by transmission electron microscopy. *Applied Physics Letters* **2010**, *97* (15), 153102.
158. Pantelic, R. S.; Suk, J. W.; Magnuson, C. W.; Meyer, J. C.; Wachsmuth, P.; Kaiser, U.; Ruoff, R. S.; Stahlberg, H., Graphene: Substrate preparation and introduction. *J Struct Biol* **2011**, *174* (1), 234-238.
159. Rhinow, D.; Weber, N.-E.; Turchanin, A.; Götzhäuser, A.; Kühlbrandt, W., Single-walled carbon nanotubes and nanocrystalline graphene reduce beam-induced movements in high-resolution electron cryo-microscopy of ice-embedded biological samples. *Applied Physics Letters* **2011**, *99* (13), 133701.
160. Russo, C. J.; Passmore, L. A., Controlling protein adsorption on graphene for cryo-EM using low-energy hydrogen plasmas. *Nature Methods* **2014**, *11* (6), 649-652.
161. Russo, C. J.; Passmore, L. A., Ultrastable gold substrates for electron cryomicroscopy. *Science* **2014**, *346* (6215), 1377.
162. Georgakilas, V.; Otyepka, M.; Bourlinos, A. B.; Chandra, V.; Kim, N.; Kemp, K. C.; Hobza, P.; Zboril, R.; Kim, K. S., Functionalization of Graphene: Covalent and Non-Covalent Approaches, Derivatives and Applications. *Chemical Reviews* **2012**, *112* (11), 6156-6214.

163. Li, X.; Cai, T.; Chung, T.-S., Anti-Fouling Behavior of Hyperbranched Polyglycerol-Grafted Poly(ether sulfone) Hollow Fiber Membranes for Osmotic Power Generation. *Environmental Science & Technology* **2014**, *48* (16), 9898-9907.
164. Weber, T.; Bechthold, M.; Winkler, T.; Dauselt, J.; Terfort, A., Direct grafting of anti-fouling polyglycerol layers to steel and other technically relevant materials. *Colloids and Surfaces B: Biointerfaces* **2013**, *111*, 360-366.
165. Silverstein, R. M.; Webster, F. X.; Kiemle, D. J.; Bryce, D. L., *Spectrometric Identification of Organic Compounds*. 8 ed. John Wiley & Sons, INC.: USA, 2014.
166. Neffe, A. T.; von Ruesten-Lange, M.; Braune, S.; Lützwow, K.; Roch, T.; Richau, K.; Krüger, A.; Becherer, T.; Thünemann, A. F.; Jung, F.; Haag, R.; Lendlein, A., Multivalent grafting of hyperbranched oligo- and polyglycerols shielding rough membranes to mediate hemocompatibility. *Journal of Materials Chemistry B* **2014**, *2* (23), 3626-3635.
167. Puziy, A. M.; Poddubnaya, O. I.; Ziatdinov, A. M., On the chemical structure of phosphorus compounds in phosphoric acid-activated carbon. *Applied Surface Science* **2006**, *252* (23), 8036-8038.
168. Graf, N.; Yegen, E.; Gross, T.; Lippitz, A.; Weigel, W.; Krakert, S.; Terfort, A.; Unger, W. E. S., XPS and NEXAFS studies of aliphatic and aromatic amine species on functionalized surfaces. *Surface Science* **2009**, *603* (18), 2849-2860.
169. Pham, M.-C., Voltammetric and XPS Analysis of Metal-Complexed Polytyramine Films : Geometry-Dependent Electron Transfer Therein. *Journal of The Electrochemical Society* **1984**, *131* (4), 777.
170. Shircliff, R. A.; Stradins, P.; Moutinho, H.; Fennell, J.; Ghirardi, M. L.; Cowley, S. W.; Branz, H. M.; Martin, I. T., Angle-Resolved XPS Analysis and Characterization of Monolayer and Multilayer Silane Films for DNA Coupling to Silica. *Langmuir* **2013**, *29* (12), 4057-4067.
171. Heil, C. S.; Rittner, A.; Goebel, B.; Beyer, D.; Grininger, M., Site-Specific Labelling of Multidomain Proteins by Amber Codon Suppression. *Scientific Reports* **2018**, *8* (1), 14864.
172. Kashani-Poor, N.; Kerscher, S.; Zickermann, V.; Brandt, U., Efficient large scale purification of his-tagged proton translocating NADH:ubiquinone oxidoreductase (complex I) from the strictly aerobic yeast *Yarrowia lipolytica*. *Biochimica et Biophysica Acta (BBA) - Bioenergetics* **2001**, *1504* (2), 363-370.

173. Parey, K.; Haapanen, O.; Sharma, V.; Köfeler, H.; Züllig, T.; Prinz, S.; Siegmund, K.; Wittig, I.; Mills, D. J.; Vonck, J.; Kühlbrandt, W.; Zickermann, V., High-resolution cryo-EM structures of respiratory complex I: Mechanism, assembly, and disease. *Science Advances* **2019**, *5* (12), eaax9484.
174. D'Imprima, E.; Floris, D.; Joppe, M.; Sánchez, R.; Grininger, M.; Kühlbrandt, W., Protein denaturation at the air-water interface and how to prevent it. *eLife* **2019**, *8*, e42747.
175. Lixue, Z.; Li, W.; Yingqi, W.; Caroline, M.; Sunny, Y.; Xiwen, L., Trends Analysis of Graphene Research and Development. *Journal of Data and Information Science* **2018**, *3* (1), 82-100.
176. Reiss, T.; Hjelt, K.; Ferrari, A. C., Graphene is on track to deliver on its promises. *Nature Nanotechnology* **2019**, *14* (10), 907-910.
177. Kuila, T.; Bose, S.; Mishra, A. K.; Khanra, P.; Kim, N. H.; Lee, J. H., Chemical functionalization of graphene and its applications. *Progress in Materials Science* **2012**, *57* (7), 1061-1105.
178. Isabella Anna, V.; Cécilia, M.-M.; Alberto, B., Chemical Functionalization of Graphene Family Members. *Physical Sciences Reviews* **2017**, *2* (1), 20160103.
179. Medina, H.; Lin, Y.-C.; Obergfell, D.; Chiu, P.-W., Tuning of Charge Densities in Graphene by Molecule Doping. *Advanced Functional Materials* **2011**, *21* (14), 2687-2692.
180. Mann, J. A.; Dichtel, W. R., Noncovalent Functionalization of Graphene by Molecular and Polymeric Adsorbates. *The Journal of Physical Chemistry Letters* **2013**, *4* (16), 2649-2657.
181. Yan, Z.; Sun, Z.; Lu, W.; Yao, J.; Zhu, Y.; Tour, J. M., Controlled Modulation of Electronic Properties of Graphene by Self-Assembled Monolayers on SiO₂ Substrates. *ACS Nano* **2011**, *5* (2), 1535-1540.
182. Kwong Hong Tsang, D.; Lieberthal, T. J.; Watts, C.; Dunlop, I. E.; Ramadan, S.; del Rio Hernandez, A. E.; Klein, N., Chemically Functionalised Graphene FET Biosensor for the Label-free Sensing of Exosomes. *Scientific Reports* **2019**, *9* (1), 13946.
183. An, Y.; Behnam, A.; Pop, E.; Ural, A., Metal-semiconductor-metal photodetectors based on graphene/p-type silicon Schottky junctions. *Applied Physics Letters* **2013**, *102* (1), 013110.

184. Zhao, Y.; Bertolazzi, S.; Samori, P., A Universal Approach toward Light-Responsive Two-Dimensional Electronics: Chemically Tailored Hybrid van der Waals Heterostructures. *ACS Nano* **2019**, *13* (4), 4814-4825.
185. Merino, E.; Ribagorda, M., Control over molecular motion using the cis-trans photoisomerization of the azo group. *Beilstein journal of organic chemistry* **2012**, *8*, 1071-1090.
186. Osella, S.; Minoia, A.; Beljonne, D., Combined Molecular Dynamics and Density Functional Theory Study of Azobenzene–Graphene Interfaces. *The Journal of Physical Chemistry C* **2016**, *120* (12), 6651-6658.
187. Hou, I. C.-Y.; Diez-Cabanes, V.; Galanti, A.; Valášek, M.; Mayor, M.; Cornil, J.; Narita, A.; Samori, P.; Müllen, K., Photomodulation of Two-Dimensional Self-Assembly of Azobenzene–Hexa-peri-hexabenzocoronene–Azobenzene Triads. *Chemistry of Materials* **2019**, *31* (17), 6979-6985.
188. Zhao, Q.; Zhu, Y.; Sun, Z.; Li, Y.; Zhang, G.; Zhang, F.; Fan, X., Combining palladium complex and organic amine on graphene oxide for promoted Tsuji–Trost allylation. *Journal of Materials Chemistry A* **2015**, *3* (6), 2609-2616.
189. Feng, Y.; Liu, H.; Luo, W.; Liu, E.; Zhao, N.; Yoshino, K.; Feng, W., Covalent functionalization of graphene by azobenzene with molecular hydrogen bonds for long-term solar thermal storage. *Scientific Reports* **2013**, *3* (1), 3260.
190. Zorn, G.; Liu, L.-H.; Árnadóttir, L.; Wang, H.; Gamble, L. J.; Castner, D. G.; Yan, M., X-ray Photoelectron Spectroscopy Investigation of the Nitrogen Species in Photoactive Perfluorophenylazide-Modified Surfaces. *The Journal of Physical Chemistry C* **2014**, *118* (1), 376-383.
191. Liu, Z. F.; Morigaki, K.; Enomoto, T.; Hashimoto, K.; Fujishima, A., Kinetic studies on the thermal cis-trans isomerization of an azo compound in the assembled monolayer film. *The Journal of Physical Chemistry* **1992**, *96* (4), 1875-1880.
192. Kumar, A. S.; Ye, T.; Takami, T.; Yu, B.-C.; Flatt, A. K.; Tour, J. M.; Weiss, P. S., Reversible Photo-Switching of Single Azobenzene Molecules in Controlled Nanoscale Environments. *Nano Letters* **2008**, *8* (6), 1644-1648.

193. Krekieh, N. R.; Müller, M.; Jung, U.; Ulrich, S.; Herges, R.; Magnussen, O. M., UV/Vis Spectroscopy Studies of the Photoisomerization Kinetics in Self-Assembled Azobenzene-Containing Adlayers. *Langmuir* **2015**, *31* (30), 8362-8370.
194. Moldt, T.; Przyrembel, D.; Schulze, M.; Bronsch, W.; Boie, L.; Brete, D.; Gahl, C.; Klajn, R.; Tegeder, P.; Weinelt, M., Differing Isomerization Kinetics of Azobenzene-Functionalized Self-Assembled Monolayers in Ambient Air and in Vacuum. *Langmuir* **2016**, *32* (42), 10795-10801.
195. Kobayashi, S.; Nishikawa, T.; Takenobu, T.; Mori, S.; Shimoda, T.; Mitani, T.; Shimotani, H.; Yoshimoto, N.; Ogawa, S.; Iwasa, Y., Control of carrier density by self-assembled monolayers in organic field-effect transistors. *Nature Materials* **2004**, *3* (5), 317-322.
196. Petro, A. J., The Dipole Moment of the Carbon-Carbon Bond. *Journal of the American Chemical Society* **1958**, *80* (16), 4230-4232.
197. Ashkenasy, G.; Cahen, D.; Cohen, R.; Shanzer, A.; Vilan, A., Molecular Engineering of Semiconductor Surfaces and Devices. *Accounts of Chemical Research* **2002**, *35* (2), 121-128.
198. Zhang, X.; Marschewski, E.; Penner, P.; Weimann, T.; Hinze, P.; Beyer, A.; Götzhäuser, A., Large-Area All-Carbon Nanocapacitors from Graphene and Carbon Nanomembranes. *ACS Nano* **2018**, *12* (10), 10301-10309.

7. Curriulum Vitae

- 05/2015 – now **Ph.D. Student**
Friedrich-Schiller-Universität Jena (FSU Jena)
- Group of Applied Physical Chemistry and Molecular Nanotechnology
- Supervisor: Prof. Dr. Andrey Turchanin
- 10/2011 – 05/2014 **Master of Science**
Technische Universität Dresden (TUD)
- Thesis: Poly(2-methyl-2-oxazoline) Surface Coating based on Bio-inspired Dopamine. (in collaboration with Universität Siegen, Note: 1.9)
- Supervisor:
Prof. Rainer Jordan. TUD,
Prof. Holger Schönherr. Uni Siegen, (12/2013 – 03/2014)
Dr. Ihsan Amin. TUD.
- 04/2011 – 09/2011 **Internship**
De Dung Building Material Ltd. China.
- 10/2010 – 03/2011 **Language Learning**
TUDIAS, Germany
- TEST DaF 4
- 09/2006 – 07/2010 **Bachelor of Science**
Sun Yat-sen University (SYSU)
- Thesis: Synthesis and Characterization of 3D Metal Complexes build from designed V style anhydride Ligand (Note: 88, 1.9)
- Supervisor:
Prof. Chengyong Su, SYSU, China

8. Publication List

9. **Z. Tang**, C. Neumann, A. Winter, A. Turchanin

Electrochemical delamination assisted transfer of molecular nanosheets

NANOSCALE, **2020**, 12, 8656 - 8663.

DOI: 10.1039/D0NR01084G

8. **Z. Tang**, A. George, A. Winter, D. Kaiser, C. Neumann, T. Weimann, A. Turchanin

Optically triggered control of the charge carrier density in chemically functionalized graphene field effect transistors

CHEMISTRY: A EUROPEAN JOURNAL, **2020**.

DOI: 10.1002/chem.202000431

7. Y. D. Sirmaci, **Z. Tang**, S. Fasold, C. Neumann, T. Pertsch, A. Turchanin, I. Staude

Plasmonic Metasurfaces Situated on Ultrathin Carbon Nanomembranes

ACS PHOTONICS, **2020**, 7, 1060-1066.

DOI: 10.1021/acsp Photonics.0c00073

6. F. J. F. Löchner, R. Mupparapu, M. Steinert, A. George, **Z. Tang**, A. Turchanin, T. Pertsch, I. Staude, F. Setzpfandt

Controlling second-harmonic diffraction by nano-patterning MoS₂ monolayers.

OPTICS EXPRESS **2019** 27, 35475-35484

DOI: 10.1364/OE.27.035475

5. P. van Deursen, **Z. Tang**, A. Winter, M. Mohn, U. Kaiser, A. Turchanin, G. Schneider

Selective ion sieving through arrays of sub-nanometer nanopores in chemically tunable 2D carbon membranes.

NANOSCALE **2019** 11, 20785-20791

DOI: 10.1039/C9NR05537A

4. C. Neumann, M. Szwed, M. Frey, **Z. Tang**, K. Koziel, P. Cyganik, A. Turchanin

Preparation of carbon nanomembranes without chemically active groups.

ACS APPLIED MATERIALS & INTERFACES **2019** 11, 31176-31181

DOI: 10.1021/acsaami.9b09603

3. A. George, C. Neumann, D. Kaiser, R. Mupparapu, T. Lenert, U. Hübner, **Z. Tang**, A. Winter, U. Kaiser, I. Staude, A. Turchanin

Controlled growth of transition metal dichalcogenide monolayers using Knudsen-type effusion cells for the precursors

JOURNAL OF PHYSICS: MATERIALS **2019** 2, 016001

DOI: 10.1088/2515-7639/aaf982

2. A. Winter, A. George, C. Neumann, **Z. Tang**, M. J. Mohn, J. Biskupek, N. Masurkar, L. M. R. Arava, T. Weimann, U. Hübner, U. Kaiser, A. Turchanin

Lateral heterostructures of two-dimensional materials by electron-beam induced stitching

CARBON **2018** 128, 106-116

DOI: 10.1016/j.carbon.2017.11.034

1. M. Schneider, **Z. Tang**, M. Richter, C. Marschelke, P. Förster, E. Wegener, I. Amin, H. Zimmermann, D. Scharnweber, H. Braun, R. Luxenhofer, R. Jordan

Patterned Polypeptoid Brushes

MACROMOLECULAR BIOSCIENCE **2016** 16, 75

DOI: 10.1002/mabi.201500314

Publications for This Thesis: P1 to P5

P1. Electrochemical delamination assisted transfer of molecular nanosheets

Z. Tang, C. Neumann, A. Winter, A. Turchanin

NANOSCALE, **2020**, 12, 8656-8663, DOI: 10.1039/d0nr01084g.



Cite this: *Nanoscale*, 2020, **12**, 8656

Received 7th February 2020,

Accepted 17th March 2020

DOI: 10.1039/d0nr01084g

rsc.li/nanoscale

Electrochemical delamination assisted transfer of molecular nanosheets†

Zian Tang,^a Christof Neumann,^a Andreas Winter^a and Andrey Turchanin  ^{*a,b}

Delamination and transfer of two-dimensional (2D) materials from their synthesis substrates onto target substrates is an important task for their implementation in both fundamental and applied research. To this end, the electrochemical delamination based transfer has been successfully applied to a variety of inorganic 2D materials grown on conductive substrates. However, this promising method has not yet been demonstrated for organic 2D materials, which have recently gained significant importance in the 2D materials family. Here, we present a transfer method of molecular nanosheets covalently bonded to metal substrates based on electrochemical delamination, which involves the cleavage of an Au–S bond and hydrogen evolution. We demonstrate a successful transfer of different types of carbon nanomembranes (CNMs) – about 1 nm thick molecular nanosheets – synthesized from aromatic thiol-based self-assembled monolayers on various polycrystalline gold substrates, onto new target substrates such as SiO₂/Si wafers and transmission electron microscopy grids. We analyze the subsequent nanofabrication steps, and chemical and structural characteristics of the transferred supported and suspended CNMs by X-ray photoelectron spectroscopy (XPS), optical microscopy, atomic force microscopy (AFM) and scanning electron microscopy (SEM). The XPS analysis enables us to reveal the chemical mechanisms during the delamination process, whereas the complementary microscopy measurements confirm a high structural integrity of the transferred molecular nanosheets. We expect that the developed methodology can be applied to a broad variety of organic 2D materials synthesized on conductive substrates.

Introduction

Due to their outstanding physical and chemical properties, two-dimensional (2D) materials like inorganic and organic

nanosheets with atomic or molecular thickness, respectively, have attracted enormous research interest.^{1–5} These materials are synthesized typically on solid inorganic substrates, which requires their transfer onto target substrates for their functional applications. Similarly, as has been suggested in the pioneering works on this topic, the transfer process of 2D materials is typically assisted by their separation from the growth substrates *via* chemical etching (CE).^{6–8} Although a variety of 2D materials including inorganic and organic nanosheets can be transferred in this way, the CE of the substrates may result in the precipitation of contaminants on the nanosheets,⁹ which significantly restricts their implementation in nanotechnology and in particular in areas such as nanoelectronics or nanobiotechnology, where materials with a high purity grade are indispensable.^{10–12} Moreover, concentrated corrosive solutions containing heavy metal ions are used for CE, which presents a potential environmental threat for applications. Reusing the growth substrates for the repeatable 2D materials growth is also impossible here, making the CE assisted transfer both environmentally and economically unfriendly. Therefore, the development of alternative methods for the transfer of 2D sheets is highly important. Loh and co-workers demonstrated a route to separate graphene sheets from Cu foils by means of their electrochemical delamination (ECD).¹³ In this approach, single-layer graphene is detached from the substrate *via* mechanical force arising from hydrogen bubbles generated during the electrolysis of water on Cu substrate. In the ECD assisted transfer method, harmful chemicals are absent during the whole process, the growth substrates can be reused many times and it is also less time-consuming in comparison with the CE assisted transfer. With the same method, the repeated growth and transfer of graphene from platinum substrates¹¹ as well as WS₂ monolayers grown on Au¹² were demonstrated.^{14,15} Although the ECD has been widely applied to the transfer of inorganic 2D sheets,¹⁶ its implementation for the transfer of organic nanosheets has not yet been deeply studied.¹⁷ Besides the above-mentioned advantages for the transfer of chemically inert 2D materials such as graphene, for organic nanosheets the ECD assisted transfer may provide an additional benefit as it is more gentle in comparison with the

^aInstitute of Physical Chemistry, Friedrich Schiller University Jena, 07743 Jena, Germany. E-mail: andrey.turchanin@uni-jena.de

^bJena Center for Soft Matter (JCSM), 07743 Jena, Germany

†Electronic supplementary information (ESI) available. See DOI: 10.1039/d0nr01084g

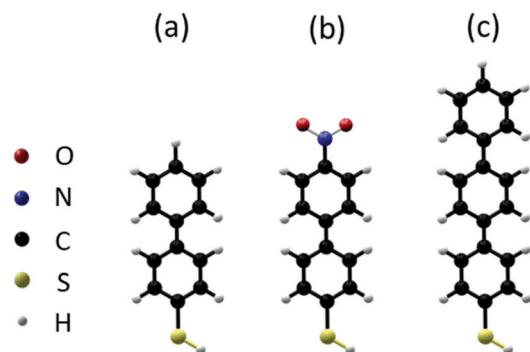


Fig. 1 Structures of molecular compounds used for the synthesis of CNMs: (a) 1,1'-biphenyl-4-thiol (BPT), (b) 4'-nitro-1,1'-biphenyl-4-thiol (NBPT) and (c) [1'',4',1',1]-terphenyl-4-thiol (TPT).

CE transfer, where strongly oxidizing solutions are typically applied.

Here, we demonstrate the implementation of ECD assisted transfer in molecular nanosheets – carbon nanomembranes (CNMs). CNMs are about 1 nm thick molecular nanosheets synthesized *via* low-energy electron irradiation induced cross-linking of aromatic self-assembled monolayers (SAMs).^{2,18–20} Their high application potential in various fields including nanoelectronics, nanooptics, nanobiotechnology and ultrafiltration has been demonstrated during recent years.^{2,21–23} In contrast to other 2D materials bound to the growth substrates by weak van der Waals forces,^{4,24–26} CNMs are bound to the substrates *via* strong covalent bonds,² which makes their exfoliation and transfer non-trivial. Furthermore, CNMs can have different functional groups on both sides and it is crucial to maintain their functionality for further applications.²⁷ We report on the electrochemical delamination and transfer of CNMs synthesized from three molecular compounds 1,1'-biphenyl-4-thiol (BPT, Fig. 1a), 4'-nitro-1,1'-biphenyl-4-thiol (NBPT, Fig. 1b) and [1'',4',1',1]-terphenyl-4-thiol (TPT, Fig. 1c), and SAMs on various gold substrates having different roughness values and cross-linked to the respective CNMs. We conducted a comparative structural and chemical analysis of the CNMs transferred *via* EC and ECD assisted transfer procedures onto the SiO₂/Si substrates and of the free-standing CNMs on grids employing optical microscopy, atomic force microscopy, scanning electron microscopy (OM, AFM and SEM) and X-ray photoelectron spectroscopy (XPS). We show that the developed ECD assisted transfer of CNMs results in large area transfer of CNMs without folds and ruptures preserving the chemical composition and enabling the reuse of the gold growth substrates. Moreover, we demonstrate a clear correlation between the roughness of the synthesized CNMs and the roughness of the employed growth substrates.

Results and discussion

First, we describe the applied steps of the ECD of CNMs from gold substrates. In Fig. 2, a schematic representation of the

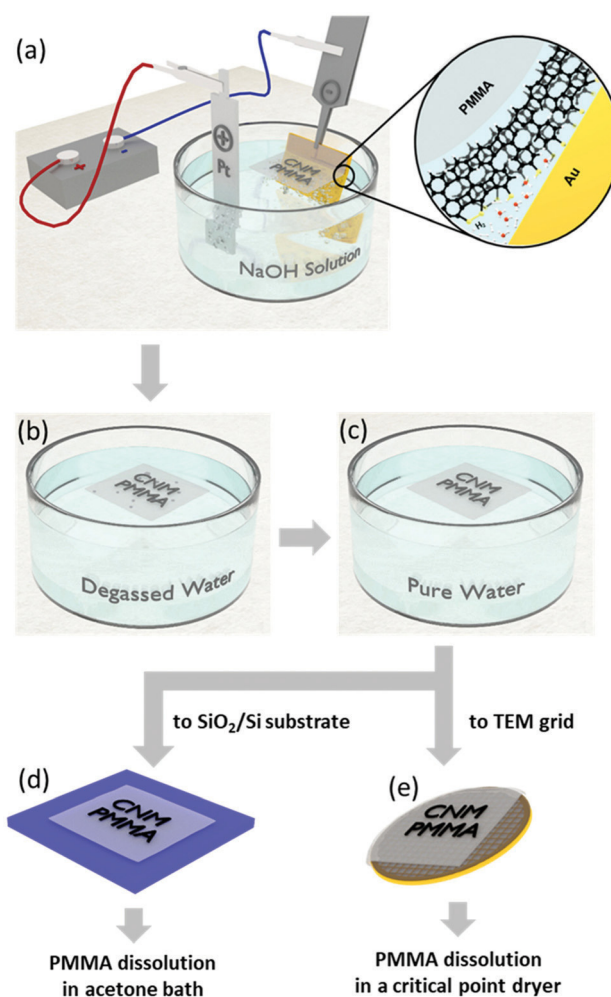


Fig. 2 Schematic representation of the ECD assisted transfer: (a) ECD set-up and CNM/substrate interface during ECD; (b) dissolution of hydrogen bubbles in degassed water; (c) washing with pure water; (d) transfer onto SiO₂/Si substrates; and (e) transfer onto TEM grids.

ECD set-up and the transfer process of CNMs is shown. To stabilize about 1 nm thick CNMs upon ECD, an ~70 nm thick poly(methyl methacrylate) (PMMA) layer is initially spin-coated on the surface (see Experimental for details). Then, to induce the delamination, a potential of 2.5–3.5 V is applied to the electrodes and the sample is slowly dipped into the electrolyte (Fig. 2a), which results in complete delamination of a PMMA/CNM sandwich from the substrates (Fig. 2b). Two different aqueous electrolytes were used in this study: NaOH solution (0.2 M) and ammonia solution (30 wt%). The ammonia-based electrolyte was primarily applied to all CNM samples on Au/SiO₂/Si substrates in order to avoid the chemical damage of Si and thereby to enable the reusability of the substrates. Moreover, ammonia is a less corrosive electrolyte in comparison with NaOH, which is favorable for the preservation of the functional groups in CNMs such as amino groups or thiols. As schematically shown in Fig. 2b, after the delamination, hydrogen bubbles remain on the CNM surface. If transferred on a

solid substrate, these bubbles would result in CNM ruptures. To avoid this unwanted effect, after the delamination a PMMA/CNM sandwich is placed in a bath with degassed water, which results in the dissolution of the bubbles. In the next step, to completely remove the electrolyte residuals, the CNMs are washed in pure water, Fig. 2c. Finally, a PMMA/CNM sandwich is transferred on a solid substrate (Fig. 2d) or on a grid (Fig. 2e) and the PMMA layer is removed by dissolving it in acetone by the well-established procedures.^{6,28} Note that in order to obtain large areas of free-standing CNMs on grids, acetone is removed in a critical point dryer.²⁸

In Fig. 3, the optical microscopy and scanning electron microscopy (SEM) images of supported and suspended nanosheets from three different molecular precursors – BPT-CNMs, NBPT-CNMs and TPT-CNMs – are shown. For better visibility with an optical microscope, SiO₂/Si substrates with a 300 nm oxide layer were used as solid substrates for the

supported CNMs.²⁹ It can be seen from Fig. 3 that all studied CNMs can be homogeneously transferred onto these substrates without macroscopic ruptures. Note that in the case of the suspended CNMs on transmission electron microscope (TEM) grids with ~2 μm openings, ruptured places were imaged in order to visualize the CNMs, as otherwise their presence on the grids is difficult to confirm due to a very homogeneous contrast of the free-standing areas.

In contrast to inorganic monolayers, which are only weakly bonded to the growth substrates, CNMs interact with the substrates *via* covalent thiolate bonds.^{2,30} Therefore, for their ECD not only hydrogen evolution on the gold electrode but also the electrochemical removal of the thiolate bonds needs to take place. As suggested by Reinhoudt *et al.*,³¹ by applying a negative voltage of 1.0–1.3 V the thiolate SAMs can be completely removed from the gold substrate. Thus, with a typical ECD negative potential of 2.5–3.5 V the following electrochemical

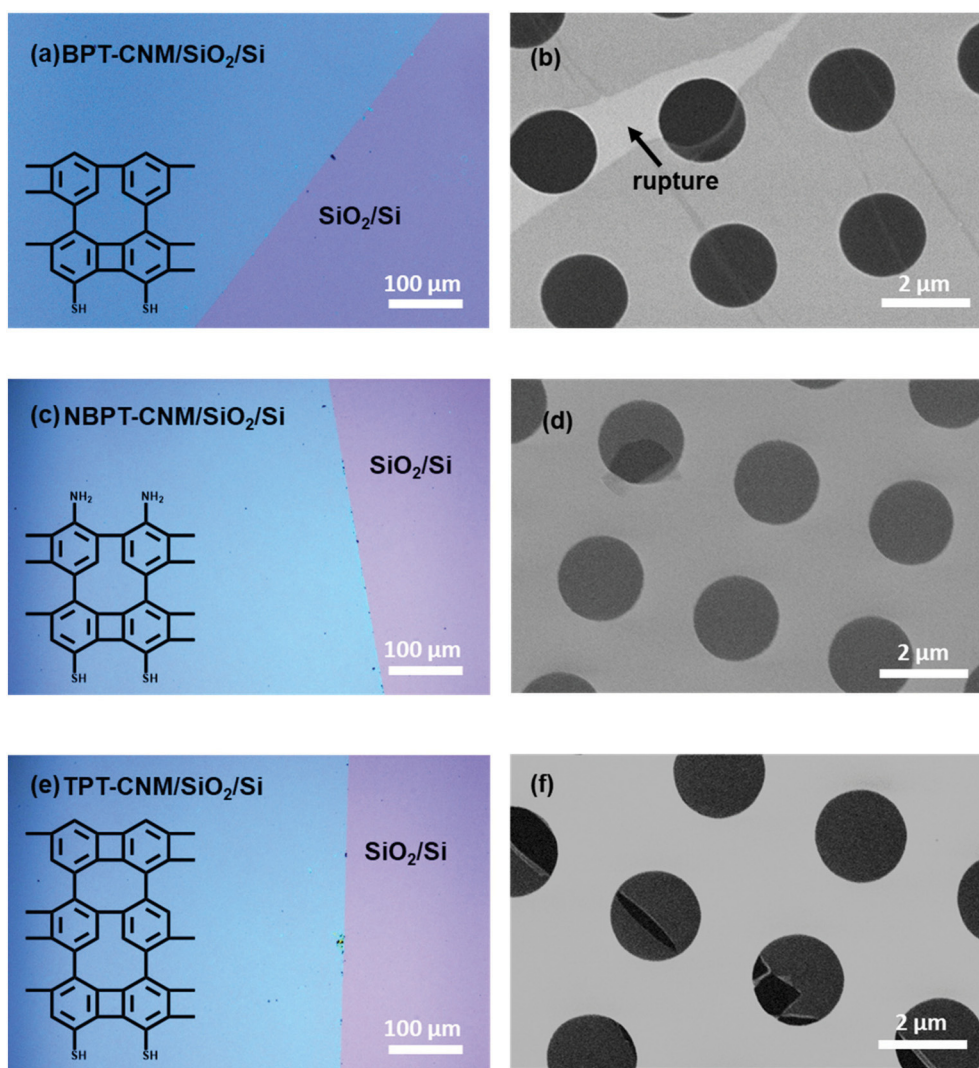
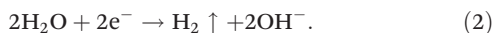
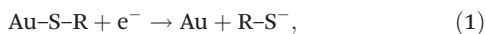


Fig. 3 Optical microscopy and scanning electron microscopy images of CNMs synthesized on 30 nm Au/Si substrates and transferred onto SiO₂/Si and Quantifoil transmission electron microscope (TEM) grids: (a) and (b) BPT-CNMs; (c) and (d) NBPT-CNMs; and (e) and (f) TPT-CNMs.

half-reactions at the gold electrode due to the reduction of the thiolate bonds (1)³² and hydrogen evolution (2)³³ can take place:



By these processes, a lower oxidation state of sulfur on the bottom side of the CNMs is also stabilized by the alkaline environment after the delamination, and the generated hydrogen bubbles lift the nanosheets from the gold surface making their detachment irreversible. In a control experiment (see Fig. S1†), we could clearly observe that a thiolate SAM is released from the gold substrate by applying a negative potential of 2.5 V.

Next, we show that the above-discussed behavior is confirmed by the XPS measurements. Fig. 4 shows the XP spectra of the CNMs transferred on a SiO₂/Si substrate. First, we analyze the S 2p signal. For all three types of the CNMs, it consists of two doublets with the S 2p_{3/2} binding energies (BE) of 163.3 eV and 167.6 eV (see ESI Table 1† for details), respectively. The doublet with the lower BEs is attributed to the R-S-H as well as the R-S-S-R species, which cannot be distinguished by XPS^{34,35} and the doublet with the higher BEs is attributed to the oxidized sulfur species.^{36,37} Note that its intensity is significantly lower in comparison with the R-S-H/R-S-S-R species. Most probably, the partial oxidation of

sulfur takes place upon washing process (Fig. 2b and c), during the transfer of the samples under ambient conditions for the XPS measurements or due to the interaction with the SiO₂ substrates. Interestingly, beyond the expected cleavage of the Au-S bonds, the applied negative potential also results in a partial cleavage of the C-S bonds during the delamination. This is reflected in both the reduced S:N and S:C elemental ratios in comparison with the CNMs on their original gold substrates as well as in some remaining sulfur (detected) on these substrates after the applied ECD (see Fig. S2†). Finally, we analyze the C 1s XP spectrum of the CNMs after the ECD transfer onto the SiO₂/Si substrates. The spectrum can be described with four different peaks (see ESI Table 1†). The peak located at 284.6 eV is assigned to the aromatic moieties in the CNMs; the peak at 285.3 eV indicates the presence of C-S bonds as well as C-N bonds in NBPT-CNMs; and the peaks located at 286.5 eV and 288.6 eV are attributed to the C-O and O=C-O carbons, which are most likely due to some PMMA residues³⁸⁻⁴⁰ remaining after the transfer. In agreement with the presence of these high BE peaks and also considering the fact that the target SiO₂ substrate is not atomically clean, we detected an effective increase of the BPT-CNM, NBPT-CNM and TPT-CNM thicknesses from the respective values on the original gold substrates of about 0.9 nm, 1.0 nm and 1.3 nm to about 1.2 nm, 1.7 nm and 1.8 nm (see ESI† p.2 for details). As expected, for the transferred NBPT-CNMs onto the SiO₂ substrate,⁴¹ the N 1s spectrum consists of a peak at 399.5 eV (ref. 42) due to the amino groups as well as a low intensity shoulder at 402.0 eV, which is assigned to the protonated nitrogen.⁴³ Interestingly, after the transfer of the CNMs onto the gold substrates, about 30% of sulfur can rebond to the substrates *via* the formation of thiolates, which can be clearly confirmed by XPS (see Fig. S3 and ESI Table 2†). These results further demonstrate the preservation of the functional properties of CNMs after their ECD assisted transfer.

In order to study the influence of the gold substrates and the ECD transfer on the topography of CNMs, we studied the samples prepared on gold substrates with different roughness values, transferred them onto the SiO₂/Si substrates and compared these results with the transfer procedures based on the standard chemical etching (CE)^{6,44} of the substrates. To this end, we employed 300 nm Au/mica, 100 nm Au/SiO₂/Si and 30 nm Au/SiO₂/Si substrates having a root mean square (RMS) roughness of 0.4 nm, 1.2 nm and 0.8 nm, respectively. The target SiO₂/Si substrates have a significantly lower RMS roughness of 0.2 nm. The bare substrates, the CNMs on their original Au substrates and after the transfer were characterized by AFM measurements. The results of this study are shown in Fig. 5. As can be seen, the RMS values of the transferred CNMs are influenced by the surface roughness of the growth substrates, *i.e.* the CNMs grown on the flattest Au/mica substrate reveal the lowest surface roughness after the transfer. Note that the precise topography of the CNMs may be influenced by the surface tension upon removal of the PMMA layer (see Fig. 2d), and in this case, the transferred CNMs will not completely reproduce the topographical features of the growth sub-

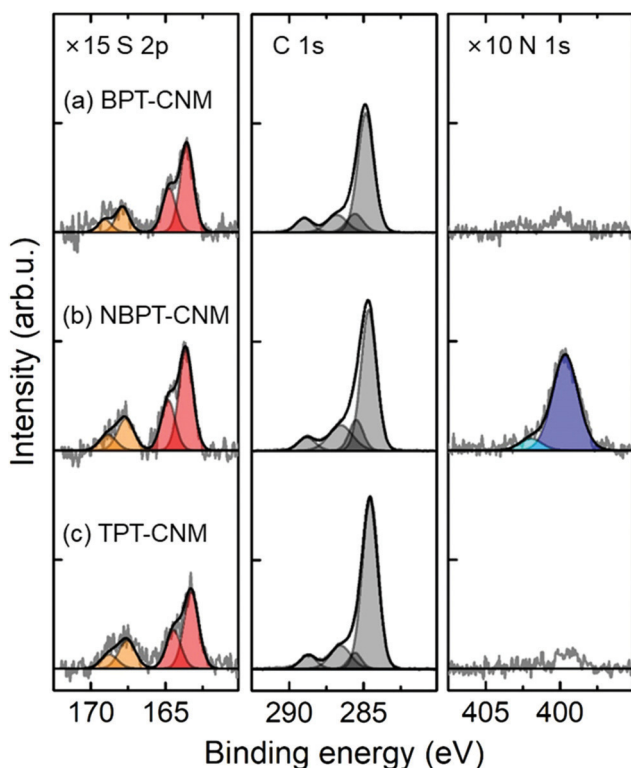


Fig. 4 XP spectra of CNMs synthesized on Au/mica substrates and transferred using ECD assisted transfer onto oxidized Si wafers with 300 nm of SiO₂: (a) BPT-CNM, (b) NBPT-CNM and (c) TPT-CNM.

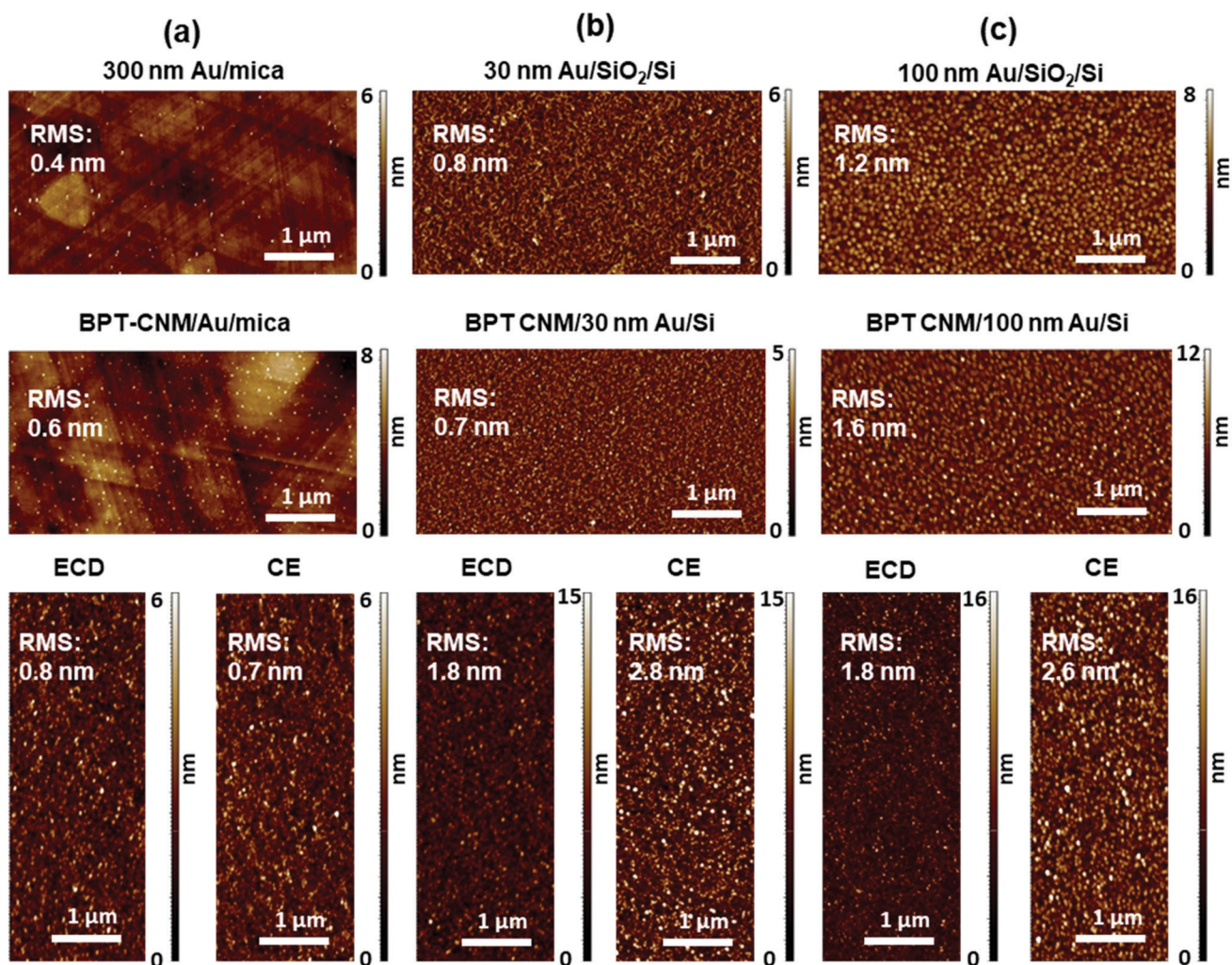


Fig. 5 AFM images of BPT-CNMs grown on Au substrates with different roughness values before and after the transfer onto target SiO_2/Si substrates (RMS: 0.2 nm) by both ECD and CE assisted transfer procedures. (a–c) CNMs grown on 300 nm Au/mica (a), 30 nm Au/Si (b), and 100 nm Au/Si (c) substrates.

strates. However, a clear correlation is observed between the RMS values of the growth substrates and the respective CNM roughness on the SiO_2/Si substrates (see Fig. 5). As can be expected, the growth substrates with higher roughness also result in higher roughness of the CNMs on the SiO_2/Si substrates. In general, upon the transfer, the roughness of the CNMs increases in comparison with their growth substrates for both ECD and CE methods and is more pronounced for the growth substrates with higher roughness. With an exception of the CNMs grown from the Au/mica substrates, the CNMs transferred by the ECD method exhibit a lower roughness than the CNMs transferred by the CE method. For the CNMs grown on the 30 nm Au/ SiO_2/Si substrates, the roughness of CNMs transferred by the ECD method increased $\sim 150\%$, while the roughness of CNMs transferred by the CE method increased $\sim 300\%$. For the CNMs grown on the 100 nm Au/ SiO_2/Si substrates, the roughness of CNMs transferred by the ECD method increased $\sim 10\%$, while the roughness of

CNMs transferred by the CE method increased $\sim 60\%$. The higher roughness of the CNMs transferred by the CE method can be attributed to the harsh conditions involved in the etching process, such as a relatively high temperature (45°C) and concentrated basic solution ($0.5\text{ mol L}^{-1}\text{ KOH}$). As the CE process that was carried out for the transfer of Au/mica grown CNMs was conducted with a less harsh etching solution, it induces lower roughness to the CNMs after the transfer.

Finally, the ECD method enables the reuse of the growth substrates for the CNM production. To prove this, we carried out three successive growth/delamination procedures from the same Au/ SiO_2/Si substrate and transferred the respective BPT CNMs onto SiO_2/Si wafers. As seen from the OM images in Fig. S4,[†] all transferred CNMs can be successfully grown and transferred (compare with Fig. 3). We could not detect any diminishing of their quality upon the subsequent growth and the ECD assisted transfer. This opens up the possibility for a cost-effective CNM fabrication by reusing the expensive growth substrates.

Conclusion

In summary, we have presented an economical, efficient and environmentally friendly alternative method to chemical etching (CE) for transferring the chemically bonded molecular nanosheets from their growth substrates onto arbitrary solid and holey substrates. The method is based on the electrochemical delamination (ECD) of the nanosheets from their growth substrates and their subsequent polymer assisted transfer. In this non-destructive transfer method, the growth substrates can be reused for the nanosheet synthesis repeatedly. Moreover, the mild conditions of the ECD based transfer enable the preservation of the functional chemical groups in the molecular nanosheets, which is favorable for their subsequent post-functionalization. We also showed that the topographical features of the nanosheets, *i.e.* their roughness, correlate with the roughness of the growth substrates, which has to be considered during their synthesis as well as for their applications. Note that the developed transfer method can be applied not only to the carbon nanomembranes (CNMs) studied in this work, but also to a large variety of other molecular nanosheets, which can both be covalently or non-covalently¹⁷ attached to the substrates and which are stable under the electrochemical conditions applied for their delamination.

Experimental

CNM preparation

Formation of self-assembled monolayers (SAMs). 1,1'-Biphenyl-4-thiol (BPT, Sigma-Aldrich, 97%) and 4'-nitro-1,1'-biphenyl-4-thiol (NBPT, Taros, 98%, sublimated before use) SAMs were prepared by immersing oxygen plasma-cleaned Au substrates into a ~ 0.1 mM solution of BPT (or NBPT) dissolved in degassed *N,N*-dimethylformamide (DMF, Alfa Aesar, 99.9%) for 72 h under inert conditions. After the substrates were taken out, they were immediately washed with DMF followed by ethanol (Sigma-Aldrich, >98%) three times to remove physically adsorbed molecules on the surface. The samples were later dried by a stream of nitrogen.

1,1':4',1''-Terphenyl-4-thiol (TPT, Sigma-Aldrich, 97%) SAMs were prepared by immersing Au substrates into a ~ 0.1 mM solution of TPT dissolved in degassed DMF. The solution was then heated at 70 °C for 24 h under inert conditions.

Electron irradiation of BPT, NBPT and TPT SAMs. The SAMs were cross-linked into carbon nanomembranes (CNMs) using a low-energy electron gun (Specs FG 15/40) using an electron energy of 100 eV with a dose of 50 mC cm⁻² in a high vacuum chamber (<10⁻⁸ mbar).

Transfer of CNMs

Transfer of the CNMs using electrochemical delamination (ECD). A PMMA layer (70 nm, M_w 495 K, Microchem, 2% in anisole) was spin-coated (2000 rpm) onto the CNMs on the Au/SiO₂/Si substrates and prebaked at 90 °C for 5 minutes. Then an electrolytic cell consisting of the PMMA/CNM/substrate

cathode, a platinum anode and 0.2 M NaOH solution (for Au/SiO₂/Si substrates, 30% ammonia) was used. To start the delamination, the current was increased to ~ 0.01 A and adjusted to a value of ~ 0.01 A cm⁻², depending on the sample size, until the membranes were cleaved completely from the substrates. The overall speed of the delamination is about 1 cm² min⁻¹. Thus to delaminate the sample with an area of 2 × 2 cm², the total current starts by ~ 0.01 A and gradually increases to ~ 0.04 A with the increase in the area of the Au substrate contact to the solution. The whole delamination process takes usually 3 to 4 minutes. The H₂ bubbles under the PMMA/CNMs were absorbed by degassed pure water after the delamination. The PMMA supported CNMs were subsequently rinsed with ultrapure water (0.056 μS, MembraPure Aquinity² E35) 4 times and transferred onto the target substrates. After drying at room temperature, the samples were baked at 90 °C for 20 min to remove the remaining moisture. The stabilized PMMA layer was removed by immersing in acetone (Sigma-Aldrich, 99.9%) for 1 h.

Transfer of the CNMs using the chemical etching method.

Firstly, a PMMA layer (100 nm, 50 kDa, All-Resist, AR-P 671.04) was spin-coated onto the CNMs on the Au substrates and dried for 10 min at 90 °C. Subsequently, the second layer of PMMA (200 nm, 950 kDa, All-Resist, AR-P 679.04) was spin-coated on top of the first one and dried for 10 min at 90 °C.

To transfer the CNMs from Au/SiO₂/Si substrates onto the target substrates, the sample was added to a 45 °C, 0.5 M KOH solution and was allowed to float for 60 to 90 minutes. CNM-PMMA layer was separated from the Au substrates due to the cleavage of the Au-S bond at a high pH value.⁴⁵ The CNM-PMMA layer was then washed 4 times with pure water and finally transferred onto the target substrates, followed by baking at 90 °C for 1 h.

To transfer the CNMs from Au/mica substrates onto the target substrates, the gold layer was cleaved from the mica substrate by gradually dipping the sample into water using the surface tension of the water. Then, an etching solution (I₂/KI/H₂O; 1 : 4 : 10) was used to etch the gold layer at room temperature (5–10 minutes). I₂, which adheres to the bottom side of the CNMs, was removed by floating the CNM-PMMA layer on Na₂O₃ (Sigma-Aldrich, 99%) solution (0.1 wt%) for 5 min. The washing process was carried out in the same way as for the transfer from Au/SiO₂/Si substrates.

After the stabilized PMMA layer was removed by immersing in acetone for 1 h, the samples were washed with 2-propanol (Sigma-Aldrich, 99.9%) and dried by a gentle stream of nitrogen. To obtain free-standing CNMs, the same transfer protocol was applied to transfer the structures onto TEM grids (Quantifoil TEM grid R2/2, Plano) with the exception that the PMMA layer was removed using a CO₂ critical point dryer (Autosamdri 815, Tousimis). This avoids the ruptures in the CNMs which were caused by the surface tension of the evaporating acetone.

Characterization techniques

Optical microscopy. Optical microscopy (Axio Imager Z1.m microscope equipped with a 5 megapixel CCD camera

(AxioCam ICc5), Carl Zeiss) was used to study the morphology of the transferred films. In order to achieve an optimal optical contrast, the CNMs were transferred onto silicon substrates with 300 nm of the dry thermal oxide layer (Sil'tronix).

Scanning electron microscopy (SEM). The SEM images were taken using a Sigma VP (Carl Zeiss) at a beam energy of 7 kV using the in-lens detector of the system.

Atomic force microscopy (AFM). The surface topography was characterized by AFM using an Ntegra (NT-MDT) in semi-contact mode using *n*-doped silicon cantilevers (NT-MDT) with resonance frequencies of 87–230 kHz and a tip radius of < 10 nm.

X-ray photoelectron spectroscopy (XPS). XPS was carried out in a Multiprobe UHV system (Scienta Omicron) using a monochromatic X-ray source (Al K α , 1486.7 eV) and an electron analyzer (Argus CU) with a resolution of 0.6 eV. The XP spectra were fitted using Voigt functions (30:70) after the Shirley (C 1s) or the linear (N 1s, S 2p) background subtraction. The spectra were peak shift calibrated by setting the Si 2p signal to 103.5 eV.

Conflicts of interest

There are no conflicts to declare.

Acknowledgements

This project was funded by the Deutsche Forschungsgemeinschaft (DFG, German Research Foundation) – Projektnummer 364549901 – TRR 234 (B7, Z2). We also acknowledge the funding from the DFG research grants TU149/5-1 and TU149/8-2 as well as the DFG research infrastructure grant (INST 275/257-1 FUGG). We thank Stephanie Höppener and Ulrich S. Schubert for providing access to the scanning electron microscope. The SEM facilities of the Jena Center for Soft Matter (JCSM) were established with a grant from the DFG.

References

- C. Backes, A. M. Abdelkader, C. Alonso, *et al.*, *2D Mater.*, 2020, **7**, 022001.
- A. Turchanin and A. Götzhäuser, *Adv. Mater.*, 2016, **28**, 6075–6103.
- X. Feng and A. D. Schlüter, *Angew. Chem., Int. Ed.*, 2018, **57**, 13748–13763.
- Y. Zhang, Y. Yao, M. G. Sendeku, L. Yin, X. Zhan, F. Wang, Z. Wang and J. He, *Adv. Mater.*, 2019, **31**, 1901694.
- B.-M. Jun, S. Kim, J. Heo, C. M. Park, N. Her, M. Jang, Y. Huang, J. Han and Y. Yoon, *Nano Res.*, 2019, **12**, 471–487.
- A. Turchanin, A. Beyer, C. T. Nottbohm, *et al.*, *Adv. Mater.*, 2009, **21**, 1233–1237.
- X. Li, Y. Zhu, W. Cai, M. Borysiak, B. Han, D. Chen, R. D. Piner, L. Colombo and R. S. Ruoff, *Nano Lett.*, 2009, **9**, 4359–4363.
- Y. Lee, S. Bae, H. Jang, S. Jang, S.-E. Zhu, S. H. Sim, Y. I. Song, B. H. Hong and J.-H. Ahn, *Nano Lett.*, 2010, **10**, 490–493.
- G. Lupina, J. Kitzmann, I. Costina, *et al.*, *ACS Nano*, 2015, **9**, 4776–4785.
- A. Ambrosi and M. Pumera, *Nanoscale*, 2014, **6**, 472–476.
- H. G. Sudibya, Q. He, H. Zhang and P. Chen, *ACS Nano*, 2011, **5**, 1990–1994.
- C. Wang, X. Cui, Y. Li, *et al.*, *Sci. Rep.*, 2016, **6**, 21711.
- Y. Wang, Y. Zheng, X. Xu, E. Dubuisson, Q. Bao, J. Lu and K. P. Loh, *ACS Nano*, 2011, **5**, 9927–9933.
- L. Gao, W. Ren, H. Xu, *et al.*, *Nat. Commun.*, 2012, **3**, 699.
- Y. Gao, Z. Liu, D.-M. Sun, *et al.*, *Nat. Commun.*, 2015, **6**, 8569.
- A. Ambrosi, C. K. Chua, N. M. Latiff, A. H. Loo, C. H. A. Wong, A. Y. S. Eng, A. Bonanni and M. Pumera, *Chem. Soc. Rev.*, 2016, **45**, 2458–2493.
- C. Neumann, M. Szwed, M. Frey, Z. Tang, K. Koziel, P. Cyganik and A. Turchanin, *ACS Appl. Mater. Interfaces*, 2019, **11**, 31176–31181.
- W. Eck, A. Küller, M. Grunze, B. Völkel and A. Götzhäuser, *Adv. Mater.*, 2005, **17**, 2583–2587.
- A. Turchanin, D. Käfer, M. El-Desawy, C. Wöll, G. Witte and A. Götzhäuser, *Langmuir*, 2009, **25**, 7342–7352.
- C. Neumann, R. Wilhelm, M. Küllmer and A. Turchanin, *Faraday Discuss.*, 2020, DOI: 10.1039/C9FD00119K.
- A. Turchanin, *Chimia*, 2019, **73**, 473–479.
- A. Turchanin, *Ann. Phys.*, 2017, **529**, 1700168.
- A. Turchanin and A. Götzhäuser, *Prog. Surf. Sci.*, 2012, **87**, 108–162.
- M. Batzill, *Surf. Sci. Rep.*, 2012, **67**, 83–115.
- Y. Zhan, Z. Liu, S. Najmaei, P. M. Ajayan and J. Lou, *Small*, 2012, **8**, 966–971.
- Z. Zhang, P. Yang, M. Hong, S. Jiang, G. Zhao, J. Shi, Q. Xie and Y. Zhang, *Nanotechnology*, 2019, **30**, 182002.
- Z. Zheng, C. T. Nottbohm, A. Turchanin, H. Muzik, A. Beyer, M. Heilemann, M. Sauer and A. Götzhäuser, *Angew. Chem., Int. Ed.*, 2010, **49**, 8493–8497.
- A. Winter, A. George, C. Neumann, *et al.*, *Carbon*, 2018, **128**, 106–116.
- C. T. Nottbohm, A. Turchanin, A. Beyer, R. Stosch and A. Götzhäuser, *Small*, 2011, **7**, 874–883.
- J. C. Love, L. A. Estroff, J. K. Kriebel, R. G. Nuzzo and G. M. Whitesides, *Chem. Rev.*, 2005, **105**, 1103–1170.
- M. W. J. Beulen, M. I. Kastenbergh, F. C. J. M. van Veggel and D. N. Reinhoudt, *Langmuir*, 1998, **14**, 7463–7467.
- T. W. Schneider and D. A. Buttry, *J. Am. Chem. Soc.*, 1993, **115**, 12391–12397.
- P. Millet and S. Grigoriev, in *Renewable Hydrogen Technologies*, ed. L. M. Gandía, G. Arzamendi and P. M. Diéguez, Elsevier, Amsterdam, 2013, pp. 19–41.
- P. E. Laibinis, G. M. Whitesides, D. L. Allara, Y. T. Tao, A. N. Parikh and R. G. Nuzzo, *J. Am. Chem. Soc.*, 1991, **113**, 7152–7167.

- 35 D. G. Castner, K. Hinds and D. W. Grainger, *Langmuir*, 1996, **12**, 5083–5086.
- 36 F.-J. Liu, X.-Y. Wei, Y.-G. Wang, P. Li, Z.-K. Li and Z.-M. Zong, *RSC Adv.*, 2015, **5**, 7125–7130.
- 37 L. D. Setiawan, H. Baumann and D. Gribbin, *Surf. Interface Anal.*, 1985, **7**, 188–195.
- 38 C. T. Nottbohm, A. Turchanin, A. Beyer and A. Götzhäuser, *J. Vac. Sci. Technol., B: Microelectron. Nanometer Struct.-Process., Meas., Phenom.*, 2009, **27**, 3059–3062.
- 39 J. Lee, Y. Kim, H.-J. Shin, C. Lee, D. Lee, C.-Y. Moon, J. Lim and S. C. Jun, *Appl. Phys. Lett.*, 2013, **103**, 103104.
- 40 C. Holroyd, A. B. Horn, C. Casiraghi and S. P. K. Koehler, *Carbon*, 2017, **117**, 473–475.
- 41 M. Schnietz, A. Turchanin, C. T. Nottbohm, A. Beyer, H. H. Solak, P. Hinze, T. Weimann and A. Götzhäuser, *Small*, 2009, **5**, 2651–2655.
- 42 L. Kankate, A. Turchanin and A. Götzhäuser, *Langmuir*, 2009, **25**, 10435–10438.
- 43 J. Ederer, P. Janoš, P. Ecorchard, J. Tolasz, V. Štengl, H. Beneš, M. Perchacz and O. Pop-Georgievski, *RSC Adv.*, 2017, **7**, 12464–12473.
- 44 M. Woszczyna, A. Winter, M. Grothe, A. Willunat, S. Wundrack, R. Stosch, W. Thomas, F. Ahlers and A. Turchanin, *Adv. Mater.*, 2014, **26**, 4831–4837.
- 45 N. Bhatt, P.-J. J. Huang, N. Dave and J. Liu, *Langmuir*, 2011, **27**, 6132–6137.

P2. Selective ion sieving through arrays of sub-nanometer nanopores in chemically tunable 2D carbon membranes.

P. van Deursen, Z. Tang, A. Winter, M. Mohn, U. Kaiser, A. Turchanin, G. Schneider

NANOSCALE **2019** 11, 20785- 20791, DOI: 10.1039/C9NR05537A



Cite this: *Nanoscale*, 2019, **11**, 20785

Selective ion sieving through arrays of sub-nanometer nanopores in chemically tunable 2D carbon membranes†

Pauline M. G. van Deursen,^a Zian Tang,^b Andreas Winter,^b Michael J. Mohn,^c Ute Kaiser,^c Andrey A. Turchanin^{b,d} and Grégory F. Schneider^{id}*^a

Two-dimensional (2D) membranes featuring arrays of sub-nanometer pores have applications in purification, solvent separation and water desalination. Compared to channels in bulk membranes, 2D nanopores have lower resistance to transmembrane transport, leading to faster passage of ions. However, the formation of nanopores in 2D membranes requires expensive post-treatment using plasma or ion bombardment. Here, we study bottom-up synthesized porous carbon nanomembranes (CNMs) of biphenyl thiol (BPT) precursors. Sub-nanometer pores arise intrinsically during the BPT-CNM synthesis with a density of 2 ± 1 pore per 100 nm^2 . We employ BPT-CNM based pore arrays as efficient ion sieving channels, and demonstrate selectivity of the membrane towards ion transport when exposed to a range of concentration gradients of KCl, CsCl and MgCl_2 . The selectivity of the membrane towards K^+ over Cl^- ions is found to be 16.6 mV at a 10 : 1 concentration ratio, which amounts to $\sim 30\%$ efficiency relative to the Nernst potential for complete ion rejection. The pore arrays in the BPT-CNM show similar transport and selectivity properties to graphene and carbon nanotubes, whilst the fabrication method *via* self-assembly offers a facile means to control the chemical and physical properties of the membrane, such as surface charge, chemical nature and pore density. CNMs synthesized from self-assembled monolayers open the way towards the rational design of 2D membranes for selective ion sieving.

Received 1st July 2019,
Accepted 10th October 2019

DOI: 10.1039/c9nr05537a

rsc.li/nanoscale

Introduction

In ultrafiltration, solvent separation, desalination and reverse osmosis, 2D materials represent an ultimately thin barrier for passing solutes and are therefore prospected to compete with conventional membranes in energy efficiency.^{1–6} The unique filtration properties of nanopores can best be exploited when pore dimensions are brought down to the size of single molecules and ions, so that the pores reject the passage of ions and molecules based on size exclusion and electrostatic repulsion. However, the reproducible formation of sub-nanometer pores in 2D membranes with high pore density remains a challenge.^{7,8} Porous 2D membranes are commonly fabricated

via top-down methods: starting with a continuous 2D layer, followed by the formation of pores by ion bombardment, electron bombardment or reactive plasma exposure.⁹ As evident from a recent review focusing on top-down approaches to fabricate porous 2D membranes, pore densities of 1–10 pores per 100 nm^2 were the highest obtained.¹⁰ To achieve these densities, as well as effective control over the pore sizes, the post-modification of a pristine 2D membrane requires highly advanced facilities for controlled electron or ion exposure.

A more versatile route is the bottom-up synthesis of porous 2D membranes from precursor molecules.^{11,12} A straightforward advantage of the bottom-up approach is its scalability without the need for post-modification steps, high-end lithographic facilities or cleanrooms. In bottom-up fabrication, pore formation is intrinsic to the membrane synthesis, arising from stacking defects during molecular self-assembly. Another advantage lies in the wide variety of precursor molecules that can be incorporated in the membrane. The choice of precursor molecule gives control over pore size and density, as well as over the chemical composition of the membrane – for instance to tune the hydrophobicity of the membrane or to induce specific interactions between the membrane and solute ions

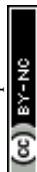
^aLeiden University, Leiden Institute of Chemistry, Einsteinweg 55, 2333 CC Leiden, Leiden, The Netherlands. E-mail: g.f.schneider@chem.leidenuniv.nl

^bFriedrich Schiller University Jena, Institute of Physical Chemistry, Lessingstraße 10, 07743 Jena, Germany

^cUlm University, Central Facility of Electron Microscopy, Albert Einstein Allee 11, D-89081 Ulm, Germany

^dCenter for Energy and Environmental Chemistry Jena (CEEC Jena), Philosophenweg 7a, 07743 Jena, Germany

†Electronic supplementary information (ESI) available. See DOI: 10.1039/c9nr05537a



or molecules. In particular, carbon nanomembranes (CNMs), formed *via* self-assembly of aromatic thiol-precursor molecules, have been shown to display pore densities in the range required for applications such as desalination by reverse osmosis and as separation membranes.^{13–15} Beside the pore density, which determines through-put, a key factor in the efficiency of filtration is the pore size distribution in a 2D membrane, with smaller pores yielding higher selectivity in trans-membrane transport. Previous studies have revealed that the pore size in CNMs is determined by the size and structure of the precursor molecules. Precursors of decreasing molecular size yield membranes with decreasing pore diameter, as well as a thinner membrane. In the current work, we use the precursor molecule 1,1'-biphenyl-4-thiol (BPT): one of the smallest precursor that still forms a stable CNM, with a near-2D thickness of ~0.9 nm and strong enough to be suspended over micrometers.

The BPT-CNMs are therefore an ideal candidate for ion filtration applications. However, the porosity of the BPT-CNMs has not been characterized to date, due to the difficulty of imaging sub-nanometer features in 2D membranes.¹⁶ Whereas nanopores of sub-nanometer sizes have been resolved in crystalline graphene layers produced *via* pyrolysis of CNMs, the disordered nature of the CNMs complicates the visualization of sub-nanometer pores. The smallest CNM in which porosity has been resolved was made from [1'',4',1',1]-terphenyl-4-thiol (TPT) precursors, for which pore dimensions of 0.7 ± 0.1 nm have recently been reported.¹³

Here, we determine the pore density in the BPT-CNMs for the first time, using a combination of high-resolution transmission electron microscopy (HR-TEM) imaging and ionic conductance measurements. In an earlier study, TEM has been used to resolve BPT-CNMs membrane based pores of several nanometers in diameter, which were induced by ion beam exposure, and did not reveal any pores with smaller sizes.³² On the other hand, we show here that pores are in fact present in the pristine BPT-CNMs, as evident from transmembrane ion conductivity through the BPT-CNMs membrane. The number and size of pores in a well-defined area of the membrane are determined using the ion flow through the membrane. In this way, the porosity of each membrane sample can be determined *in operando*. Next, we demonstrate the use of the BPT-CNMs as ion-sieving membranes. In saline solution, one ion type is preferentially transmitted through the sub-nanometer pores in the BPT-CNMs while counter-ions are rejected. This ion selectivity is essential to applications in desalination, energy generation and energy storage. Ion selectivity in transport through the membrane pores is based on electrostatic repulsion by charges present on the membrane surface, as shown by a range of studies probing charge-selective ion transport through nanoporous 2D membranes.^{17–19} In the BPT-CNMs, charged groups include residual sulfide groups.²⁰ Moreover, ion selectivity in 2D nanoporous membranes has been observed even in chemically neutral membranes, including graphene and molybdenum sulfide. It has therefore been suggested that in aqueous environment, adsorbed oxygen

species add a negative surface charge to 2D membranes irrespective of the chemical composition of the membrane.²¹

Results and discussion

To estimate the pore density in the BPT-CNMs, we expressed the measured ionic conductance in terms of the length and diameter of the membrane-based pores, according to a model developed for the description of conductance through nanopores in SiN membranes,²² assuming continuous charge flow:

$$G = \sigma_e \left(\frac{4l}{\pi d^2} + \frac{1}{d} \right)^{-1} \quad (1)$$

Herein, d and l describe the average diameter and length of a single pore through which the conductance G is measured. The bulk electrolyte conductivity σ_e , with the units Siemens per meter ($S\ m^{-1}$), is determined by the ionic strength of the solution. We adjusted this model to describe not the conductance of a single pore, but of an array of pores in a suspended CNM, defining the number of sub-nanometer pores in the exposed membrane area in terms of the recorded conductance (G_{meas}) of the carbon nanomembrane:

$$n_A = \frac{G_{\text{meas}}}{\sigma_e} \cdot \left(\frac{4l}{\pi \langle d \rangle^2} + \frac{1}{\langle d \rangle} \right) \quad (2)$$

Here, n_A is the number of pores in the suspended membrane area A and $\langle d \rangle$ the average pore diameter.

In order to expose a well-defined BPT-CNMs area, the CNM was deposited on a SiN chip featuring an aperture that was sculpted in the SiN membrane using the focused beam of an electron microscope. The diameter of the nano-aperture ranged between 20 and 80 nm. Fig. 1a depicts the deposition method: the CNM was synthesized by self-assembly of precursor molecules on a gold film on a mica support (Fig. 1a, step 1). Subsequent cross-linking by electron irradiation (step 2) resulted in a covalent 2D network.¹⁶ The membrane was then transferred onto the SiN aperture-chip using PMMA-assisted transfer, as presented in Fig. 1a and in detail in the Experimental section. Fig. 1b shows a SiN aperture prior to membrane deposition imaged by TEM after sculpting the aperture. The aperture chip was imaged again after deposition of the CNM, using aberration-corrected high-resolution (HR) TEM. Fig. 1c shows one membrane imaged by HR-TEM, revealing an integral membrane with no visible pores. From the integrity of the membrane in the electron images, we can assume that the size of the pores in BPT-CNMs does not exceed 1 nm. This is a rather conservative estimate, given the instrumental resolution that can be attained in principle by aberration-corrected HR-TEM at the 80 kV operating voltage is 0.18 nm. However, we take into account several factors limiting the resolution attained in TEM imaging: firstly, a high defocus was required to gain sufficient contrast from the amorphous BPT-CNMs membrane, which reduced the resolution. Secondly, the applicable electron dose for imaging is limited because the BPT-CNMs was observed to deteriorate significantly at too high



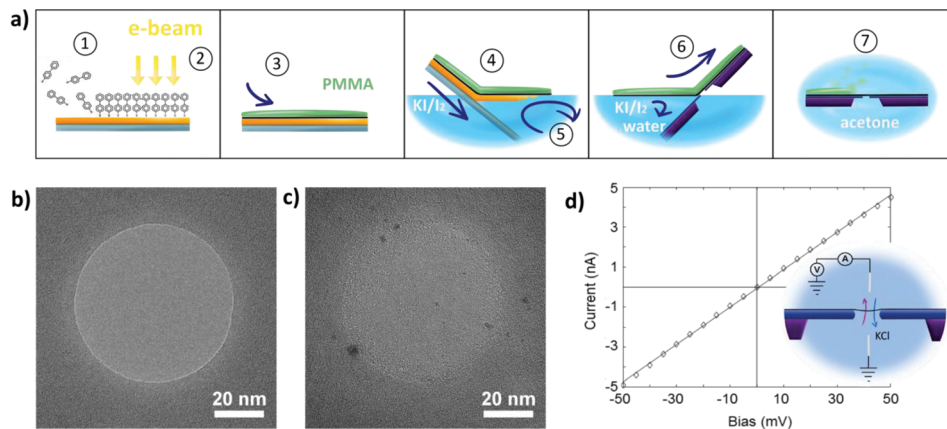


Fig. 1 Fabrication of suspended biphenyl thiol carbon nanomembrane (BPT-CNM) chips. (a) Schematic procedure used to fabricate free-standing BPT-CNM, starting with the formation of the BPT-SAM on the surface of gold on mica (1). Subsequent electron irradiation cross-links the BPT-SAM to form the BPT-CNM (2). A protective layer of PMMA is spin-coated onto the stack (3). The PMMA/CNM/gold stack is exfoliated from the mica support (4) and suspended on water, after which it is transferred to the surface of a KI/I₂ solution that etches away the gold film (5). Through a sequence of washing steps (see Experimental section) the KI/I₂ solution is replaced by ultrapure water from which the stack is scooped up onto the SiN/SiO₂ wafer (6). After drying, PMMA is removed in acetone (7), which is exchanged for supercritical CO₂ to prevent left-over contaminations on the final membrane. (b) A 60 nm diameter aperture in SiN after drilling by the focused beam of a TEM. (c) The aperture from (b) after deposition of the BPT-CNM imaged by HR-TEM. (d) Typical IV curve measured on a CNM suspended over a SiN aperture in 1 M KCl solution. Inset: The suspended BPT-CNM integrated in the ionic conductivity measurement circuit, in between two electrolyte compartments both connected through Ag/AgCl electrodes.

electron doses, with holes forming during imaging at dose rates $>10^5 \text{ e}^- \text{ nm}^{-2} \text{ s}^{-1}$.

To collect information about the pores in the BPT-CNM, trans-membrane ionic conductance measurements were performed. The ionic conductance through the CNM exposed by the SiN aperture was determined from current–voltage curves recorded in the flow cell, such as shown in the inset of Fig. 1d. The conductance of the membrane can in principle be simply determined using Ohm's law. However, for ion transport through 2D nanopores, deviations from ohmic behavior have been reported in literature^{23–25} and observed in our measurements, too. Two types of non-linear IV-characteristics occurred: rectification and activation. Rectification is a difference in conductance in the positive voltage range respective to the negative voltage range. Activation is the superlinear increase of conductance with increasing voltage across the pore. Both effects have been shown to be related to dehydration phenomena in the confinement of 2D nanochannels. In this work, our sole interest lies with the conductance of the pore towards hydrated ions. Therefore, the conductance was determined applying Ohm's law in the region close to zero bias, where the conductance of hydrated ions is most closely approximated.

The ionic conductance through eleven CNM-coated SiN apertures was measured, both before and after CNM deposition. The data are presented in Fig. 2a. Typically, deposition of the membrane (blue) led to a 30% drop in the measured conductance relative to the bare SiN aperture (red). The conductance of the CNM samples with different free-standing areas falls faithfully on the same line, reflecting the homogeneity of the membrane. The linearity of the conductance *versus* membrane area furthermore confirms that the conductance

stems from the ionic current passing through the membrane, without significant contributions from leak currents.

The membrane conductance in 1 M KCl was used to make a quantitative statement about the porosity of the BPT-CNM. From the linear regression of the conductance value in Fig. 2a (blue data points), the average membrane conductance (G_{CNM}) per area was found to be $G_{\text{CNM}} = 4.8 \frac{\text{nS}}{100 \text{ nm}^2}$. Based on this value, we estimated the porosity of the BPT-CNM according to eqn (2). Note that the contribution to the resistance from the SiN aperture is not negligible and was accounted for by subtracting the bare aperture conductance (red) from the CNM conductance (blue) – see ESI S1.†

Eqn (2) contains two unknown parameters: n , the number of pores contributing to ion transport and $\langle d \rangle$, the average diameter of the pores. The solution, thus, is a set of possible combinations of n and $\langle d \rangle$, shown in Fig. 2b. To find the actual values for both n and $\langle d \rangle$, we considered first, a lower limit to the size of the pores contributing to the ionic current, which is given by the radius of the smallest charge carrier. Of the main charge carriers in KCl electrolyte, K⁺ is the smallest, with a hydrated diameter of 0.56 nm.²⁶ As ions are expected to be excluded by pores smaller than the hydrated ion diameter, K⁺ sets the lower limit to the pore diameter at $d_{\text{min}} = 0.56 \text{ nm}$. The upper limit to the pore diameter was defined considering that the membrane imaged by HR-TEM appears free of pores larger than 1 nm.

We concluded that the diameter of the pores contributing to the ionic current falls in the range of $0.56 < \langle d \rangle < 1 \text{ nm}$ (indicated by the yellow region in Fig. 2b). It follows that the pore density of the BPT-CNM lies between 1 and 2.7 pores per 100 nm². The exposed membrane area ranged from 20 to



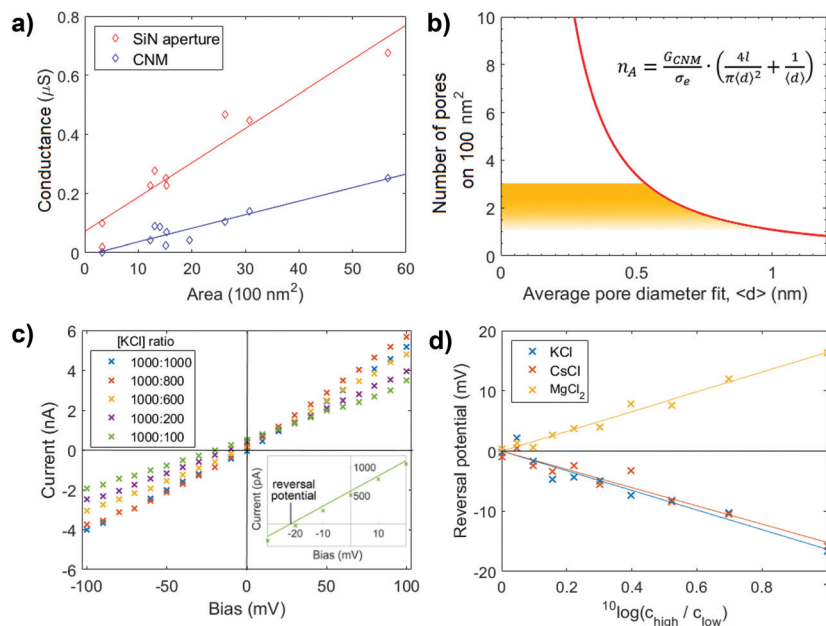


Fig. 2 Ion transport measurements. (a) Ionic conductance through BPT-CNM with varying free-standing membrane area exposed on both sides to 1 M KCl solution. The solid line represents the linear regression through the data points. (b) Geometric model relating the average pore diameter to the number of pores in a 100 nm² area (eqn (2)). The yellow region indicating the physically relevant solutions to the equation, from which the pore density is predicted to lie between 1 and 2.7 pores per 100 nm². (c) Ionic current–voltage (IV) curves measured in the presence of an electrolyte concentration gradient over a 50 nm diameter CNM membrane. The inset shows a close-up of one of the measurements, highlighting the reversal potential at which the osmotic potential due to the concentration gradient is compensated. (d) The reversal potential over the membrane in (c) at concentration ratios ranging between 1 and 10, with the higher concentration kept constant at 1000 mM. The reversal potential is of equal magnitude and opposite sign to the membrane potential.

80 nm diameter, so that between 10 and 200 pores partook as conductive channels.

Next, the membrane potential across the BPT-CNM was determined following Nernst-Planck membrane theory.²⁷ The membrane potential is the potential difference between the two sides of the membrane in the presence of an electrolyte concentration gradient. In the presence of such a concentration gradient, diffusion drives ions to the lower concentration side of the membrane. If both cations and anions pass through the membrane at equal rates, no potential would arise. However, in the case of an ion selective membrane, preferential transport of one ion type over the counter-ion results in a net ionic current. The membrane potential is the voltage associated with this current.

Current–voltage characteristics measured in the presence of varying concentration ratios are shown in Fig. 2c. The inset shows the IV-curve measured at a 1 : 10 concentration ratio in close-up around the origin. To find the membrane potential, we determined the voltage measured at zero current (*i.e.*, the intersection with the *x*-axis of the linear fit through the data points). This is the potential at which the selective ionic current was exactly compensated, called the reversal potential. The reversal potential is of equal magnitude (although of opposite sign) to the membrane potential. To obtain a reliable value of the reversal potential, the concentration ratio was varied and the linear regression gave an accurate value of the reversal potential. Fig. 2d shows the reversal potential as a

function of the concentration ratio. At a concentration ratio of 1 : 10 in KCl, the reversal potential was found to be −16.6 mV. The membrane potential, thus, is +16.6 mV.

The efficiency of ion rejection in the BPT-CNM can be quantified by comparing the measured membrane potential to the Nernst membrane potential. The Nernst membrane potential is the theoretical potential that would arise from a membrane that allows only the passage of one ion type and completely rejects counter ions. The Nernst potential at a concentration ratio of 1 : 10 is 52 mV (the calculation of the Nernst potential is presented in Table S2†). The BPT-CNM membrane potential is thus 32% of the Nernst potential.

For the BPT-CNM, a higher value than 32% of the theoretical Nernst potential may have been expected, since ion selectivity should be very efficient in pores that approach the size of hydrated ions – as is the case in the BPT-CNM. This discrepancy can be understood considering that the Nernst-Planck membrane theory was developed for conventional, 3D ion selective membranes. In 3D porous membranes, ion selectivity arises due to a bulk membrane phase that is distinct from the adjacent electrolyte phases. In 2D membranes, on the other hand, a bulk membrane phase is ill-defined because of the near-zero length of pore channels. The use of 2D membrane thus allows easier ion transport because of the minimal barrier separating the bulk electrolyte phases on either side of the membrane, resulting in a membrane potential of only 32% of the expected membrane potential for 3D membranes. From these results it is



clear that the description of ion selective transport in 2D membranes requires an extension of Nernst-Planck theory to accurately describe measured membrane potentials.

The positive membrane voltage reveals the selectivity towards cations in KCl electrolyte. Conversely, repeated measurement of the membrane potential in MgCl₂ and CsCl solutions revealed the dependence of selectivity to the valency of the electrolyte salt used, as the membrane potential changes sign in the case of divalent MgCl₂ (Fig. 2d). This observation may be attributed to charge inversion, a phenomenon in which divalent cations overcompensate the negative charge on a surface, effectively changing the sign of the surface charge.²⁸ An alternative explanation is that the electrostatic charges causing selectivity are screened more efficiently in a divalent salt solution – that has a three times higher ionic strength than a monovalent salt solution of the same concentration. When charges on the pore edge are efficiently screened, the factor determining selective transport is the ion mobility. The Cl⁻ ion, with a higher diffusion coefficient than the Mg²⁺ ion,²⁹ becomes the main charge carrier in MgCl₂ electrolyte. This results in an opposite membrane potential to KCl and CsCl, where the cations were the main charge carriers. The selectivity of the membrane is thus responsive to the electrolyte composition and valency.

More insight in the specific interactions between membrane and electrolyte can be obtained by changing the chemical composition of the membrane. As the chemical synthesis of the CNM allows control over the membrane chemistry, such as the addition of specific charged groups, this kind of membranes hold the prospect of increasing our understanding into the nature of membrane–electrolyte interactions, and result in new selective transport phenomena.

To conclude, the bottom-up synthesized carbon nanomembranes provide a scalable and reproducible approach to obtain high density sub-nanometer pores in a 2D membrane. Integrating the BPT-CNM in an ionic conductance measurement flow-cell, we showed that the pores in the BPT-CNM act as effective ion sieving channels. We were able to determine the density of ion channels *in operando*, allowing the individual characterization of the porosity in each membrane sample and finding a highly uniform and reproducible pore density. The density of pores contributing to ion transport in the BPT-CNM was 1–2.7 pores per 100 nm², comparable with the high-end top-down approaches where pores are induced in post-modification steps involving ion or electron bombardment. The significant deviation of the membrane potential from the Nernst potential, as well as membrane charge inversion in the presence of MgCl₂, are typical to transport through 2D membranes. The BPT-CNM membrane is thus a suitable platform to study the mechanisms underlying ion transport through 2D sub-nanometer pores, more easily obtained than for instance in carbon nanotubes or graphene nanopores produced by lithography. In addition, the possibility of tuning – chemically – the composition of the membrane holds the prospect of rational design of membranes with desired surface properties and chemical functionality.

Experimental

SiN aperture sculpting

SiN windows of 50 × 50 μm², supported on SiO₂ chips, were purchased from Norcada. The SiN/SiO₂ chips were cleaned in piranha solution before insertion in the electron microscope (Tecnai T20 operating at 200 keV; Thermo Fischer Scientific, previously FEI). Nano-apertures were sculpted in the SiN window using the focused electron beam.³⁰ After sculpting, the SiN/SiO₂ chips were stored in a sonicated mixture of 50 : 50 EtOH : H₂O (absolute ethanol, >98%, Sigma Aldrich; Milli-Q) for protection against vibrations as well as prevention of clogging the nano-aperture by contaminations, until the moment BPT-CNM deposition.

BPT-CNM fabrication

A gold/mica substrate (Georg Albert PVD-Coatings) was cleaned for 1 minute in oxygen plasma (Zepto 115320, Diener). The gold/mica substrate was then immersed in a ~0.1 mM solution of 1,1'-biphenyl-4-thiol (BPT, Sigma Aldrich) in degassed DMF (Sigma Aldrich, 99.9%) for 72 h under dark conditions, during which a self-assembled BPT monolayer formed on the gold surface. After the self-assembly, the substrate was taken out and immediately washed three times with DMF followed by three times washing with ethanol (Sigma Aldrich, 99.8%) to remove possible residual BPT molecules that may have adsorbed on top of the monolayer. The samples were then dried under nitrogen flow (5.0, Linde) and transferred to a high vacuum chamber (1 × 10⁻⁸ mbar) for electron exposure. An electron beam at 100 eV and 50 mC cm⁻² electron dose induced molecular cross-linking of the BPT-SAM molecules on the gold surfaces to form a stable membrane. The quality of the formed BPT-SAMs and BPT-CNMs were monitored using X-ray photoelectron spectroscopy (XPS, Fig. S3 and S4†). XPS was carried out on an ultra-high vacuum Multiprobe UHV system (base pressure 1 × 10⁻¹⁰ mbar) from Scienta Omicron, using a monochromatic X-ray source (Al K_α) and an electron analyzer (Argus) with a spectral resolution of 0.6 eV.

Transfer of the CNMs onto SiN/SiO₂ chips

The transfer procedure was conducted as described elsewhere.³¹ A PMMA layer (100 nm, 50 kDa, All-Resist, AR-P 671.04) was spin coated onto the CNM on gold/mica and hardened for 10 min at 90 °C. Subsequently, a thicker layer of PMMA (200 nm, 950 kDa, All-Resist, AR-P 679.04) was spin coated on top of the first one and hardened for 10 min at 90 °C. The PMMA-CNM-Au sandwich was cleaved from the mica substrate by repeatedly and gradually dipping the sample into water. An etching solution (I₂/KI/H₂O, 1 : 4 : 10 by mass) was used to dissolve the gold layer at room temperature. Molecular I₂ which adheres to the bottom side of the CNM was removed by floating the CNM-PMMA layer on Na₂S₂O₃ (0.1 wt%) solution for 5 min. The CNM-PMMA layer was washed 6 times with ultrapure water before transfer to the target substrate, followed by baking at 90 °C for 1 h. The PMMA layer was removed by dipping the sample into acetone (Sigma Aldrich, 99.9%).



To clean the free-standing areas from PMMA impurities, and to avoid rupture of the free-standing CNMs caused by the drying of acetone, acetone was exchanged with liquid CO₂ in a critical point dryer (Autosamdri 815, Tousimis) and the CO₂ was removed by forming a super critical fluid.

HR-TEM imaging

Aberration-corrected high-resolution TEM (AC-HRTEM) on the BPT-CNM after deposition on the Si₃N₃ aperture was performed using an FEI Titan 80–300 microscope with third-order aberration correction by a hexapole image corrector. The TEM acceleration voltage was set to 80 kV in order to minimize electron beam-induced damage. The AC-HRTEM images of BPT-CNMs were recorded using a Gatan Ultrascan 1000XP CCD camera with frame sizes of 2048 × 2048 pixels, at electron dose rates of the order of 10⁶ e⁻ nm⁻² s⁻¹.

Ionic conductance measurements

Current–voltage traces were recorded in a custom fabricated flow cell designed to clamp the SiN/SiO₂ chip between two electrolyte reservoirs of approximately 150 μL. After insertion of the chip into the flow-cell, both reservoirs were flushed with a sonicated mixture of ethanol in ultrapure water (50 : 50) to prevent air bubbles from sticking to the membrane surface. Subsequently, ultrapure water (Milli-Q) was flushed three times, followed by two times flushing electrolyte solution. When the electrolyte was changed during measurements of reversal potential, the reservoir was flushed twice with the new concentration electrolyte.

For the preparation of fresh Ag/AgCl electrodes, silver wire (Alfa Aesar, 99.999% percent purity) was cut to pieces ~2 cm pieces. The tip of the cut piece was immersed in bleach for at least 30 minutes. After formation of a AgCl layer, the electrode tip was rinsed with ultrapure water and used the same day. The flow cell was placed in a Faraday cage and the two compartments of the flow cell were connected to an Axopatch 200B Patch Clamp setup, through freshly prepared Ag/AgCl electrodes. Current–voltage traces were recorded and analyzed using pCLAMP software.

Conflicts of interest

There are no conflicts of interest to declare.

Acknowledgements

GFS and PMGD acknowledge the funding received from the Netherlands Organization for Scientific Research (NWO) under the VIDI program (723.013.007) and from the European Research Council under the European Union's Seventh Framework Program (FP/2007-2013/ERC Grant Agreement no. 335879 project acronym Biographene). ZT, AW, AAT, MM and UK acknowledge the Deutsche Forschungsgemeinschaft (DFG) for the funding received through the CataLight program

(SFB/TRR 234) under projects B07, Z02 (ZT, AW, AAT), and C04 (UK). M. J. M. and U. K. acknowledge funding from the European Union's Horizon 2020 research and innovation program under grant agreement No. 785219. In addition, ZT, AW and AAT acknowledge the DFG Research Infrastructure Grant (INST 275/257-1 FUGG). Furthermore the authors would like to thank Mandakranta Ghosh and Jeffery A. Wood (University of Twente, Faculty of Science and Technology, Department of Soft matter, Fluidics and Interfaces) for the discussions on the results presented in this work.

References

- 1 D. Cohen-Tanugi, L. Lin and C. Grossman, Multilayer nanoporous graphene membranes for water desalination, *Nano Lett.*, 2016, **16**, 1027–1033.
- 2 E. N. Wang and R. Karnik, Graphene cleans up water, *Nat. Nanotechnol.*, 2012, **7**, 552–554.
- 3 P. Sun, K. Wang and H. Zhu, Recent developments in graphene-based membranes: structure, mass-transport mechanism and potential applications, *Adv. Mater.*, 2016, **28**, 2287–2310.
- 4 J. Park, P. Bazlewski and G. Fanchini, Porous graphene-based membranes for water purification from metal ions at low differential pressures, *Nanoscale*, 2016, **8**, 9563–9571.
- 5 D. G. Haywood, A. Saha-shah, L. A. Baker and S. C. Jacobson, Fundamental studies of nano fluidics: nanopores, nanochannels, and nanopipets, *Anal. Chem.*, 2014, **87**, 172–187.
- 6 L. Cao, *et al.*, On the Origin of Ion Selectivity in Ultrathin Nanopores: Insights for Membrane-Scale Osmotic Energy Conversion, *Adv. Funct. Mater.*, 2018, **28**, 1–8.
- 7 G. Liu, W. Jin and N. Xu, Two-dimensional-material membranes: a new family of high-performance separation membranes, *Angew. Chem., Int. Ed.*, 2016, **55**, 13384–13397.
- 8 L. Madauß, *et al.*, Fabrication of nanoporous graphene/polymer composite membranes, *Nanoscale*, 2017, 10487–10493.
- 9 G. Liu, W. Jin and N. Xu, Graphene-based membranes, *Chem. Soc. Rev.*, 2015, **44**, 5016–5030.
- 10 L. Wang, M. S. H. Boutilier, P. R. Kidambi, D. Jang and N. G. Hadjiconstantinou, Fundamental transport mechanisms, fabrication and potential applications of nanoporous atomically thin membranes, *Nat. Nanotechnol.*, 2017, **12**, 509–522.
- 11 P. Angelova, *et al.*, A universal scheme to convert aromatic molecular monolayers into functional carbon nanomembranes, *ACS Nano*, 2013, **7**, 6489–6497.
- 12 A. Turchanin and A. Götzhäuser, Carbon Nanomembranes, *Adv. Mater.*, 2016, **28**, 6075–6103.
- 13 Y. Yang, *et al.*, Rapid water permeation through carbon nanomembranes with sub-nanometer channels, *ACS Nano*, 2018, **12**, 4695–4701.
- 14 A. Beyer, *et al.*, Imaging of carbon nanomembranes with helium ion microscopy, *Beilstein J. Nanotechnol.*, 2015, **6**, 1712–1720.



- 15 C. Sun, B. Wen and B. Bai, Recent advances in nanoporous graphene membrane for gas separation and water purification, *Sci. Bull.*, 2015, **60**, 1807–1823.
- 16 A. Turchanin, *et al.*, One nanometer thin carbon nanosheets with tunable conductance and stiffness, *Adv. Mater.*, 2009, **21**, 1233–1237.
- 17 S. P. Koenig, L. Wang, J. Pellegrino and J. S. Bunch, Selective molecular sieving through porous graphene, *Nat. Nanotechnol.*, 2012, **7**, 728–732.
- 18 S. Sarkar and A. K. Sengupta, The donnan membrane principle: opportunities for sustainable engineered processes and materials, *Environ. Sci. Technol.*, 2010, **44**, 1161–1166.
- 19 M. Ghosh, K. F. A. Jorissen, A. Wood and R. G. H. Lammertink, Ion Transport through Perforated Graphene, *J. Phys. Chem. Lett.*, 2018, **9**, 6339–6344.
- 20 Z. Zheng, *et al.*, Hybrid van der Waals heterostructures of zero-dimensional and two-dimensional materials, *Nanoscale*, 2015, **7**, 13393–13397.
- 21 M. I. Walker, *et al.*, Extrinsic cation selectivity of 2D membranes, *ACS Nano*, 2017, **11**, 1340–1346.
- 22 S. W. Kowalczyk, A. Y. Grosberg, Y. Rabin and C. Dekker, Modeling the conductance and DNA blockade of solid-state nanopores, *Nanotechnology*, 2011, **22**, 315101.
- 23 T. Jain, *et al.*, Heterogeneous sub-continuum ionic transport in statistically isolated graphene nanopores, *Nat. Nanotechnol.*, 2015, **10**, 1–6.
- 24 J. Feng, *et al.*, Observation of ionic Coulomb blockade in nanopores, *Nat. Mater.*, 2016, **15**, 850–855.
- 25 E. R. Cruz-Chu, A. Aksimentiev and K. S, Ionic current rectification through silica nanopores, *J. Phys. Chem. C*, 2010, **113**, 1850.
- 26 Y. Marcus, Ionic Radii in Aqueous Solutions, *Chem. Rev.*, 1988, **88**, 1475–1498.
- 27 T. Sata, *Ion exchange membranes: preparation, characterization, modification and application*, Royal Society of Chemistry, Cambridge, 2007, pp. 13–16.
- 28 Y. He, D. Gillespie, D. Boda, I. Vlassioux, R. S. Eisenberg and A. Z. S. Siwy, Tuning transport properties of nanofluidic devices with local charge inversion, *J. Am. Chem. Soc.*, 2009, **131**, 5194–5202.
- 29 L. Yuan-Hui and S. Gregory, Diffusion of ions in sea water and in deep-sea sediments, *Geochim. Cosmochim. Acta*, 1974, **38**, 703–714.
- 30 A. J. Storm, J. H. Chen, X. S. Ling, H. W. Zandbergen and C. Dekker, Fabrication of solid-state nanopores with single-nanometre precision, *Nat. Mater.*, 2003, **2**, 537.
- 31 A. Winter, *et al.*, Lateral heterostructures of two-dimensional materials by electron-beam induced stitching, *Carbon*, 2018, **128**, 106–116.
- 32 R. A. Wilhelm, *et al.*, Threshold and efficiency for perforation of 1 nm thick carbon nanomembranes with slow highly charged ions, *2D Mater.*, 2015, **2**, 35009.



P3. Plasmonic metasurfaces situated on ultrathin carbon nanomembranes

Y. D. Sirmaci, Z. Tang, S. Fasold, C. Neumann, T. Pertsch, A. Turchanin, I. Staude

ACS PHOTONICS, **2020**, 7, 1060-1066.

Plasmonic Metasurfaces Situated on Ultrathin Carbon Nanomembranes

Y. Denizhan Sirmaci,* Zian Tang, Stefan Fasold, Christof Neumann, Thomas Pertsch, Andrey Turchanin,* and Isabelle Staude

Cite This: *ACS Photonics* 2020, 7, 1060–1066

Read Online

ACCESS |

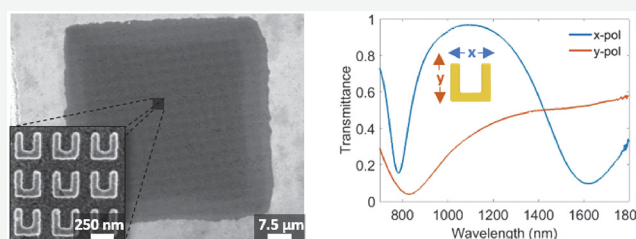
Metrics & More

Article Recommendations

Supporting Information

ABSTRACT: During the past decade, optical metasurfaces consisting of designed nanoresonators arranged in a planar fashion were successfully demonstrated to allow for the realization of a large variety of flat optical components. However, in common implementations of metasurfaces and metasurface-based devices, their flat nature is thwarted by the presence of a substrate of macroscopic thickness, which is needed to mechanically support the individual nanoresonators. Here, we demonstrate that carbon nanomembranes (CNMs) having nanoscale thicknesses can be used as a basis for arranging an array of plasmonic nanoresonators into a metamembrane, allowing for the realization of genuinely flat optical devices. CNMs belong to the family of two-dimensional materials, and their thicknesses and mechanical, chemical, and electrical properties can be tailored by the choice of the molecular precursors used for their fabrication. We experimentally fabricate gold split-ring-resonator (SRR) metasurfaces on top of a free-standing CNM, which has a thickness of only about 1 nm and shows a negligible interaction with the incident light field. For optical characterization of the fabricated SRR CNM metasurfaces, we perform linear-optical transmittance spectroscopy, revealing the typical resonance structure of an SRR metasurface. Furthermore, numerical calculations assuming free-standing SRR arrays are in good overall agreement with corresponding experimental transmittance spectra. We believe that our scheme offers a versatile solution for the realization of ultrathin, ultra lightweight metadevices, and may initiate various future research directions and applications including complex sensor technologies, conformal coating of complex topographies with functional metasurfaces, fast prototyping of multilayer metasurfaces, and studying the optical properties of effectively free-standing nanoparticles without the need for levitation schemes.

KEYWORDS: metasurfaces, carbon nanomembranes, two-dimensional materials, flat-optics, nanoplasmonics



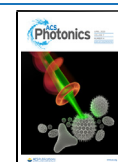
Optical metasurfaces, namely, two-dimensional arrangements of designed nanoresonators, opened a path to a new class of flat and compact optical components beyond conventional optics and have been at the limelight of nanophotonics research over the past few years.^{1,2} Metasurfaces are optical structures with a thickness of only a few tens to hundreds of nanometers that impose abrupt phase, amplitude, and/or polarization changes onto an incident light field.³ This is in contrast to conventional wavefront-shaping components that rely on the accumulation of phase delay during propagation through macroscopic distances inside a material. It is well-known that one can engineer the overall metasurface functionality by tailoring the optical responses of the individual nanoresonators via their size, shape, arrangement, and material composition as a function of in-plane position. As such, a large variety of optical components, including blazed gratings,^{4,5} lenses,⁶ color filters,⁷ vortex beam plates,⁸ holographic phase masks,^{9–12} quantum state analyzers,¹³ and many other functionalities, were demonstrated. Furthermore, resonant metasurfaces can exhibit strong near-field enhancement, which can be harnessed for the enhance-

ment of various light–matter interaction processes, such as spontaneous emission¹⁴ or nonlinear frequency generation.^{15,16} This is especially interesting for nanomaterials with a small optical cross-section such as 2D materials.^{17–19}

In practice, metasurfaces are almost exclusively fabricated on top of macroscopically thick supporting substrates, most typically a wafer made of glass or another material that is transparent in the relevant spectral range. However, these substrates have a pronounced effect on the optical response of the nanoresonators and can alter the properties of the metasurfaces undesirably in many ways. In particular, substrates typically induce a resonance red-shift, they break the mirror symmetry through the metasurface plane, and complicate the theoretical and numerical analysis of the optical

Received: January 15, 2020

Published: March 2, 2020



modes of the structure. Substrates can furthermore introduce new diffractive channels and they add additional interfaces, thereby increasing reflection losses. Considering also dielectric metasurfaces, they reduce the index contrast between the nanoresonators and their environment, which can impact the confinement of light in the nanoresonators. Finally and most importantly, macroscopically thick substrates degrade the 2D nature of the metasurfaces, which not only increases their weight but also poses limitations for certain application scenarios such as stacked, wrapped, rolled-up, and conformal metasurfaces. Consequently, a variety of platforms were already suggested in order to create, what we call metamembranes in the following, metasurface structures that are either free-standing or situated on as thin as possible substrates. For example, Ong et al. theoretically study the use of free-standing dielectric nanohole arrays for wavefront shaping in the mid-infrared spectral range.²⁰ Prämasing et al. experimentally demonstrate freestanding metasurfaces operating at optical frequencies having a thickness of 40 nm.²¹ In the latter work, fabrication is performed by the milling of nanovoids in a carbon transmission electron microscopy membrane using a focused ion beam, followed by thermal evaporation of gold and plasma ashing of the carbon membrane. Note, however, that approaches based on milling of nanoholes or voids into a membrane are limited to connected structures to preserve the structural integrity. As such, this approach does not allow for the realization of metamembranes composed of individual free-standing nanoresonators, such as metallic split-ring resonators. At THz frequencies, free-standing polyimide membranes with a thickness of several to tens of micrometers have been used as substrates to create resonant metamaterials.^{22,23} While this platform offers a large design freedom in the shape of the nanoresonators, it cannot be scaled to optical frequencies due to the relatively large thickness of the polyimide membranes, which, while thin with respect to THz wavelengths, appear macroscopic for visible and near-infrared light and are thus sufficient to introduce most of the mentioned detrimental substrate effects. In another approach, THz metamaterials consisting of S-shaped gold strings suspended in free space by means of window frames were micromanufactured via a lithography-based process.²⁴ However, this approach is also limited to connected metamaterial architectures. Also, scaling of this approach to optical frequencies was not demonstrated and will be limited by the larger structural fragility as the structure dimensions are reduced. Altogether, a method for the realization of plasmonic metamembranes, which preserves the design freedom available for structures supported by macroscopically thick substrates and in particular allows for disconnected structures such as particle arrays, is still missing.

Here we demonstrate, for the first time, optically resonant plasmonic metamembranes using carbon nanomembranes (CNMs)²⁵ as substrate material having only monomolecular thickness. The CNMs are chosen as a substrate because of their ultrasmall thickness, high mechanical stability and their negligible interaction with light. For our proof-of-concept demonstration, we choose a metamembrane consisting of square arrays of gold split-ring resonators (SRRs)^{26–28} with resonance frequencies in the near-infrared spectral range as a well-understood, prototypical plasmonic metasurface design. Figure 1 shows a conceptual image of the realized metamembrane. CNMs are prepared by low-energy electron-induced cross-linking of aromatic self-assembled monolayers

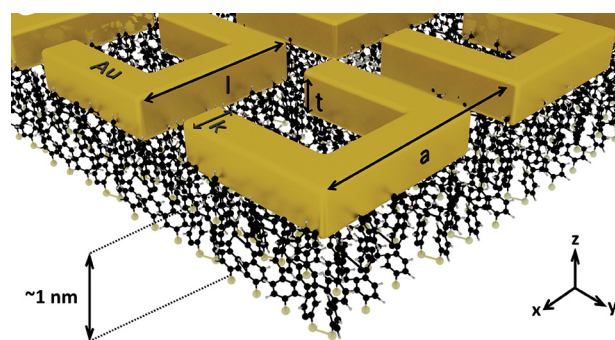


Figure 1. An artist's view of the fabricated gold split-ring resonator (SRR) array situated on a carbon nanomembrane (CNM; not to scale). The SRR dimensions are $l = 260$ nm, $t = 45$ nm, $a = 350$ nm, and $k = 75$ nm.

(SAMs). The membrane parameters can be precisely controlled by the fabrication process. Most importantly, by choice of the precursor molecule the thickness of the membrane can be tuned between 0.5 and 3 nm.²⁵ Their high mechanical stability enables the preparation of large free-standing areas up to several hundred micrometers in diameter.^{25,29} Owing to their small thickness,²⁹ high mechanical strength,³⁰ dielectric properties,^{31,32} and high temperature stability,^{31,33,34} CNMs were previously proposed for applications such as gas and liquid filtration,³⁵ TEM supports,³⁶ functionalized membranes,³⁷ and nondestructive chemical functionalization of graphene field-effect transistors.³⁸ Furthermore, we found very weak light–matter interaction of CNMs, as evidenced by a very high broadband linear-optical transmission (above 99%, see Figure 2d). Altogether, these properties make CNMs highly suitable for the realization of metamembranes in their fundamental thickness limit.

RESULTS AND DISCUSSION

For the experimental realization of the metamembrane, we developed a three-step fabrication scheme consisting of (1) the preparation of the CNMs, (2) the fabrication of the metasurface via an electron-beam lithography (EBL)-based process, and (3) the transfer of the metamembrane onto a TEM grid. The steps of the fabrication scheme are illustrated in Figure 2. First, (1) for preparation of the CNMs, silicon substrates coated with a 30 nm thick gold layer (Georg Albert PVD) were immersed in a 0.1 mM dimethylformamide solution of the molecular precursor 1,1',4',1''-terphenyl-4-thiol (TPT, 97% Sigma-Aldrich) for 24 h at 60 °C to form a self-assembled monolayer (SAM).²⁹ TPT was chosen as molecular precursor for the CNM preparation as it forms densely packed membranes with sufficient mechanical stability³⁰ to support the plasmonic SRRs. Figure 2b shows the structure of the precursor molecules. Next, the SAM was cross-linked into CNM in a high vacuum chamber ($<5 \times 10^{-8}$ mbar) using a low energy electron gun (Specs) with an electron energy of 100 eV and a dose of 50 mC/cm².³⁹ The described synthetic procedure results in a mechanically stable CNM of a monomolecular thickness of 1.2 nm²⁹ (see Figure 2a(i) and Supporting Information, Figure S1 and pp 2–3 for details). The fabricated CNMs show short-range ordered molecular structures due to the cross-linking.²⁵ Its schematic representation is given in Figure 2c. The successful CNM preparation was controlled using X-ray photoelectron spectroscopy (XPS). High-resolution XP C 1s and S 2p spectra of

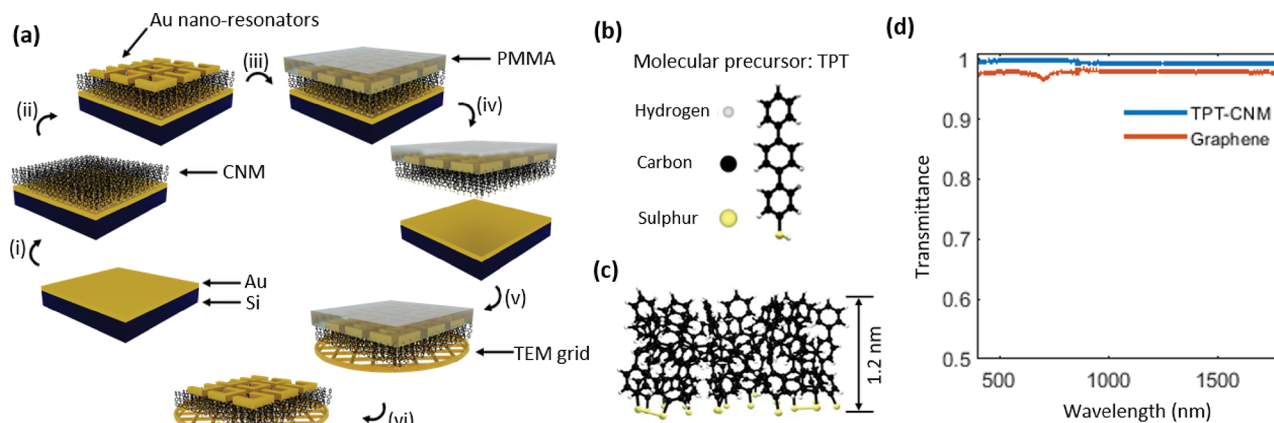


Figure 2. (a) Steps performed for fabrication of the plasmonic metamembranes (not to a scale). As the first step, starting from a gold-coated silicon substrate (i), a 1.2 nm thick TPT-CNM is synthesized via self-assembly and electron-beam irradiation on top of the gold layer (ii). Next, the plasmonic SRR array is fabricated using a standard electron-beam lithography based process (iii). Then, electrochemical delamination in combination with a PMMA-assisted wet transfer technique is used to detach the CNM as well as the SRR array situated on top of it from the gold-coated silicon substrate (iv) and to transfer it onto a TEM grid with 45 μm square openings (vi). Finally, the PMMA is removed by dissolving it in acetone (vi). A critical point dryer is used to protect the free-standing areas of the metamembrane from breaking. (b) Molecular structure of the employed precursor used for the CNM synthesis. (c) Schematic representation of the molecular structure of the TPT-CNM used as the metasurface substrate. (d) Measured linear-optical transmittance spectra of the TPT-CNM (blue) and graphene (red).

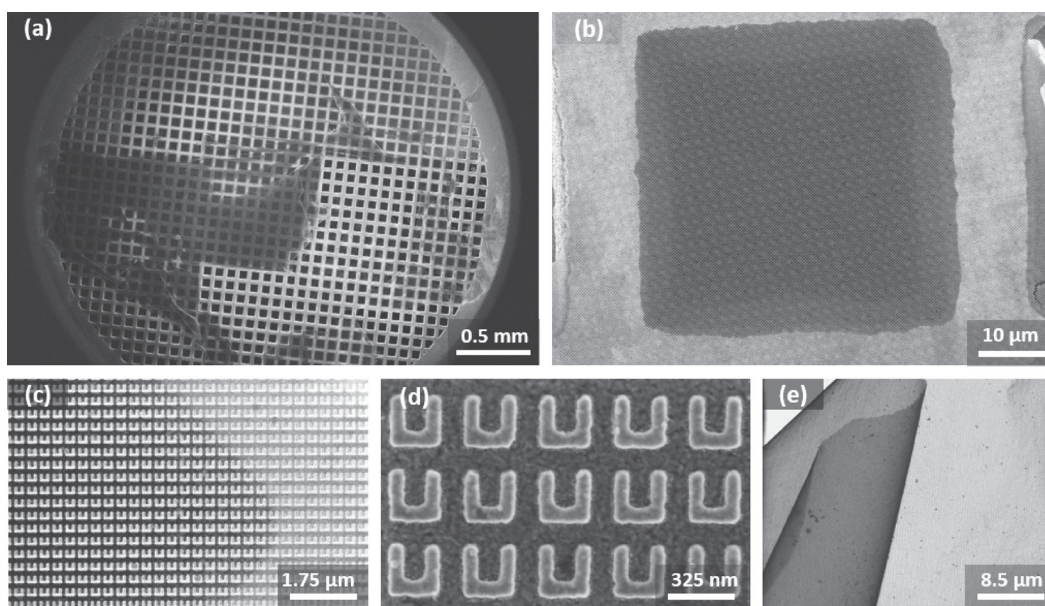


Figure 3. Scanning-electron micrographs (SEMs) of the fabricated SRR metamembranes at different magnifications. (a) Overview SEM of the TEM grid covered by the metamembranes (dark areas). (b) Close-up of one of the TEM-grid openings with metamembrane. (c) Magnified view of the top left corner in (b). The right (brighter) part of the image shows a part of the membrane that is supported by the TEM grid, whereas the left (darker) part is completely free-standing. Note that the image is rotated with respect to (b) because of the arbitrary orientation of the SRRs with respect to the TEM grid. (d) Close-up of the fabricated square array of gold SRRs. (e) SEM of a broken, partly rolled-up metamembrane.

the CNM formed after electron irradiation on gold are presented in Figure S1 (see Supporting Information).

As a second step (2), after the preparation of the CNM on top of a silicon–gold substrate as described above, a square array of U-shaped nano-resonators was fabricated using an EBL-based process. To this end, the sample was spin-coated with a bilayer electron-beam resist (AR-P 617 and AR-P 6200 (CSAR 62)). The exposure was performed using a variable-shaped electron-beam lithography system (Vistec SB 350). We exposed several SRR arrays, each with a large footprint of 1 × 1 mm. After development in AR600–546 (40 s) and 1:1 MIBK/IPA (20 s) the samples were covered by 3 nm titanium as

adhesion promoter and 45 nm gold by electron-beam evaporation.⁴⁰ Finally, a standard lift-off procedure was performed. Overall, the second step results in arrays of gold SRRs situated on the CNM which at this stage is still on top of a gold-coated silicon wafer (see Figure 2a(ii)).

During the third and last step (3), electrochemical delamination was used to detach the CNM holding the metasurface from the supporting substrate. For this purpose, a sacrificial PMMA layer with a thickness of 70 nm was spin-coated onto the metasurface sample (see Figure 2a (iii)). Next, the delamination procedure was performed by immersing the sample into NaOH (0.2 mol/L) and applying a voltage of 2–3

V to the solution, as described in the literature⁴¹ (see Figure 2(iv)). After rinsing the sample with water, which now consisted of the metamembrane attached to the PMMA layer, it was transferred onto standard transmission-electron microscope (TEM) grids (Plano) with square openings of $45 \times 45 \mu\text{m}^2$ (see Figure 2a (v)). Finally, the PMMA was dissolved in acetone and the sample was dried in a critical point dryer to avoid rupture of the membranes during solvent evaporation (see Figure 2a (vi)). Details of the transfer procedure are described in ref 42 as well as in the Supporting Information, Part 2. Altogether, the process resulted in free-standing SRR metamembranes stretched over the openings of the TEM grids. The optical measurements were performed upon these free-standing membranes.

Using the same procedure but leaving out the second step, we also fabricated reference samples consisting of TPT-CNM on a glass substrate. To assess the suitability of the optical properties of the fabricated CNM as ultrathin metasurface substrates, we measured the linear-optical transmittance spectra of these reference samples in the visible and near-infrared region. To this end, we used a PerkinElmer Lambda 900 UV–vis–NIR spectrometer. These results are shown in Figure 2d. These results reveal that CNMs are highly transparent, with a transmittance exceeding 99% over the entire measured wavelength range. To verify the validity of our measurements considering the very weak interaction of the CNMs with light, we also measured the transmittance of CVD-grown graphene samples on identical glass substrates as a reference, yielding a value of 97.7% in accord with the literature.⁴³ Additionally, we measured the transmittance spectra of another type of CNM (1,1'-biphenyl-4-thiol (BPT)) (see Supporting Information, Figure S2), also yielding high transmission values over the entire measured spectral range. Altogether, we conclude that CNMs are a promising platform for ultrathin optical elements due to their high optical transparency and mechanical stability.

To confirm the successful preparation of free-standing areas of CNM-supported metasurfaces, we imaged the resulting samples using scanning electron microscopy (SEM). Corresponding top-view SEM images with varying magnifications are displayed in Figure 3. Figure 3a shows an overview image of the TEM grid, which is partly covered by the SRR metamembranes. Figure 3b shows a close-up of one of the TEM-grid openings with a metamembrane. A magnified view of the top-left corner of Figure 3b is displayed in Figure 3c. The contrast difference between the free-standing and the grid supported areas is clearly visible. Zooming in even further, Figure 3d shows a close-up of the fabricated gold SRRs. Finally, to more clearly illustrate the extremely thin nature of the CNM substrate, Figure 3e shows an SEM image of a broken and rolled metamembrane.

To assess the optical quality of the fabricated SRR metamembranes, we measured their linear-optical transmittance spectra using a Bruker 80v Fourier Transform InfraRed (FTIR) spectrometer attached to a Hyperion 2000 microscope. To cover the entire relevant spectral range spanning from visible to near-infrared wavelengths, we combine measurements taken with a Si and an InGaAs detector. A knife-edge aperture was used to confine the measurement area to a $30 \times 30 \mu\text{m}^2$ window within the free-standing areas of the membranes, that is, the openings of the TEM grid. Note that the employed 15 \times reflective microscope objectives (NA = 0.4) only support illumination/collection

angles in the range of 12–23.6°. A linear polarizer is introduced in the illumination beam path to selectively measure the metamembrane's optical response along the two different lattice directions of the SRR metamembrane. As a result of the wet transfer process employed during fabrication to place the metamembranes on the TEM grid, the orientation of the SRRs with respect to the borders of the TEM-grid openings is not known a priori. To identify the structure orientation, we performed a series of transmittance measurements for a variation of the polarization angle of the incident light from 0–90° in 18° steps (see Supporting Information, Figure S3). The characteristic resonance features observed in the measured spectra provide a clear indication of the orientation of the SRRs (see Supporting Information, Figure S3). Nevertheless, small deviations from perfect polarization adjustment in the excitation cannot be fully excluded. Experimentally measured transmittance spectra for the incident light polarized in the direction across the SRR slit (*x*-polarization) and perpendicular to it (*y*-polarization) are shown in Figure 4a. For *x*-polarization, in accord with earlier

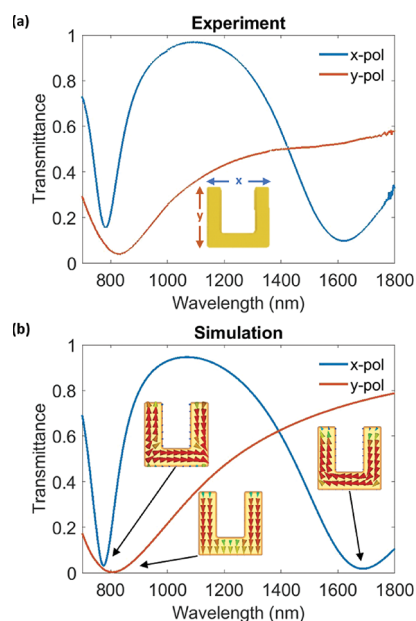


Figure 4. (a) Measured and (b) numerically calculated normal incidence linear-optical transmittance spectra for *x*-polarized (blue) and *y*-polarized (red) light. In (b), calculated surface current distributions at the three different resonances are indicated by the corresponding insets.

literature,²⁶ we observe two pronounced transmission minima, which are located at 1619 and 780 nm wavelength. For *y*-polarization, a single transmission minimum is observed at 820 nm wavelength.

To compare our experimental results with theory, we performed numerical finite-integral frequency-domain calculations using the commercial software package CST Microwave Studio and sample parameters taken from SEM images ($l = 260 \text{ nm}$, $t = 45 \text{ nm}$, $a = 350 \text{ nm}$, and $k = 75 \text{ nm}$; see Figure 1 for definitions). We considered linearly polarized normal-incidence plane wave illumination and unit-cell boundary conditions. For the dispersive optical properties of gold, we used experimental values from Johnson and Christy.⁴⁴ Considering the experimentally confirmed weak interaction of the CNMs with light, we neglected the presence of the

CNMs in our calculations, that is, the SRR arrays were modeled to be suspended in vacuum. In order to justify this assumption, we have compared the calculated transmittance spectra without any substrate with a matching calculation, including a 1.2 nm thin dielectric substrate having a refractive index of up to 1.5. This value exceeds the TPT-CNM refractive index estimated from the transmission spectra. We found a maximum resonance shift of 4.2 nm, which occurred for the fundamental magnetic resonance and which is negligible compared to the spectral width of the resonance. The numerically calculated transmittance spectra for the two perpendicular linear polarizations of the incident light are shown in Figure 4b. Good overall agreement with corresponding experimental data is obtained. We note that the spectral position of the lowest-order resonance occurs at a slightly higher wavelength in the calculated spectra as compared to the experimental ones. The small differences observed between calculated and measured transmittance spectra can be attributed to the non-normal incidence conditions present in the experiment, sample imperfections such as roughness and small deviations of the geometrical structure, as well as possible deviations of the CNM morphology from a perfectly planar membrane caused by the weight of the nanostructures. In order to gain further insight into the nature of the observed transmission minima, we also calculated the local surface currents excited in the SRRs at the three resonance wavelengths. These results are displayed as insets in Figure 4b. As expected, the fundamental mode of the SRR metasurface,²⁸ which occurs at 1685 nm for *x*-polarized excitation, is characterized by a circulating current along the entire SRR loop, giving rise to a magnetic dipole moment out of the SRR plane. The second-order mode, which appears for *y*-polarized incident light at 805 nm, is an electric-dipole dominated mode characterized by in-phase currents along the two legs of the SRR. Finally, the third-order resonance observed at 775 nm for *x*-polarized excitation is an electric quadrupolar dominated mode with out-of-phase currents in the SRR legs.

CONCLUSION AND OUTLOOK

In conclusion, we have experimentally demonstrated a new scheme that allows for the realization of ultrathin plasmonic metamembranes operating at near-infrared frequencies, a geometry not accessible by any existing fabrication method. This is achieved by using a carbon nanomembrane (CNM) of only about one nanometer thickness as a substrate for fabrication of a plasmonic metasurface. As a prototypical plasmonic metasurface structure, we have realized quasi free-standing square arrays of gold split-ring resonators (SRRs). Note, however, that our approach essentially offers the full design freedom of electron-beam lithography-based approaches to realize any nonconnected or connected pattern and is not limited to the chosen exemplary design. Transmittance spectra of the fabricated free-standing metamembranes reveal high-quality resonances exhibiting the well-known resonance structure of SRR metasurfaces. Numerical calculations, which assume the SRRs to be fully free-standing, are in good agreement with experimental data. Our demonstrated approach offers important new opportunities for the fabrication of previously inaccessible, complex metasurface and metamaterial architectures. Specifically, owing to their ultrathin nature, the metamembranes are ideally suited for stacking of several metasurfaces layers, thus, offering a new

route for the fabrication of multilayer⁴⁵ or chiral^{46–48} metasurfaces or even approaching bulk metamaterials, without the need for time-consuming and delicate multistep electron-beam lithography procedures. As such, the metasurface membranes are also highly compatible with the concept of van der Waals heterostructures,⁴⁹ namely, structures consisting of two or more two-dimensional materials like graphene or two-dimensional transition metal dichalcogenides stacked on top of each other. The possibility to include ultrathin plasmonic metasurfaces in such stacks of two-dimensional materials may add layers with new and enhanced functionalities to the toolbox. Apart from planar stacking, the metasurface membranes also show large potential for their use in rolled-up metamaterials,⁵⁰ offering lateral nanostructuring and dense wrapping as new degrees of freedom. Finally, the metasurface membranes may also find applications as conformal metasurface coatings⁵¹ of complicated topographies. This way, they could, for example, serve to decouple topographic and optical properties of surfaces.

ASSOCIATED CONTENT

Supporting Information

The Supporting Information is available free of charge at <https://pubs.acs.org/doi/10.1021/acsphotonics.0c00073>.

- (1) X-ray photoelectron spectroscopy (XPS) of fabricated the CNM (Figure S1).
- (2) Detailed description of the wet transfer procedure of CNMs.
- (3) Measured linear optical transmittance spectra of two types of CNMs and their comparison with corresponding spectra of graphene (Figure S2).
- (4) Experimental linear-optical transmittance spectra of the metamembranes for a systematic variation of the polarization direction of the incident light (Figure S3) (PDF)

AUTHOR INFORMATION

Corresponding Authors

Y. Denizhan Sirmaci – Institute of Applied Physics and Abbe Center of Photonics, Friedrich Schiller University Jena, 07745 Jena, Germany; orcid.org/0000-0003-2357-3920;
Email: yunus.denizhan.sirmaci@uni-jena.de

Andrey Turchanin – Abbe Center of Photonics and Institute of Physical Chemistry, Friedrich Schiller University Jena, 07745 Jena, Germany; Jena Center for Soft Matter (JCSM), 07743 Jena, Germany; orcid.org/0000-0003-2388-1042;
Email: andrey.turchanin@uni-jena.de

Authors

Zian Tang – Institute of Physical Chemistry, Friedrich Schiller University Jena, 07743 Jena, Germany

Stefan Fasold – Institute of Applied Physics and Abbe Center of Photonics, Friedrich Schiller University Jena, 07745 Jena, Germany; orcid.org/0000-0001-5330-2465

Christof Neumann – Institute of Physical Chemistry, Friedrich Schiller University Jena, 07743 Jena, Germany

Thomas Pertsch – Institute of Applied Physics and Abbe Center of Photonics, Friedrich Schiller University Jena, 07745 Jena, Germany; Fraunhofer Institute for Applied Optics and Precision Engineering IOF, 07745 Jena, Germany

Isabelle Staude – Institute of Applied Physics and Abbe Center of Photonics, Friedrich Schiller University Jena, 07745 Jena, Germany; orcid.org/0000-0001-8021-572X

Complete contact information is available at:

<https://pubs.acs.org/10.1021/acsp Photonics.0c00073>

Notes

The authors declare no competing financial interest.

ACKNOWLEDGMENTS

We thank Waltraud Gräf, Holger Schmidt, and Detlef Schelle for support in the fabrication process. This work was funded by the German Research Foundation DFG (CRC 1375 NOA, IRTG 2101, STA 1426/2-1, TU149/5-1, and TU149/8-2) and by the German Federal Ministry for Education and Research (03ZZ0451). Financial support by the Thuringian State Government within its ProExcellence initiative (ACP²⁰²⁰) is also gratefully acknowledged.

REFERENCES

- (1) Yu, N.; Capasso, F. Flat optics with designer metasurfaces. *Nat. Mater.* **2014**, *13*, 139–150.
- (2) Meinzer, N.; Barnes, W. L.; Hooper, I. R. Plasmonic meta-atoms and metasurfaces. *Nat. Photonics* **2014**, *8*, 889–898.
- (3) Aieta, F.; Genevet, P.; Yu, N.; Kats, M. A.; Gaburro, Z.; Capasso, F. Out-of-Plane Reflection and Refraction of Light by Anisotropic Optical Antenna Metasurfaces with Phase Discontinuities. *Nano Lett.* **2012**, *12*, 1702–1706.
- (4) Lalanne, P.; Astilean, S.; Chavel, P.; Cambil, E.; Launois, H. Blazed binary subwavelength gratings with efficiencies larger than those of conventional échellette gratings. *Opt. Lett.* **1998**, *23*, 1081–1083.
- (5) Yu, N.; Genevet, P.; Kats, M. A.; Aieta, F.; Tetienne, J.-P.; Capasso, F.; Gaburro, Z. Light Propagation with Phase Discontinuities: Generalized Laws of Reflection and Refraction. *Science* **2011**, *334*, 333–337.
- (6) Lin, D.; Fan, P.; Hasman, E.; Brongersma, M. L. Dielectric gradient metasurface optical elements. *Science* **2014**, *345*, 298–302.
- (7) Nagasaki, Y.; Hotta, I.; Suzuki, M.; Takahara, J. Metal-Masked Mie-Resonant Full-Color Printing for Achieving Free-Space Resolution Limit. *ACS Photonics* **2018**, *5*, 3849–3855.
- (8) Chong, K. E.; Staude, I.; James, A.; Dominguez, J.; Liu, S.; Campione, S.; Subramania, G. S.; Luk, T. S.; Decker, M.; Neshev, D. N.; Brener, I.; Kivshar, Y. S. Polarization-Independent Silicon Metadevices for Efficient Optical Wavefront Control. *Nano Lett.* **2015**, *15*, 5369–5374.
- (9) Zheng, G.; Mühlenbernd, H.; Kenney, M.; Li, G.; Zentgraf, T.; Zhang, S. Metasurface holograms reaching 80% efficiency. *Nat. Nanotechnol.* **2015**, *10*, 308–312.
- (10) Arbabi, A.; Horie, Y.; Bagheri, M.; Faraon, A. Dielectric metasurfaces for complete control of phase and polarization with subwavelength spatial resolution and high transmission. *Nat. Nanotechnol.* **2015**, *10*, 937–943.
- (11) Chong, K. E.; Wang, L.; Staude, I.; James, A. R.; Dominguez, J.; Liu, S.; Subramania, G. S.; Decker, M.; Neshev, D. N.; Brener, I.; Kivshar, Y. S. Efficient Polarization-Insensitive Complex Wavefront Control Using Huygens' Metasurfaces Based on Dielectric Resonant Meta-atoms. *ACS Photonics* **2016**, *3*, 514–519.
- (12) Jin, C.; Afsharnia, M.; Berlich, R.; Fasold, S.; Zou, C.; Arslan, D.; Staude, I.; Pertsch, T.; Setzpfandt, F. Dielectric metasurfaces for distance measurements and three-dimensional imaging. *Advanced Photonics* **2019**, *1*, 1–9.
- (13) Wang, K.; Titchener, J. G.; Kruk, S. S.; Xu, L.; Chung, H.-P.; Parry, M.; Kravchenko, I. I.; Chen, Y.-H.; Solntsev, A. S.; Kivshar, Y. S.; Neshev, D. N.; Sukhorukov, A. A. Quantum metasurface for multiphoton interference and state reconstruction. *Science* **2018**, *361*, 1104–1108.
- (14) Vaskin, A.; Kolkowski, R.; Koenderink, A. F.; Staude, I. Light-emitting metasurfaces. *Nanophotonics* **2019**, *8*, 1151–1198.
- (15) Shcherbakov, M. R.; Neshev, D. N.; Hopkins, B.; Shorokhov, A. S.; Staude, I.; Melik-Gaykazyan, E. V.; Decker, M.; Ezhov, A. A.; Miroshnichenko, A. E.; Brener, I.; Fedyanin, A. A.; Kivshar, Y. S. Enhanced third-harmonic generation in silicon nanoparticles driven by magnetic response. *Nano Lett.* **2014**, *14*, 6488–6492.
- (16) Li, G.; Zhang, S.; Zentgraf, T. Nonlinear photonic metasurfaces. *Nat. Rev. Mater.* **2017**, *2*, 523.
- (17) Butun, S.; Tongay, S.; Aydin, K. Enhanced Light Emission from Large-Area Monolayer MoS₂ Using Plasmonic Nanodisc Arrays. *Nano Lett.* **2015**, *15*, 2700–2704.
- (18) Bucher, T.; Vaskin, A.; Mupparapu, R.; Löchner, F. J. F.; George, A.; Chong, K. E.; Fasold, S.; Neumann, C.; Choi, D.-Y.; Eilenberger, F.; Setzpfandt, F.; Kivshar, Y. S.; Pertsch, T.; Turchanin, A.; Staude, I. Tailoring Photoluminescence from MoS₂ Monolayers by Mie-Resonant Metasurfaces. *ACS Photonics* **2019**, *6*, 1002–1009.
- (19) Cotrufo, M.; Sun, L.; Choi, J.; Alu, A.; Li, X. Enhancing functionalities of atomically thin semiconductors with plasmonic nanostructures. *Nanophotonics* **2019**, *8* (4), 577–598.
- (20) Ong, J. R.; Chu, H. S.; Chen, V. H.; Zhu, A. Y.; Genevet, P. Freestanding dielectric nanohole array metasurface for mid-infrared wavelength applications. *Opt. Lett.* **2017**, *42*, 2639.
- (21) Prämassing, M.; Leuteritz, T.; Schill, H. J.; Fassbender, A.; Irsen, S.; Linden, S. Freestanding metasurfaces for optical frequencies. *Opt. Lett.* **2019**, *44*, 2105–2108.
- (22) Tao, H.; Strikwerda, A. C.; Fan, K.; Bingham, C. M.; Padilla, W. J.; Zhang, X.; Averitt, R. D. Terahertz metamaterials on free-standing highly-flexible polyimide substrates. *J. Phys. D: Appl. Phys.* **2008**, *41*, 232004.
- (23) Fan, K.; Strikwerda, A. C.; Tao, H.; Zhang, X.; Averitt, R. D. Stand-up magnetic metamaterials at terahertz frequencies. *Opt. Express* **2011**, *19*, 12619.
- (24) Moser, H. O.; Kong, J. A.; Jian, L. K.; Chen, H. S.; Liu, G.; Bahou, M.; Kalaiselvi, S. M. P.; Maniam, S. M.; Cheng, X. X.; Wu, B. I.; Gu, P. D.; Chen, A.; Heussler, S. P.; bin Mahmood, S.; Wen, L. Free-standing THz electromagnetic metamaterials. *Opt. Express* **2008**, *16*, 13773.
- (25) Turchanin, A.; Götzhäuser, A. Carbon Nanomembranes. *Adv. Mater.* **2016**, *28*, 6075–6103.
- (26) Linden, S.; Enkrich, C.; Wegener, M.; Zhou, J.; Koschny, T.; Soukoulis, C. M. Magnetic Response of Metamaterials at 100 Terahertz. *Science* **2004**, *306*, 1351–1353.
- (27) Enkrich, C.; Wegener, M.; Linden, S.; Burger, S.; Zschiedrich, L.; Schmidt, F.; Zhou, J. F.; Koschny, T.; Soukoulis, C. M. Magnetic Metamaterials at Telecommunication and Visible Frequencies. *Phys. Rev. Lett.* **2005**, *95*, 203901.
- (28) Rockstuhl, C.; Lederer, F.; Etrich, C.; Zentgraf, T.; Kuhl, J.; Giessen, H. On the reinterpretation of resonances in split-ring-resonators at normal incidence. *Opt. Express* **2006**, *14*, 8827.
- (29) Angelova, P.; et al. A universal scheme to convert aromatic molecular monolayers into functional carbon nanomembranes. *ACS Nano* **2013**, *7*, 6489–6497.
- (30) Zhang, X.; Neumann, C.; Angelova, P.; Beyer, A.; Götzhäuser, A. Tailoring the Mechanics of Ultrathin Carbon Nanomembranes by Molecular Design. *Langmuir* **2014**, *30*, 8221–8227.
- (31) Turchanin, A.; Beyer, A.; Nottbohm, C. T.; Zhang, X.; Stosch, R.; Sologubenko, A.; Mayer, J.; Hinze, P.; Weimann, T.; Götzhäuser, A. One Nanometer Thin Carbon Nanosheets with Tunable Conductivity and Stiffness. *Adv. Mater.* **2009**, *21*, 1233–1237.
- (32) Zhang, X.; Marschewski, E.; Penner, P.; Beyer, A.; Götzhäuser, A. Investigation of electronic transport through ultrathin carbon nanomembrane junctions by conductive probe atomic force microscopy and eutectic Ga–In top contacts. *J. Appl. Phys.* **2017**, *122*, 055103.
- (33) Turchanin, A.; El-Desawy, M.; Götzhäuser, A. High thermal stability of cross-linked aromatic self-assembled monolayers: Nanopatterning via selective thermal desorption. *Appl. Phys. Lett.* **2007**, *90*, 053102.
- (34) Turchanin, A.; Käfer, D.; El-Desawy, M.; Wöll, C.; Witte, G.; Götzhäuser, A. Molecular Mechanisms of Electron-Induced Cross-Linking in Aromatic SAMs. *Langmuir* **2009**, *25*, 7342–7352.

(35) Yang, Y.; Dementyev, P.; Biere, N.; Emmrich, D.; Stohmann, P.; Korzetz, R.; Zhang, X.; Beyer, A.; Koch, S.; Anselmetti, D.; Götzhäuser, A. Rapid Water Permeation Through Carbon Nanomembranes with Sub-Nanometer Channels. *ACS Nano* **2018**, *12*, 4695–4701.

(36) Rhinow, D.; Büenfeld, M.; Weber, N. E.; Beyer, A.; Götzhäuser, A.; Kühlbrandt, W.; Hampp, N.; Turchanin, A. Energy-filtered transmission electron microscopy of biological samples on highly transparent carbon nanomembranes. *Ultramicroscopy* **2011**, *111*, 342–349.

(37) Zheng, Z.; Zhang, X.; Neumann, C.; Emmrich, D.; Winter, A.; Vieker, H.; Liu, W.; Lensen, M.; Götzhäuser, A.; Turchanin, A. Hybrid van der Waals heterostructures of zero-dimensional and two-dimensional materials. *Nanoscale* **2015**, *7*, 13393–13397.

(38) Woszczyna, M.; Winter, A.; Grothe, M.; Willunat, A.; Wundrack, S.; Stosch, R.; Weimann, T.; Ahlers, F.; Turchanin, A. All-Carbon Vertical van der Waals Heterostructures: Non-destructive Functionalization of Graphene for Electronic Applications. *Adv. Mater.* **2014**, *26*, 4831–4837.

(39) Turchanin, A. Synthesis of Molecular 2D Materials via Low-energy Electron Induced Chemical Reactions. *Chimia* **2019**, *73*, 473–479.

(40) Beyer, A.; Turchanin, A.; Nottbohm, C. T.; Mellech, N.; Schnietz, M.; Götzhäuser, A. Fabrication of metal patterns on freestanding graphenoid nanomembranes. *J. Vac. Sci. Technol., B: Nanotechnol. Microelectron.: Mater., Process., Meas., Phenom.* **2010**, *28*, C6D5–C6D10.

(41) Wang, Y.; Zheng, Y.; Xu, X.; Dubuisson, E.; Bao, Q.; Lu, J.; Loh, K. P. Electrochemical Delamination of CVD-Grown Graphene Film: Toward the Recyclable Use of Copper Catalyst. *ACS Nano* **2011**, *5*, 9927–9933.

(42) Winter, A.; Ekinci, Y.; Götzhäuser, A.; Turchanin, A. Freestanding carbon nanomembranes and graphene monolayers nanopatterned via EUV interference lithography. *2D Mater.* **2019**, *6*, 021002.

(43) Nair, R. R.; Blake, P.; Grigorenko, A. N.; Novoselov, K. S.; Booth, T. J.; Stauber, T.; Peres, N. M. R.; Geim, A. K. Fine Structure Constant Defines Visual Transparency of Graphene. *Science* **2008**, *320*, 1308–1308.

(44) Johnson, P. B.; Christy, R. W. Optical Constants of the Noble Metals. *Phys. Rev. B* **1972**, *6*, 4370–4379.

(45) Menzel, C.; Sperrhake, J.; Pertsch, T. Efficient treatment of stacked metasurfaces for optimizing and enhancing the range of accessible optical functionalities. *Phys. Rev. A: At, Mol., Opt. Phys.* **2016**, *93*, 063832.

(46) Decker, M.; Ruther, M.; Kriegler, C. E.; Zhou, J.; Soukoulis, C. M.; Linden, S.; Wegener, M. Strong optical activity from twisted-cross photonic metamaterials. *Opt. Lett.* **2009**, *34*, 2501–2503.

(47) Liu, N.; Liu, H.; Zhu, S.; Giessen, H. Stereometamaterials. *Nat. Photonics* **2009**, *3*, 157–162.

(48) Fasold, S.; Linß, S.; Kawde, T.; Falkner, M.; Decker, M.; Pertsch, T.; Staude, I. Disorder-Enabled Pure Chirality in Bilayer Plasmonic Metasurfaces. *ACS Photonics* **2018**, *5*, 1773–1778.

(49) Geim, A. K.; Grigorieva, I. V. Van der Waals heterostructures. *Nature* **2013**, *499*, 419–425.

(50) Smith, E. J.; Liu, Z.; Mei, Y. F.; Schmidt, O. G. System investigation of a rolled-up metamaterial optical hyperlens structure. *Appl. Phys. Lett.* **2009**, *95*, 083104.

(51) Kamali, S. M.; Arbabi, A.; Arbabi, E.; Horie, Y.; Faraon, A. Decoupling optical function and geometrical form using conformal flexible dielectric metasurfaces. *Nat. Commun.* **2016**, *7*, 11618.

P4. Smart molecular nanosheets for advanced preparation of biological samples in electron cryo-microscopy

J. Scherr, Z. Tang, M. Küllmer, S. Balsler, A. Winter, K. Parey, A. Rittner, M. Grininger, V.

Zickermann, W. Kühlbrandt, D. Rhinow, A. Terfort, A. Turchanin

Submitted to ACS NANO (under review).

This document is confidential and is proprietary to the American Chemical Society and its authors. Do not copy or disclose without written permission. If you have received this item in error, notify the sender and delete all copies.

Smart molecular nanosheets for advanced preparation of biological samples in electron cryo-microscopy

Journal:	ACS Nano
Manuscript ID	Draft
Manuscript Type:	Article
Date Submitted by the Author:	n/a
Complete List of Authors:	Scherr, Julian; University of Frankfurt Tang, Zian; Friedrich Schiller University Jena Küllmer, Maria; Friedrich Schiller University Jena Balsler, Sebastian; University of Frankfurt Scholz, Alexander; University of Frankfurt Winter, Andreas; Friedrich Schiller University Jena Parey, Kristian; Max Planck Institute of Biophysics Rittner, Alexander; University of Frankfurt Grininger, Martin; Goethe-Universität Frankfurt am Main, Institute of Organic Chemistry and Chemical Biology Zickermann, Volker; Goethe-Universität Frankfurt am Main Institut für Biochemie II, Rhinow, Daniel; Max Planck Institute of Biophysics Terfort, Andreas; Goethe-Universität Frankfurt am Main, Turchanin, Andrey; Friedrich-Schiller-Universität Jena, Institute of Physical Chemistry

SCHOLARONE™
Manuscripts

1
2
3 **Smart molecular nanosheets for advanced preparation**
4 **of biological samples in electron cryo-microscopy**
5
6
7

8 Julian Scherr^{1,+}, Zian Tang^{2,+}, Maria Küllmer², Sebastian Balsler¹, Alexander Stefan
9 Scholz¹, Andreas Winter², Kristian Parey³, Alexander Rittner⁴, Martin Grininger⁴,
10 Volker Zickermann⁵, Daniel Rhinow^{3*}, Andreas Terfort^{1*}, Andrey Turchanin^{2*}
11
12
13
14

15 *¹University of Frankfurt, Department of Chemistry,
16 Max-von-Laue-Str. 7, 60438 Frankfurt, Germany*

17
18 *²Friedrich Schiller University Jena, Institute of Physical Chemistry,
19 Lessingstr. 10, 07743 Jena, Germany*

20
21
22 *³Max Planck Institute of Biophysics, Department of Structural Biology,
23 Max-von-Laue-Str. 3, 60438 Frankfurt, Germany*

24
25
26 *⁴Institute of Organic Chemistry and Chemical Biology,
27 Buchmann Institute for Molecular Life Sciences, University of Frankfurt,
28 Max-von-Laue-Str. 15, 60438 Frankfurt, Germany*

29
30
31 *⁵University of Frankfurt, Institute of Biochemistry II, Medical School,
32 Max-von-Laue-Str. 9, 60438 Frankfurt, Germany*

33
34
35
36
37
38
39
40
41
42
43
44
45
46
47
48
49
50
51 +These authors contributed equally to this work

52
53 *Corresponding authors:

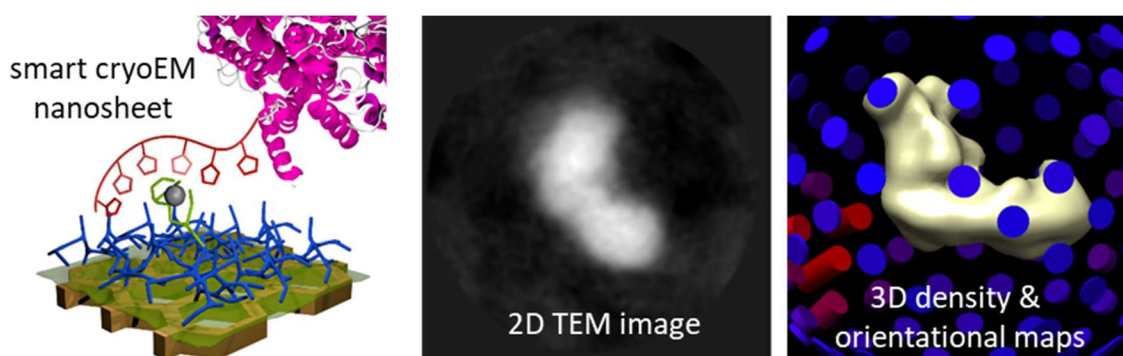
54 aterfort@chemie.uni-frankfurt.de, daniel.rhinow@biophys.mpg.de
55 andrey.turchanin@uni-jena.de
56
57
58
59
60

Abstract

Transmission electron cryo-microscopy (cryoEM) of vitrified biological specimens is a powerful tool for structural biology. Current preparation of vitrified biological samples starts off with sample isolation and purification, followed by the fixation in a freestanding layer of amorphous ice. Here, we demonstrate that ultrathin (~10 nm) smart molecular nanosheets having specific bio-recognition sites embedded in a biorepulsive layer covalently bound to a mechanically stable carbon nanomembrane allow for a much simpler isolation and structural analysis. We characterize in detail the engineering of these nanosheets and their biorecognition properties employing complementary methods such as X-ray photoelectron and infrared spectroscopy, atomic force microscopy as well as surface plasmon resonance measurements. The desired functionality of the developed nanosheets is demonstrated by *in situ* selection of a His-tagged protein from a mixture and its subsequent structural analysis by cryoEM.

Keywords: molecular nanosheets, 2D materials, electron microscopy, structural biology, biorecognition

TOC Image



TOC Text: Ultrathin molecular nanosheets (~10 nm) having bio-recognition sites embedded in a biorepellent layer on top of a mechanically stable carbon nanomembrane have been developed. These smart nanosheets enable the selective binding of suitably tagged biomolecules for their advanced structural analysis by transmission electron cryo-microscopy.

1
2
3 Biological macromolecules are essential building blocks of living cells accomplishing
4 fundamental functions such as energy conversion, signal transduction, and protein
5 synthesis. To understand the function of these macromolecules in health and disease,
6 it is indispensable to resolve their structure on the atomic scale. A powerful tool for
7 high-resolution structural analysis is electron cryo-microscopy (cryoEM), as it covers
8 the entire range of biological structures ranging from single molecules up to whole
9 cells.¹⁻³ There have been numerous successful efforts to improve instrumentation for
10 transmission electron microscopy (TEM), e.g., *via* correction of spherical and
11 chromatic aberration^{4, 5} or the implementation of CMOS detectors enabling data
12 acquisition with unprecedented signal-to-noise ratios.⁶⁻⁸ These improvements open the
13 door for automated data acquisition schemes,⁹ which in turn provide the means to
14 match the demands of high-throughput structural proteomics.¹⁰ However, the most
15 critical factor in biological cryoEM remains the specimen itself, which is typically
16 embedded in a thin layer of vitreous ice on holey carbon films to avoid electron-beam
17 induced structure disturbances.¹¹ Like most other methods, cryoEM of biomolecules
18 suffers from low protein expression rates and denaturation of labile entities during
19 purification, typically providing only small amounts of analyzable specimen.
20 Additionally, the number of observable particles becomes reduced in the vitreous ice
21 films, e.g., by non-specific adhesion to the carrier material (carbon film) or by the
22 formation of strongly curved menisci.¹² The latter are typically enhanced by the
23 presence of detergents, which lead to thinning of the water films, pushing the specimen
24 to the periphery, where they hardly can be observed.

25
26 In an effort to improve TEM sample preparation, we figured out that it would be
27 advantageous to deposit the specimen particles onto nanosheets that are thin enough
28 to allow the undisturbed transmission of electrons. If these nanosheets would
29
30

1
2
3 additionally be equipped with specific binding groups for the selective immobilization
4 of the protein of interest, a selective binding from mixtures, such as cell lysates or crude
5 extracts, should become possible, making the isolation and purification of the
6 specimen before the cryoEM obsolete. Apart from the routinely used amorphous
7 carbon films, very few materials have been reported as support films for TEM including
8 metallic glasses^{13, 14}, graphene¹⁵⁻¹⁸ and gold¹⁹. The biocompatibility of these materials
9 is restricted and it is difficult to functionalize them with biorecognition sites. Graphene
10 oxide (obtained by oxidation of graphene sheets with strong acids), is hydrophilic and
11 therefore more favorable for the preparation of aqueous biological samples.^{20, 21}
12 However, the controlled chemical functionalization of graphene oxide is not trivial,²²
13 what hinders the introduction of specific binding groups. Lipid layers^{23, 24} or 2D protein
14 crystals²⁵ functionalized with affinity groups mounted on conventional carbon films
15 were also applied as supporting substrates for the selective immobilization of proteins.
16 A disadvantage of these materials is their sensitivity towards detergents, making them
17 incompatible with structural analysis of, e.g., detergent-solubilized membrane proteins.
18 Recently, carbon nanomembranes (CNMs) – ultrathin molecular nanosheets, which
19 can be obtained by cross-linking of aromatic self-assembled monolayers (SAMs) –
20 have been established as alternative support films for TEM.^{26, 27} Based on this
21 approach, we have developed smart nanosheets for biological cryoEM solving the
22 problems related to specimen preparation outlined above. These molecular sheets (i)
23 are ultrathin and highly homogeneous, which minimizes inelastic scattering of
24 electrons, (ii) are mechanically stable as free-standing sheets during specimen
25 preparation and TEM analysis, (iii) can be equipped with specific biorecognition sites
26 for selective binding of biomolecules, and (iv) contain a bio-repellent interlayer to avoid
27
28
29
30
31
32
33
34
35
36
37
38
39
40
41
42
43
44
45
46
47
48
49
50
51
52
53
54
55
56
57
58
59
60

1
2
3 unspecific binding of biomolecules. The structure of these smart molecular nanosheets
4
5 is schematically shown in Figure 1.
6
7

8 **RESULTS AND DISCUSSION**

9

10
11 As a platform for the fabrication of the nanosheets, we used ~1 nm thick CNMs
12
13 obtained via low energy electron-induced cross-linking of self-assembled 4'-nitro-4-
14
15 biphenylthiol (NBPT) monolayers on gold.²⁸⁻³⁰ Upon the electron irradiation of NBPT
16
17 SAMs, the nitro groups are reduced to amino groups providing reactive sites for
18
19 subsequent chemical functionalization of the formed NH₂-terminated CNM (NH₂-
20
21 CNMs).^{29, 31} An essential prerequisite for the selective immobilization of a tagged
22
23 biomolecule onto a surface is the formation of a bio-repellent layer that suppresses
24
25 non-specific adsorption of other biomolecules present in the analyte solution. Using
26
27 surface-initiated ring-opening polymerization of glycidol,^{32, 33} we covalently bound
28
29 hyperbranched polyglycerol (PG) units to the amino-terminated surface of NH₂-CNMs,
30
31 forming PG functionalized nanosheets (PG-CNMs). To equip these nanosheets with
32
33 specific biorecognition sites, we chose the nitrilotriacetic acid (NTA) unit, the metal
34
35 complexes of which are routinely used for the selective binding of proteins that carry
36
37 an oligo-histidine chain (His-tag).³⁴ In the course of our investigation, it turned out to
38
39 be useful to employ binding sites with more than one NTA unit, so we decided to use
40
41 a tetrakisNTA derivative of cyclen (NTA₄cyclen) to form the bioselective nanosheets
42
43 (NTA-PG-CNMs, Figure 1).^{35, 36} For the covalent attachment, we activated one acid
44
45 moiety of the NTA₄cyclen with oxalyl chloride to form a reactive NTA₄cyclen derivative,
46
47 which then reacts with one of the hydroxyl groups of the PG-layer (see Supporting
48
49 Information (SI) for details of the synthetic procedure). The fabrication steps were
50
51 monitored by infrared reflection absorption spectroscopy (IRRAS) and X-ray
52
53
54
55
56
57
58
59
60

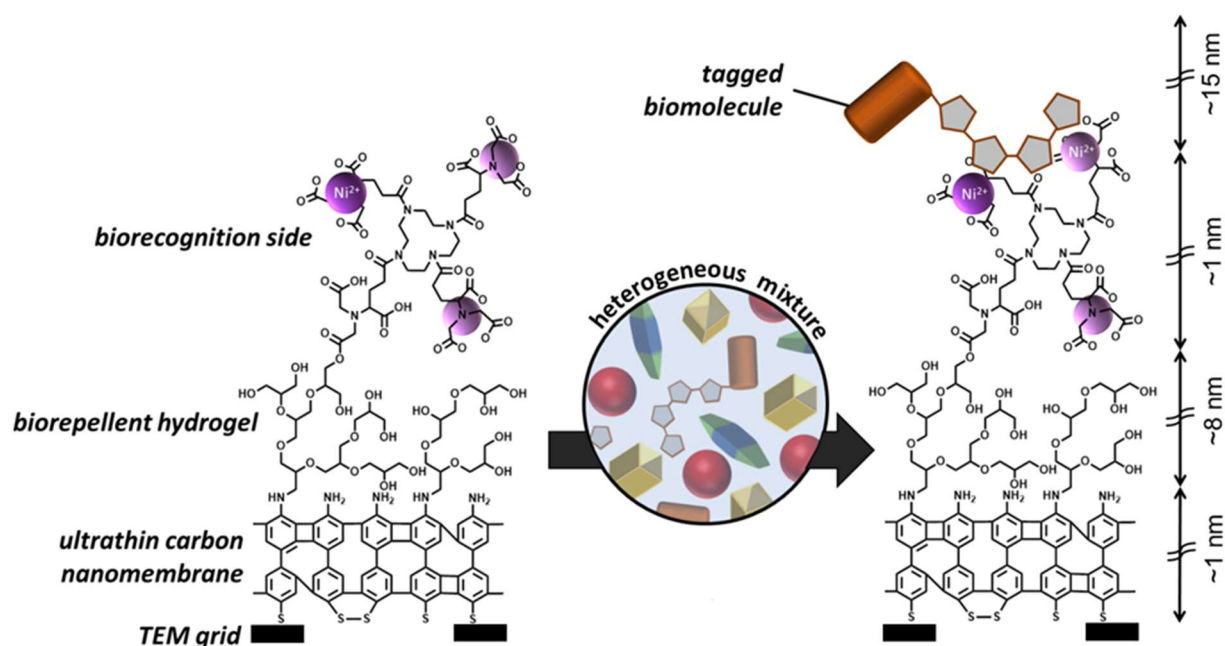


Figure 1. Schematic representation of the structure and the functional principle of the developed smart nanosheets for biological TEM. The functionalized nanosheets contain an NTA₄cyclen moiety as well as a bio-repellant hydrogel, which enables selective immobilization of His-tagged biomolecules for their subsequent analysis by cryoEM while preventing the unspecific binding of other proteins.

1
2
3 photoelectron spectroscopy (XPS) accompanied by atomic force microscopy (AFM)
4 and surface plasmon resonance measurements (SPR). The IRRAS spectra in Figure
5 2 show the successful grafting of an ~8 nm PG-layer on top of the NH₂-CNM (see AFM
6 and XPS results in SI Figure S1 and S2, respectively). This PG-thickness was found
7 to be sufficient to provide the optimal protein repellent properties of the nanosheet (see
8 below). The bands at 3200-3600 cm⁻¹ (OH-stretching mode), 2875 cm⁻¹ and 2940 cm⁻¹
9 (sym/asym C-H stretching mode), as well as the band at 1140 cm⁻¹ (C-O-C stretching
10 mode), are characteristic for PG (black spectrum in Figure 2).³⁷ The small, but
11 significant band at 1740 cm⁻¹ is characteristic for PG layers grafted at higher
12 temperature (~140 °C, see SI p. S4 for details) and is typically assigned to epoxy
13 groups rearranged to carbonyl groups. After the coupling of the NTA₄cyclen units to
14 the PG-layer, the intensity of this band increased (red spectrum in Figure 2), because
15 of the introduction of additional carboxylic acid and carboxylic ester groups.³⁸
16 Moreover, a new band appeared at 1645 cm⁻¹, which was caused by C=O stretching
17 vibrations of amide groups further confirming the effective attachment of the NTA-
18 derivative.³⁸

19
20
21
22
23
24
25
26
27
28
29
30
31
32
33
34
35
36
37
38
39
40 Figure 3 presents C 1s, N 1s, S 2p and O 1s XP spectra after the respective
41 functionalization steps of an NH₂-CNM. The spectra of the pristine NH₂-CNM shown in
42 Figure 3a are fully consistent with previous reports^{29, 31} (see SI Table S1 for details).
43 After the functionalization with PG, all spectra experienced significant changes. Due to
44 the surface sensitivity of XPS, the formation of an ~8 nm thick PG-layer results in the
45 disappearance of the NH₂-CNM spectral features and the respective spectra show only
46 O 1s and C 1s signals, Figure 3b. The XP O 1s signal at 533.4 eV is due to the
47 formation of C-O-C bonds and due to some minor amount of species with higher
48 oxidation states (see next);³⁹ the respective C 1s signal at 286.3 eV forms ~70% of the
49
50
51
52
53
54
55
56
57
58
59
60

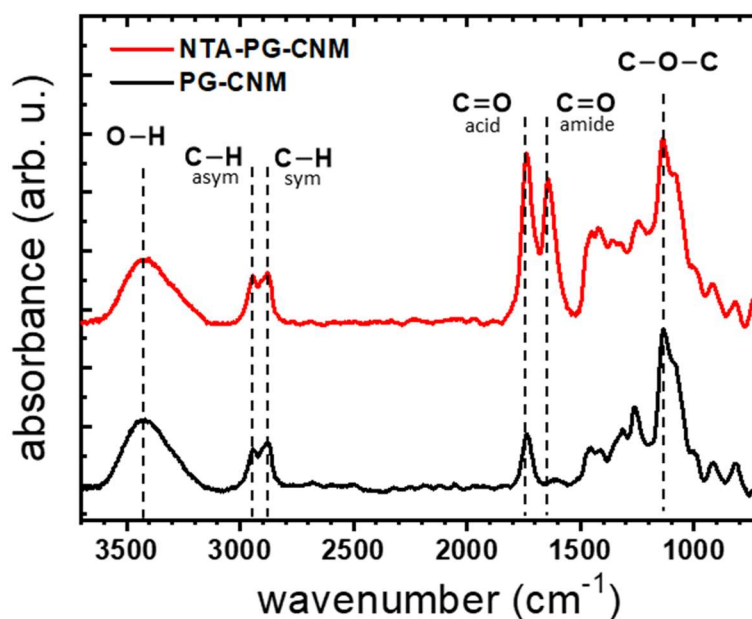


Figure 2. Analysis of the engineered nanosheets by IRRAS: PG polymerization on the NH_2 -CNM (black) and subsequent NTA functionalization of the PG (red). The bands at $3200\text{--}3600\text{ cm}^{-1}$ (OH-stretching mode), 2950 and 2875 cm^{-1} (sym/asym CH_2 -stretching mode) as well as the band at 1140 cm^{-1} (C-O-C-stretching mode) clearly show the successful grafting of PG on the NH_2 -CNM and formation of the PG-CNM. The appearance of the bands at 1740 cm^{-1} ($\text{C}=\text{O}_{\text{acid}}$) and 1650 cm^{-1} and ($\text{C}=\text{O}_{\text{amide}}$ and N- H_{amide}) in the red spectrum shows the coupling of the NTA derivative to the PG-surface and formation of the NTA-PG-CNM.

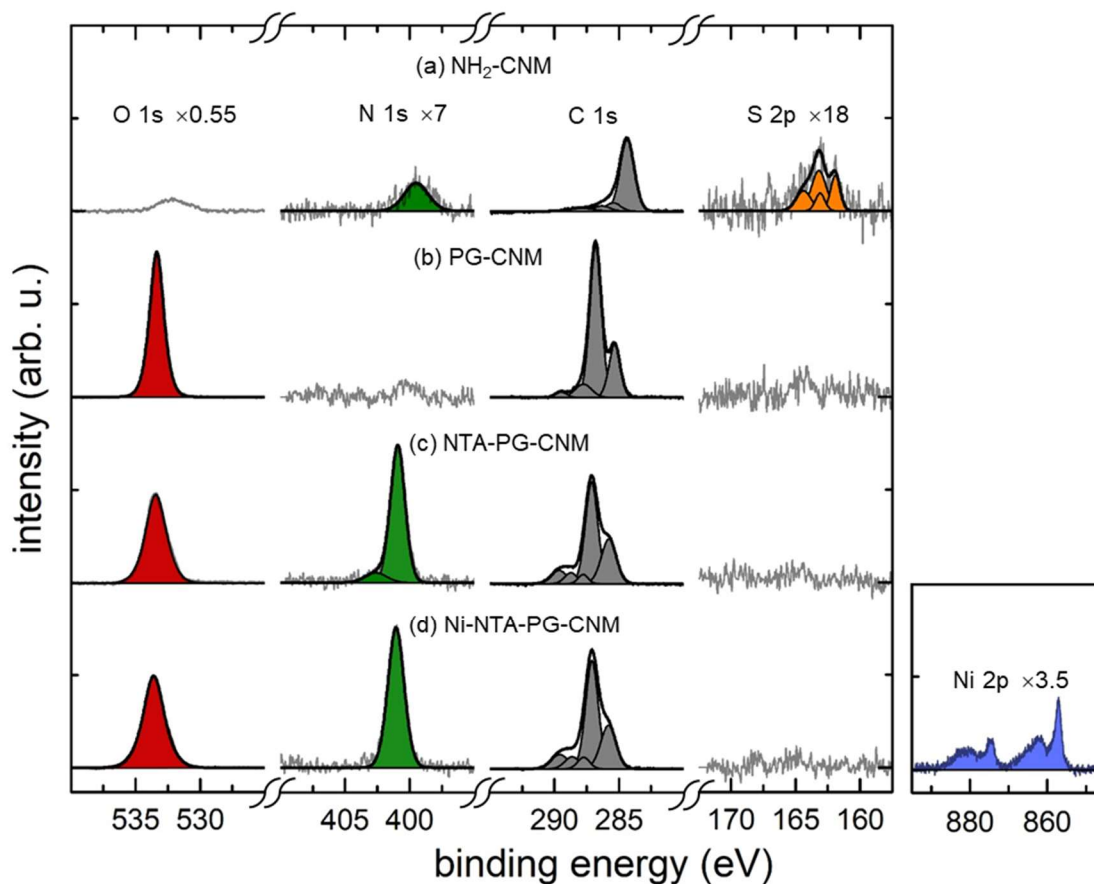


Figure 3. XPS analysis of the subsequent functionalization steps. High-resolution XP spectra of the O1s, N1s, C1s, S2p and Ni2p. The spectra are scaled for better visibility as indicated. (a) Pristine NH₂-CNM on Au/mica. (b) Grafting of the PG layer, PG-CNM. (c) Grafting of the NTA₄cyclen layer, NTA-PG-CNM. (d) Chelating of Ni²⁺ to NTA-PG-CNM. See text for discussion of the spectra and for the peak assignment and quantitative analysis SI Table S1.

1
2
3 total carbon intensity. Besides this peak also lower intensity C 1s peaks at 285.3 eV,
4
5 287.8 eV and 289.5 eV (see SI Table S1 for quantification) are recognized, which are
6
7 assigned to aliphatic,⁴⁰ carbonylic⁴¹ and carboxylic⁴¹ species, respectively. These
8
9 additional carbon species with a total intensity of ~30% result from rearrangement of
10
11 glycidol, because of the elevated temperatures during the PG-grafting (see above).
12
13 Figure 3c shows the XP spectra after the attachment of the NTA₄cyclen units. As can
14
15 be detected from attenuation of the C 1s (C-O-C) signal at 286.3 eV, the thickness of
16
17 the nanosheets increases by ~1 nm to a total thickness of ~10 nm. The respective N
18
19 1s signals of the NTA groups appear in the spectrum at 400.4 eV^{42, 43} and are
20
21 accompanied by a shoulder at 402.1 eV due to some protonated species (see SI Table
22
23 S1). Because of the presence of carboxylic groups in the NTA units, an additional peak
24
25 at 289.6 eV appears in the C 1s spectrum and the full width at half maximum of the O
26
27 1s peak increases from 1.4 eV (PG layer) to 2.0 eV, whereas the total O 1s intensity
28
29 decreases due to the presence of the NTA₄cyclen layer on top of the PG layer. Note
30
31 that in the as-synthesized nanosheet samples we reproducibly found traces of Zn²⁺
32
33 ions (see SI Figure S3a), the origin of which remains unclear. We believe that this
34
35 phenomenon hints on the strong chelation properties of NTA, collecting even trace
36
37 amounts of Zn²⁺ ions from the applied solvents. These Zn²⁺ traces were completely
38
39 removed after loading of the chelators with Ni²⁺ (see Figure 3d and SI Figure S3b).
40
41 The quantitative evaluation of the Ni 2p and N 1s intensities reveals a stoichiometric
42
43 ratio of Ni:N = 1:2.4, which is in a very good agreement with the expected one of 1:2.7
44
45 (see Figure 1) supporting the expected binding chemistry, in which one of the NTA
46
47 groups is sacrificed for the binding of the NTA₄cyclen unit, while the other three remain
48
49 fully functional. We further confirmed by XPS the functionality of the NTA chelators by
50
51 subsequent loading and unloading of Ni²⁺, which is presented in SI Figures S3b-d, S4.
52
53
54
55
56
57
58
59
60 To sum up, the detailed XPS study together with the complementary IRRAS

1
2
3 characterization unambiguously demonstrate the successful synthesis of our
4
5 bioselective nanosheets, as schematically shown in Figure 1a.
6
7

8 Besides the spectroscopic characterization, we tested the general biofunctionality of
9
10 the nanosheets. To this end, SPR measurements (see SI Figure S5) were employed
11
12 using bovine serum albumin (BSA, without His-tag to test for unspecific bioadhesion,
13
14 67 kDa) and His₈-tagged green fluorescent protein (His₈-GFP, as a specific analyte,
15
16 39 kDa)⁴⁴. As shown in Figure 1b, after incubation of the nanosheet with Ni²⁺,
17
18 biorecognition sites with a strong affinity towards His-tagged biomolecules together
19
20 with a biorepellent background due to the PG-functionalization are provided. From the
21
22 SPR data, we found a complete biorepulsivity of the nanosheet for the untagged BSA.
23
24 In contrast to this, the His-tagged GFP became strongly bound to the nanosheet, as
25
26 demonstrated by the flat line during the washing step with buffer (Figure S5).
27
28

29
30
31 Finally, we demonstrated that the NTA-PG-CNM nanosheets are indeed suitable for
32
33 the *in situ* selection of His-tagged proteins from heterogeneous mixtures and their
34
35 subsequent structural analysis by cryo-EM. We chose His-tagged complex I from
36
37 *Yarrowia lipolytica* and GroEL (without His-tag) from *E. coli* as the test specimens.^{45, 46}
38
39
40 When a 1.16:1 mixture of tenside-stabilized complex I and GroEL was prepared in the
41
42 conventional way on a continuous amorphous carbon film, the TEM images of the
43
44 negatively stained samples showed that both proteins adsorb equally well (Figure S6).
45
46 If the same mixture was exposed to a nanosheet previously activated with Ni²⁺,
47
48 followed by washing, and blotting (see SI pp. S7-S8 for details), a clear preference for
49
50 the immobilization of the His-tagged complex I particles was found in the cryoEM
51
52 images (Figure 4A). An automatic analysis using 2D class averages of complex I and
53
54 GroEL as templates (Figures 4B and 4C) found 1176 complex I particles and 41 GroEL
55
56 particles in a total of 73 images, corresponding to a more than 24-fold
57
58
59
60

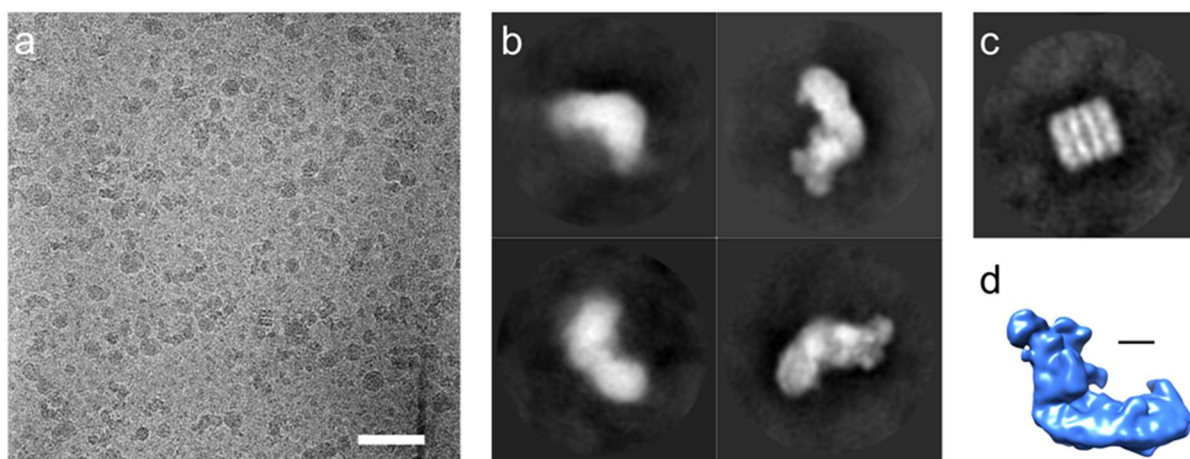


Figure 4. CryoEM analysis of His-tagged complex I selectively bound to NTA-PG-CNM with ~10 nm thickness. (A) CryoEM image of a vitrified sample, which was prepared by selective immobilization of His-tagged complex I onto the functionalized nanosheets. For this, the Ni²⁺-activated NTA-PG-CNM was exposed to a 1.16:1 mixture of complex I and GroEL. The scale bar is 100 nm. (B) Representative 2-D class averages of complex I. (C) Representative class average of GroEL. (D) 3-D density map of complex I obtained from the sample. The scale bar is 5 nm.

1
2
3 enrichment of the tagged species. This analysis demonstrates that the NTA-PG-CNM
4 nanosheets bind His-tagged particles with a high selectivity. The enrichment together
5 with the very homogeneous distribution of the particles enabled structural analysis of
6 the respective protein. Figure 4D shows the 3D density map of complex I at 17.8 Å
7 resolution calculated from 1786 particles. This analysis was possible, because
8 particles in basically all 3D orientations were present on the functionalized nanosheets
9 (Figure S7), which presumably is feasible due to the conformational softness of the PG
10 layer in the nanosheets. We also want to point out that our approach might be extended
11 to further biorecognition principles, e.g., the biotin-streptavidin system. It is also worth
12 noting that smart nanosheets could prevent proteins from denaturing at the air-water
13 interface. It has been shown recently, that a fraction of proteins denatures at the air-
14 water face of the thin water film during plunge freezing.⁴⁷ Binding of tagged
15 biomolecules to NTA-PG-CNM nanosheets keeps them in a safe position deep under
16 the surface of the thin water film thus avoiding interaction with the air-water interface.
17
18
19
20
21
22
23
24
25
26
27
28
29
30
31
32
33
34
35
36
37

38 CONCLUSIONS

39
40
41 In conclusion, we have developed ultrathin support nanosheets for the selection of
42 biological specimens from mixtures for their structural analysis by cryoEM. Although
43 these engineered smart nanosheets have a low thickness (~10 nm), which permits an
44 almost undisturbed penetration of the imaging electron beam, they possess enough
45 mechanical stability to withstand the forces during *in situ* protein immobilization,
46 blotting, and vitrification. Their homogeneity and the conformational softness of the
47 biorepulsive PG layer permit an optimized lateral and orientational distribution of the
48 particles what is essential for automated cryoEM. As the nanosheets consist of
49 covalently bonded moieties, they are stable towards detergents and allow specimen
50
51
52
53
54
55
56
57
58
59
60

1
2
3 preparation of detergent-solubilized membrane protein complexes. Furthermore, smart
4
5 nanosheets could prevent proteins from denaturation at the water-air interface during
6
7 plunge freezing. We expect that these smart nanosheets can also be applied in various
8
9 other fields of nanobiotechnology, e.g., in the engineering of ultrathin coatings with
10
11 biorecognition sites for sensors based on two-dimensional materials like graphene or
12
13 transition metal dichalcogenides.
14
15
16
17
18
19

20 **MATERIALS AND METHODS**

21
22
23 Materials and methods are described in detail in Supporting Information.
24
25
26
27

28 **SUPPORTING INFORMATION**

29
30
31 Full description of sample preparation and methods, additional XPS spectra,
32
33 quantitative analysis of the XPS spectra, AFM and SPR data, TEM analysis and image
34
35 processing.
36
37
38
39
40

41 **ACKNOWLEDGMENT**

42
43 This work was supported by the German Research Council (DFG) via RH 134/1-1, TE
44
45 247/14-1, TU149/5-1 and ZI552/4-2. We thank Werner Kühlbrandt (Max Planck
46
47 Institute of Biophysics) for providing the experimental infrastructure for cryoEM
48
49 measurements and a critical reading of the manuscript.
50
51
52
53
54
55
56
57
58
59
60

References

1. Cheng, Y.; Walz, T., The Advent of Near-Atomic Resolution in Single-Particle Electron Microscopy. *Annu. Rev. Biochem* **2009**, *78* (1), 723-742.
2. Milne, J. L. S.; Subramaniam, S., Cryo-electron tomography of bacteria: progress, challenges and future prospects. *Nat. Rev. Microbiol.* **2009**, *7*, 666.
3. Lučić, V.; Förster, F.; Baumeister, W., STRUCTURAL STUDIES BY ELECTRON TOMOGRAPHY: From Cells to Molecules. *Annu. Rev. Biochem* **2005**, *74* (1), 833-865.
4. Haider, M.; Rose, H.; Uhlemann, S.; Schwan, E.; Kabius, B.; Urban, K., A spherical-aberration-corrected 200kV transmission electron microscope. *Ultramicroscopy* **1998**, *75* (1), 53-60.
5. Evans, J. E.; Hetherington, C.; Kirkland, A.; Chang, L.-Y.; Stahlberg, H.; Browning, N., Low-dose aberration corrected cryo-electron microscopy of organic specimens. *Ultramicroscopy* **2008**, *108* (12), 1636-1644.
6. Bai, X.-c.; Fernandez, I. S.; McMullan, G.; Scheres, S. H. W., Ribosome structures to near-atomic resolution from thirty thousand cryo-EM particles. *eLife* **2013**, *2*, e00461.
7. Li, X.; Mooney, P.; Zheng, S.; Booth, C. R.; Braunfeld, M. B.; Gubbens, S.; Agard, D. A.; Cheng, Y., Electron counting and beam-induced motion correction enable near-atomic-resolution single-particle cryo-EM. *Nat. Methods* **2013**, *10*, 584.
8. Liao, M.; Cao, E.; Julius, D.; Cheng, Y., Structure of the TRPV1 ion channel determined by electron cryo-microscopy. *Nature* **2013**, *504*, 107.
9. Suloway, C.; Pulokas, J.; Fellmann, D.; Cheng, A.; Guerra, F.; Quispe, J.; Stagg, S.; Potter, C. S.; Carragher, B., Automated molecular microscopy: The new Legimon system. *J. Struct. Biol.* **2005**, *151* (1), 41-60.
10. Sali, A.; Glaeser, R.; Earnest, T.; Baumeister, W., From words to literature in structural proteomics. *Nature* **2003**, *422* (6928), 216-225.
11. Orlova, E. V.; Saibil, H. R., Structural Analysis of Macromolecular Assemblies by Electron Microscopy. *Chem. Rev.* **2011**, *111* (12), 7710-7748.
12. Scherr, J.; Parey, K.; Klusch, N.; Murphy, B. J.; Balsler, S.; Neuhaus, A.; Zickermann, V.; Kühlbrandt, W.; Terfort, A.; Rhinow, D., Self-Perforated Hydrogel Nanomembranes Facilitate Structural Analysis of Proteins by Electron Cryo-Microscopy. *ACS Nano* **2017**, *11* (6), 6467-6473.

- 1
2
3 13. Rhinow, D.; Kühlbrandt, W., Electron cryo-microscopy of biological specimens
4 on conductive titanium–silicon metal glass films. *Ultramicroscopy* **2008**, *108* (7), 698-
5 705.
6
- 7
8 14. Yoshioka, C.; Carragher, B.; Potter, C. S., Cryomesh™: A New Substrate for
9 Cryo-Electron Microscopy. *Microsc. Microanal.* **2010**, *16* (1), 43-53.
10
- 11 15. Nair, R. R.; Blake, P.; Blake, J. R.; Zan, R.; Anissimova, S.; Bangert, U.;
12 Golovanov, A. P.; Morozov, S. V.; Geim, A. K.; Novoselov, K. S.; Letychevskaia, T.,
13 Graphene as a transparent conductive support for studying biological molecules by
14 transmission electron microscopy. *Appl. Phys. Lett.* **2010**, *97* (15), 153102.
15
- 16 16. Pantelic, R. S.; Suk, J. W.; Magnuson, C. W.; Meyer, J. C.; Wachsmuth, P.;
17 Kaiser, U.; Ruoff, R. S.; Stahlberg, H., Graphene: Substrate preparation and
18 introduction. *J. Struct. Biol.* **2011**, *174* (1), 234-238.
19
- 20 17. Rhinow, D.; Weber, N.-E.; Turchanin, A.; Götzhäuser, A.; Kühlbrandt, W.,
21 Single-walled carbon nanotubes and nanocrystalline graphene reduce beam-induced
22 movements in high-resolution electron cryo-microscopy of ice-embedded biological
23 samples. *Appl. Phys. Lett.* **2011**, *99* (13), 133701.
24
- 25 18. Russo, C. J.; Passmore, L. A., Controlling protein adsorption on graphene for
26 cryo-EM using low-energy hydrogen plasmas. *Nat. Methods* **2014**, *11*, 649.
27
- 28 19. Russo, C. J.; Passmore, L. A., Ultrastable gold substrates for electron
29 cryomicroscopy. *Science* **2014**, *346* (6215), 1377-1380.
30
- 31 20. Liu, Z.; Jiang, L.; Galli, F.; Nederlof, I.; Olsthoorn, R. C. L.; Lamers, G. E. M.;
32 Oosterkamp, T. H.; Abrahams, J. P., A Graphene Oxide·Streptavidin Complex for
33 Biorecognition – Towards Affinity Purification. *Adv. Funct. Mater.* **2010**, *20* (17), 2857-
34 2865.
35
- 36 21. Pantelic, R. S.; Meyer, J. C.; Kaiser, U.; Baumeister, W.; Plitzko, J. M.,
37 Graphene oxide: A substrate for optimizing preparations of frozen-hydrated samples.
38 *J. Struct. Biol.* **2010**, *170* (1), 152-156.
39
- 40 22. Georgakilas, V.; Otyepka, M.; Bourlinos, A. B.; Chandra, V.; Kim, N.; Kemp,
41 K. C.; Hobza, P.; Zboril, R.; Kim, K. S., Functionalization of Graphene: Covalent and
42 Non-Covalent Approaches, Derivatives and Applications. *Chem. Rev.* **2012**, *112* (11),
43 6156-6214.
44
- 45 23. Kelly, D. F.; Abeyrathne, P. D.; Dukovski, D.; Walz, T., The Affinity Grid: A Pre-
46 fabricated EM Grid for Monolayer Purification. *J. Mol. Biol.* **2008**, *382* (2), 423-433.
47
48
49
50
51
52
53
54
55
56
57
58
59
60

- 1
2
3 24. Benjamin, C. J.; Wright, K. J.; Hyun, S.-H.; Krynski, K.; Yu, G.; Bajaj, R.;
4 Guo, F.; Stauffacher, C. V.; Jiang, W.; Thompson, D. H., Nonfouling NTA-PEG-Based
5 TEM Grid Coatings for Selective Capture of Histidine-Tagged Protein Targets from Cell
6 Lysates. *Langmuir* **2016**, *32* (2), 551-559.
7
8
9
10 25. Han, B.-G.; Watson, Z.; Kang, H.; Pulk, A.; Downing, K. H.; Cate, J.; Glaeser,
11 R. M., Long shelf-life streptavidin support-films suitable for electron microscopy of
12 biological macromolecules. *J. Struct. Biol.* **2016**, *195* (2), 238-244.
13
14 26. Turchanin, A.; Götzhäuser, A., Carbon Nanomembranes. *Adv. Mater.* **2016**, *28*
15 (29), 6075-6103.
16
17 27. Rhinow, D.; Bünenfeld, M.; Weber, N.-E.; Beyer, A.; Götzhäuser, A.;
18 Kühlbrandt, W.; Hampp, N.; Turchanin, A., Energy-filtered transmission electron
19 microscopy of biological samples on highly transparent carbon nanomembranes.
20 *Ultramicroscopy* **2011**, *111* (5), 342-349.
21
22 28. Eck, W.; Stadler, V.; Geyer, W.; Zharnikov, M.; Götzhäuser, A.; Grunze, M.,
23 Generation of Surface Amino Groups on Aromatic Self-Assembled Monolayers by Low
24 Energy Electron Beams—A First Step Towards Chemical Lithography. *Adv. Mater.*
25 **2000**, *12* (11), 805-808.
26
27 29. Turchanin, A.; Tinazli, A.; El-Desawy, M.; Großmann, H.; Schnietz, M.; Solak,
28 H. H.; Tampé, R.; Götzhäuser, A., Molecular Self-Assembly, Chemical Lithography,
29 and Biochemical Tweezers: A Path for the Fabrication of Functional Nanometer-Scale
30 Protein Arrays. *Adv. Mater.* **2008**, *20* (3), 471-477.
31
32 30. Neumann, C.; Wilhelm, R.; Küllmer, M.; Turchanin, A., Low-energy electron
33 irradiation induced synthesis of molecular nanosheets: An influence of the electron
34 beam energy. *Faraday Discuss.* **2020**, DOI: 10.1039/C9FD00119K.
35
36 31. Schnietz, M.; Turchanin, A.; Nottbohm, C. T.; Beyer, A.; Solak, H. H.; Hinze,
37 P.; Weimann, T.; Götzhäuser, A., Chemically Functionalized Carbon Nanosieves with
38 1-nm Thickness. *Small* **2009**, *5* (23), 2651-2655.
39
40 32. Weber, T.; Gies, Y.; Terfort, A., Bacteria-Repulsive Polyglycerol Surfaces by
41 Grafting Polymerization onto Aminopropylated Surfaces. *Langmuir* **2012**, *28* (45),
42 15916-15921.
43
44 33. Wanka, R.; Aldred, N.; Finlay, J. A.; Amuthalingam, A.; Clarke, J. L.; Clare,
45 A. S.; Rosenhahn, A., Antifouling Properties of Dendritic Polyglycerols against Marine
46 Macrofouling Organisms. *Langmuir* **2019**, *35* (50), 16568-16575.
47
48
49
50
51
52
53
54
55
56
57
58
59
60

- 1
2
3 34. Ueda, E. K. M.; Gout, P. W.; Morganti, L., Current and prospective applications
4 of metal ion–protein binding. *J. Chromatogr. A* **2003**, *988* (1), 1-23.
5
6 35. Gatterdam, K.; Joest, E. F.; Gatterdam, V.; Tampé, R., The Scaffold Design of
7 Trivalent Chelator Heads Dictates Affinity and Stability for Labeling His-tagged
8 Proteins in vitro and in Cells. *Angew. Chem. Int. Ed.* **2018**, *57* (38), 12395-12399.
9
10 36. Lata, S.; Reichel, A.; Brock, R.; Tampé, R.; Piehler, J., High-Affinity Adaptors
11 for Switchable Recognition of Histidine-Tagged Proteins. *J. Am. Chem. Soc.* **2005**, *127*
12 (29), 10205-10215.
13
14 37. Weber, T.; Bechthold, M.; Winkler, T.; Dauselt, J.; Terfort, A., Direct grafting
15 of anti-fouling polyglycerol layers to steel and other technically relevant materials.
16 *Colloids Surf. B* **2013**, *111*, 360-366.
17
18 38. Robert M. Silverstein, F. X. W., David J. Kiemle, David L. Bryce, *Spectrometric*
19 *Identification of Organic Compounds*. 8 ed.; John Wiley & Sons, INC.: USA, 2014; p
20 92-101.
21
22 39. Neffe, A. T.; von Ruesten-Lange, M.; Braune, S.; Lützow, K.; Roch, T.;
23 Richau, K.; Krüger, A.; Becherer, T.; Thünemann, A. F.; Jung, F.; Haag, R.; Lendlein,
24 A., Multivalent grafting of hyperbranched oligo- and polyglycerols shielding rough
25 membranes to mediate hemocompatibility. *J. Mater. Chem. B* **2014**, *2* (23), 3626-3635.
26
27 40. Puziy, A. M.; Poddubnaya, O. I.; Ziatdinov, A. M., On the chemical structure of
28 phosphorus compounds in phosphoric acid-activated carbon. *Appl. Surf. Sci.* **2006**,
29 *252* (23), 8036-8038.
30
31 41. Graf, N.; Yegen, E.; Gross, T.; Lippitz, A.; Weigel, W.; Krakert, S.; Terfort,
32 A.; Unger, W. E. S., XPS and NEXAFS studies of aliphatic and aromatic amine species
33 on functionalized surfaces. *Surf. Sci.* **2009**, *603* (18), 2849-2860.
34
35 42. Shircliff, R. A.; Stradins, P.; Moutinho, H.; Fennell, J.; Ghirardi, M. L.; Cowley,
36 S. W.; Branz, H. M.; Martin, I. T., Angle-Resolved XPS Analysis and Characterization
37 of Monolayer and Multilayer Silane Films for DNA Coupling to Silica. *Langmuir* **2013**,
38 *29* (12), 4057-4067.
39
40 43. Pham, M.-C., Voltammetric and XPS Analysis of Metal-Complexed
41 Polytyramine Films : Geometry-Dependent Electron Transfer Therein. *J. Electrochem.*
42 *Soc.* **1984**, *131* (4), 777.
43
44 44. Heil, C. S.; Rittner, A.; Goebel, B.; Beyer, D.; Grininger, M., Site-Specific
45 Labelling of Multidomain Proteins by Amber Codon Suppression. *Sci. Rep.* **2018**, *8* (1),
46 14864.
47
48
49
50
51
52
53
54
55
56
57
58
59
60

1
2
3 45. Kashani-Poor, N.; Kerscher, S.; Zickermann, V.; Brandt, U., Efficient large
4 scale purification of his-tagged proton translocating NADH:ubiquinone oxidoreductase
5 (complex I) from the strictly aerobic yeast *Yarrowia lipolytica*. *Biochim. Biophys. Acta*,
6 *Bioenerg.* **2001**, 1504 (2), 363-370.
7
8

9
10 46. Parey, K.; Haapanen, O.; Sharma, V.; Köfeler, H.; Züllig, T.; Prinz, S.;
11 Siegmund, K.; Wittig, I.; Mills, D. J.; Vonck, J.; Kühlbrandt, W.; Zickermann, V., High-
12 resolution cryo-EM structures of respiratory complex I: Mechanism, assembly, and
13 disease. *Sci. Adv.* **2019**, 5 (12), eaax9484.
14
15

16 47. D'Imprima, E.; Floris, D.; Joppe, M.; Sánchez, R.; Grininger, M.; Kühlbrandt,
17 W., Protein denaturation at the air-water interface and how to prevent it. *eLife* **2019**, 8,
18 e42747.
19
20
21
22
23
24
25
26
27
28
29
30
31
32
33
34
35
36
37
38
39
40
41
42
43
44
45
46
47
48
49
50
51
52
53
54
55
56
57
58
59
60

Supporting Information (SI)

Smart molecular nanosheets for advanced preparation of biological samples in electron cryo-microscopy

Julian Scherr^{1,+}, Zian Tang^{2,+}, Maria Küllmer², Sebastian Balsler¹, Alexander Stefan Scholz¹, Andreas Winter², Kristian Parey³, Alexander Rittner⁴, Martin Grininger⁴, Volker Zickermann⁵, Daniel Rhinow^{3*}, Andreas Terfort^{1*}, Andrey Turchanin^{2*}

¹*University of Frankfurt, Department of Chemistry,
Max-von-Laue-Str. 7, 60438 Frankfurt, Germany*

²*Friedrich Schiller University Jena, Institute of Physical Chemistry,
Lessingstr. 10, 07743 Jena, Germany*

³*Max Planck Institute of Biophysics, Department of Structural Biology,
Max-von-Laue-Str. 3, 60438 Frankfurt, Germany*

⁴*Institute of Organic Chemistry and Chemical Biology,
Buchmann Institute for Molecular Life Sciences, University of Frankfurt,
Max-von-Laue-Str. 15, 60438 Frankfurt, Germany*

⁵*University of Frankfurt, Institute of Biochemistry II, Medical School,
Max-von-Laue-Str. 9, 60438 Frankfurt, Germany*

⁺These authors contributed equally to this work

^{*}Corresponding authors:

aterfort@chemie.uni-frankfurt.de, daniel.rhinow@biophys.mpg.de
andrey.turchanin@uni-jena.de

Table of Contents

1		
2		
3		
4		
5	1. Synthesis of NTA ₄ cyclen	S3
6		
7	2. Fabrication of the functionalized nanosheets	S4
8		
9	3. Characterization of the functionalized nanosheets	S5
10		
11	4. Quantitative analysis of the XPS data	S9
12		
13	5. References	S13
14		
15		
16		
17		
18		
19		
20		
21		
22		
23		
24		
25		
26		
27		
28		
29		
30		
31		
32		
33		
34		
35		
36		
37		
38		
39		
40		
41		
42		
43		
44		
45		
46		
47		
48		
49		
50		
51		
52		
53		
54		
55		
56		
57		
58		
59		
60		

1. Synthesis of NTA₄cyclen

The reactions were performed under nitrogen 5.0 (≥ 99.999 vol. %) in dry glassware (dried by heating under vacuum). *N,N*-(Bis-*tert*-butylcarboxymethyl)-L-glutamic acid 1-*tert*-butyl-ester was synthesized according to literature.¹

Synthesis of N,N',N'',N'''-tetrakis(N,N-(bis-tert-butylcarboxymethyl)-L-glutam-5-yl)cyclentetra-tert-butyl ester (tBu₁₂NTA₄cyclen)

A solution of *N,N*-(bis-*tert*-butylcarboxymethyl)-L-glutamic acid 1-*tert*-butyl-ester (0.94 g, 2.2 mmol), *N,N*-diisopropylethylamine (DIPEA, ABCR GmbH, 98%, 0.8 mL, 4 mmol) and 2-(1H-benzotriazole-1-yl)-1,1,3,3-tetramethylammonium tetrafluoroborate (TBTU, Carbosynth Limited, 99%, 0.751 g, 2.34 mmol) in dichloromethane (DCM, distilled, 20 mL) was stirred for 15 minutes. Next, cyclen (Acros Organics, 99%, 89 mg, 0.52 mmol) was added and the reaction mixture stirred at room temperature overnight. All volatiles were removed in vacuum and the residue was redissolved in DCM. The obtained organic solution was washed three times with water. The solvent was removed in vacuum and the crude product was purified by column chromatography (silica gel, Merck KGaA, Geduran® Si 60, 0.063 – 0.20 mm, ethyl acetate/MeOH 4:1). Finally, 0.88 g of a yellow oil was isolated.

MS (MALDI) *m/z*: [M + H]⁺ calcd for C₉₂H₁₆₀N₈O₂₈, 1826.3; found 1826.9.

Synthesis of N,N',N'',N'''-tetrakis(N,N-biscarboxymethyl)-L-glutam-5-yl)cyclen (NTA₄cyclen)

To a solution of *N,N',N'',N'''-tetrakis(N,N-(bis-tert-butylcarboxymethyl)-L-glutam-5-yl)cyclen-tetra-tert-butyl ester* (1.68 g, 0.920 mmol) in 53 mL DCM, trifluoroacetic acid (TFA, ABCR GmbH, 99%, 7.1 mL, 92 mmol) was added. The solution was then stirred for 3 days at 40 °C. Afterwards, phenol (Riedel-de Haën, 99.5-100.5%, 0.84 g, 8.9 mmol), ethanedithiol (Acros Organics, 95%, 0.84 mL, 10 mmol), water (0.84 mL, distilled, 47 mmol, 51 eq) and triisopropylsilane (AlzChem AG, technical grade, 0.84 mL, 4.4 mmol) were added. Then the reaction mixture was stirred for 3 h at 50 °C, followed by evaporating all volatiles under vacuum. The residues were dissolved in TFA and the obtained solution was filtered under vacuum. By adding diethyl ether, white powder was precipitated from the solution. The precipitate was centrifuged off, washed five times with diethyl ether and dried in vacuum, yielding 0.796 g of white

1
2
3 powder, which was further purified by HPLC (Macherey-Nagel, EC Nucleodur 100-5
4 C18 ec; gradient: 0 – 15 min → 0 - 15% MeCN in MilliQ).

5
6 HRMS (MALDI) m/z : $[M + H]^+$ calcd for $C_{44}H_{64}N_8O_{28}$, 1153.39028; found, 1153.38964
7
8
9

10 **2. Fabrication of the functionalized nanosheets**

11 *Gold substrates*

12
13 (i) Au-on-Si substrates for SAM deposition were prepared by electron beam
14 evaporation. 2.5 nm of titanium followed by 200 nm of gold were deposited onto
15 polished single-crystal silicon wafers.
16
17

18 (ii) Au-on-flint glass for SPR measurement were prepared by electron beam
19 evaporation. 2 nm of chromium followed by 50 nm of gold were deposited onto the flint-
20 glass substrate (Ohara, S-TiH11, $n_d = 1.78472$, $20 \times 20 \times 1$ mm³).
21
22

23 (ii) Au-on-mica substrates were purchased from Georg Albert PVD Coatings with a
24 300 nm thick gold layer.
25
26
27
28

29 *CNM synthesis*

30
31 4'-Nitrobiphenyl-4-thiol (NBPT) SAMs were prepared by immersing oxygen-plasma
32 cleaned gold substrates into a ~0.1 mM solution of NBPT (Taros, 98%, sublimated
33 before use) dissolved in degassed DMF (Alfa Aesar, 99.9%) for 72 h under exclusion
34 of light in inert atmosphere. After the substrates were taken out, they were immediately
35 washed with DMF followed by ethanol rinsing three times to remove the physisorbed
36 molecules on the surface. The samples were dried by a stream of nitrogen and stored
37 under argon atmosphere. The gold substrates with SAMs were put into a high vacuum
38 chamber (1×10^{-8} mbar) and then exposed to an electron beam (electron gun FG15/40,
39 Specs) with 100 eV kinetic energy at a dose of 50 mC/cm². The molecules on the gold
40 surfaces were cross-linked during the irradiation, resulting in the formation of carbon
41 nanosheets (NH₂-CNM).²
42
43
44
45
46
47
48
49
50

51 *Surface initiated ring open polymerization of PG on the NH₂-CNM*

52
53 For the grafting of PG onto the CNM, the NH₂-CNM/Au substrate was placed in a PTFE
54 vial and purged with argon. Next, 5 mL of freshly distilled glycidol was added, the vial
55 was sealed and heated to 140 °C for 2.5 h, The reaction vial was then cooled to room
56 temperature. The substrate was taken out, thoroughly rinsed with water and ethanol
57 and dried in a stream of nitrogen.
58
59
60

Functionalization of the PG-CNM layer with NTA₄cyclen

For the activation of the NTA₄cyclen, 1 mL of absolute DMF, 0.55 μ L of freshly distilled oxalyl chloride and 2 μ L freshly distilled pyridine were added to 5 mg of NTA₄cyclen under inert conditions. The reaction mixture was stirred for 3 h at room temperature. Then 2 mL of absolute DMF and 10 μ L of *N,N*-diisopropylethylamine were added. Afterward, the gold substrate with the PG-CNM was immersed in the solution overnight under inert condition at 70 °C. After cooling to room temperature, the substrate was collected and thoroughly rinsed with water and ethanol and finally dried in steam of nitrogen.

Transfer of the NTA-PG-CNM nanosheets

For the transfer of the nanosheets to the TEM grids or silicon wafers, a protocol reported in the literature was utilized.^{3,4} In short, a PMMA solution was first spin-coated onto the assembly. Then the gold layer with the membranes was released from the silicon wafer, followed by dissolution of the gold using triiodide. After that, the sandwich consisting of PMMA and the nanosheet was transferred to the new substrate. In the final step, PMMA was dissolved with acetone in a critical-point dryer.

3. Characterization of the functionalized nanosheets

X-ray photoelectron spectroscopy (XPS)

XPS was performed in a UHV Multiprobe system (Scienta Omicron) using a monochromatic X-ray source (Al K α) and an electron analyzer (Argus CU) with a spectral resolution of 0.6 eV. The measurements were performed at a pressure $< 5 \times 10^{-10}$ mbar. The XP spectra were fitted using Voigt functions (30:70) after Shirley (C 1s) or linear (N 1s, S 2p) background subtraction. The peak fitting of the sulfur and zinc doublets was performed using the fixed intensity ratios due to the spin-orbit coupling of the p photoelectrons. For the elemental ratios mentioned in the main paper the relative sensitivity factors (RSF) of 1 for C 1s, 1.8 for N 1s, 2.9 for O 1s, 1.1 for S 2p_{3/2}, 16.7 for Ni 2p_{3/2} and 18.9 for Zn 2p_{3/2} were used. The thickness of the CNMs was calculated from the attenuation of the XP Au 4f signal in comparison to the Au 4f signal of a clean Au reference employing the Beer-Lambert law and an attenuation length of 36 Å.⁵

Test of the coordination reversibility of Ni²⁺ at the NTA-modified surface

To demonstrate the reversibility of the Ni²⁺ coordination at the NTA-PG-CNM nanosheets, we performed tests of loading-unloading-reloading. To load Ni²⁺ on the NTA-PG-CNM nanosheets, the samples were immersed in an aqueous NiSO₄ (Merck, 99%) solution (1.0 %) for 30 minutes, followed by rinsing in a bath of high-purity water for three times (each time 15 minutes) to remove the physically adsorbed Ni ions. To unload coordinated Ni²⁺ from the NTA-PG-CNM nanosheets, the samples were first immersed in EDTANa₂ solution (0.5 mmol/L) for 30 minutes, then rinsed with pure water for 30 minutes. Each step of the test was monitored by XPS. As shown in Figure S3a, after the grafting of NTA₄cyclen, the NTA groups demonstrate chelating of some traces of Zn²⁺, no Ni²⁺ was found on the surface. When the NTA-PG-CNM was immersed in NiSO₄ solution, the Ni²⁺ exchanged the Zn²⁺ ions on the nanosheet and created a strong Ni 2p doublet in the spectrum (Figure S3b). Through excessive washing with EDTANa₂ solution, the nickel ions coordinated by the NTA group on the nanosheet became removed (Figure S3c). The repeated immersion of the nanosheet in NiSO₄ solution reloaded the Ni²⁺ onto the membrane and exhibited again the Ni 2p peaks, which were nevertheless somewhat less intense compared to the first loading (Figure S3d). The signal intensity decreases of all elements may be attributed to the damage of the surface functional groups during XPS measurement as well as the loading-unloading process under ambient conditions. Note that the nitrogen peak shifted from 400.5 eV back to 401.1 eV after reloading (Figure S3c and Figure S3d), further confirming the reversible binding of Ni²⁺ on the nanosheet.⁶ Additionally, a reference PG-CNM nanosheet sample without functionalization with the NTA group was tested with the same procedure to show the importance of the NTA groups. Without NTA groups the attachment of Ni²⁺ was not possible. The results are shown in Figure S4.

Infrared reflection absorption spectroscopy (IRRAS)

IRRA-spectra were measured on a *Thermo Scientific* Nicolet 6700 FT-IR spectrometer purged with dry air and equipped with a nitrogen-cooled mercury-cadmium-telluride-detector and a Smart SAGA set-up. The measurements were performed using p-polarized light at an incidence angle of 80° relative to the surface normal. 256 scans were recorded at a resolution of 4 cm⁻¹ from 650 to 3500 cm⁻¹ at room temperature.

Surface plasmon resonance spectroscopy (SPR)

SPR measurements were carried out on a Multiskop instrument (Optrel, Germany) using the Kretschmann geometry with prism coupling and employing p-polarized laser radiation (785 nm, Thorlabs, S1FC785) for the excitation of the plasmon. The 60° prism (Edmund Optics) and the gold-covered flint glass substrate were optically connected using a matching fluid with a refractive index of $n = 1.781$. Home-made PDMS chambers with a volume of 30 μL were used as flow cells. The solutions were pumped through the cell using syringe pumps (Braun Perfusor Secura, Germany). An injection valve (Rheodyne Valve 7125 Injector) was used to insert the protein solution (2 ml) into the running buffer flow.

SPR analysis of functionalized nanosheets

The binding of the proteins to the functionalized surface was monitored using surface plasmon resonance spectroscopy. The measurements were carried out in HEPES-buffered saline (150 mM NaCl, 50 mM HEPES, pH adjusted to 7.6). Briefly, adsorption was performed by first running buffer until a stable signal was observed, followed by 2 mL of a protein solution (1 mg/mL in buffer solution) or nickel solution (0.1% NiSO₄ in MilliQ) followed by purging with buffer. For all experiments, a flow rate of 12 mL h⁻¹ was chosen.

The adsorption properties of functionalized nanosheets were analyzed by SPR (Figure S5). After the loading of the NTA-groups with Ni²⁺, bovine serum albumin (BSA, 98%, Sigma-Aldrich) and His₈-tagged green fluorescent protein (GFP) were injected in the flow-system to investigate their binding to the nanosheet. The exposure to BSA resulted in no significant adsorption to the surface, indicating a complete biorepulsion. In contrast, the His₈-tag GFP, which was applied afterwards, bound strongly to the Ni-NTA-units and therefore resulted in an increased intensity of the signal in the SPR spectrum after the protein solution was purged out of the cell.

TEM analysis and image processing

Dodecyl maltoside-solubilized complex I (with His-tag) was obtained as described in previous work,¹ GroEL (without His-tag) from *E. coli* was purchased from Sigma Aldrich. Functionalized nanosheets mounted on holey carbon TEM grids (Quantifoil) were incubated with 3 μl 0.1% NiSO₄ solution and subsequently rinsed 3x with dist. H₂O. Nanosheets were incubated with a 1.16:1 mixture of complex I and GroEL (1 mg/ml

1
2
3 each) in TSK buffer containing 0.025% DDM and subsequently rinsed 3x with TSK
4 buffer. Samples were blotted for 10-15 s in an FEI Vitrobot and plunged into liquid
5 ethane. Cryo-EM images were recorded and processed as described previously.⁷ For
6 the control experiment, samples were negatively stained using uranyl acetate (Figure
7 S6).
8
9
10
11
12
13
14
15
16
17
18
19
20
21
22
23
24
25
26
27
28
29
30
31
32
33
34
35
36
37
38
39
40
41
42
43
44
45
46
47
48
49
50
51
52
53
54
55
56
57
58
59
60

4. Quantitative analysis of the XPS data

Table S1. Quantitative analysis of the high-resolution XP spectra of the NH₂-CNM and NTA-CNM, PG-NTA-CNM and Ni-PG-NTA-CNM samples on Au presented in Figure 3 including the peak assignment, their binding energies, full width at half maximum (FWHM) values and areas obtained from the spectra deconvolution.

Peak assignment	Binding energy, eV	FWHM, eV	Area, %
NH₂-CNM			
O 1s			
–	532.1	2.7	100
N 1s			
-NH ₂	399.5	2.2	100
C 1s			
C-C aromatic	284.4	1.3	76
C-S/C-N	285.4	1.7	10
Satellite	286.4	1.4	7
Satellite	288.0	2.4	7
S 2p_{3/2}, 2p_{1/2}			
Thiolate	161.9, 163.1	0.6	30
Disulfide	163.2, 164.4	1.3	70
PG-CNM			
O 1s			
C-O/C=O	533.3	1.4	100
C 1s			
C-C aliphatic	285.3	1.1	23
C-O	286.8	1.1	66
C=O	287.8	1.5	8.5
O-C=O	289.5	1.1	2.5
NTA-PG-CNM			
O 1s			
C-O/C=O/O=C-O	533.4	2.0	100
N 1s			

amide/ amine	400.4	1.3	91
protonated nitrogen	402.1	1.8	9
C 1s			
C-N/C-C aliphatic	285.8	1.4	27
C-O	287.1	1.2	51
C=O	287.7	1.2	7
N-C=O	288.7	1.1	4
O-C=O	289.6	1.5	11
Zn 2p_{3/2}, p_{1/2}			
Zn	1023.0, 1046.1	1.7	100
Ni-NTA-PG-CNM			
O 1s			
C-O/C=O/O-C=O	533.5	2.0	100
N 1s			
amide/amine	400.5	1.5	100
C 1s			
C-N/C-C aliphatic	285.8	1.2	26
C-O	287.1	1.2	52
C=O	287.7	1.2	5
N-C=O	288.6	1.4	8
O-C=O	289.6	1.6	9
Ni 2p_{3/2}			
Ni	857.1	NA	NA
Ni _{sat}	860-870	NA	NA

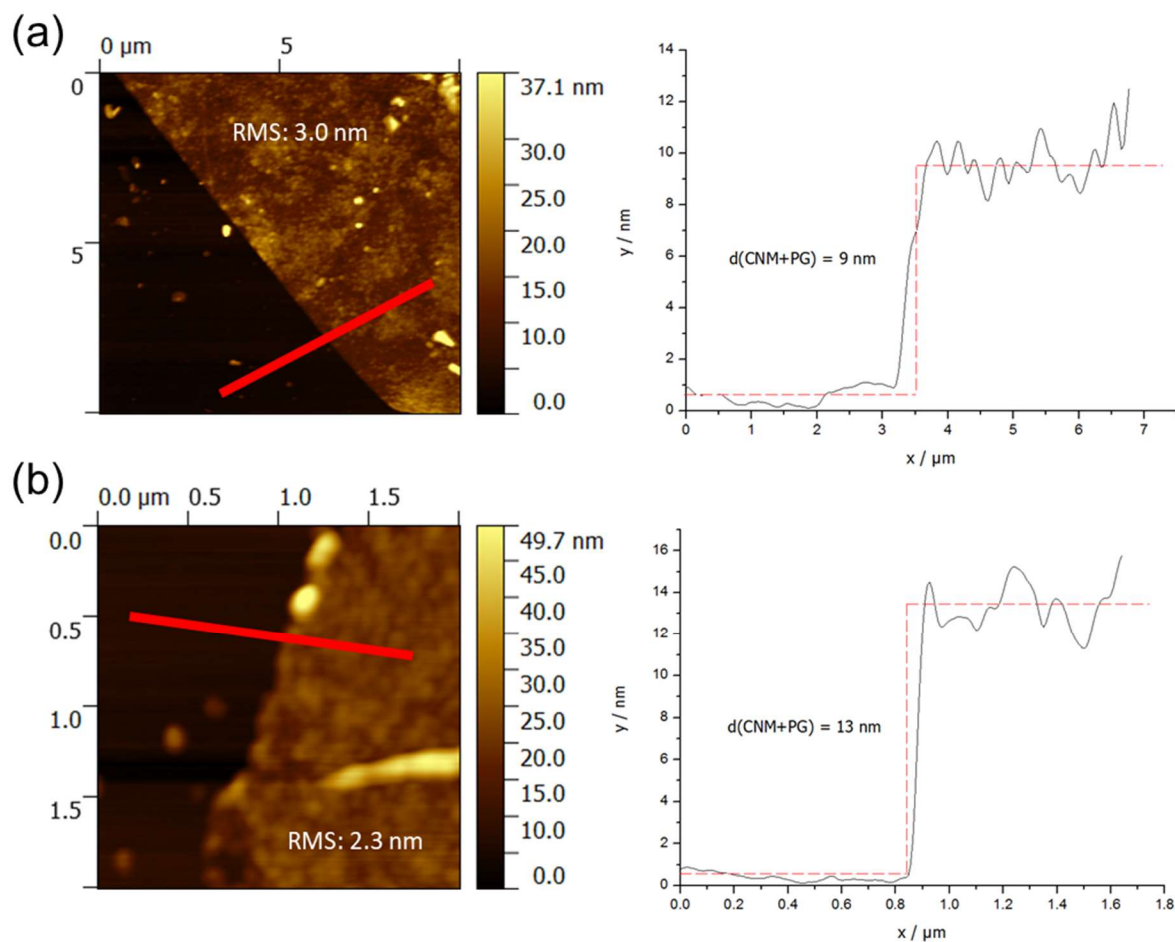


Figure S1. AFM images of PG-CNMs transferred onto SiO_2/Si substrates. PG-CNMs fabricated with polymerization times of (a) 2 hours and (b) 3 hours are demonstrated. The thicknesses of the PG-CNMs were obtained by analyzing the edge profiles of the transferred CNMs.

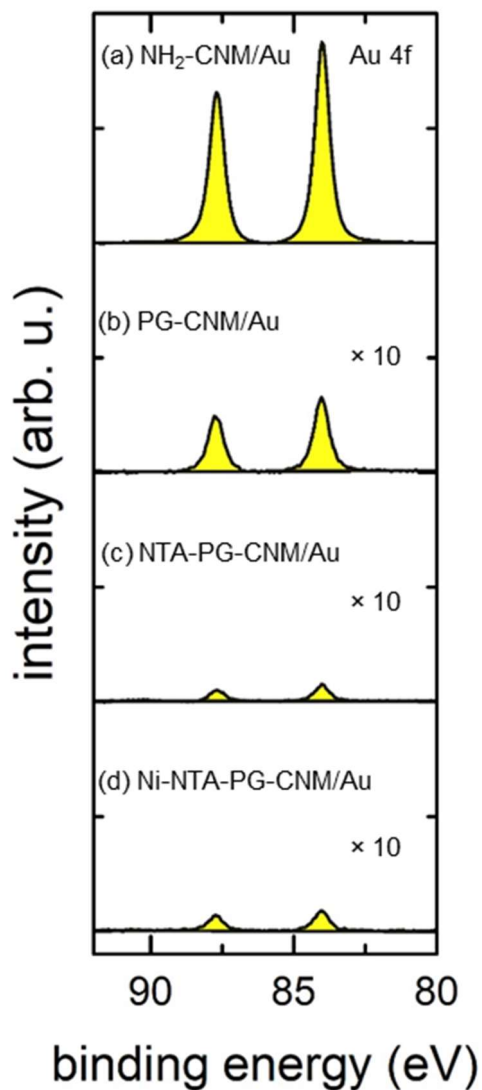


Figure S2. XP Au 4f spectra of gold substrates corresponding to each functionalization step presented in Figure 3. (a) Au-on-mica substrate after synthesis of pristine NH₂-CNM-on-Au. (b) After grafting of the PG layer, PG-CNM-on-Au. (c) After attachment of the NTA₄cyclen recognition sites, NTA-PG-CNM-on-Au. (d) After chelating of Ni²⁺, Ni-NTA-PG-CNM-on-Au.

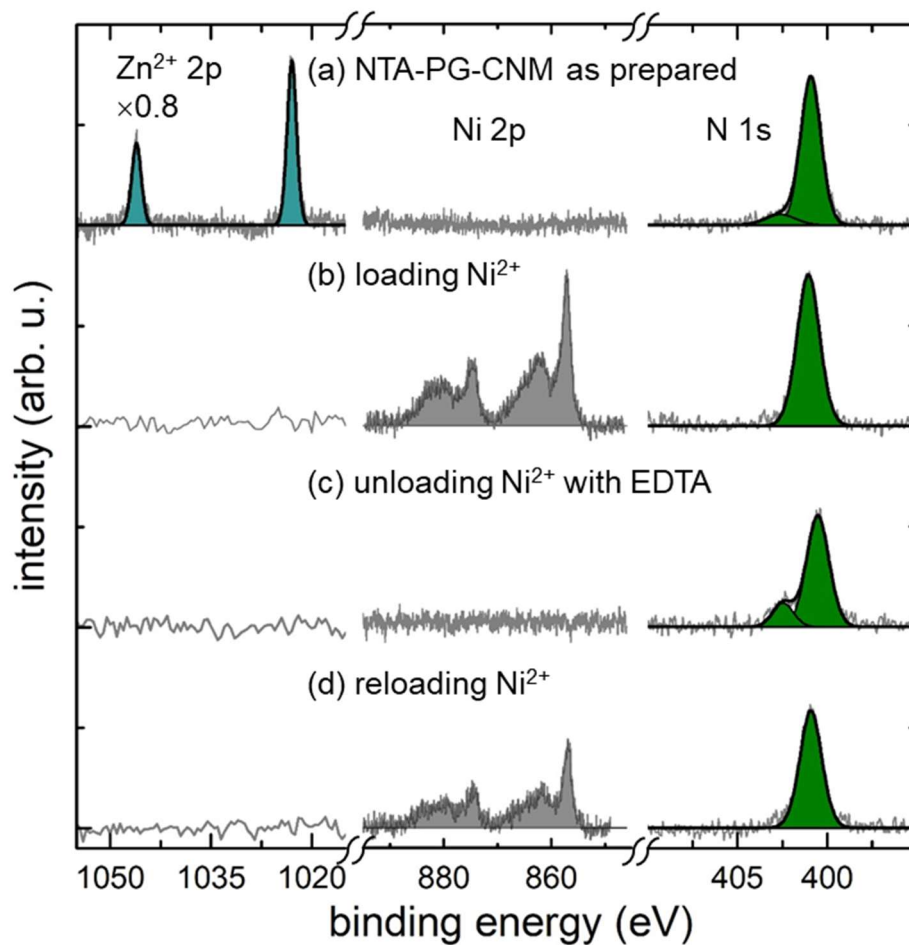
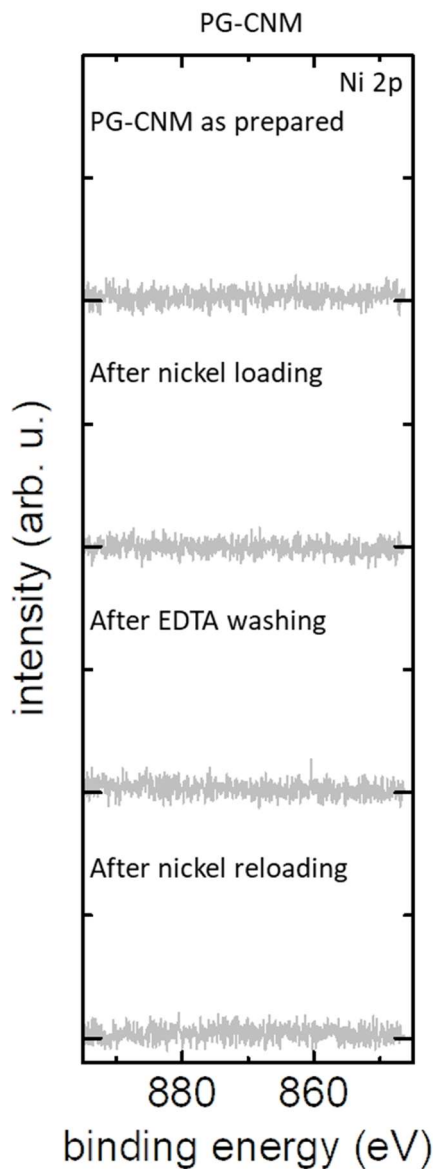


Figure S3. XPS analysis of the chelation and dechelation cycles. (a) As prepared NTA-PG-CNM. (b) After loading with Ni²⁺. (c) After removing of the chelated Ni²⁺ with EDTA. (d) After reloading of Ni²⁺ to the NTA-PG-CNM.



41
42
43
44
45
46
47
48
49
50
51
52
53
54
55
56
57
58
59
60

Figure S4. Control experiment of the chelation and dechelation test. A PG-CNM sample without NTA groups was treated with the same process as the NTA-PG-CNM sample in the chelation and dechelation test. For each step, the deposition was monitored by XPS (Ni 2p). No Ni signal is detected.

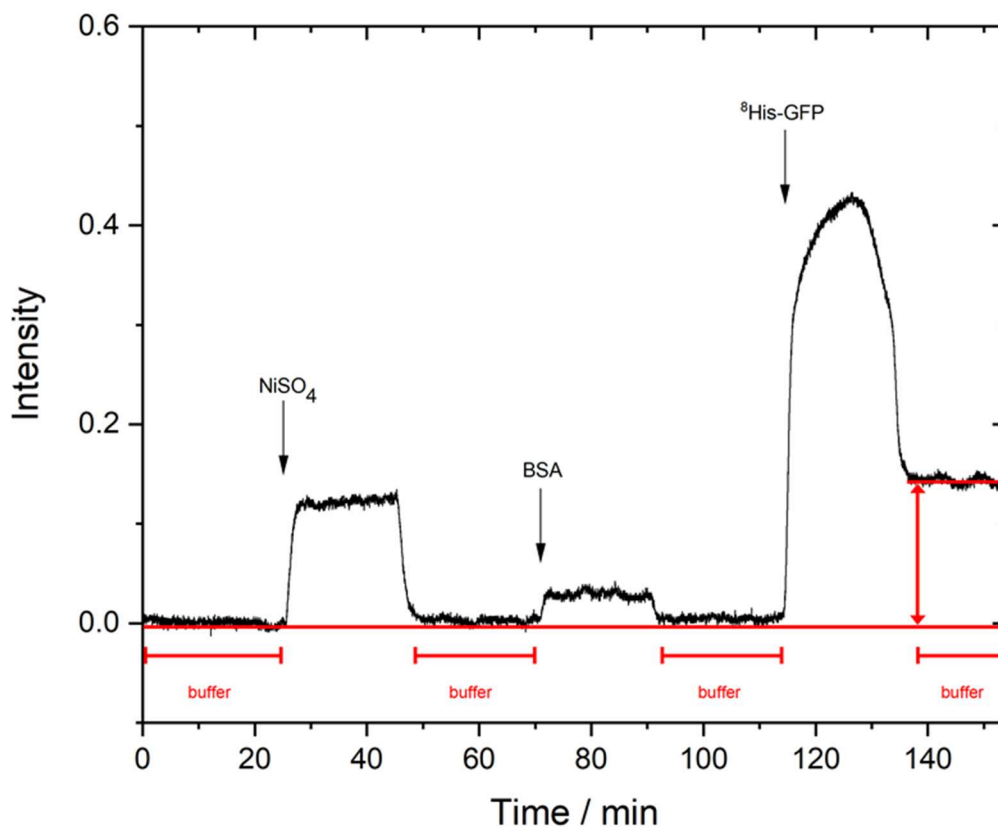


Figure S5. SPR analysis of the biorecognition of NTA-PG-CNM. The nanosheets were activated with nickel (0.1% in MilliQ) followed by a washing step with buffer. The change in signal is within the baseline noise. When incubated with BSA (1 mg/mL in 50 mM HEPES-buffer + 150 mM NaCl), no adhesion was found after switching back to pure buffer, demonstrating an efficient biorepulsion for non-labelled proteins. In contrast, the His₈-tagged GFP became strongly bound and did not become removed even after prolonged washing with buffer.

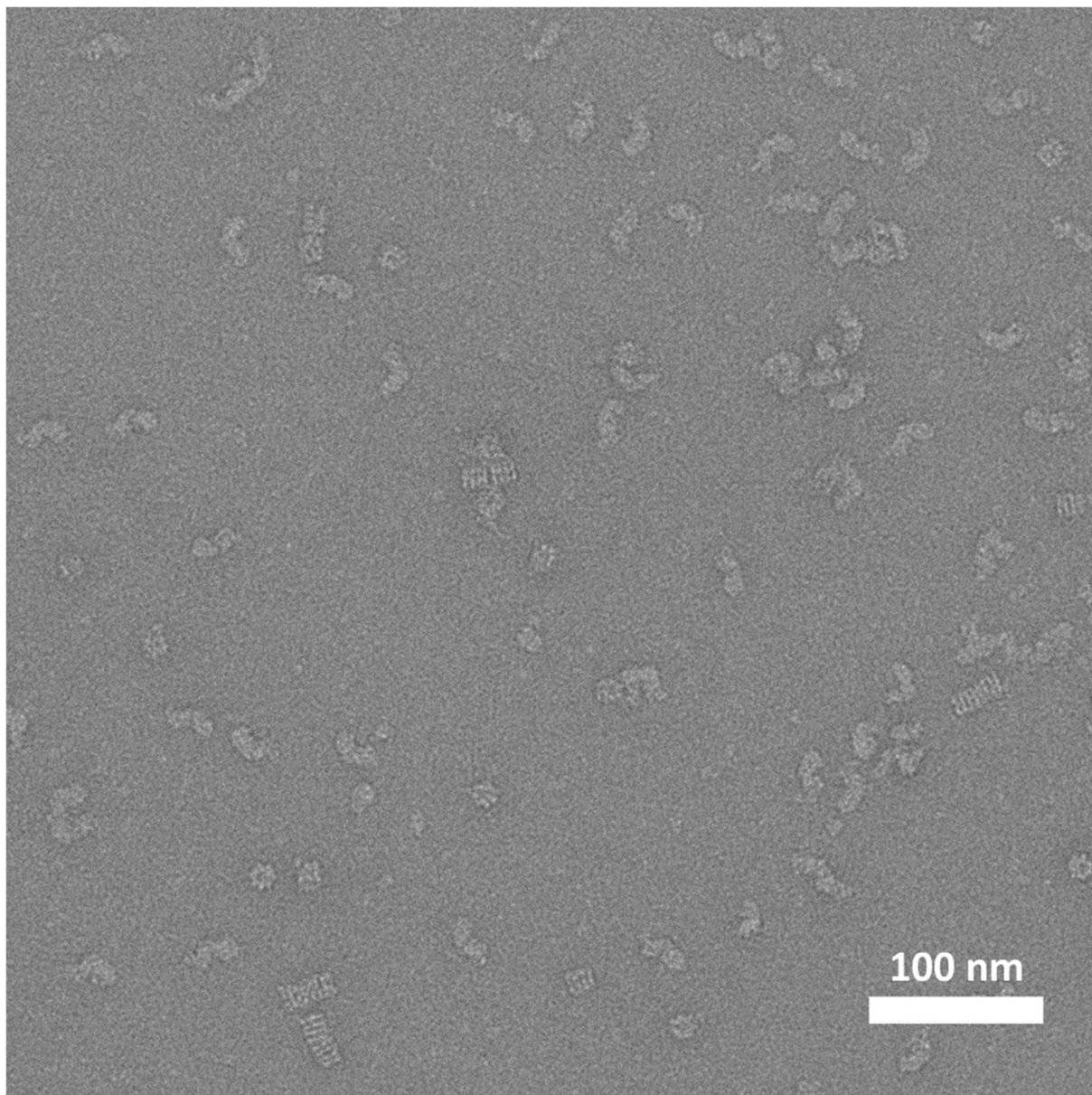


Figure S6. The TEM image of a negatively stained 1.16:1 mixture of complex I and GroEL deposited onto a conventional film of amorphous carbon. As the protein particles can be easily distinguished, it becomes apparent that no differentiation occurred during deposition.

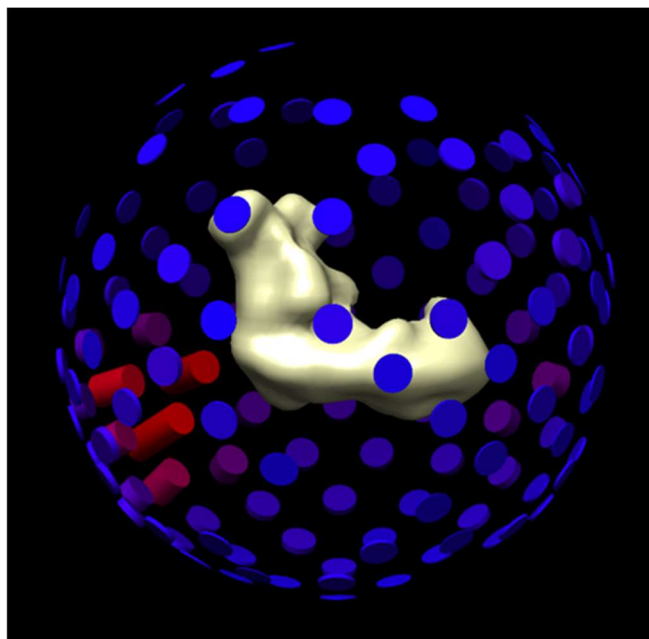


Figure S7. 3D density map of complex I from *Y. lipolytica* at 16 Å resolution together with the angular distribution plot for 3D reconstruction of the particles on the NTA-PG-CNM nanosheet.

5. References

1. Heeres, J. T.; Kim, S.-H.; Leslie, B. J.; Lidstone, E. A.; Cunningham, B. T.; Hergenrother, P. J., Identifying Modulators of Protein–Protein Interactions Using Photonic Crystal Biosensors. *J. Am. Chem. Soc.* **2009**, *131* (51), 18202-18203.
2. Turchanin, A.; Käfer, D.; El-Desawy, M.; Wöll, C.; Witte, G.; Götzhäuser, A., Molecular Mechanisms of Electron-Induced Cross-Linking in Aromatic SAMs. *Langmuir* **2009**, *25* (13), 7342-7352.
3. Turchanin, A.; Beyer, A.; Nottbohm, C. T.; Zhang, X.; Stosch, R.; Sologubenko, A.; Mayer, J.; Hinze, P.; Weimann, T.; Götzhäuser, A., One Nanometer Thin Carbon Nanosheets with Tunable Conductivity and Stiffness. *Adv. Mater.* **2009**, *21* (12), 1233-1237.
4. Winter, A.; George, A.; Neumann, C.; Tang, Z.; Mohn, M. J.; Biskupek, J.; Masurkar, N.; Reddy, A. L. M.; Weimann, T.; Hübner, U.; Kaiser, U.; Turchanin, A., Lateral heterostructures of two-dimensional materials by electron-beam induced stitching. *Carbon* **2018**, *128*, 106-116.
5. Turchanin, A.; El-Desawy, M.; Götzhäuser, A., High thermal stability of cross-linked aromatic self-assembled monolayers: Nanopatterning via selective thermal desorption. *Appl. Phys. Lett.* **2007**, *90* (5), 053102.
6. Pham, M.-C., Voltammetric and XPS Analysis of Metal-Complexed Polytyramine Films : Geometry-Dependent Electron Transfer Therein. *J. Electrochem. Soc.* **1984**, *131* (4), 777.
7. Scherr, J.; Parey, K.; Klusch, N.; Murphy, B. J.; Balsler, S.; Neuhaus, A.; Zickermann, V.; Kühlbrandt, W.; Terfort, A.; Rhinow, D., Self-Perforated Hydrogel Nanomembranes Facilitate Structural Analysis of Proteins by Electron Cryo-Microscopy. *ACS Nano* **2017**, *11* (6), 6467-6473.

P5. Optically triggered control of the charge carrier density in chemically functionalized graphene field effect transistors

Z. Tang, A. George, A. Winter, D. Kaiser, C. Neumann, T. Weimann, A. Turchanin

CHEMISTRY: A EUROPEAN JOURNAL, **2020**, DOI: 10.1002/chem.202000431

Carbon Materials | Hot Paper |

Optically Triggered Control of the Charge Carrier Density in Chemically Functionalized Graphene Field Effect Transistors

Zian Tang,^[a] Antony George,^[a] Andreas Winter,^[a] David Kaiser,^[a] Christof Neumann,^[a] Thomas Weimann,^[b] and Andrey Turchanin*^[a, c]

Abstract: Field effect transistors (FETs) based on 2D materials are of great interest for applications in ultrathin electronic and sensing devices. Here we demonstrate the possibility to add optical switchability to graphene FETs (GFET) by functionalizing the graphene channel with optically switchable azobenzene molecules. The azobenzene molecules were incorporated to the GFET channel by building a van der Waals heterostructure with a carbon nanomembrane (CNM), which is used as a molecular interposer to attach the azobenzene molecules. Under exposure with 365 nm and 455 nm light, azobenzene molecules transition between *cis* and *trans* molecular conformations, respectively, resulting in a switching of the molecular dipole moment. Thus, the effective electric field acting on the GFET channel is tuned by optical stimulation and the carrier density is modulated.

Graphene field effect transistors (GFETs) have attracted immense research attention due to their superior physical properties including high carrier mobility, ambipolar transport behaviour, high thermal conductivity, flexibility, transparency and high mechanical/chemical stability.^[1] The development of chemical vapour deposition (CVD) technique to synthesise large area high electronic quality graphene^[2] accelerated the evolution of GFETs and identified them as a promising candidate for ultrathin flexible electronics and sensing.^[3] Controlling

the electronic properties of GFET channel is highly desirable for the design and realization of devices and related applications. Charge carrier doping is an effective method to control the electronic properties of graphene. In recent years, several approaches were developed which enable effective control of charge carriers in GFET channels, including covalent functionalization of graphene with functional molecules,^[4] substitutional doping of other elements replacing carbon,^[5] and noncovalent functionalization by physisorption^[4b,6] or by interaction with self-assembled monolayers.^[5d,7] However, these methodologies possess certain drawbacks. The covalent functionalization of graphene requires the generation of dangling bonds^[4b] by chemical or plasma treatment resulting in increased charge carrier scattering leading to the decrease of conductivity and carrier mobility.^[4b] Substitutional doping of graphene with other elements results in similar issues.^[8] The noncovalent functionalization is a promising way towards non-destructive functionalization of graphene FETs, however, simple physisorption of functional molecules results in unstable doping of graphene, the doping effect varies significantly due to desorption/resorption of the adsorbates at different temperatures and humidity.^[9]

The functionalization of the graphene channel with responsive molecules provides additional opportunities to incorporate novel functionalities into GFETs. Such molecules can be used to modulate charge carrier concentration in the graphene channel.^[10] However, the chemically inert nature of graphene restricts the direct covalent functionalization of graphene surfaces.^[4b,11] In 2014, Woszczyzna et al. demonstrated an efficient non-destructive chemical functionalization method using atomically thin amino terminated carbon nanomembranes (NH₂-CNM)^[12] as a molecular ~1 nm thick interposer.^[13] In this approach, a van der Waals (vdW) heterostructure is fabricated with graphene and NH₂-CNM. As the amino groups of the CNM can be covalently functionalized, this method enables non-destructive functionalization of graphene while its original structural/electronic quality is preserved.^[13]

In this contribution, we demonstrate the integration of optically active azobenzene molecules with graphene channel to realize optically switchable GFET devices. The azobenzene molecules undergo reversible transformations between *cis* and *trans* molecular conformations under exposure to 365 nm and 455 nm light, respectively.^[1c,10a] The azobenzene molecule in its *cis*-conformation has a dipole moment of ≈ 3 D while in its *trans*-conformation does not possess any dipole moment.^[6b,14] By switching the azobenzene molecules between *cis*- (by

[a] Z. Tang, Dr. A. George, Dr. A. Winter, D. Kaiser, C. Neumann, Prof. Dr. A. Turchanin
Institute of Physical Chemistry, Friedrich Schiller University Jena
Lessingstraße 10, 07743 Jena (Germany)
E-mail: andrey.turchanin@uni-jena.de

[b] Dr. T. Weimann
Physikalisch-Technische Bundesanstalt (PTB), Bundesallee 100
38116 Braunschweig (Germany)

[c] Prof. Dr. A. Turchanin
Jena Center for Soft Matter, Philosophenweg 7, 07743 Jena (Germany)

Supporting information and the ORCID identification number(s) for the author(s) of this article can be found under:
<https://doi.org/10.1002/chem.202000431>.

© 2020 The Authors. Published by Wiley-VCH Verlag GmbH & Co. KGaA. This is an open access article under the terms of the Creative Commons Attribution License, which permits use, distribution and reproduction in any medium, provided the original work is properly cited.

Part of a Special Issue focusing on the "Chemical Functionalization of 2D Materials", which supports the symposium on the topic held at the E-MRS 2020 Spring Meeting. To view the complete issue, visit Issue 29.

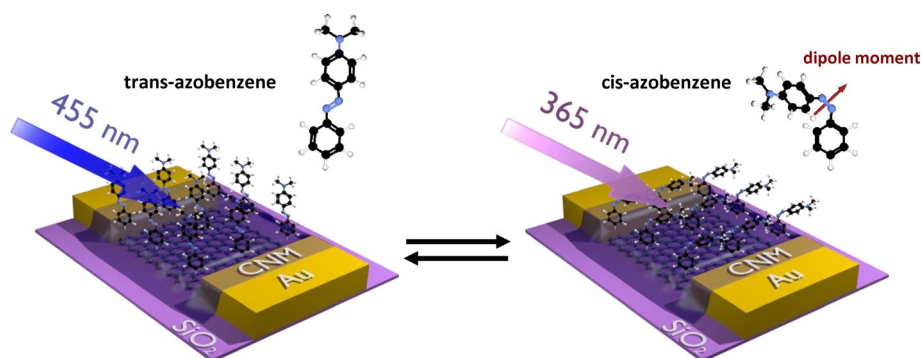


Figure 1. Schematic illustration of the working principle of an optically switchable GFET device. The azobenzene molecules immobilized on the amino-CNM undergo *cis*- and *trans*-transformations by exposure with 365 nm and 455 nm light, respectively. The red arrow in the magnified azobenzene molecule points towards the direction of the molecular dipole moment.

365 nm light) and *trans*- (by 455 nm light) conformation, the effective molecular field acting on the GFET channel can be modulated, thus changing doping level of the device.^[10a,15] In order to incorporate the graphene channel with azobenzene molecules, we prepared a van der Waals (vdW) heterostructure of azobenzene functionalized CNM (azo-CNM) with graphene. This is achieved by transferring a layer of the functionalized NH₂-CNM on top of an array of GFET devices. The optically switchable hybrid azo-GFET device in its two different conformations is schematically illustrated in Figure 1. The successful functionalization was confirmed by a detailed X-ray photoelectron spectroscopy (XPS) analysis. Electric transport measurements after irradiation with 365 nm and 455 nm light were performed to understand the operational characteristics of the optically switchable azo-GFET devices. Based on these data, we correlate the density of the functional azobenzene groups on the azo-GFET channel with the transport characteristics and therewith rationalize the observed switching behaviour.

First, we describe the synthesis of azo-CNMs. To this end, the NH₂-CNMs were prepared by electron beam induced cross-linking of 4'-nitro-1,1'-biphenyl-4-thiol (NBPT) self-assembled monolayers (SAMs) on gold/mica substrates.^[13,16] Subsequently, their functionalization with azobenzene was performed using the NHS-ester coupling reaction, as schematically shown in the supporting information (SI), Figure S1. The efficiency of the functionalization was studied by XPS. Thus, based on the attenuation of the substrate Au 4f signal (see Figure S2), an increase of the NH₂-CNM effective thickness from 1.2 nm to 1.4 nm was detected after the functionalization. In Figure 2a the XP N 1s spectra of a NH₂-CNM before and after the functionalization with azobenzene are presented. In the spectrum of a pristine NH₂-CNM (top) the peak at 399.4 eV (blue) corresponds to amino (-NH₂) groups. After the functionalization, the N 1s spectrum consists of two peaks showing in comparison to the pristine NH₂-CNM more than one type of nitrogen. The peak at 399.1 eV (blue) is due to both amino and tertiary amine^[17] groups; the peak at 400.3 eV (red) corresponds to nitrogen in the azo groups^[18] and in the amide^[19] groups connecting the azobenzene molecules to the CNM. Assuming the *trans*-conformation for the azobenzene and analysing quantitatively the N 1s intensities before and after the functionaliza-

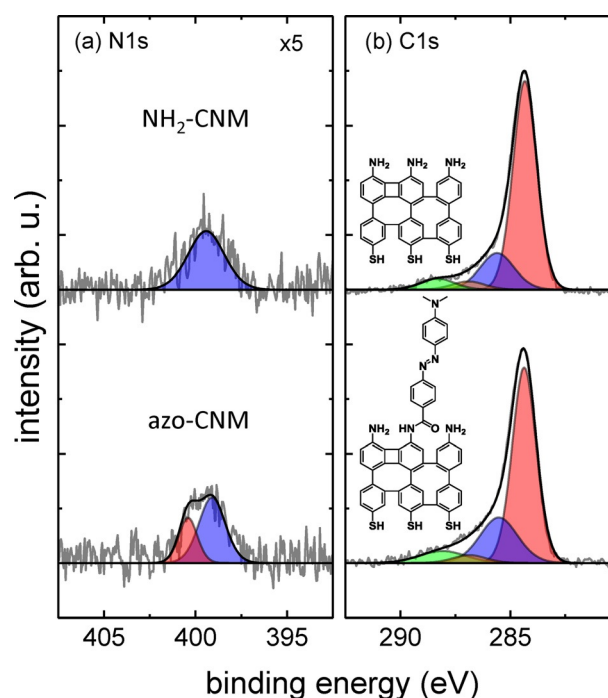


Figure 2. High-resolution N1s (a) and C1s (b) XP spectra of NH₂-CNM and azo-CNM.

tion, we estimate that 20(±3)% of the amino groups initially present in an NH₂-CNM are functionalized with azobenzene (see SI for details). In Figure 2b the respective XP C 1s signals are shown. After the functionalization, we observe an enhancement of the intensity at 285.5 eV (blue), which is due to carbon connected to azo and tertiary amine groups in the azobenzene. The amide group that links azobenzene to the CNM results in an increase (≈20%) of the C1s intensity at 288.1 eV (green) corresponding to a highly oxidized carbon species.^[20] Note that due to an attenuation caused by the grafted azobenzene layer, the C 1s peaks representing the aromatic (284.3 eV, red) and ketone (286.9 eV, orange) carbon species became less intensive. In comparison to the pristine NH₂-CNM sample, we observe also an attenuation of the S 2p signal in the functionalized sample, Figure S2. All these findings clearly

demonstrate a successful grafting of the azobenzene molecules to the terminal amino groups of NH_2 -CNMs and thereafter with the synthesis of azo-CNMs.

Next, we describe the fabrication and characterization of azo-CNM/GFET devices. The single layer graphene (SLG) was grown by chemical vapour deposition (CVD) on Cu foils and transferred onto a Si substrate with 600 nm thermally grown SiO_2 layer using the non-destructive transfer method.^[21] The graphene quality was controlled by optical microscopy and Raman spectroscopy (Figure S3). The GFET devices were fabricated by defining an array of source-drain contacts (30 nm Au/5 nm Ti) on the previously transferred graphene by electron beam lithography, metallization, lift-off and etching procedure.^[13] After the basic optical and electrical characterization of the device arrays (SI, Figure S4 a-c), an azo-CNM was transferred on top of the devices. In this way, the vdW heterostructure was formed at the channel region of the GFET device as shown schematically in Figure 1. The typical field-effect mobility of the charge carriers in the fabricated devices was $\approx 2500 \text{ cm}^2/\text{Vs}$.

To investigate the electrical characteristics and to test the optical switchability of the heterostructure devices, we have performed a series of field-effect transport measurements with and without optical excitation. We used two light emitting diodes (LED) with emission wavelengths of 365 nm and 455 nm to optically excite the azobenzene molecules to *cis* and *trans* conformation. We initially measured the pristine GFET devices before transferring the azo-CNM to test any effect on pristine devices within the range of illumination intensities used for the switching experiments. Transfer curves of a pristine GFET device before and after illumination with 365 nm and 455 nm wavelengths are presented in SI Figure S4a and Figure S4b, respectively. Each transfer curve was recorded under dark condition, immediately after 15 minutes of illumination. The results show no significant difference in the transfer curves and confirm that the light has no noticeable effect on pristine graphene devices within the range of illumination intensities we used. We have also tested a GFET device with a transferred NH_2 -CNM (without azobenzene functionalization) on top with similar illumination conditions as presented in SI Figures S4 d and e, which also did not show

any significant difference in the transfer characteristics after irradiation.

We present in Figure 3a the typical transfer characteristics of an azo-CNM/GFET device, immediately after irradiation with 365 or 455 nm for about 1 hour. The measurements were recorded in dark after the light exposure. By exposing the device with the two different wavelengths, the charge neutrality point (commonly known as Dirac point) of the device can be switched reversibly. When the device is exposed with the light of 365 nm wavelength, the Dirac point shifts to lower values of the gate voltage, V_G , which shows a doping of the device with negative charge carriers. When the device is exposed with the light of 455 nm wavelength, the Dirac point shifts towards a higher gate voltage, indicating removal of the *n*-doping effect caused by the exposure of shorter wavelength light. In Figure 3b, we present the time-dependent switching behaviour of the same azo-CNM/GFET device for two exposure cycles with 365 nm and 455 nm. The transfer curves were recorded every minute during exposure until the transfer characteristics did not any longer shift significantly. Before exposure with 365 nm wavelength, the Dirac point of the device was at 131 V. After exposure to 365 nm wavelength for $\approx 1 \text{ h}$ the Dirac point shifted to 94 V, corresponding to a doping with negative charge carriers. When the device is exposed with 455 nm wavelength the induced *n*-doping was lifted and the Dirac point of the device shifted back to 125 V. The corresponding transfer curves for each time dependent exposure are presented in Figure S5. As was demonstrated earlier,^[22] the photoswitching of azobenzene molecules incorporated into alkanethiol SAMs follows a simple exponential behaviour. Therefore, the shift of the Dirac point was fitted with single exponential functions in order to obtain the respective time constants (see Figure S5e). Both *trans* to *cis* and *cis* to *trans* photoswitching were found to be of a similar value of $10(\pm 0.5) \text{ min}$. Note that in our experiments the intensity of the 455 nm light was a factor of 1.5 higher than the intensity of the 365 nm light (see Experimental for details), which implies that the *trans* to *cis* switching is more efficient than the *cis* to *trans*. These results are in a good qualitative agreement with the respective photoswitching cross sections measured for different azobenzene SAMs on gold.^[23] Employing this finding, we used subse-

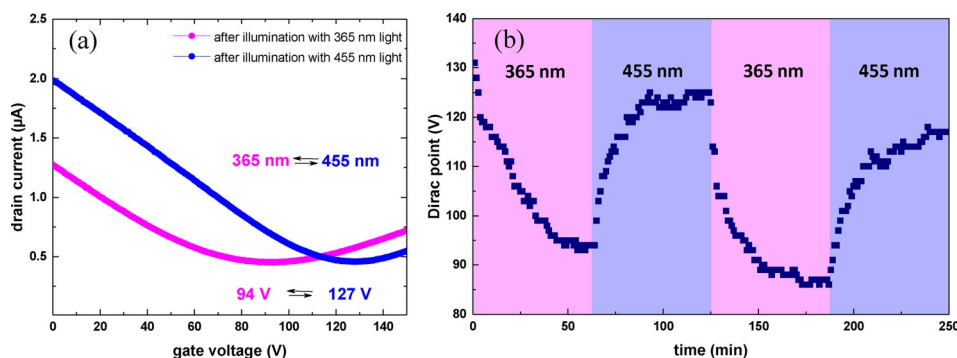


Figure 3. Photoresponsive behaviour of azo-CNM/GFET devices. (a) The transfer curves of an azo-CNM/GFET after illumination for 60 min with 365 nm and 455 nm light. (b) Time dependent change of the position of Dirac point until sequential illumination with 365 nm and 455 nm light; the corresponding curves are presented in Figure S5.

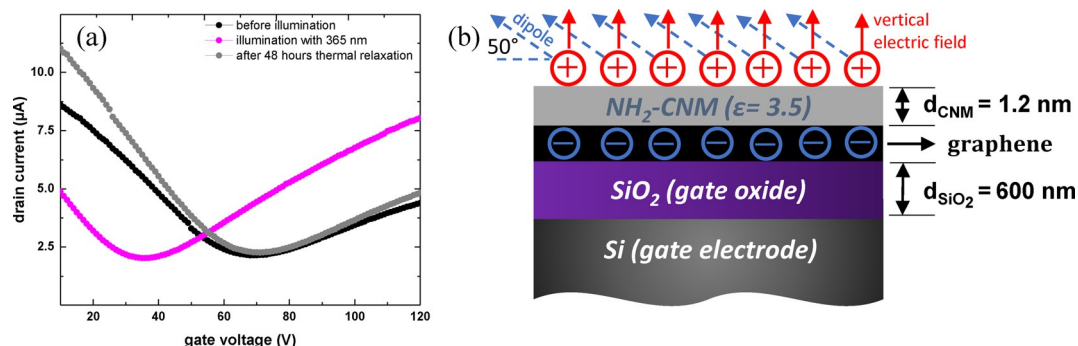


Figure 4. (a) Transfer curves of an azo-CNM/GFET device recorded before exposure, after exposure with 365 nm light and after thermal relaxation at RT for two days. (b) Schematic illustration of the induced electric field effect due to the conformational change of azobenzene from *trans* to *cis*.

quent 15 min irradiations with 365 nm and 455 nm to modulate a reversible shift of the Dirac point by ~ 20 V in the azo-CNM/GFETs (see Figure S6).

In the following, we analyse the observed photoswitching behaviour considering the surface density azobenzene molecules on the azo-CNM/GFET channel and the respective induced electrical field in their *cis* conformation. In Figure 4a, we show the transport curves of a device before and after a single irradiation with 365 nm wavelength. The black curve represents the transfer characteristics of the pristine device. The Dirac point of the device is at 69 V. The purple curve represents the transfer characteristics after irradiation with 365 nm wavelength, which results in a shift of the Dirac point to 35 V. The grey curve represents the transfer curve of the device after thermal relaxation at room temperature (RT) for 48 hours, which demonstrates that the device restored the original position of the Dirac point, that is, its doping level. We estimate from the time dependent measurements the time constant of the thermally induced *cis* to *trans* relaxation to ≈ 15 h, which is in good qualitative agreement with an earlier study for azobenzene SAMs.^[24] We attribute the observed photoswitching behaviour on the modulation of the Dirac point, that is, doping level, of the azo-GFET devices to the variation of the local electric field acting on the graphene channel due to the *cis* and *trans* conformations of the azobenzene molecules triggered by the light excitation. Assuming that initially all molecules are in the thermally stable *trans*-state with a dipole moment $\mu_{trans} \approx 0$ D, no effective electric field is present in the azobenzene layer before irradiation with 365 nm light. After the irradiation, the azobenzene molecules adopt the *cis*-conformation with a dipole moment of 3 D.^[25] The effective electric field induced by the molecules can be calculated then (see Figure 4b) using the relation [Eq. (1)]:^[26]

$$E = N \left(\frac{\sin\theta \mu_{mol}}{\epsilon_r \epsilon_0 d_{mol}} \right) \quad (1)$$

where N and d_{mol} are the surface density and length of the azobenzene molecules in the *cis*-conformation, μ_{mol} is the dipole moment of the molecule, θ is the angle between the dipole moment and the surface, which is approximately 50° ^[25a] and ϵ_r is the relative dielectric constant within the azobenzene

layer.^[26] Based on the surface density of the amino groups in a NH_2 -CNM and their functionalization efficiency with the azobenzene molecules obtained by XPS, we can estimate the surface density of the azobenzene species on the channel of an azo-CNM/GFET. The density of amino groups in a NH_2 -CNM is ~ 3.3 molecules/ nm^2 (i.e., $3.3 \times 10^{14} \text{ cm}^{-2}$).^[12] Considering that only $\sim 20\%$ of these groups are functionalized with azobenzene, their surface density is then $6.6 \times 10^{13} / \text{cm}^2$. The length of the azobenzene molecule in the *cis*-conformation is ≈ 0.7 nm. The typical relative dielectric constant of organic molecules can be taken as ≈ 3 .^[26,27] Therewith, the vertical effective electric field within the azobenzene layer is calculated to be 272 MV m^{-1} . With the azobenzene thickness in its *cis*-conformation of 0.7 nm, the effective gate voltage applied to the NH_2 -CNM, acting as a gate dielectric for the graphene channel, is 0.19 V. Figure 4b schematically illustrates this consideration. Thus, the variation of the charge carrier concentration induced by the presence of the molecular dipoles can be calculated using Equation (2):

$$\Delta n_{cis \rightarrow trans} = \frac{C_{CNM} \Delta V_{cis \rightarrow trans}}{e} \quad (2)$$

where C_{CNM} is the capacitance of NH_2 -CNM, $\Delta V_{cis \rightarrow trans}$ is the variation in the top gate voltage caused by the molecular dipoles and e is the charge of an electron. The capacitance of NH_2 -CNM is calculated as $2.6 \times 10^{-2} \text{ F m}^{-2}$ using Equation (3):

$$C_{CNM} = \epsilon_0 \epsilon_{CNM} / d_{CNM} \quad (3)$$

where the dielectric constant $\epsilon_{CNM} = 3.5$ ^[28] and $d_{CNM} = 1.2$ nm. Thus the charge carrier concentration induced by the molecular field can be estimated to $3.11 \times 10^{12} \text{ cm}^{-2}$. From our transport measurements, we have estimated the variation in charge carrier concentration using Equation (4):

$$\Delta n = \frac{C_{SiO_2} (\Delta V_{Dirac})}{e} \quad (4)$$

where C_{SiO_2} is the capacitance of the silicon oxide layer of thickness 600 nm, which is calculated as $5.75 \times 10^{-5} \text{ F m}^{-2}$ and ΔV_{Dirac} is the shift in Dirac point, which is on average 35 V. The estimated change in charge carrier concentration from the

transport measurement is $1.26 \times 10^{12} \text{ cm}^{-2}$. This result demonstrates a very fair correspondence between the estimation and the experimentally observed changes in the charge carrier concentration between due to the *trans*–*cis* conformational change in the azobenzene.

In this work, we presented a route towards optically triggered control of the charge carrier density in GFET devices by functionalizing them via the van der Waals assembly of ~ 1 nm thick molecular nanosheets—azo-CNMs. The density of azobenzene functional groups in these molecular nanosheets was obtained from XPS analysis enabling us to study the photoresponse of the devices quantitatively. By illuminating azo-CNM/GFET devices with 365 nm light, the azobenzene molecules undergo a change from *trans* to *cis* conformation, which induces a positive voltage at the device gate resulting in a respective shift of the Dirac point towards lower voltages, that is, its effective *n*-doping. The application of the 455 nm light induces a reversible change of the device transport characteristics. The observed modification of the charge carrier concentration in the graphene channel corresponds well with a simple model, considering the surface density of azobenzene molecules in an azo-CNM and a respective induced electrical field due to the *trans*–*cis* transformation. Therewith, a new methodology towards chemical functionalization of graphene FETs with light responsive molecules is presented, which in perspective also can be adapted to other electronic two-dimensional materials like, e.g., transition metal dichalcogenides.

Experimental Section

Synthesis of NH₂-CNMs

NH₂-CNMs were synthesised by electron-beam-induced crosslinking of 4'-nitro-1,1'-biphenyl-4-thiol (NBPT, Taros 99%, sublimated before use) self-assembled monolayers (SAMs) on gold. To form the SAMs, we used 300 nm thermally evaporated Au on mica substrates (Georg Albert PVD-Coatings). The substrates were cleaned in an oxygen plasma for 30 seconds, rinsed with ethanol (VWR, HPLC grade) and dried in a stream of nitrogen. The substrates were then immersed in a ≈ 0.1 mmol solution of NBPT in dry, degassed *N,N*-dimethylformamide (DMF, Alfa Aesar 99.9%) for 72 h in a sealed flask under nitrogen. After the formation of the SAM, the samples were rinsed with DMF and ethanol several times and blown dry in a nitrogen stream. Finally, the samples were irradiated using a low-energy electron gun (FG15/40, Specs) with an energy of 100 eV and an electron dose of 50 mC cm^{-2} under high vacuum conditions (1×10^{-8} mbar). This converts the SAM into a CNM by an established electron beam induced crosslinking process.^[29]

Functionalization of NH₂-CNM with azobenzene molecules

Triethylamine (TEA, Sigma Aldrich 99.5%) was used as a de-protonating agent for amino groups. 4-[4-(Dimethylamino)phenylazo]benzoic acid *N*-succinimidyl ester (azobenzene-NHS, Sigma Aldrich 98%) was used as an azobenzene derivative to functionalize the NH₂-CNMs. The NH₂-CNM on an Au substrate is rinsed with ethanol and then blown dry under a stream of nitrogen. Afterwards it is placed in a clean test tube along with 2 mL DMF, 10 μL TEA and ≈ 0.1 mg azobenzene-NHS. The solution was then shaken for 5 minutes and put into the dark for 72 h at room temperature.

X-ray photoelectron spectroscopy

XPS was carried out in a Multiprobe UHV system (Scienta Omicron) using a monochromatic X-ray source (Al K_α, 1486.7 eV) and an electron analyser (Argus CU) with a resolution of 0.6 eV. The XP spectra were fitted using Voigt functions (30:70) after Shirley (C1s) or linear (N1s, S2p) background subtraction. The thickness of the CNMs was calculated from the attenuation of the XP Au4f signal in comparison to the Au4f signal of a clean Au reference employing the Beer–Lambert law and the attenuation length of 36 Å.^[30]

Raman spectroscopy

The Raman spectra were acquired using a Bruker Senterra spectrometer operated in backscattering mode. Measurements at 532 nm were obtained with a frequency-doubled Nd:YAG Laser, a 50 \times objective and a thermoelectrically cooled CCD detector. The spectral resolution of the system is 2–3 cm^{-1} . For all spectra, the Si peak at 520.7 cm^{-1} was used for peak shift calibration of the instrument.

Fabrication steps of GFET devices

Single-layer graphene is grown by chemical vapor deposition (CVD) on Cu foils following the protocol of Li et al.^[2a] The fabricated graphene was delaminated from the Cu foil with the electrochemical method then transferred to highly doped silicon wafers with 600 nm dry thermal oxide. Then, Ti (2 nm)/Au (100 nm) metal contacts of two-terminal were defined using standard e-beam lithography and lift-off process.

Irradiation of GFET, NH₂-CNM/GFET and azo-CNM/GFET devices with light

The light-emitting diodes (THORLABS) with dominant wavelengths of 365 nm (M365L2) and 455 nm (M455L3) were used in this study. For irradiation of the FET devices their irradiation intensities were adjusted to $\approx 6 \text{ mW cm}^{-2}$ for 365 nm LED and $\approx 9 \text{ mW cm}^{-2}$ for 455 nm LED.

Electrical characterization

The electrical characterization was carried out with Keithley 2614B/2634B Source Measure Units. One SMU was used to change the voltage of the gate with respect to the source/drain in the range between -80 and 150 V for the back-gated devices in vacuum. The other SMU was used to apply the Source-Drain Voltage of 10 mV. A lakeshore vacuum needle probe station TTPX was used to measure the devices in vacuum with back gate.

Acknowledgements

We acknowledge funding from the European Union's Horizon 2020 research and innovation program under grant agreement No. 634415, the DFG research infrastructure grant (INST 275/257-1 FUGG), the DFG research grants TU149/5-1 and TU149/8-2 as well as the DFG TRR 234 "CataLight" (Projects B7, Z2). We thank Stephanie Höppener and Ulrich S. Schubert for enabling our Raman spectroscopy studies at the JCSM.

Conflict of interest

The authors declare no conflict of interest.

Keywords: 2D materials · chemical functionalization · field effect transistors · graphene · photoresponsive devices

- [1] a) F. Schwierz, *Nat. Nanotechnol.* **2010**, *5*, 487–496; b) J. L. Xia, F. Chen, P. Wiktor, D. K. Ferry, N. J. Tao, *Nano Lett.* **2010**, *10*, 5060–5064; c) Y. An, A. Behnam, E. Pop, A. Ural, *Appl. Phys. Lett.* **2013**, *102*, 013110; d) B. Zhan, C. Li, J. Yang, G. Jenkins, W. Huang, X. Dong, *Small* **2014**, *10*, 4042–4065.
- [2] a) X. Li, W. Cai, J. An, S. Kim, J. Nah, D. Yang, R. Piner, A. Velamakanni, I. Jung, E. Tutuc, S. K. Banerjee, L. Colombo, R. S. Ruoff, *Science* **2009**, *324*, 1312–1314; b) X. Li, L. Colombo, R. S. Ruoff, *Adv. Mater.* **2016**, *28*, 6247–6252.
- [3] a) B. Aissa, N. K. Memon, A. Ali, M. K. Khraisheh, *Front. Mater.* **2015**, *2*, <https://doi.org/10.3389/fmats.2015.00058>; b) A. Nag, A. Mitra, S. C. Mukhopadhyay, *Sens. Actuator A Phys.* **2018**, *270*, 177–194; c) S. K. Krishnan, E. Singh, P. Singh, M. Meyyappan, H. S. Nalwa, *RSC Adv.* **2019**, *9*, 8778–8881.
- [4] a) W. Fu, L. Jiang, E. P. van Geest, L. M. C. Lima, G. F. Schneider, *Adv. Mater.* **2017**, *29*, 1603610; b) V. Georgakilas, M. Otyepka, A. B. Bourlino, V. Chandra, N. Kim, K. C. Kemp, P. Hobza, R. Zboril, K. S. Kim, *Chem. Rev.* **2012**, *112*, 6156–6214.
- [5] a) H. Liu, Y. Liu, D. Zhu, *J. Mater. Chem.* **2011**, *21*, 3335–3345; b) Z.-S. Wu, K. Parvez, A. Winter, H. Vieker, X. Liu, S. Han, A. Turchanin, X. Feng, K. Müllen, *Adv. Mater.* **2014**, *26*, 4552–4558; c) S. Agnoli, M. Favaro, *J. Mater. Chem. A* **2016**, *4*, 5002–5025; d) J. Zhang, C. Zhao, N. Liu, H. Zhang, J. Liu, Y. Q. Fu, B. Guo, Z. Wang, S. Lei, P. Hu, *Sci. Rep.* **2016**, *6*, 28330; e) L. Feng, Z. Qin, Y. Huang, K. Peng, F. Wang, Y. Yan, Y. Chen, *Sci. Total Environ.* **2020**, *698*, 134239.
- [6] a) H. Medina, Y.-C. Lin, D. Oberfell, P.-W. Chiu, *Adv. Funct. Mater.* **2011**, *21*, 2687–2692; b) J. A. Mann, W. R. Dichtel, *J. Phys. Chem. Lett.* **2013**, *4*, 2649–2657.
- [7] a) Z. Yan, Z. Sun, W. Lu, J. Yao, Y. Zhu, J. M. Tour, *ACS Nano* **2011**, *5*, 1535–1540; b) D. K. Hong Tsang, T. J. Lieberthal, C. Watts, I. E. Dunlop, S. Ramadan, A. E. del Rio Hernandez, N. Klein, *Sci. Rep.* **2019**, *9*, 13946.
- [8] L. Tsetseris, B. Wang, S. T. Pantelides, *Phys. Rev. B* **2014**, *89*, 035411.
- [9] L. Kong, A. Enders, T. S. Rahman, P. A. Dowben, *J. Phys. Condens. Matter* **2014**, *26*, 443001.
- [10] a) Y. Zhao, S. Bertolazzi, P. Samori, *ACS Nano* **2019**, *13*, 4814–4825; b) Y. Zhao, S. Ippolito, P. Samori, *Adv. Opt. Mater.* **2019**, *7*, 1900286.
- [11] a) T. Kaila, S. Bose, A. K. Mishra, P. Khanra, N. H. Kim, J. H. Lee, *Prog. Mater. Sci.* **2012**, *57*, 1061–1105; b) G.-h. Yang, D.-d. Bao, H. Liu, D.-q. Zhang, N. Wang, H.-t. Li, *J. Inorg. Organomet. Polym. Mater.* **2017**, *27*, 1129–1141.
- [12] A. Turchanin, A. Götzhäuser, *Adv. Mater.* **2016**, *28*, 6075–6103.
- [13] M. Woszczyna, A. Winter, M. Grothe, A. Willunat, S. Wundrack, R. Stosch, T. Weimann, F. Ahlers, A. Turchanin, *Adv. Mater.* **2014**, *26*, 4831–4837.
- [14] a) E. Merino, M. Ribagorda, *Beilstein J. Org. Chem.* **2012**, *8*, 1071–1090; b) S. Osella, A. Minoia, D. Beljonne, *J. Phys. Chem. C* **2016**, *120*, 6651–6658.
- [15] I. C.-Y. Hou, V. Diez-Cabanes, A. Galanti, M. Valášek, M. Mayor, J. Cornil, A. Narita, P. Samori, K. Müllen, *Chem. Mater.* **2019**, *31*, 6979–6985.
- [16] Z. Zheng, C. T. Nottbohm, A. Turchanin, H. Muzik, A. Beyer, M. Heilemann, M. Sauer, A. Götzhäuser, *Angew. Chem. Int. Ed.* **2010**, *49*, 8493–8497; *Angew. Chem.* **2010**, *122*, 8671–8675.
- [17] Q. Zhao, Y. Zhu, Z. Sun, Y. Li, G. Zhang, F. Zhang, X. Fan, *J. Mater. Chem. A* **2015**, *3*, 2609–2616.
- [18] Y. Feng, H. Liu, W. Luo, E. Liu, N. Zhao, K. Yoshino, W. Feng, *Sci. Rep.* **2013**, *3*, 3260.
- [19] R. A. Shircliff, P. Stradins, H. Moutinho, J. Fennell, M. L. Ghirardi, S. W. Cowley, H. M. Branz, I. T. Martin, *Langmuir* **2013**, *29*, 4057–4067.
- [20] G. Zorn, L.-H. Liu, L. Árnadóttir, H. Wang, L. J. Gamble, D. G. Castner, M. Yan, *J. Phys. Chem. C* **2014**, *118*, 376–383.
- [21] Y. Wang, Y. Zheng, X. Xu, E. Dubuisson, Q. Bao, J. Lu, K. P. Loh, *ACS Nano* **2011**, *5*, 9927–9933.
- [22] A. S. Kumar, T. Ye, T. Takami, B.-C. Yu, A. K. Flatt, J. M. Tour, P. S. Weiss, *Nano Lett.* **2008**, *8*, 1644–1648.
- [23] N. R. Krekieleh, M. Müller, U. Jung, S. Ulrich, R. Herges, O. M. Magnussen, *Langmuir* **2015**, *31*, 8362–8370.
- [24] T. Moldt, D. Przyrembel, M. Schulze, W. Bronsch, L. Boie, D. Brete, C. Gahl, R. Klajn, P. Tegeder, M. Weinelt, *Langmuir* **2016**, *32*, 10795–10801.
- [25] a) G. S. Hartley, R. J. W. Le Fèvre, *J. Chem. Soc.* **1939**, 531–535; b) A. J. Petro, *J. Am. Chem. Soc.* **1958**, *80*, 4230–4232; c) R. J. Ouellette, J. D. Rawn, *Organic Chemistry*, 2nd ed., Academic Press, **2018**, p. 1–30.
- [26] S. Kobayashi, T. Nishikawa, T. Takenobu, S. Mori, T. Shimoda, T. Mitani, H. Shimotani, N. Yoshimoto, S. Ogawa, Y. Iwasa, *Nat. Mater.* **2004**, *3*, 317–322.
- [27] G. Ashkenasy, D. Cahen, R. Cohen, A. Shanzer, A. Vilan, *Acc. Chem. Res.* **2002**, *35*, 121–128.
- [28] X. Zhang, E. Marschewski, P. Penner, T. Weimann, P. Hinze, A. Beyer, A. Götzhäuser, *ACS Nano* **2018**, *12*, 10301–10309.
- [29] A. Turchanin, D. Käfer, M. El-Desawy, C. Wöll, G. Witte, A. Götzhäuser, *Langmuir* **2009**, *25*, 7342–7352.
- [30] A. Turchanin, M. El-Desawy, A. Götzhäuser, *Appl. Phys. Lett.* **2007**, *90*, 053102.

Manuscript received: January 9, 2020

Revised manuscript received: February 22, 2020

Accepted manuscript online: March 9, 2020

Version of record online: March 27, 2020

Documentation of Authorship

P1. Electrochemical delamination assisted transfer of molecular nanosheets				
Z. Tang,¹ C. Neumann,² A. Winter,³ A. Turchanin⁴				
<i>Nanoscale</i> . 2020 , 12, 8656 - 8663				
Author	1	2	3	4
Conceptual contributions	X			X
CNMs preparation	X			
XPS analysis	X	X	X	
Transfer of the CNMs	X			
SEM characterization		X	X	
AFM analysis	X			
Evaluation of the data	X			
Writing of the manuscript	X			X
Proposal for crediting publication equivalents	1.0			

<p>P2. Selective ion sieving through arrays of sub-nanometer nanopores in chemically tunable P. van Deursen,¹ Z. Tang,² A. Winter,³ M. Mohn,⁴ U. Kaiser,⁵ A. Turchanin,⁶ G. Schneider.⁷ <i>Nanoscale</i>. 2019 11, 20785-20791</p>							
Author	1	2	3	4	5	6	7
Conceptual contributions	X					X	X
CNMs preparation		X	X				
XPS analysis		X	X				
Preparation of the substrates	X						
Transfer of the CNMs		X	X				
Microscopic characterization (TEM)				X	X		
Electrochemical characterization	X						
Evaluation of the data	X					X	X
Writing of the manuscript	X	X				X	X
Proposal for crediting publication equivalents	1.0	0.75					

P3. Plasmonic Metasurfaces Situated on Ultra-thin Carbon Nanomembranes							
Y. Denizhan Sirmaci, ¹ Zian Tang , ² Stefan Fasold, ³ Christof Neumann, ⁴ Thomas Pertsch, ⁵ Andrey Turchanin, ⁶ and Isabelle Staude ⁷							
ACS. Photonics. 2020, 7, 1060-1066.							
Author	1	2	3	4	5	6	7
Conceptual contributions					X	X	X
CNMs preparation		X					
XPS analysis		X		X			
Linear-optical transmittance spectra	X						
Transfer of the CNMs		X		X			
Fabrication of the nanostructures			X				
Preparation metamembranes	X						
Characterization metamembranes	X						
Microscopic characterization (SEM)	X		X				
Writing of the manuscript	X				X	X	X
Proposal for crediting publication equivalents	1.0	0.75					

P4. Smart molecular nanosheets for advanced preparation of biological samples in electron cryo-microscopy

J. Scherr,¹ **Z. Tang**,² M. Küllmer,³ S. Balsler,⁴ A. S. Scholz,⁵ A. Winter,⁶ K. Parey,⁷ A. Rittner,⁸ M. Grininger,⁹ V. Zickermann,¹⁰ D. Rhinow,¹¹ A. Terfort,¹² A. Turchanin¹³

Submitted to ACS Nano. 2020.

Author	1	2	3	4	5	6	7	8	9	10	11	12	13
Conceptual contributions											X	X	X
SAMs preparation		X	X			X							
CNMs fabrication		X				X							
CNMs functionalization	X	X	X										
IRRAS analysis	X												
SPR analysis	X				X								
XPS analysis		X	X			X							
AFM analysis	X	X											
Protein synthesis								X	X	X			
Protein immobilization				X									
cryoEM characterization							X						
Writing of the manuscript	X	X									X	X	X
Proposal for crediting publication equivalents	1.0	1.0	0.5										

<p>P5. Optically triggered control of the charge carrier density in chemically functionalized graphene field effect transistors</p> <p>Z. Tang,¹ A. George,² A. Winter,³ D. Kaiser,⁴ C. Neumann,⁵ T. Weimann,⁶ A. Turchanin⁷</p> <p><i>Chem. Eur. J.</i> 2020, DOI: 10.1002/chem.202000431</p>							
Author	1	2	3	4	5	6	7
Conceptual contributions	X	X					X
CNMs preparation	X						
XPS analysis	X		X		X		
Transfer of the CNMs	X						
Raman spectroscopy	X				X		
Preparation of the FET device		X		X		X	
Characterization of the FET device		X		X			
Evaluation of the data	X	X		X			X
Writing of the manuscript	X	X					X
Proposal for crediting publication equivalents	1.0						

Declaration on Consent Given by the Co-Authors

Für alle in dieser kumulativen Dissertation verwendeten Manuskripte liegen die notwendigen Genehmigungen der Verlage („reprint permissions“) für die Zweitpublikation vor.

Die Co-Autorinnen/-Autoren der in dieser kumulativen Dissertation verwendeten Manuskripte sind sowohl bei der Nutzung, als auch über die oben angegebenen Eigenanteile der weiteren Doktorandinnen/Doktoranden als Co-Autorinnen/-Autoren an den Publikationen und Zweitpublikationsrechten bei einer kumulativen Dissertation informiert und stimmen dem zu. Die Anteile des Promovenden sowie der weiteren Doktorandinnen/Doktoranden als Co-Autorinnen/Co-Autoren an den Publikationen und Zweitpublikationsrechten bei einer kumulativen Dissertation sind in der Anlage aufgeführt.

Declaration of Consent by the Supervisor

Ich bin mit der Abfassung der Dissertation als publikationsbasierte Dissertation, d.h. kumulativ, einverstanden und bestätige die vorstehenden Angaben.

Declaration of Originality/Selbständigkeitserklärung

I certify that the work presented here is, to the best of my knowledge and belief, original and the result of my own investigations, except as acknowledged, and has not been submitted, either in part or whole, for a degree at this or any other university.

Ich erkläre, dass ich die vorliegende Arbeit selbständig und unter Verwendung der angegebenen Hilfsmittel, persönlichen Mitteilungen und Quellen angefertigt habe.

Jena May, 2020

Zian Tang

Acknowledgement

I would like to extend my sincere appreciation to all the people that helped me during my PhD study!

At the first place, I want to faithfully thank my supervisor Prof. Andrey Turchanin for the patient guidance. His thorough attitude towards scientific research sets an excellent example for my future academic life, and his profound knowledge inspired me a lot in the study. I also want to thank Prof. Benjamin Dietzek for the revision of this thesis.

Science relies on communication and discussion. It is my great pleasure to work with scientists in a different research area. This experience boards my academic vision and maintains my curiosity to science. Prof. Andreas Terfort and Dr. Julian Scherr, from the Goethe University Frankfurt as well as Prof. Ulrich S. Schubert and Dr. Andreas Winter from the University of Jena, their deep understanding in organic chemistry and consummate skill in synthesis pave the way for my study. Prof Ute Kaiser from the University Ulm is an “artist” in the field of TEM. The TEM images she provided always amazed me. Prof. Daniel Rhinow from the Max Planck Institute of Biophysics, he is skilful in imaging biospecimens with cryoEM. Prof. Thomas Pertsh, Prof. Isabella Staude, Yunus Denizhan Sirmaci and Rajeshkumar Mupparapu from the University of Jena, with their help, a lot of good ideas to combine the 2D materials and the quantum optics were realized. Prof. Grégory F. Schneider and Dr. Pauline M. G. van Deursen from the Leiden University, Prof. Peter Steeneken and Masoud Seyyed Fakhrabadi from the Delft University of Technology, Prof. Heidemarie Schmidt and Sahitya Varma Vegesna from the IPHT Jena, Prof. Volker Deckert and Dr. Felix Herrmann-Westendorf from the University of Jena, they offered an excellent help for application and characterization of CNMs. I am thankful to all of them!

According to a report from Nature, a considerable amount of PhD students suffer stressful relationship with their colleagues.[§] Fortunately, I have never experienced any unpleasant situation with my colleagues. Instead, I enjoyed the relaxed, delightful and enthusiastic atmosphere in the workgroup. My colleagues, also my friends Dr. Andreas Arnlind, Anna Schmidt, Dr. Antony George, Christof Neumann, David Kaiser, Emad Najafidehaghani, Maria Küllmer, Dr. Vladislav Stroganov, and Ziyang Gan, they not only supported me to complete my study but also helped me to overcome a lot of difficulties in life. Especially Dr. Antony George, Christof Neumann, David Kaiser and Maria Küllmer, they helped me a lot for improving my language skills in English as well as in German.

Acknowledgement

The master and bachelor students also offered vital support to the group. Daniel Hüger, Martha Frey, Nikita Alistratov, Rebecka Gläßner, Verena Müller, and Xingcheng Li, they are intelligent and reliable and have made a significant contribution to the young and energetic group culture.

I am also deeply grateful to Prof. Zhikun Zheng, Prof. Wei Liu, Dr. Ihsan Amine, Dr. Tao Zhang, Dr. Maximilian Schneider and all other friends in academic society who have given me a leg-up in research and life. Without them, I will lose a lot of opportunities for improving myself. I want to sincerely thank my family, especially my parents and my wife Wenyu Li, for supporting me in all aspects.

Additionally, I would like to thank Mr. Wenmin Huo, The CEO of Runlong Ltd. in China for offering me financial support for the first four-year study.

§ Chris Woolston. PhDs: the tortuous truth. *Nature*, **2019**, 575, 403-406. DOI: 10.1038/d41586-019-03459-7